



## City Research Online

### City, University of London Institutional Repository

---

**Citation:** Poles, R. R. (1997). Free-surface flow in a shallow laterally heated cavity. (Unpublished Doctoral thesis, City, University of London)

This is the accepted version of the paper.

This version of the publication may differ from the final published version.

---

**Permanent repository link:** <https://openaccess.city.ac.uk/id/eprint/31100/>

**Link to published version:**

**Copyright:** City Research Online aims to make research outputs of City, University of London available to a wider audience. Copyright and Moral Rights remain with the author(s) and/or copyright holders. URLs from City Research Online may be freely distributed and linked to.

**Reuse:** Copies of full items can be used for personal research or study, educational, or not-for-profit purposes without prior permission or charge. Provided that the authors, title and full bibliographic details are credited, a hyperlink and/or URL is given for the original metadata page and the content is not changed in any way.

Free-surface flow in a shallow laterally heated  
cavity

by  
Richard R. Poles

Thesis submitted for the degree of  
Doctor of Philosophy

Department of Mathematics,  
City University,  
London.

February 1997

# Contents

0.1	Acknowledgments . . . . .	5
0.2	Abstract . . . . .	6
<b>1</b>	<b>Introduction</b>	<b>7</b>
1.1	The basic problem . . . . .	7
1.2	Previous work . . . . .	8
1.3	Governing equations and non-dimensionalisation . . . . .	12
1.4	Structure of the thesis . . . . .	16
<b>2</b>	<b>Steady-state solutions for the non-rotating cavity</b>	<b>18</b>
2.1	Introduction . . . . .	18
2.2	Governing equations . . . . .	19
2.3	Core flow . . . . .	21
2.4	End-regions . . . . .	22
2.5	End-zone eigenvalue problem . . . . .	24
2.6	Numerical solution of the eigenvalue problem. . . . .	25
2.7	Numerical results . . . . .	28

2.7.1	Infinite Prandtl number . . . . .	28
2.7.2	Small Prandtl number . . . . .	29
2.8	Asymptotic results for large $R_1$ . . . . .	30
2.8.1	Infinite Prandtl number . . . . .	31
2.8.2	Finite Prandtl number . . . . .	32
2.9	Asymptotic expansion of the end region solution for small $R_1$ . . . . .	33
2.10	Discussion . . . . .	42
<b>3</b>	<b>Stability of the non-rotating core flow</b>	<b>57</b>
3.1	Introduction . . . . .	57
3.2	The transverse stability equations . . . . .	58
3.2.1	Solution of the transverse stability equations . . . . .	59
3.2.2	Numerical solution of the transverse stability equations . . . . .	61
3.2.3	Numerical results . . . . .	62
3.2.4	Neutral Curves . . . . .	63
3.3	Asymptotic solution of the transverse stability equations for large $R_1$ . . . . .	65
3.3.1	Asymptotic results for $k = O(R_1^{-1})$ , $\omega = O(1)$ . . . . .	65
3.3.2	Asymptotic results for $k = O(1)$ , $\omega = O(R_1)$ . . . . .	67
3.3.3	Collapse of the neutral stability curve . . . . .	68
3.4	Stability of the core flow to longitudinal perturbations . . . . .	70

3.4.1	Solution of the perturbation equations . . . . .	71
3.4.2	Numerical results . . . . .	73
3.4.3	Asymptotic solution of the stability equations for large $R_1$ . . .	75
3.4.4	Asymptotic analysis of the reduced problem at large $k_0$ . . . .	76
3.4.5	Asymptotic analysis of the full problem with $k = O(1)$ . . . .	79
3.5	Discussion . . . . .	82
<b>4</b>	<b>Steady-state solutions for the rotating cavity</b>	<b>101</b>
4.1	Introduction . . . . .	101
4.2	Governing equations . . . . .	103
4.3	Core flow . . . . .	104
4.4	End regions . . . . .	107
4.5	Discussion . . . . .	109
<b>5</b>	<b>Steady-state solution of the rotating end zone eigenvalue problem</b>	<b>114</b>
5.1	Introduction . . . . .	114
5.2	Derivation of the eigenvalue problem . . . . .	115
5.3	Small Rayleigh numbers, $R_1 \ll 1$ . . . . .	116
5.3.1	Small $T$ . . . . .	116
5.3.2	General $T$ . . . . .	117
5.3.3	Large $T$ . . . . .	118
5.4	General Rayleigh numbers . . . . .	123
5.5	Large Rayleigh numbers, $R_1 \gg 1$ . . . . .	124

5.6	Discussion . . . . .	132
<b>6</b>	<b>Solutions for the rotating end zones at low Rayleigh numbers</b>	<b>141</b>
6.1	Introduction . . . . .	141
6.2	End region solution for small $R_1$ and general $T$ . . . . .	142
6.3	Leading order end-zone solution for general $T$ . . . . .	145
6.4	Numerical results . . . . .	149
6.5	Leading order end zone solution for small $T$ . . . . .	151
6.6	Leading order end zone solution for large $T$ . . . . .	153
6.7	Discussion . . . . .	155
<b>7</b>	<b>Conclusion</b>	<b>164</b>
7.1	Summary . . . . .	164
7.2	Future work . . . . .	167

## 0.1 Acknowledgments

I am very grateful to my supervisor, Professor P.G. Daniels, whose encouragement and advice have not only been of great assistance in the research and presentation of this thesis, but have made it most enjoyable. I would also like to thank Dr N.G. Wright for the useful discussions about, and the use of, his numerical multigrid algorithm. The financial support for the work in this thesis was provided by the Engineering and Physical Sciences Research Council.

I grant powers of discretion to the University Librarian to allow this thesis to be copied in whole or in part without further reference to me. This permission covers only single copies made for study purposes, subject to normal conditions of acknowledgement.

## 0.2 Abstract

This thesis is concerned with free surface flow in a non-rotating or rotating shallow laterally heated cavity which is assumed to be of infinite length in the third dimension. The flow is driven by a horizontal temperature difference: the two vertical walls are kept at constant, but different, temperatures, giving rise in general to a large scale circulation known as a Hadley cell. The flow is considered to be subdivided into three main regions: a parallel-flow core region away from the end walls and two end zones close to the vertical walls where the fluid is turned through 180 degrees. This study is concerned with identifying the main features of both the basic flow and temperature fields generated in the cavity and, in the non-rotating case, with the stability of that flow.

There are two main parts to this thesis: the first part is dedicated to the flow in the non-rotating cavity and, in the second part, the flow in the rotating cavity is considered. In each case the steady-state free surface problem is initially studied. An analytical solution for the parallel-flow core is found; the flow in the end regions close to the vertical walls is then investigated. Results are presented which determine the extent of these regions. These complement asymptotic results which are found for large Rayleigh number (based on the temperature difference between the vertical walls and cavity depth) in the non-rotating case and small Rayleigh number in the limit of large rotation rate. Asymptotic solutions are also found in the limit of large Rayleigh number and rotation rate where a novel boundary layer structure is identified near the horizontal surfaces.

The linear stability of the non-rotating parallel-flow core is investigated. Here the neutral curves which delineate the boundary for which instabilities persist are found and an investigation of the large Rayleigh number behaviour of the neutral curves is undertaken.

Numerical and analytical methods are used to give complete solutions for the flow in the end regions from the small rotation rate limit where the solutions match with the non-rotating results to the large rotation rate limit where the double vertical boundary-layer structure identified by the asymptotic analysis evolves.

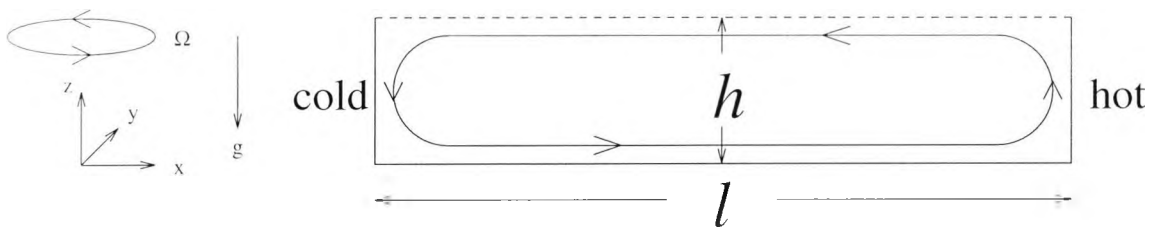
# Chapter 1

## Introduction

### 1.1 The basic problem

This thesis is concerned with free surface flow in a non-rotating or rotating shallow laterally heated cavity. This chapter starts with an explanation of the basic problem and its geometry, and then gives examples of why this flow is of interest and of work that has been done before. The non-dimensional governing equations used as a basis for study throughout the thesis are derived and an outline of the structure and content of the thesis is given.

Fluid is contained within a rectangular cavity, the depth of which ( $h$ ) is generally much less than the length,  $l$ , and hence is described as shallow. It is assumed to be of infinite length in the third dimension, or equivalently may be viewed as the cross section of a large annulus. The cavity is assumed to be lid-less, that is the upper surface of the fluid is free, and the problem is thus distinct from that with a rigid upper surface for which there is much previous work and with which comparisons will be made. The geometry is represented in the diagram below.



The flow is driven by a horizontal temperature difference: the two vertical

walls are kept at constant, but different, temperatures. The two horizontal surfaces are taken to be adiabatic, that is thermally insulating. Gravity acts downwards and the density of the fluid is assumed to decrease linearly with increases in temperature, so that motion is generated by buoyancy forces. Close to the hotter of the two end walls, the fluid becomes less dense and rises, and closer to the cooler end the fluid becomes more dense and sinks, giving rise in general to a large scale circulation of the type shown diagrammatically above. This is known as a Hadley cell after consideration of the motion of the atmosphere generated by equatorial–polar temperature differences by Hadley (1735). For a shallow cavity it is often possible to consider the flow to be subdivided into three main regions: a core region away from the end walls where the flow near the top is moving from the hot wall to the cold wall and is returning at the bottom, and two end zones close to the vertical walls where the fluid is turned through 180 degrees.

The effect on the flow of rotation of the cavity with angular velocity  $\Omega$  is addressed in the second half of the thesis. The cavity is rotated about a vertical axis as indicated in the diagram above. In the rotating problem there is a component of flow perpendicular to the Hadley cell which in the geophysical context resembles the trade-winds in the atmosphere of the tropics. This study is concerned with identifying the main features of both the basic flow and temperature fields generated in the cavity and, in the non-rotating case, with the stability of that flow.

## 1.2 Previous work

Much of the previous work on shallow rotating or non-rotating laterally heated systems has been motivated by applications to the large scale motions of the atmosphere and oceans (Hadley 1735, Jeffreys 1925, Defant 1961, Stern 1975). However, there has also been interest in flows in a shallow laterally heated rectangular cavity in connection with the process of growing metal and semi-conductor crystals from a liquid melt by the gradient-freeze technique (Hurle 1966, Hurle *et al.* 1974). Such flows are also of interest in relation to the dynamics of shallow estuaries where the temperature gradient may be caused naturally or by the discharge of pollutants into the estuary (Cormack *et al.* 1974). Other technological examples where convective motion is driven by temperature gradients not aligned with the gravitational field

include cooling systems for nuclear reactors (Boyack and Kearney 1972) and solar collectors (Bejan and Rossie 1981).

Early theoretical work such as that of Batchelor (1954) and Gill (1966) concentrated on the two dimensional tall or square cavity with applications to the heat transfer across the air gap between walls in buildings. The steady non-rotating flow in a shallow laterally heated rectangular cavity has been studied before, but mostly for the case of a rigid upper surface. In a series of papers by Cormack, Leal and Imberger (1974), Cormack, Leal and Seinfeld (1974) and Imberger (1974), an asymptotic theory, numerical solutions and experimental results, were presented respectively. The asymptotic theory regarded the flow in the cavity as composed of two symmetric end-regions and a parallel flow core, the solutions for which were matched asymptotically to gain a leading order solution valid throughout the cavity for Rayleigh numbers (based on the cavity height  $h$ ) small compared with the cavity aspect ratio ( $l/h$ ). This result was then compared with the numerical solutions for square and shallow cavities and the experimental results for shallow cavities. Further experimental results at higher Rayleigh numbers were presented by Bejan, Al-Homoud and Imberger (1981) and a parameter range determined for which the parallel-flow core solution is valid. Hart(1983a) also discussed the range of parameters for which there are separate end-regions near the vertical walls, and a parallel-flow core, and presented numerical solutions for the nonlinear motion in the end regions at general Rayleigh numbers comparable with the cavity aspect ratio. The behaviour of the temperature and flow in the end regions was investigated in detail by Daniels, Blythe and Simpkins (1987) for general Rayleigh number and finite and infinite Prandtl numbers, by assuming that the edge behaviour in the end zones could be represented by the sum of an infinite number of eigenfunctions which decay into a parallel-flow core. Their analysis includes a determination of the size of the end regions, obtained numerically for general Rayleigh number and asymptotically for Rayleigh numbers large compared with the cavity aspect ratio. Wang and Daniels (1994a,b) obtained full numerical solutions for the end zones for both adiabatic and conducting horizontal boundaries and Wright, Gaskell and Sleigh (1995) presented numerical solutions for the whole cavity. Other numerical investigations have been reported, for example by Quon (1972) and Shiralkar and Tien (1981) and other experimental work includes that by Rossby (1965), Simpkins and Dudderar (1981) and Simpkins and Chen (1986). Daniels and Wang (1994) discussed the evolution of the flow in a shallow cavity for Rayleigh numbers comparable with the

aspect ratio using a combination of asymptotic and numerical methods.

Cormack, Stone and Leal (1975) examined the effect of upper surface boundary conditions on the non-rotating flow, including the case with adiabatic horizontal boundaries and a stress-free upper surface, and presented asymptotic solutions for the end-regions for low Rayleigh numbers and large aspect ratio. The geophysical application of free-surface flows in rectangular channels with surface cooling has been studied by Sturm (1981) and by Jain (1982) for sidearms of cooling lakes of water from electricity power generation. The response of a wedge shaped sidearm to diurnal heating and cooling is presented by Farrow and Patterson (1993).

There has been considerable discussion of the stability of the non-rotating parallel-flow core, both analytical and experimental. Gill (1974) considered the stability of the flow in a cavity with both horizontal surfaces either rigid or free, and compared his analytical solutions with the experimental results of Skafel (1972) and Hurle, Jakeman and Johnson (1974), who included the stabilising effect of a transverse magnetic field in their free surface experiments with gallium. Hart (1972) presented neutral stability curves for oscillatory perturbations in the rigid surface case, and later (Hart 1983b) for the rigid and free surface cases for the onset of longitudinal and transverse instabilities – with axes parallel and perpendicular to the core flow respectively. Results for the free surface transverse mode of instability were not presented. As in Gill (1974), there was discussion of the “strong geometric effects” that make comparisons with the results of experiments difficult. Laure and Roux (1989) also presented neutral curves for the rigid and free surface cases and gave plots of the streamlines and isotherms of the perturbations and an indication of their effect on the core flow. Kuo and Korpela (1987) discussed transverse and longitudinal instabilities at small Prandtl number for the rigid surface case. In all of this previous work, the results which are presented focus on the ‘critical’ parameter values, including the lowest values at which instabilities occur, and the neutral curves are not discussed in detail for general values of the parameters.

Other related work, but excluding the effect of buoyancy, includes that by Smith and Davis (1983) who considered the instability of the dynamic thermocapillary layer. The stability of the combined buoyancy and thermocapillary driven flow at small Prandtl number was considered numerically by Ben Hadid and Roux (1992).

In the rotating case there is a body of work for tall laterally heated cavities, including that by Fowlis and Hide (1965) and Hide (1967) which gives a range of parameters for which there is axisymmetric flow in an annulus with differentially heated walls. Both free and rigid upper surfaces are considered. The theory for an axisymmetric annulus with a square cross section and rigid upper surface is given by McIntyre (1968) for large Prandtl number. The application of a rotating laterally-heated cavity to the planetary equatorial–polar temperature difference and to the atmosphere of Venus is discussed by Stone (1968), who considers a shallow cavity with a free upper surface, but driven by a varying heat flux on the horizontal boundaries. Other theoretical work on convection induced between rotating planes includes that by Robinson (1959) and Duncan (1966) while Douglas and Mason (1973) describe experiments in an annulus with differentially heated walls and a rigid upper surface designed to determine the temperature structure and the transition from axisymmetric to non-axisymmetric flow for a range of aspect ratios. The asymptotic structure of the rapidly rotating, small Rayleigh number flow driven by differentially heated vertical walls in a rectangular cavity was considered by Hunter (1967) for both the free and rigid upper surface cases. The boundary layer structure was described in detail: the horizontal flow is confined to thin Ekman layers close to the horizontal boundaries, and the vertical flow is confined to thin Stewartson layers (Stewartson 1957) close to the vertical walls; in the free surface case there are double Stewartson layers. The flow induced in a rotating annulus by a radial temperature gradient along the lower horizontal surface was considered at large rotation rates by Daniels (1976), who made comparisons between this theoretical work and experiments reported by Stern (1975). Further aspects of the flow and its stability were considered in a series of papers by Daniels and Stewartson (1977, 1978a,b).

The structure of a rapidly rotating fluid in a shallow cylinder was considered by Dijkstra and van Heijst (1983), and the effect of rotation on many fluid flows is discussed in the review by Hopfinger and Linden (1990). The effect of the free-surface on spin-up of a fluid in a cylinder is studied by O'Donnell and Linden (1991). Experiments on the spin-up and spin-down on a  $\beta$  plane are presented by Williams and Maxworthy (1994); the spin-up of fluid in a rectangular container with a sloping base is considered by van Heijst, Maas and Williams (1994). Hignett *et al.* (1981) considered rotating thermal convection in a cylinder with a radial temperature gradient supplied from below and more recently Miller and Reynolds

(1991) presented experimental results on thermal convection in a rotating annulus. The effect of topography was discussed by Bell and Soward (1996). The instability of flow in a differentially heated rotating annulus has been investigated by Busse (1986), Busse and Or (1986) and Or and Busse (1987), and in a rotating channel by Finlay (1990). The transition to turbulent flow was discussed by Finlay (1992) and by Kristoffersen and Andersson (1993). The instability of the boundary layer on a rotating disk has been studied by Lingwood (1995) and experimental results presented by Lingwood (1996).

### 1.3 Governing equations and non-dimensionalisation

The dynamic equations with respect to a coordinate system rotating with uniform angular velocity  $\Omega^*$ , representing the conservation of mass, momentum and energy, as given by Greenspan (1968), are

$$\frac{\partial \rho^*}{\partial t^*} + \nabla^* \cdot (\rho^* \mathbf{u}^*) = 0, \quad (1.3.1)$$

$$\rho^* \left[ \frac{\partial \mathbf{u}^*}{\partial t^*} + (\mathbf{u}^* \cdot \nabla^*) \mathbf{u}^* + 2\Omega^* \times \mathbf{u}^* \right] = -\nabla p^* - \rho^* \Omega^* \times (\Omega^* \times \mathbf{x}^*) + \rho^* \mathbf{F} + \mu \nabla^{*2} \mathbf{u}^* + \left( \lambda + \frac{1}{3} \mu \right) \nabla^* \nabla^* \cdot \mathbf{u}^*, \quad (1.3.2)$$

and

$$\rho^* c_p \left( \frac{\partial \theta^*}{\partial t^*} + \mathbf{u}^* \cdot \nabla^* \theta^* \right) + \frac{\theta^*}{\rho^*} \frac{\partial \rho^*}{\partial \theta^*} \left( \frac{\partial p^*}{\partial t^*} + \mathbf{u}^* \cdot \nabla^* p^* \right) = \alpha \nabla^{*2} \theta^* - \frac{2}{3} \mu (\nabla^* \cdot \mathbf{u}^*)^2 + \lambda (\nabla^* \cdot \mathbf{u}^*)^2 + \mu [\nabla^{*2} \mathbf{u}^* \cdot \mathbf{u}^* + 2 \nabla^* \cdot (\nabla^* \times \mathbf{u}^*) \times \mathbf{u}^* - 2 \mathbf{u}^* \cdot \nabla^* \nabla^* \cdot \mathbf{u}^* + \nabla^* \times \mathbf{u}^* \cdot \nabla^* \times \mathbf{u}^*], \quad (1.3.3)$$

where  $\lambda$  is the bulk viscosity,  $\mu$  is the coefficient of viscosity,  $\kappa$  is the thermal diffusivity,  $c_p$  is the specific heat capacity at constant pressure,  $\alpha$  is the thermal conductivity,  $\rho^*$  is the density and  $p^*$  is the pressure. The Cartesian coordinates  $\mathbf{x}^* = (x^*, y^*, z^*)$  have their origin at the axis of rotation such that  $z^*$  is in the vertical direction and  $x^*$  and  $y^*$  are in the horizontal plane. The velocity relative to the rotating frame is  $\mathbf{u}^* = (u^*, v^*, w^*)$ , where  $u^*$ ,  $v^*$  and  $w^*$  are the components in the  $x^*$ ,  $y^*$  and  $z^*$  directions respectively, and  $\theta^*$  is the temperature. The external force per unit mass is denoted by  $\mathbf{F}$  and  $t^*$  is the time.

The acceleration due to gravity,  $g$ , acts in the negative  $z^*$  direction, and the

frame of reference is rotating around the  $z^*$  axis so that

$$\mathbf{F} = -g\hat{\mathbf{k}} \quad \text{and} \quad \boldsymbol{\Omega}^* = \Omega\hat{\mathbf{k}}, \quad (1.3.4)$$

where  $\hat{\mathbf{k}}$  is the unit vector in the  $z^*$  direction. Density differences are assumed to be linearly dependent on temperature, so that

$$\rho^* = \rho_0(1 - \beta(\theta^* - \theta_c^*)), \quad (1.3.5)$$

where  $\rho_0$  is the density at temperature  $\theta_c^*$ , and  $\beta$  is the coefficient of thermal expansion. The Oberbeck–Boussinesq approximation is used so that the variation of density is assumed negligible apart from when multiplied by  $g$ .

The cavity is at rest relative to the rotating frame with its cross section lying parallel to the  $x^*, z^*$  plane and its vertical walls located at  $x^* = hx_0$  and  $x^* = hx_1$ . A length scale,  $x$ , is introduced, non-dimensionalised with respect to the depth of the cavity,  $h$ , such that  $\mathbf{x}^* = h(x + x_0, y, z)$ . The cavity is therefore assumed to lie between  $z = 0$  and  $z = 1$  and between  $x = 0$  and  $x = x_1 - x_0 = L$ , where  $L$  is the aspect ratio of the cavity  $L = l/h$ . The velocity field  $\mathbf{u}^*$  and the time  $t^*$  are non-dimensionalised with respect to the thermal diffusivity,  $\kappa$ , and  $h$ , so that

$$\mathbf{u}^* = \bar{\mathbf{u}} \frac{\kappa}{h} \quad \text{and} \quad t^* = \frac{h^2}{\kappa} t. \quad (1.3.6)$$

The two vertical walls of the cavity  $x = 0$  and  $x = L$  are held at constant temperature  $\theta_c^*$  and  $\theta_h^*$  respectively with  $\theta_h^* > \theta_c^*$ , and a temperature  $\bar{\theta}$  is introduced, non-dimensionalised with respect to the temperature difference between the two vertical walls. Thus

$$\theta^* = \theta_c^* + \bar{\theta}(\theta_h^* - \theta_c^*), \quad (1.3.7)$$

so that the temperature on the cold wall is  $\bar{\theta} = 0$  and on the hot wall is  $\bar{\theta} = 1$ . The centrifugal terms are included with the pressure so that a scaled non-dimensional pressure  $\bar{p}$  is introduced such that

$$\nabla p^* = \nabla(\rho_0 \frac{\kappa^2}{h^2} \bar{p}) - \rho_0 g \hat{\mathbf{k}} - \rho_0 \Omega^2 \hat{\mathbf{k}} \times (\hat{\mathbf{k}} \times \mathbf{x}^*). \quad (1.3.8)$$

At the free surface the stress in the fluid must vanish and to a first approximation the pressure  $p^*$  is constant. In order that in the rotating case  $p^*$  is constant on the free surface, and since the modified pressure  $\bar{p}$  will be small compared to the hydrostatic pressure generated by gravity, (1.3.8) implies a change in the height of the free

surface with  $x$ . For the free surface to be taken as level to a first approximation, it is necessary for this change in height to be small compared to the depth of the cavity,  $h$ . On integrating (1.3.8) and since the far end of the cavity is at distance  $hx_1$  from the axis of rotation, the requirement for a small change in height across the cavity is

$$\frac{\Omega^2 h^2 x_1^2}{2g} \ll h \quad (1.3.9)$$

which can be written as an inequality for the ratio of the centrifugal and gravitational accelerations,

$$\frac{\Omega^2 h x_1}{g} \ll 2x_1^{-1}. \quad (1.3.10)$$

Thus, for sufficiently large gravitational acceleration, the height of the free surface can be taken as constant, and the boundary conditions are defined below for such a surface.

With these assumptions the dynamic equations become

$$\nabla \cdot \bar{\mathbf{u}} = 0, \quad (1.3.11)$$

$$\frac{\partial \bar{\mathbf{u}}}{\partial t} + (\bar{\mathbf{u}} \cdot \nabla) \bar{\mathbf{u}} + \sigma T^{\frac{1}{2}} (\hat{\mathbf{k}} \times \bar{\mathbf{u}}) = -\nabla \bar{p} + R\sigma \bar{\theta} \hat{\mathbf{k}} + \sigma \nabla^2 \bar{\mathbf{u}} \quad (1.3.12)$$

and

$$\begin{aligned} \frac{\partial \bar{\theta}}{\partial t} + \bar{\mathbf{u}} \cdot \nabla \bar{\theta} &= \nabla^2 \bar{\theta} \\ &+ \frac{h\beta g}{c_p} R^{-1} [\nabla^2 \bar{\mathbf{u}} \cdot \bar{\mathbf{u}} + 2\nabla \cdot (\nabla \times \bar{\mathbf{u}}) \times \bar{\mathbf{u}} + \nabla \times \bar{\mathbf{u}} \cdot \nabla \times \bar{\mathbf{u}}], \end{aligned} \quad (1.3.13)$$

where the three non-dimensional numbers — the Rayleigh, Taylor and Prandtl numbers — are defined by

$$R = \beta g (\theta^*_h - \theta^*_c) h^3 / \nu \kappa, \quad T = \frac{4\Omega^2 h^4}{\nu^2} \text{ and } \sigma = \frac{\nu}{\kappa}, \quad (1.3.14)$$

respectively. The last term in the energy equation is usually assumed to be small, which is the case if

$$\frac{h\beta g}{c_p} R^{-1} \ll 1, \quad (1.3.15)$$

and then the non-dimensional governing equations are

$$\nabla \cdot \bar{\mathbf{u}} = 0, \quad (1.3.16)$$

$$\frac{\partial \bar{\mathbf{u}}}{\partial t} + (\bar{\mathbf{u}} \cdot \nabla) \bar{\mathbf{u}} + \sigma T^{\frac{1}{2}} (\hat{\mathbf{k}} \times \bar{\mathbf{u}}) = -\nabla p + R\sigma \bar{\theta} \hat{\mathbf{k}} + \sigma \nabla^2 \bar{\mathbf{u}} \quad (1.3.17)$$

and

$$\frac{\partial \bar{\theta}}{\partial t} + \bar{\mathbf{u}} \cdot \nabla \bar{\theta} = \nabla^2 \bar{\theta}. \quad (1.3.18)$$

The boundary conditions are now considered. The horizontal and vertical velocity components must vanish on the three solid boundaries, but on the upper surface only the vertical component of velocity vanishes. Then the requirement that the tangential stress vanishes on the upper surface implies that the first derivatives of the horizontal velocity components vanish. This gives the conditions

$$\bar{u} = \bar{v} = \bar{w} = 0 \text{ on } x = 0 \text{ and } x = L, \quad (1.3.19)$$

$$\bar{u} = \bar{v} = \bar{w} = 0 \text{ on } z = 0 \quad (1.3.20)$$

and

$$\bar{u}_z = \bar{v}_z = \bar{w} = 0 \text{ on } z = 1. \quad (1.3.21)$$

Strictly speaking the free surface conditions should derive from the requirement that the three components of stress vanish at the free surface. In practice these conditions would only be satisfied in general through a displacement of the free surface from the horizontal. As mentioned earlier, this displacement effect will be assumed sufficiently small to be neglected, and given that the free surface is horizontal, it follows that to a first approximation  $\bar{w} = 0$  there. As stated previously, the temperatures at the two vertical walls are

$$\bar{\theta} = 0 \quad \text{on } x = 0 \text{ and } \quad \bar{\theta} = 1 \text{ on } x = L, \quad (1.3.22)$$

and the two horizontal surfaces are taken to be adiabatic so that

$$\bar{\theta}_z = 0 \text{ on } z = 0 \text{ and } z = 1. \quad (1.3.23)$$

In the case of a flow which has no  $y$  dependence, the system can be simplified by using a two dimensional stream function  $\bar{\psi}$  such that

$$\bar{\mathbf{u}} = (\bar{\psi}_z, \bar{v}, -\bar{\psi}_x), \quad (1.3.24)$$

where the subscripts denote the partial derivative. The conservation of mass equation (1.3.16) is then satisfied and the other two equations (1.3.17) and (1.3.18) become

$$\nabla^4 \bar{\psi} - R \frac{\partial \bar{\theta}}{\partial x} + T^{\frac{1}{2}} \frac{\partial \bar{v}}{\partial z} = \sigma^{-1} \frac{\partial}{\partial t} (\nabla^2 \bar{\psi}) + \sigma^{-1} \frac{\partial (\nabla^2 \bar{\psi}, \bar{\psi})}{\partial (x, z)}, \quad (1.3.25)$$

$$\nabla^2 \bar{v} - T^{\frac{1}{2}} \frac{\partial \bar{\psi}}{\partial z} = \sigma^{-1} \frac{\partial \bar{v}}{\partial t} + \sigma^{-1} \frac{\partial (\bar{v}, \bar{\psi})}{\partial (x, z)}, \quad (1.3.26)$$

and

$$\nabla^2 \bar{\theta} = \frac{\partial \bar{\theta}}{\partial t} + \frac{\partial(\bar{\theta}, \bar{\psi})}{\partial(x, z)}, \quad (1.3.27)$$

The boundary conditions in this case are now

$$\bar{\psi} = \bar{\psi}_x = \bar{v} = 0 \text{ on } x = 0, L, \quad (1.3.28)$$

$$\bar{\psi} = \bar{\psi}_z = \bar{v} = 0 \text{ on } z = 0, \quad (1.3.29)$$

and

$$\bar{\psi} = \bar{\psi}_{zz} = \bar{v}_z = 0 \text{ on } z = 1. \quad (1.3.30)$$

The temperature conditions remain unchanged.

## 1.4 Structure of the thesis

There are two main parts to this thesis: the first part is dedicated to the flow in the non-rotating cavity and, in the second part, the flow in the rotating cavity is considered. In each case the theory is based on an assumption that the cavity aspect ratio  $L$  is large.

In chapter 2, the steady-state free surface problem for the non-rotating cavity is studied. The flow in this case is two dimensional. An analytical solution for the parallel-flow core is found, and the flow in the end regions close to the vertical walls is then investigated. At low Rayleigh numbers an analytical solution valid throughout the whole cavity is found, similar to that found numerically by Cormack, Leal and Stone (1975). For general Rayleigh numbers  $R$  comparable with the aspect ratio  $L$ , an eigenvalue analysis is used to determine the effect of the Rayleigh and Prandtl numbers on the size of the end regions. The numerical scheme for solving the eigenvalue problem, which is used extensively in various forms throughout this work is described in detail in this chapter. The results of the numerical work complement asymptotic results that are obtained for large Rayleigh number. A comparable study of the end-regions in the rigid surface case was carried out by Daniels, Blythe and Simpkins (1987), but the free surface case has not previously been considered.

The linear stability of the non-rotating parallel-flow core is investigated in chapter 3. Neutral curves which delineate the boundary of values of the Rayleigh

number, Prandtl number and wavenumbers for which instabilities persist, are presented for both transverse and longitudinal perturbations, and the structure of the perturbed flow is discussed. Previous results pertaining to the free surface have been obtained by Hart (1983) and Laure and Roux (1989), but only for the critical points at which instabilities are first sustainable. Here the neutral curves are found for general Rayleigh number, Prandtl number and wavenumbers and an investigation of the large Rayleigh number behaviour of the neutral curves is undertaken. The physical implications of the results are discussed.

The steady-state free surface problem for the rotating cavity is introduced in chapter 4. The governing equations are derived for the core and the end-regions for general Rayleigh numbers comparable with the aspect ratio  $L$  and for general Taylor and Prandtl numbers, and an analytical parallel-flow core solution is found. Here the core flow is three dimensional and dependent on the rotation speed. For large Taylor number, Ekman layers develop near the horizontal surfaces and the solution relates to that determined by Hunter (1967).

Chapter 5 concentrates on the properties of the rotating end-regions. Eigenvalue results are presented for general Taylor and Rayleigh numbers which determine the extent of these regions and complement asymptotic results which are found for large Taylor number and small Rayleigh number. Asymptotic solutions are also found in the limit of large Rayleigh and Taylor numbers where a novel boundary layer structure is identified near the horizontal surfaces. Comparison is also made with asymptotic solutions for small Taylor number which relate to the non-rotating case studied in chapter 2.

Numerical and analytical methods are used in chapter 6 to give complete solutions for the flow in the end regions for small Rayleigh number and general Taylor number. These allow the evolution of the flow with increasing Taylor number to be traced from the small Taylor number limit where the solutions match with the non-rotating results of chapter 2, to the large Taylor number limit where the double vertical boundary-layer structure identified by Hunter (1967) evolves.

The results are summarised in chapter 7 and an indication is given of possible avenues for future research.

## Chapter 2

# Steady-state solutions for the non-rotating cavity

### 2.1 Introduction

The steady free-surface flow in a shallow non-rotating rectangular two dimensional cavity subject to a horizontal temperature gradient is considered in this chapter. Initially an exact parallel-flow solution is found for the core region away from the end walls. This core-flow is turned through 180 degrees in approximately square regions near the end walls, where the flow is fully nonlinear for Rayleigh numbers comparable to the cavity aspect ratio. The solution of the two end-region problems is shown to lead to the determination of the first order correction to the flow and temperature fields in the core of the cavity. At general Rayleigh numbers the behaviour of the end-regions away from the vertical walls is characterised by an infinite number of eigenfunctions which decay exponentially away from the walls; the corresponding eigenvalues control the distance into the core that these end-zones encroach.

The behaviour of the eigenvalues with respect to the Rayleigh and Prandtl numbers is investigated by numerical solution of the eigenvalue problem, and a limiting form of the eigenvalues for large Rayleigh number is found. This strategy was employed by Daniels, Blythe and Simpkins (1987) for the rigid surface cavity and comparisons of the end region size for the two different surface conditions are made.

Unlike the rigid surface problem for which there exist symmetries discussed by Gill (1966), in the free surface case there are no symmetries and so both hot and cold end-zones require individual consideration. Also, there appear to be no multicellular steady-solutions of the type obtained for the rigid surface by Hart (1983) and Daniels *et al.* (1987).

An analytical solution of the end-zone problem is then presented where the solution is considered as an asymptotic expansion in small Rayleigh number. This is similar to the large aspect ratio expansion performed by Cormack, Stone and Leal (1975) but is based on an analytical rather than a numerical solution of the governing equations. The results of this expansion determine the first order correction to the core solution explicitly for small Rayleigh numbers. The results are also compared with a full solution of the end region problem obtained using a multigrid algorithm.

## 2.2 Governing equations

The system considered here is a rectangular two dimensional cavity of length  $l$  and height  $h$ . The left hand vertical wall is at temperature  $\theta_c^*$  and the right hand wall is at temperature  $\theta_h^* > \theta_c^*$ . The bottom of the cavity is rigid and adiabatic; the top is adiabatic, but has no rigid boundary.

Coordinates are non-dimensionalised with respect to the height  $h$ , such that the cavity lies between  $z = 0$  and  $1$ , and  $x = 0$  and  $L$ , where  $L = l/h$ . The temperature is non-dimensionalised with respect to the temperature difference  $\theta_h^* - \theta_c^*$ , and is measured relative to the cold wall. The stream-function  $\bar{\psi}$  is made dimensionless with respect to the thermal diffusivity,  $\kappa$ .

As shown in section 1.3, subject to the Boussinesq approximation, the steady dimensionless vorticity and energy equations for the non-rotating cavity are

$$\nabla^4 \bar{\psi} - R \frac{\partial \bar{\theta}}{\partial x} = \sigma^{-1} \frac{\partial(\nabla^2 \bar{\psi}, \bar{\psi})}{\partial(x, z)}, \quad (2.2.1)$$

$$\nabla^2 \bar{\theta} = \frac{\partial(\bar{\theta}, \bar{\psi})}{\partial(x, z)}. \quad (2.2.2)$$

Here the Prandtl number

$$\sigma = \frac{\nu}{\kappa}, \quad (2.2.3)$$

where  $\nu$  is the kinematic viscosity and  $\kappa$  is the thermal diffusivity; the Rayleigh number

$$R = \beta g (\theta_h^* - \theta_c^*) h^3 / \nu \kappa, \quad (2.2.4)$$

where  $\beta$  is the coefficient of thermal expansion and  $g$  is the acceleration due to gravity.

The boundary conditions are

$$\bar{\psi} = \frac{\partial \bar{\psi}}{\partial z} = \frac{\partial \bar{\theta}}{\partial z} = 0 \text{ on } z = 0, \quad (2.2.5)$$

$$\bar{\psi} = \frac{\partial^2 \bar{\psi}}{\partial z^2} = \frac{\partial \bar{\theta}}{\partial z} = 0 \text{ on } z = 1, \quad (2.2.6)$$

$$\bar{\psi} = \frac{\partial \bar{\psi}}{\partial x} = 0 \text{ on } x = 0, L, \quad (2.2.7)$$

$$\bar{\theta} = 0 \text{ on } x = 0, \quad \bar{\theta} = 1 \text{ on } x = L. \quad (2.2.8)$$

In keeping with previous work (Cormack, Leal and Imberger 1974; Daniels, Blythe and Simpkins 1987; Hart 1983) the aspect ratio of the cavity is considered to be large,  $L \gg 1$ . It was noted by Daniels *et al.* (1987) that for the rigid surface case there are strong non-linear effects in the end regions when the Rayleigh number  $R$  is comparable with the aspect ratio  $L$ , or equivalently when

$$R_1 = R/L = O(1). \quad (2.2.9)$$

This is the parameter range investigated here. The strategy employed in solving this problem follows that of Daniels *et al.* (1987). An exact parallel-flow solution is found for the core — the region away from the vertical walls. Near the ends the flow is turned through 180 degrees by local nonlinear adjustments to this core flow which decay exponentially away from the walls; this decay is described by solving an eigenvalue problem obtained on substituting the perturbed core flow into the governing equations.

There are no symmetry properties for this system of the type described by Gill (1966) for the system with a rigid upper surface. Therefore there are distinct solutions associated with the end regions near the hot and cold walls.

## 2.3 Core flow

In the core region away from the end walls, the order one variable  $\xi = x/L$  is used so that  $0 < \xi < 1$ . In this region the flow is parallel to the horizontal boundaries and the temperature is linearly dependent on  $\xi$ , equivalent to an exact solution of the Boussinesq equations obtained by setting

$$\bar{\psi} = f(z), \quad (2.3.1)$$

$$\bar{\theta} = A\xi + g(z), \quad (2.3.2)$$

for some constant  $A$  and functions  $f(z)$  and  $g(z)$ .

The governing equation (2.2.1) then simplifies to

$$f^{iv} = R_1 A, \quad (2.3.3)$$

with  $f = f' = 0$  on  $z = 0$  and  $f = f'' = 0$  on  $z = 1$ , where primes denote derivatives with respect to  $z$ . This has the solution

$$f = \frac{R_1 A}{24} \left( z^4 - \frac{5}{2} z^3 + \frac{3}{2} z^2 \right). \quad (2.3.4)$$

From (2.2.2)

$$g'' = A f' L^{-1}, \quad (2.3.5)$$

with  $g' = 0$  on  $z = 0, 1$ . On substitution of (2.3.4) into (2.3.5), and consideration of the boundary conditions,

$$g = \frac{A^2 R_1}{24L} \left( \frac{1}{5} z^5 - \frac{5}{8} z^4 + \frac{1}{2} z^3 \right) + B, \quad (2.3.6)$$

where  $B$  is a constant.

By defining

$$G(z) = \frac{1}{120} z^5 - \frac{5}{192} z^4 + \frac{1}{48} z^3 \quad (2.3.7)$$

the parallel-flow core solution can be written as

$$\bar{\psi} = R_1 A G', \quad (2.3.8)$$

$$\bar{\theta} = A\xi + B + R_1 A^2 G L^{-1}. \quad (2.3.9)$$

In order that the boundary conditions for  $\bar{\theta}$  are satisfied at the two end walls, it is necessary that

$$A = 1 + L^{-1} A_1 + \dots \quad (2.3.10)$$

and

$$B = 0 + L^{-1}B_1 + \dots \quad (2.3.11)$$

in the limit as  $L \rightarrow \infty$ . The order  $L^{-1}$  corrections are generated by the temperature field produced in the end regions of the cavity to be considered in section 2.4 below.

Plots of  $G$ ,  $G'$  and  $G''$  against  $z$  are given in figure 2.1. These show graphically how the temperature, stream function and horizontal velocity depend upon  $z$ . The graph of  $G$  shows how the temperature increases towards the top of the cavity; that of  $G''$  shows that the hotter fluid moving towards the cold wall occupies approximately the top 40% of the cavity: when  $G'' = 0$ ,  $z = 0.578$ .

The results (2.3.8)–(2.3.11) can also be obtained by formally expanding the solution in inverse powers of  $L$  and solving the individual problems which arise at each order of magnitude in the Boussinesq system. In summary, the core solution can be expanded in the form

$$\left. \begin{aligned} \bar{\psi} &= R_1 G'(1 + L^{-1}A_1) + O(L^{-2}) \\ \bar{\theta} &= \xi + L^{-1}(A_1\xi + B_1 + R_1G) + O(L^{-2}) \end{aligned} \right\} (L \rightarrow \infty). \quad (2.3.12)$$

## 2.4 End-regions

The flow is turned through 180 degrees in approximately square regions at the end walls. Near the cold wall

$$\bar{\psi} = \psi(x, z) + \dots, \quad \bar{\theta} = L^{-1}\theta(x, z) + \dots, \quad (L \rightarrow \infty), \quad (2.4.1)$$

and substitution into (2.2.1) and (2.2.2) shows that  $\psi$  and  $\theta$  satisfy the full governing equations with  $R$  replaced by  $R_1$ :

$$\nabla^4\psi - R_1\frac{\partial\theta}{\partial x} = \sigma^{-1}\frac{\partial(\nabla^2\psi, \psi)}{\partial(x, z)}, \quad (2.4.2)$$

$$\nabla^2\theta = \frac{\partial(\theta, \psi)}{\partial(x, z)}. \quad (2.4.3)$$

The solution must satisfy the wall conditions

$$\psi = \frac{\partial\psi}{\partial x} = \theta = 0 \text{ on } x = 0, \quad (2.4.4)$$

$$\psi = \frac{\partial\psi}{\partial z} = \frac{\partial\theta}{\partial z} = 0 \text{ on } z = 0, \quad (2.4.5)$$

and the free surface conditions

$$\psi = \frac{\partial^2 \psi}{\partial z^2} = \frac{\partial \theta}{\partial z} = 0 \text{ on } z = 1. \quad (2.4.6)$$

Finally, the solution must match with the core solution, requiring that

$$\left. \begin{aligned} \psi &\rightarrow R_1 G' \\ \theta &\sim x + c + R_1 G \end{aligned} \right\} (x \rightarrow \infty) \quad (2.4.7)$$

where, from matching with (2.3.12),

$$c = B_1 \quad (2.4.8)$$

Near the hot wall

$$\bar{\psi} = \tilde{\psi}(\bar{x}, z) + \dots, \quad \bar{\theta} = 1 + L^{-1} \tilde{\theta}(\bar{x}, z) + \dots, \quad (L \rightarrow \infty), \quad (2.4.9)$$

where  $\bar{x} = L - x$ . Substitution into (2.2.1) and (2.2.2) yields similar equations to those of the cold end-zone, except that because of the replacement of  $x$  by  $L - x$ , the two Jacobian terms and the buoyancy term have opposite sign:

$$\tilde{\nabla}^4 \tilde{\psi} + R_1 \frac{\partial \tilde{\theta}}{\partial \bar{x}} = -\sigma^{-1} \frac{\partial(\tilde{\nabla}^2 \tilde{\psi}, \tilde{\psi})}{\partial(\bar{x}, z)}, \quad (2.4.10)$$

$$\tilde{\nabla}^2 \tilde{\theta} = -\frac{\partial(\tilde{\theta}, \tilde{\psi})}{\partial(\bar{x}, z)}. \quad (2.4.11)$$

The solution must satisfy the wall conditions

$$\tilde{\psi} = \frac{\partial \tilde{\psi}}{\partial \bar{x}} = \tilde{\theta} = 0 \text{ on } \bar{x} = 0, \quad (2.4.12)$$

$$\tilde{\psi} = \frac{\partial \tilde{\psi}}{\partial z} = \frac{\partial \tilde{\theta}}{\partial z} = 0 \text{ on } z = 0, \quad (2.4.13)$$

and the free surface conditions

$$\tilde{\psi} = \frac{\partial^2 \tilde{\psi}}{\partial z^2} = \frac{\partial \tilde{\theta}}{\partial z} = 0 \text{ on } z = 1. \quad (2.4.14)$$

As in the case of the cold end-zone problem the solution must also match with the core solution, requiring that

$$\left. \begin{aligned} \tilde{\psi} &\rightarrow R_1 G' \\ \tilde{\theta} &\sim -\bar{x} + \bar{c} + R_1 G \end{aligned} \right\} (\bar{x} \rightarrow \infty) \quad (2.4.15)$$

where from (2.3.12),

$$\bar{c} = A_1 + B_1. \quad (2.4.16)$$

The two end region problems must be solved to determine the constant parameters  $c = c(R_1, \sigma)$  and  $\bar{c} = \bar{c}(R_1, \sigma)$  as functions of both  $R_1$  and  $\sigma$ . The core solution (2.3.12) is then completed to order  $L^{-1}$ , given that

$$A_1 = \bar{c} - c, \quad B_1 = c. \quad (2.4.17)$$

Properties of the end region solutions will now be considered.

## 2.5 End-zone eigenvalue problem

Insight into the behaviour of the end region solutions for general  $R_1$  and  $\sigma$  can be gained by considering the manner in which the core flow is recovered as  $x \rightarrow \infty$  and  $\bar{x} \rightarrow \infty$ . For the cold end-zone it is expected that

$$\psi \sim R_1 G' + \sum_{\alpha} \phi(z, R_1, \sigma) e^{\alpha x}, \quad (2.5.1)$$

$$\theta \sim x + c + R_1 G + \sum_{\alpha} \Theta(z, R_1, \sigma) e^{\alpha x}, \quad (2.5.2)$$

for  $Re(\alpha) < 0$ ,  $x \gg 1$ , while for the hot end-zone it is expected that

$$\bar{\psi} \sim R_1 G' + \sum_{\alpha} \phi(z, R_1, \sigma) e^{-\alpha \bar{x}}, \quad (2.5.3)$$

$$\bar{\theta} \sim -\bar{x} + \bar{c} + R_1 G + \sum_{\alpha} \Theta(z, R_1, \sigma) e^{-\alpha \bar{x}}, \quad (2.5.4)$$

for  $Re(\alpha) > 0$ ,  $\bar{x} \gg 1$ . Substituting (2.5.1)–(2.5.4) into the governing equations and linearising leads to a single eigenvalue problem for both end-zones:

$$\phi^{iv} + 2\alpha^2 \phi'' + \alpha^4 \phi - \alpha R_1 \Theta = \frac{\alpha R_1}{\sigma} (G''(\phi'' + \alpha^2 \phi) - G^{iv} \phi), \quad (2.5.5)$$

$$\Theta'' + \alpha^2 \Theta - \phi' = \alpha R_1 (G'' \Theta - G' \phi), \quad (2.5.6)$$

with  $\phi = \phi' = \Theta' = 0$  on  $z = 0$  and  $\phi = \phi'' = \Theta' = 0$  on  $z = 1$ . In general the eigenvalue  $\alpha$  is complex:  $\alpha = \alpha_r + i\alpha_i$ . Solutions where  $\alpha_r > 0$  relate to the hot end-zone; where  $\alpha_r < 0$  the solutions correspond to the cold end-zone. By taking the complex conjugate of (2.5.5) and (2.5.6) it can be seen that if  $\alpha$  is an eigenvalue corresponding to eigenfunctions  $\phi$  and  $\Theta$  then  $\alpha^*$  is the eigenvalue corresponding to

the eigenfunctions  $\phi^*$  and  $\Theta^*$ , where the asterisk denotes the complex conjugate. To avoid confusion, the imaginary part of the eigenvalue,  $\alpha_i$ , is taken to be positive at the hot end and negative at the cold end.

For general  $R_1$  it is necessary to solve the eigenvalue equations (2.5.5) and (2.5.6) numerically. Results were obtained using a fourth order Runge–Kutta scheme with Newton iteration, which found  $\alpha$  while keeping  $R_1$  fixed. The initial estimate of  $\alpha$  needed for such a scheme was taken to be the result at the previous  $R_1$  value. Thus values of  $\alpha$  were traced out for increasing  $R_1$  starting from  $R_1 = 0$  where the eigenvalue problem is analytically solvable, as follows.

When  $R_1 = 0$  the end zone eigenvalue problem simplifies to

$$\phi^{iv} + 2\alpha^2\phi'' + \alpha^4\phi = 0, \quad (2.5.7)$$

$$\Theta'' + \alpha^2\Theta - \phi' = 0, \quad (2.5.8)$$

with  $\phi = \phi' = \Theta' = 0$  on  $z = 0$  and  $\phi = \phi'' = \Theta' = 0$  on  $z = 1$ .

For the trivial solution of (2.5.7),  $\phi = 0$ , the solution of (2.5.8) yields the real eigenvalues

$$\alpha = \pm n\pi, \quad n = 1, 2, \dots, \quad (2.5.9)$$

with eigenfunctions of the form  $\Theta = \cos n\pi z$ . Note that any multiple of the eigenfunction is a solution of the eigenvalue problem.

Alternatively, the relevant non-trivial solutions of (2.5.7) are

$$\phi = \sin \alpha z - \alpha z \tan \alpha \sin \alpha z - \alpha z \cos \alpha z, \quad (2.5.10)$$

where  $\alpha$  is a solution of

$$\sin 2\alpha - 2\alpha = 0. \quad (2.5.11)$$

The complex roots of (2.5.11) are tabulated by Hillman and Salzer (1943), giving

$$\alpha = \pm(3.7489 + 1.3844i), \pm(6.9500 + 1.6761i), \dots \quad (2.5.12)$$

## 2.6 Numerical solution of the eigenvalue problem.

It is necessary to solve the eigenvalue problem numerically for general values of  $R_1$ . A fourth order Runge–Kutta scheme was used to integrate the equations from the

specified boundary conditions at  $z = 0$  to give accurate results at  $z = 1$ . These results were made consistent with the boundary conditions at  $z = 1$  by combining three independent solutions and using a Newton iteration. A similar scheme was used successfully by Daniels *et al.* (1987). It has good accuracy, converges well and the computer encoded version is relatively easy to check. These advantages generally outweigh those of alternative methods, such as those based on Galerkin techniques. The computations were carried out on a Sparc workstation.

The Runge–Kutta scheme requires the eigenvalue problem to be re-written as a set of first order equations. On separating the problem into real and imaginary parts, (2.5.5) and (2.5.6) yield twelve first-order equations of the form

$$\begin{aligned}
y_1 &= \phi_r, & y_2 &= \phi_i, \\
y_3 &= \phi'_r = y'_1, & y_4 &= \phi'_i = y'_2, \\
y_5 &= \phi''_r = y'_3, & y_6 &= \phi''_i = y'_4, \\
y_7 &= \phi'''_r = y'_5, & y_8 &= \phi'''_i = y'_6, \\
y_9 &= \Theta_r, & y_{10} &= \Theta_i, \\
y_{11} &= \Theta'_r = y'_9, & y_{12} &= \Theta'_i = y'_{10},
\end{aligned} \tag{2.6.1}$$

with boundary conditions

$$\begin{aligned}
y_1 &= y_2 = 0, \\
y_3 &= y_4 = 0, \\
y_{11} &= y_{12} = 0, \quad \text{on } z = 0,
\end{aligned} \tag{2.6.2}$$

and

$$\begin{aligned}
y_1 &= y_2 = 0, \\
y_5 &= y_6 = 0, \\
y_{11} &= y_{12} = 0, \quad \text{on } z = 1.
\end{aligned} \tag{2.6.3}$$

The twelve first order equations of the form  $y'_i = f_i(z, y_1, \dots, y_{12})$  are solved by the Runge–Kutta scheme

$$y_{i,n+1} = y_{i,n} + \frac{1}{6} (k(i, 1) + 2k(i, 2) + 2k(i, 3) + k(i, 4)) \tag{2.6.4}$$

where

$$\begin{aligned}
k(i, 1) &= hf(z_n, y_{1,n}, \dots, y_{12,n}), \\
k(i, 2) &= hf(z_n + \frac{1}{2}h, y_{1,n} + \frac{1}{2}k(1, 1), \dots, y_{12,n} + \frac{1}{2}k(12, 1)), \\
k(i, 3) &= hf(z_n + \frac{1}{2}h, y_{1,n} + \frac{1}{2}k(1, 2), \dots, y_{12,n} + \frac{1}{2}k(12, 2)), \\
k(i, 4) &= hf(z_n + h, y_{1,n} + k(1, 3), \dots, y_{12,n} + k(12, 3)).
\end{aligned} \tag{2.6.5}$$

For most calculations the step size from  $z = 0$  to  $z = 1$  was usually taken to be  $h = 0.01$ , with  $n$  taking values from 0 to 99. The outcome of this procedure is to obtain the values of  $y_1, \dots, y_{12}$  at  $z = 1$ .

Values of  $y_{i,0}$  are given by the boundary conditions at  $z = 0$ , except for  $i = 5, 6, 7, 8, 9, 10$ , corresponding to the values of  $\phi'$ ,  $\phi'''$  and  $\Theta$  at  $z = 0$ . Thus three solutions are computed, the general solution being a linear combination of the three:

$$y = Ay^{(1)} + By^{(2)} + Cy^{(3)}. \quad (2.6.6)$$

Here  $y^{(1)}$  is the solution for non-zero  $\phi''$  at  $z = 0$ ,  $y^{(2)}$  is the solution for non-zero  $\phi'''$  at  $z = 0$  and  $y^{(3)}$  is the solution for non-zero  $\Theta$  at  $z = 0$ . In order to satisfy the boundary conditions  $\phi = \phi'' = \Theta' = 0$  at  $z = 1$  it is required that

$$\begin{aligned} A(y_1^{(1)} + iy_2^{(1)}) + B(y_1^{(2)} + iy_2^{(2)}) + C(y_1^{(3)} + iy_2^{(3)}) &= 0, \\ A(y_5^{(1)} + iy_6^{(1)}) + B(y_5^{(2)} + iy_6^{(2)}) + C(y_5^{(3)} + iy_6^{(3)}) &= 0, \\ A(y_{11}^{(1)} + iy_{12}^{(1)}) + B(y_{11}^{(2)} + iy_{12}^{(2)}) + C(y_{11}^{(3)} + iy_{12}^{(3)}) &= 0, \end{aligned} \quad (2.6.7)$$

at  $z = 1$ . Thus a non-trivial solution for  $A$ ,  $B$  and  $C$  requires that the complex determinant

$$D = D_r + iD_i = \begin{vmatrix} y_1^{(1)} + iy_2^{(1)} & y_1^{(2)} + iy_2^{(2)} & y_1^{(3)} + iy_2^{(3)} \\ y_5^{(1)} + iy_6^{(1)} & y_5^{(2)} + iy_6^{(2)} & y_5^{(3)} + iy_6^{(3)} \\ y_{11}^{(1)} + iy_{12}^{(1)} & y_{11}^{(2)} + iy_{12}^{(2)} & y_{11}^{(3)} + iy_{12}^{(3)} \end{vmatrix} \quad (2.6.8)$$

vanishes at  $z = 1$ . Thus the pair of equations

$$D_r(\alpha_r, \alpha_i) = 0, \quad D_i(\alpha_r, \alpha_i) = 0, \quad (2.6.9)$$

must be solved to determine  $\alpha_r$  and  $\alpha_i$ , the real and imaginary parts of the eigenvalue  $\alpha$ .

The determinant is brought sufficiently close to zero by the Newton iteration

$$D_r + \frac{\partial D_r}{\partial \alpha_r} \delta \alpha_r + \frac{\partial D_r}{\partial \alpha_i} \delta \alpha_i = 0, \quad (2.6.10)$$

$$D_i + \frac{\partial D_i}{\partial \alpha_r} \delta \alpha_r + \frac{\partial D_i}{\partial \alpha_i} \delta \alpha_i = 0, \quad (2.6.11)$$

where  $\delta \alpha_r$ ,  $\delta \alpha_i$  are increments in the values of  $\alpha_r$  and  $\alpha_i$ . In practice, the derivatives were estimated by computing three solutions for  $D$  at  $\alpha$ ,  $\alpha + \delta$  and  $\alpha + i\delta$ , with  $\delta$  usually taken to be  $10^{-4}$ . The partial derivatives were then approximated at  $\alpha$  by using a simple forward difference approximation.

By solving (2.6.10) and (2.6.11) for  $\delta \alpha_r$  and  $\delta \alpha_i$ , the values of  $\alpha_r$  and  $\alpha_i$  were updated and the whole process repeated usually until the change in  $\alpha_r$  and  $\alpha_i$  was less than  $\delta$ . Values of  $D_r$  and  $D_i$  were monitored to check convergence. The accuracy of the computations was also checked by comparison with the results obtained by halving the step size in the Runge-Kutta scheme from the usual  $10^{-2}$  and by reducing the tolerance of the Newton iteration.

## 2.7 Numerical results

The eigenvalue problem (2.5.5), (2.5.6) was solved numerically by the method described in section 2.6 for a range of Prandtl numbers including both infinite Prandtl number and small values of around 0.1 or less. Results are given in sections 2.7.1 and 2.7.2 respectively. Results for a Prandtl number equivalent to that of water,  $\sigma \approx 7$ , were found to behave in a similar manner to those for infinite Prandtl number. For each Prandtl number regime, results for both the hot and cold ends are given, and each end has both ‘real’ and ‘complex’ eigenvalue branches which stem from the limiting behaviours at  $R_1 = 0$  defined by (2.5.9) and (2.5.12).

As discussed in section 2.5,  $\alpha$  and its complex conjugate  $\alpha^*$  are solutions of the eigenvalue problem, and thus for simplicity both real and imaginary parts of the hot end solutions are taken as positive, while both real and imaginary parts are taken as negative for the cold end solutions.

### 2.7.1 Infinite Prandtl number

Figures 2.2 and 2.3 show values of  $\alpha$  as a function of  $R_1$  for the first four real and complex modes of the hot end solution. The fifth real mode is also shown as this interacts with the fourth real mode. Apart from this small ‘interaction’, which produces a complex solution near  $R_1 = 1800$ , the behaviour of  $\alpha$  with  $R_1$  is relatively simple; the real modes become increasingly more important than the complex modes as  $R_1 \rightarrow \infty$  in the sense of determining the scale of decay of the end-zone solution. This is indicated by the decrease in value of the real mode eigenvalues (compared with the increase in the real part of the complex mode eigenvalues) and represents an expansion of the end zone into the core as  $R_1$  increases.

Figures 2.4 and 2.5 show the corresponding eigenvalues of the real and complex modes of the cold end solutions. Here the fourth complex mode is plotted with the real eigenvalues to indicate an interaction with the fifth real mode. A detailed interpretation of these ‘interactions’ is not undertaken here because the modes decay too quickly to be of interest.

Comparison of the results for the hot and cold ends at large values of  $R_1$

shows that the magnitudes of the real eigenvalues of the cold end are smaller than those of the hot end, suggesting that the cold end-zone extends further into the core than the hot end-zone at large Rayleigh numbers.

The real eigenvalues and the real part of the complex eigenvalues remain non-zero for all values of  $R_1$  which suggests that the end-zone solution approaches the core-flow as proposed in section 2.5, and that as in the case of a rigid upper surface (Daniels *et al.* 1987) no steady multiple cell solutions develop in the system at large Prandtl number.

Figures 2.2–2.5 show that for  $R_1 \geq 3000$ , the most important modes at both the hot and cold ends are the first three real modes; the complex modes are comparatively insignificant and correspond to a strongly-damped oscillatory component. Thus most of the turning of the fluid is associated with the first three eigenfunctions  $\phi$ , which are plotted as functions of  $z$  in figure 2.6.

For both hot and cold ends the first eigenfunction of  $\phi$  (which affects the core flow first as it approaches the end wall) is similar in shape to the core-flow stream function. This basically has the effect of slowing the flow. The second and third eigenfunctions of  $\phi$  at the hot end have the greatest effect on the core-flow at the bottom of the cavity, while those of the cold end have the greatest effect in the upper part of the core-flow; at first glance there seems to be an odd symmetry between the second and third eigenfunctions at each end.

The corresponding temperature eigenfunctions  $\Theta$  in figure 2.7 show a similar odd symmetry: the largest effect on the core temperature is at the top of the hot end and at the bottom of the cold end. The first eigenfunctions have the effect of lowering the temperature towards the top of the cavity near the hot end and increasing the temperature towards the bottom of the cavity near the cold end, so that the temperature becomes more constant with depth towards the walls.

### 2.7.2 Small Prandtl number

The eigenvalue problem was solved for three different small values of the Prandtl number: 0.1, 0.05 and 0.02. The real and complex eigenvalues for the hot end are plotted in figures 2.8 and 2.9 and for the cold end in figures 2.10 and 2.11. Only

the first modes are shown as these have the most penetrating effect on the core flow and are therefore of greatest interest.

Although different in detail, the real modes at both ends are similar to those for infinite Prandtl number – similar in magnitude and decaying with  $R_1$ . A complicated interaction between the first few real modes at the hot end is shown for  $\sigma = 0.1$  in figure 2.12. The higher ‘real’ modes appear to develop extensive complex portions as  $R_1$  increases.

The behaviour of the complex modes is quite different from that of the infinite Prandtl number case. Both real and imaginary parts of the eigenvalues for the first hot end mode decay very quickly with  $R_1$ , while the eigenvalues for the first cold end mode appear to converge to constant values with increasing  $R_1$ . The eigenvalues for the second cold end mode decay quickly with increasing  $R_1$  and soon become more important than the first mode.

For both the hot and cold ends and for values of  $R_1$  up to 3000, the real part of the complex eigenvalue is smaller in magnitude than the first real eigenvalue. The results suggest that at large values of  $R_1$  the decay in the end-zones remains dominated by the complex modes, equivalent to a slowly damped oscillatory decay into the core-flow. Thus the main difference between the infinite and small Prandtl number problems is that at large values of  $R_1$  the most important modes in the latter case are the complex modes while in the former case the real modes dominate the flow. Neither the real modes nor the real part of the complex modes appear to reach zero at finite  $R_1$  and so the parallel-flow core solution remains valid, unlike the case of a rigid upper surface where at small Prandtl numbers the flow is forced to break down into stationary multicellular convection at sufficiently high values of  $R_1$ .

## 2.8 Asymptotic results for large $R_1$

The numerical solutions of the eigenvalue problem (2.5.5), (2.5.6) for infinite Prandtl number plotted in figures 2.2–2.5 suggest that the real eigenvalues  $\alpha$  have the behaviour

$$\alpha \sim \frac{\alpha_0}{R_1} \text{ as } R_1 \rightarrow \infty. \quad (2.8.1)$$

For finite Prandtl numbers, the numerical results shown in figures 2.8–2.12 suggest that there are solutions which behave in a similar manner as  $R_1 \rightarrow \infty$ , but with  $\alpha_0$  either real or complex. In this section an investigation is undertaken to identify these solutions which determine the scale of decay of each end-zone at large values of  $R_1$ .

### 2.8.1 Infinite Prandtl number

Substitution of (2.8.1) into (2.5.5) and (2.5.6) at infinite Prandtl number and retention of the leading order terms as  $R_1 \rightarrow \infty$  yields the reduced problem

$$\phi^{3v} - \alpha_0 \Theta = 0, \quad (2.8.2)$$

$$\Theta'' - \phi' = \alpha_0(G''\Theta - G'\phi), \quad (2.8.3)$$

with  $\phi = \phi' = \Theta' = 0$  on  $z = 0$  and  $\phi = \phi'' = \Theta' = 0$  on  $z = 1$ . This was solved using the Runge–Kutta iteration scheme described in section 2.6. The results for the first three real modes are given in Table 2.1, and show good agreement with the numerical solution of the full equations at  $R_1 = 3000$ , particularly in respect of the leading mode at each end of the cavity.

mode	Asymptotic		Full solution
	$\alpha_0$	$\alpha_0/R_1$ ( $R_1=3000$ )	$\alpha(R_1=3000)$
hot 1	2179	0.7262	0.7125
hot 2	8142	2.7140	2.439
hot 3	19520	6.5080	5.131
cold 1	-2009	-0.6695	-0.6534
cold 2	-7442	-2.4810	-2.2200
cold 3	-17440	-5.8140	-4.5480

Table 2.1: Comparison of the results of the asymptotic form and full-equation form of the eigenvalue  $\alpha$ .

The values of  $\alpha_0$  for these leading modes suggest that the e-folding decay length for the hot end-zone is

$$\bar{x} \sim 4.59 \times 10^{-4} R_1, \quad R_1 \rightarrow \infty, \quad (2.8.4)$$

and for the cold end-zone is

$$x \sim 4.98 \times 10^{-4} R_1, \quad R_1 \rightarrow \infty, \quad (2.8.5)$$

indicating that the cold end-zone extends somewhat further into the core than the hot end-zone. Daniels *et al.* (1987) found that the e-folding decay length for the end-zones of the problem with a rigid upper surface is

$$x \sim 2.20 \times 10^{-4} R_1, \quad (2.8.6)$$

roughly half the length of the end-zones here for the free surface problem.

## 2.8.2 Finite Prandtl number

For finite Prandtl numbers substitution of (2.8.1) into (2.5.5), (2.5.6) and retention of the leading order terms as  $R_1 \rightarrow \infty$  gives

$$\phi^{2v} - \alpha_0 \Theta = \frac{\alpha_0}{\sigma} (G'' \phi'' - G^{2v} \phi), \quad (2.8.7)$$

$$\Theta'' - \phi' = \alpha_0 (G'' \Theta - G' \phi). \quad (2.8.8)$$

The results of solving (2.8.7) and (2.8.8) by the Runge-Kutta iteration scheme are given in figures 2.13 and 2.14 as plots of  $\alpha_0$  against  $\sigma$ . The numerical solutions of both the full equations at  $R_1 = 3000$  and the asymptotic equations with  $\sigma = 0.10, 0.05, 0.02$  are given in Table 2.2 for the first complex mode relating to the hot end-zone, and in Table 2.3 for the second complex mode relating to the cold end-zone – figure 2.11 shows that for large  $R_1$  the second complex mode decays slower than the first. The results in these tables indicate good agreement between the numerical results and the asymptotic theory.

$\sigma$	Asymptotic				Full solution ( $R_1=3000$ )	
	$\alpha_{0r}$	$\alpha_{0i}$	$\alpha_{0r}/R_1$ ( $R_1=3000$ )	$\alpha_{0i}/R_1$ ( $R_1=3000$ )	$\alpha_r$	$\alpha_i$
0.10	559	414	0.186	0.138	0.180	0.137
0.05	289	219	0.0963	0.0729	0.0961	0.0725
0.02	119	88.7	0.0397	0.0296	0.0395	0.0295

Table 2.2: Comparison of the results of the asymptotic form and full-equation form of the complex eigenvalue  $\alpha$ .

$\sigma$	Asymptotic				Full solution ( $R_1=3000$ )	
	$\alpha_{0r}$	$\alpha_{0i}$	$\alpha_{0r}/R_1$ ( $R_1=3000$ )	$\alpha_{0i}/R_1$ ( $R_1=3000$ )	$\alpha_r$	$\alpha_i$
0.10	-2074	-842	-0.692	-0.281	-0.694	-0.283
0.05	-1078	-418	-0.359	-0.139	-0.360	-0.140
0.02	-434	-168	-0.145	-0.056	-0.146	-0.055

Table 2.3: Comparison of the results of the asymptotic form and full-equation form of the complex eigenvalue  $\alpha$ .

Figures 2.13 and 2.14 show that, at both ends, in general the leading complex solutions of the form  $\alpha \sim \alpha_0/R_1$  only exist for  $\sigma$  less than about 0.5. At  $\sigma = 2$ , the values of  $\alpha_0$  for the first few real modes have approached their limiting values for  $\sigma = \infty$  given in Table 2.1, and for these modes there is little dependence on Prandtl number for  $\sigma \geq 2$ .

## 2.9 Asymptotic expansion of the end region solution for small $R_1$

The asymptotic solution as  $R_1 \rightarrow 0$  for the cold end-zone is considered first; similar results for the hot end-zone are then derived, allowing the constants  $A_1$  and  $B_1$  in the first order correction to the core solution to be obtained in the limit of small Rayleigh number.

The stream function and temperature in the cold end-zone can be expanded in the form

$$\psi = R_1\psi_1 + R_1^2\psi_2 + \dots, \quad (2.9.1)$$

$$\theta = \theta_0 + R_1\theta_1 + R_1^2\theta_2 + \dots, \quad (2.9.2)$$

as  $R_1 \rightarrow 0$  with

$$c = c_0 + R_1c_1 + R_1^2c_2 + \dots \quad (2.9.3)$$

Substitution of (2.9.1) – (2.9.3) into the end-zone system (2.4.2) – (2.4.7) yields a succession of problems at each order in  $R_1$  as follows.

At order one, the heat equation gives

$$\nabla^2\theta_0 = 0, \quad (2.9.4)$$

with

$$\theta_0 = 0 \text{ on } x = 0, \quad (2.9.5)$$

$$\theta_0 \sim x + c_0 \text{ as } x \rightarrow \infty, \quad (2.9.6)$$

and

$$\frac{\partial \theta_0}{\partial z} = 0 \text{ on } z = 0, 1. \quad (2.9.7)$$

Integrating (2.9.4) between  $z = 0$  and  $1$  gives

$$\frac{\partial^2}{\partial x^2} \int_0^1 \theta_0 dz = 0 \quad (2.9.8)$$

where (2.9.7) has been used. Integrating twice with respect to  $x$  and using (2.9.5) and (2.9.6) shows that  $c_0 = 0$  and the required solution for  $\theta_0$  is

$$\theta_0 = x. \quad (2.9.9)$$

At order  $R_1$ ,  $\psi_1$  is generated by this horizontal thermal gradient and is found to satisfy

$$\nabla^4 \psi_1 = 1, \quad (2.9.10)$$

with

$$\psi_1 = \frac{\partial \psi_1}{\partial z} = 0 \text{ on } z = 0, \quad \psi_1 = \frac{\partial^2 \psi_1}{\partial z^2} = 0 \text{ on } z = 1, \quad (2.9.11)$$

$$\psi_1 = \frac{\partial \psi_1}{\partial x} = 0 \text{ on } x = 0 \quad \text{and} \quad \psi_1 \rightarrow G' \text{ as } x \rightarrow \infty. \quad (2.9.12)$$

The solution can be written in the form

$$\psi_1 = G' + \hat{\phi} \quad (2.9.13)$$

where  $\hat{\phi}(x, z)$  satisfies the biharmonic equation and can be found by separation of variables in the form

$$\hat{\phi} = Re \sum_{k=1}^{\infty} \mu_k (\sin \alpha_k z - \alpha_k z \cos \alpha_k z - \alpha_k z \tan \alpha_k \sin \alpha_k z) e^{\alpha_k x}, \quad (2.9.14)$$

where  $\mu_k$  are constants to be determined from the boundary conditions at  $x = 0$ , and  $\alpha_k$  are the roots of

$$\alpha_k = \frac{1}{2} \sin 2\alpha_k \quad (k = 1, 2, \dots) \quad (2.9.15)$$

with negative real part. These were found by Newton-Raphson iteration and checked with the results of Hillman and Salzer (1943).

The boundary conditions at  $x = 0$  given in (2.9.12) are now

$$Re \left( \sum_{k=1}^{\infty} \mu_k (\sin \alpha_k z - \alpha_k z \cos \alpha_k z - \alpha_k z \tan \alpha_k \sin \alpha_k z) \right) = -G', \quad (2.9.16)$$

and

$$Re \left( \sum_{k=1}^{\infty} \alpha_k \mu_k (\sin \alpha_k z - \alpha_k z \cos \alpha_k z - \alpha_k z \tan \alpha_k \sin \alpha_k z) \right) = 0. \quad (2.9.17)$$

The eigenfunctions and the velocity profile  $G'$  are written as Fourier sine series, giving

$$Re \left( \sum_{k=1}^{\infty} \mu_k \sum_{n=1}^{\infty} b_{n,k} \sin n\pi z \right) = - \sum_n e_n \sin n\pi z, \quad (2.9.18)$$

and

$$Re \left( \sum_{k=1}^{\infty} \alpha_k \mu_k \sum_{n=1}^{\infty} b_{n,k} \sin n\pi z \right) = 0, \quad (2.9.19)$$

where

$$b_{n,k} = b_{n,k_r} + i b_{n,k_i} = \frac{4n\pi}{(\alpha_k^2 - (n\pi)^2)^2} \alpha_k \sin^2 \alpha_k, \quad (2.9.20)$$

and

$$e_n = \frac{-1}{4(n\pi)^5} \left( (n\pi)^2 + 8((-1)^n - 1) \right). \quad (2.9.21)$$

Equating coefficients of  $\sin n\pi z$  leads to a series of equations of the form

$$\sum_{k=1}^{\infty} (\mu_{k_r} b_{n,k_r} - \mu_{k_i} b_{n,k_i}) = -e_n, \quad (2.9.22)$$

$$\sum_{k=1}^{\infty} (\mu_{k_r} (\alpha_{k_r} b_{n,k_r} - \alpha_{k_i} b_{n,k_i}) - \mu_{k_i} (\alpha_{k_i} b_{n,k_r} + \alpha_{k_r} b_{n,k_i})) = 0, \quad (2.9.23)$$

where  $\mu_k = \mu_{k_r} + i\mu_{k_i}$ . The matrix system was solved using Gaussian elimination with partial pivoting and values of the first few coefficients are given in Table 2.4; the infinite sum was truncated at  $k = 8$  at which point the first four coefficients were estimated to be accurate to three significant figures. Figure 2.15 shows the streamlines of the end-zone flow associated with  $\psi_1$  which indicate the fastest motion near the free surface.

$\mu_1$	$1.82 \times 10^{-3} - 8.49 \times 10^{-3}i$
$\mu_2$	$1.27 \times 10^{-4} + 4.58 \times 10^{-4}i$
$\mu_3$	$2.34 \times 10^{-5} - 1.14 \times 10^{-5}i$
$\mu_4$	$-9.94 \times 10^{-6} + 3.21 \times 10^{-5}i$

Table 2.4: Estimates of the first four values of  $\mu$ .

The first order temperature field  $\theta_1$  is now generated via the equation

$$\nabla^2 \theta_1 = \frac{\partial \psi_1}{\partial z} \quad (2.9.24)$$

obtained from the order  $R_1$  terms in (2.4.3). The boundary conditions are

$$\frac{\partial \theta_1}{\partial z} = 0 \text{ on } z = 0, 1 \quad (2.9.25)$$

$$\theta_1 = 0 \text{ on } x = 0 \quad \text{and} \quad \theta_1 \rightarrow G + c_1 \text{ as } x \rightarrow \infty. \quad (2.9.26)$$

Integration of (2.9.24) shows that

$$\frac{\partial^2}{\partial x^2} \int_0^1 \theta_1 dz = 0 \quad (2.9.27)$$

and it follows from (2.9.26) that

$$c_1 = - \int_0^1 G dz = - \frac{1}{720}. \quad (2.9.28)$$

The solution for  $\theta_1$  can be written in the form

$$\theta_1 = G + \hat{\Theta}(x, z) \quad (2.9.29)$$

where

$$\begin{aligned} \hat{\Theta} = & \sum_{n=0}^{\infty} \eta_n e^{-n\pi x} \cos n\pi z \quad (2.9.30) \\ & + Re \left\{ \sum_{k=1}^{\infty} \mu_k \left( \frac{-1}{4\alpha_k} \tan \alpha_k \sin \alpha_k z - \frac{\tan \alpha_k}{2} \cos \alpha_k z + \frac{1}{4} z \sin \alpha_k z \right. \right. \\ & \left. \left. + \frac{1}{4} z \tan \alpha_k \cos \alpha_k z - \frac{\alpha_k \tan \alpha_k}{4} z^2 \sin \alpha_k z - \frac{\alpha_k}{4} z^2 \cos \alpha_k z \right) e^{\alpha_k x} \right\}, \end{aligned}$$

and  $\eta_n, n = 0, 1, \dots$  are real constants to be determined from the boundary condition

$$\hat{\Theta} = -G \text{ at } x = 0. \quad (2.9.31)$$

The thermal eigenfunctions associated with  $\mu_k$  are written as a Fourier cosine series of the form

$$\sum_{n=0}^{\infty} a_{n,k} \cos n\pi z, \quad (2.9.32)$$

where

$$a_{n,k} = \frac{4\alpha_k^2 (n\pi)^2 \tan \alpha_k}{(\alpha_k^2 - (n\pi)^2)^3}. \quad (2.9.33)$$

and  $a_{0,k} = 0$ . Similarly,  $G$  is written as the Fourier cosine series

$$\sum_{n=0}^{\infty} d_n \cos n\pi z, \quad (2.9.34)$$

where

$$d_n = \frac{1}{4(n\pi)^4} + \frac{(-1)^n - 1}{2(n\pi)^6}, \quad (2.9.35)$$

and

$$d_0 = \frac{1}{720}.$$

The boundary condition  $\hat{\Theta} = -G$  at  $x = 0$  can now be written in terms of Fourier cosine series as

$$\begin{aligned} -d_0 - \sum_{n=1}^{\infty} d_n \cos n\pi z = \\ \eta_0 + \sum_{n=1}^{\infty} \eta_n \cos n\pi z + \operatorname{Re} \left\{ \sum_{k=1}^{\infty} \mu_k \sum_{n=1}^{\infty} a_{n,k} \cos n\pi z \right\}. \end{aligned} \quad (2.9.36)$$

Equating the constant terms,

$$\eta_0 = \frac{-1}{720},$$

confirming the result given earlier for  $c_1$ . Equating the coefficients of the cosines leads to

$$-d_n = \eta_n + \sum_{k=1}^{\infty} \operatorname{Re}(\mu_k a_{n,k}),$$

or

$$\eta_n = \frac{-1}{4(n\pi)^4} - \frac{((-1)^n - 1)}{2(n\pi)^6} - \sum_{k=1}^{\infty} \operatorname{Re} \left( \mu_k \frac{4\alpha_k(n\pi)^2 \tan \alpha_k}{(\alpha_k^2 - (n\pi)^2)^3} \right), \quad n = 1, 2, \dots \quad (2.9.37)$$

and the coefficients  $\eta_n$  can now be calculated using the known values of  $\mu_k$ . The first few coefficients are given in Table 2.5. Isotherms of  $\theta_1$  are shown in figure 2.16. The effect of  $\theta_1$  is to make the fluid at the bottom of the cavity cooler, and that at the top hotter, than the temperature field at leading order.

$\eta_1$	$5.93 \times 10^{-3}$
$\eta_2$	$-6.35 \times 10^{-4}$
$\eta_3$	$2.76 \times 10^{-5}$
$\eta_4$	$-3.06 \times 10^{-5}$

Table 2.5: Estimates of the first four values of  $\eta$ .

At order  $R_1^2$ ,  $\psi_2$  and  $\theta_2$  are found to satisfy

$$\nabla^4 \psi_2 = \frac{\partial \theta_1}{\partial x} + \sigma^{-1} \frac{\partial(\nabla^2 \psi_1, \psi_1)}{\partial(x, z)}, \quad (2.9.38)$$

with

$$\psi_2 = \frac{\partial \psi_2}{\partial z} = 0 \text{ on } z = 0 \quad \text{and} \quad \psi_2 = \frac{\partial^2 \psi_2}{\partial z^2} = 0 \text{ on } z = 1, \quad (2.9.39)$$

and

$$\nabla^2 \theta_2 = \frac{\partial(\theta_1, \psi_1)}{\partial(x, z)} + \frac{\partial \psi_2}{\partial z}, \quad (2.9.40)$$

with

$$\frac{\partial \theta_2}{\partial z} = 0 \text{ on } z = 0, 1. \quad (2.9.41)$$

Complete solutions for  $\psi_2$  and  $\theta_2$  are cumbersome and are not attempted here, but (2.9.40) can be integrated to obtain a formula for  $c_2$  as follows:

$$\int_0^1 \frac{\partial^2 \theta_2}{\partial x^2} dz + \left[ \frac{\partial \theta_2}{\partial z} \right]_0^1 = \int_0^1 \frac{\partial(\theta_1, \psi_1)}{\partial(x, z)} dz + [\psi_2]_0^1. \quad (2.9.42)$$

Using  $\psi_2 = \partial \theta_2 / \partial z = 0$  on  $z = 0, 1$ , and integrating with respect to  $x$  gives

$$\int_0^1 \left[ \frac{\partial \theta_2}{\partial x} \right]_{x'=x}^{\infty} dz = \int_{x'=x}^{\infty} \int_0^1 \frac{\partial(\theta_1, \psi_1)}{\partial(x', z)} dz dx' + m_1 \quad (2.9.43)$$

where  $m_1$  is a constant of integration. Since  $\theta_2 \rightarrow c_2$  as  $x \rightarrow \infty$ , this implies that  $\partial \theta_2 / \partial x \rightarrow 0$  as  $x \rightarrow \infty$  and hence that  $m_1 = 0$ . Integrating again and noting that  $\theta_2 = 0$  on  $x = 0$  yields

$$c_2 = - \int_{x=0}^{\infty} \int_{x'=x}^{\infty} \int_{z=0}^1 \frac{\partial(\theta_1, \psi_1)}{\partial(x', z)} dz dx' dx \quad (2.9.44)$$

Using the substitutions

$$\theta_1 = G + \hat{\Theta} \quad \text{and} \quad \psi_1 = G' + \hat{\phi}, \quad (2.9.45)$$

the first two integrals can be re-written as

$$\begin{aligned} \int_{x'=x}^{\infty} \int_{z=0}^1 \frac{\partial(\theta_1, \psi_1)}{\partial(x', z)} dx' dz = \\ \int_{x'=x}^{\infty} \int_0^1 \left( \frac{\partial \hat{\Theta}}{\partial x'} \left( G'' + \frac{\partial \hat{\phi}}{\partial z} \right) - \frac{\partial \hat{\phi}}{\partial x'} \left( G' + \frac{\partial \hat{\Theta}}{\partial z} \right) \right) dz dx'. \end{aligned} \quad (2.9.46)$$

On interchanging the order of integration, the right hand side can be simplified to

$$\int_0^1 \left( G' \hat{\phi} - G'' \hat{\Theta} + \hat{\phi} \frac{\partial \hat{\Theta}}{\partial z} \right) dz \quad (2.9.47)$$

and then (2.9.44) can be written as

$$c_2 = - \int_0^\infty \int_0^1 \left( G' \hat{\phi} - G'' \hat{\Theta} + \hat{\phi} \frac{\partial \hat{\Theta}}{\partial z} \right) dz dx. \quad (2.9.48)$$

The first part of the double integral was found analytically using the symbolic algebra package MAPLE. Using the first four  $\eta$  and  $\mu$  values given in Tables 2.4 and 2.5 gives

$$- \int_0^\infty \int_0^1 (G' \hat{\phi} - G'' \hat{\Theta}) dz dx \approx 1.37 \times 10^{-5}. \quad (2.9.49)$$

The contribution of the higher modes decays quickly; the contribution of the fourth mode is less by a factor of  $10^4$  than that of the first.

The second part of the integral was simplified by first noting that

$$- \int_0^\infty \int_0^1 \hat{\phi} \frac{\partial \hat{\Theta}}{\partial z} dz dx = \int_0^\infty \int_0^1 \hat{\Theta} \frac{\partial \hat{\phi}}{\partial z} dz dx \quad (2.9.50)$$

and then splitting  $\hat{\Theta}$  into its complementary and particular parts ( $\hat{\Theta} = \hat{\Theta}_c + \hat{\Theta}_p$ ) such that

$$\begin{aligned} \int_0^\infty \int_0^1 \hat{\Theta} \frac{\partial \hat{\phi}}{\partial z} dz dx &= \int_0^\infty \int_0^1 (\hat{\Theta}_c + \hat{\Theta}_p) \frac{\partial \hat{\phi}}{\partial z} dz dx \\ &= \int_0^\infty \int_0^1 \left\{ \sum_{n=0}^\infty (\eta_n e^{-n\pi x} \cos n\pi z) + \right. \\ &\quad \left. \sum_{n=1}^\infty \operatorname{Re} \left( \frac{-1}{4\alpha_n} \tan \alpha_n \sin \alpha_n z - \frac{\tan \alpha_n}{2} \cos \alpha_n z + \frac{1}{4} z \sin \alpha_n z \right. \right. \\ &\quad \left. \left. + \frac{1}{4} z \tan \alpha_n \cos \alpha_n z - \frac{\alpha_n \tan \alpha_n}{4} z^2 \sin \alpha_n z - \frac{\alpha_n}{4} z^2 \cos \alpha_n z \right) e^{\alpha_n x} \right\} \times \\ &\quad \sum_{k=1}^\infty \operatorname{Re} \left( \mu_k \left( (z \cos^2 \alpha_k - 1) \sin \alpha_k z - z \alpha_k \cos \alpha_k z \right) \alpha_k \tan \alpha_k e^{\alpha_k x} \right) dz dx. \end{aligned}$$

The complementary part of the integral can again be solved analytically:

$$\begin{aligned} \int_0^\infty \int_0^1 \hat{\Theta}_c \frac{\partial \hat{\phi}}{\partial z} dz dx &= \\ &= \sum_{n=0}^\infty \eta_n \sum_{k=1}^\infty \operatorname{Re} \left( \mu_k \tan \alpha_k \frac{2(n\pi)^2 \alpha_k^2}{((n\pi)^2 - \alpha_k^2)^2 (\alpha_k + n\pi)} \right), \end{aligned} \quad (2.9.51)$$

and using the values of  $\eta$  and  $\mu$  given in Tables 2.4 and 2.5, this gives the value of the integral as  $-1.04 \times 10^{-5}$ . The  $x$  integration of the 'particular' part of the integral

$$\int_0^\infty \int_0^1 \hat{\Theta}_p \frac{\partial \hat{\phi}}{\partial z} dz dx, \quad (2.9.52)$$

was determined analytically and then the resulting  $z$  integrations were performed numerically using Simpson's rule with a step size of  $10^{-4}$ , and the same values of  $\eta$  and  $\mu$ . This gave the value of the integral (2.9.52) as  $6.29 \times 10^{-6}$ . The earlier integrals for which analytical solutions were found were used to check that the numerical solver performed correctly. It was also adapted to perform the entire double integral

$$\int_0^\infty \int_0^1 \Theta \frac{\partial \phi}{\partial z} dz dx \quad (2.9.53)$$

directly, as a verification of the above work.

In summary, the value of  $c_2$  for the cold end-zone is determined as

$$c_2 = 1.37 \times 10^{-5} - 1.04 \times 10^{-5} - 6.29 \times 10^{-6} = 9.65 \times 10^{-6} \quad (2.9.54)$$

which agrees to within 1% with the numerical result obtained by Cormack, Stone and Leal (1975) using a finite difference approximation of the end-zone flow.

In the hot end-zone, the co-ordinate  $\bar{x} = L - x$  is used as the distance from the hot wall, and  $\bar{\theta}$  and  $\bar{\psi}$  represent the local temperature and stream function fields. These satisfy the equations and boundary conditions given in (2.4.10) - (2.4.15). For small  $R_1$ ,  $\bar{\psi}$  and  $\bar{\theta}$  can be expanded in the form

$$\bar{\psi} = R_1 \bar{\psi}_1 + R_1^2 \bar{\psi}_2 + \dots, \quad (2.9.55)$$

$$\bar{\theta} = \bar{\theta}_0 + R_1 \bar{\theta}_1 + R_1^2 \bar{\theta}_2 + \dots, \quad (2.9.56)$$

with

$$\bar{c} = \bar{c}_0 + R_1 \bar{c}_1 + R_1^2 \bar{c}_2 + \dots \quad (2.9.57)$$

Substitution into (2.4.10) and (2.4.11) yields a succession of problems at each order in  $R_1$  similar to those of the cold end-zone. At order one it is easily established that  $\bar{c}_0 = 0$  and

$$\bar{\theta}_0 = -\bar{x}. \quad (2.9.58)$$

At order  $R_1$ ,  $\bar{\psi}_1$  and  $\bar{\theta}_1$  satisfy

$$\bar{\nabla}^4 \bar{\psi}_1 = 1 \text{ and } \bar{\nabla}^2 \bar{\theta}_1 = \frac{\partial \bar{\psi}_1}{\partial z}, \quad (2.9.59)$$

with

$$\bar{\psi}_1 \rightarrow G' \text{ and } \bar{\theta}_1 \rightarrow G + \bar{c}_1 \text{ as } \bar{x} \rightarrow \infty, \quad (2.9.60)$$

$$\bar{\psi}_1 = \frac{\partial \bar{\psi}_1}{\partial x} = \bar{\theta}_1 = 0 \text{ on } \bar{x} = 0, \quad (2.9.61)$$

and the usual boundary conditions at  $z = 0$  and  $z = 1$ . These problems are identical to those for  $\psi_1$  and  $\theta_1$  in the cold end-zone so that

$$\tilde{\psi}_1(\tilde{x}, z) = \psi_1(\tilde{x}, z), \quad \tilde{\theta}_1(\tilde{x}, z) = \theta_1(\tilde{x}, z) \quad (2.9.62)$$

and

$$\tilde{c}_1 = c_1 = \frac{-1}{720}. \quad (2.9.63)$$

At order  $R_1^2$ ,

$$\tilde{\nabla}^4 \tilde{\psi}_2 = -\frac{\partial \tilde{\theta}_1}{\partial \tilde{x}} - \sigma^{-1} \frac{\partial(\tilde{\nabla}^2 \tilde{\psi}_1, \tilde{\psi}_1)}{\partial(\tilde{x}, z)}, \quad (2.9.64)$$

$$\tilde{\nabla}^2 \tilde{\theta}_2 = -\frac{\partial(\tilde{\theta}_1, \tilde{\psi}_1)}{\partial(\tilde{x}, z)} + \frac{\partial \tilde{\psi}_2}{\partial z}, \quad (2.9.65)$$

with the usual boundary conditions at  $z = 0$  and  $z = 1$  and

$$\tilde{\psi}_2 = \tilde{\theta}_2 = 0 \text{ on } x = 0, \quad (2.9.66)$$

and

$$\tilde{\psi}_2 \rightarrow 0, \tilde{\theta}_2 \rightarrow \tilde{c}_2 \text{ as } \tilde{x} \rightarrow \infty. \quad (2.9.67)$$

Comparison of (2.9.64) with (2.9.38) indicates that here

$$\tilde{\psi}_2(\tilde{x}, z) = -\psi_2(\tilde{x}, z), \quad (2.9.68)$$

and

$$\tilde{c}_2 = -c_2. \quad (2.9.69)$$

Thus at the hot end the leading order stream function and first order temperature field are 'mirror images' of those at the cold end shown in figures 2.15 and 2.16. The negative symmetry of the second order stream function is associated with a downward shift of the streamlines in the cold end and an upward shift at the hot end relative to the leading order behaviour. In the core solution (2.3.12) the two constants  $A_1$  and  $B_1$  are now determined from (2.4.17) as

$$A_1 \sim -2c_2 R_1^2 \approx -1.83 \times 10^{-5} R_1^2, \quad R_1 \rightarrow 0, \quad (2.9.70)$$

and

$$\begin{aligned} B_1 &\sim c_1 R_1 + c_2 R_1^2 \\ &\approx -\frac{1}{720} R_1 + 9.65 \times 10^{-6} R_1^2, \quad R_1 \rightarrow 0. \end{aligned} \quad (2.9.71)$$

The solution for  $A_1$  shows that as  $R_1$  increases, the influence of the end walls is to reduce both the speed of the core flow and the horizontal thermal gradient. The solution for  $B_1$  represents a downward shift in the temperature field throughout the core so that the temperature at the free surface is

$$\xi + L^{-1}R_1 \frac{1}{576} \quad (2.9.72)$$

and on the base is

$$\xi - L^{-1}R_1 \frac{1}{720}. \quad (2.9.73)$$

## 2.10 Discussion

Unlike the case of a rigid upper surface where at small Prandtl numbers the flow breaks down into multicellular convection at sufficiently high values of  $R_1$ , neither the real modes nor the real part of the complex modes appear to reach zero at finite  $R_1$  and so the parallel-flow core solution remains valid. The top 40% of the parallel-flow in the core moves from the hot to the cold end with a maximum velocity at the free surface of  $-R_1(1/48)$ , greater than the maximum velocity  $(11/16)(R_1/48)$  of the return flow in the lower 60% of the cavity. At finite  $R_1$  the cold end-zone is slightly larger than the hot end-zone, but both have an e-folding decay length of order  $R_1$  and are roughly twice as long as the end zones in the rigid surface case. The end-zones for small Prandtl number are dominated by spatial oscillatory modes; at infinite and moderate Prandtl numbers the end-zones are dominated by non-oscillatory modes.

The analysis of section 2.9 gives an almost wholly analytical first order solution throughout the cavity for small Rayleigh number and large aspect ratio. The small  $R_1$  analysis shows that to a first approximation the streamlines are symmetric in the end-zones, and the first order temperature adjustment indicates an increased temperature in the upper half of the cavity and a reduction in the lower half relative to that corresponding to the basic linear temperature gradient. The first order stream function has a negative symmetry equivalent to a slowing down of the flow near the top of the cavity in the cold end zone and a speeding up of the flow near the top of the cavity in the hot end zone.

Some solutions of the full governing equations (2.4.10) and (2.4.11) were

found numerically using a non-linear multigrid program written by N.G. Wright, and discussed in Wright, Gaskell and Sleight (1995). The original program solves the problem in the whole cavity with a rigid upper surface, but here a version was developed to solve the free surface problem for the hot end zone. Solutions were computed for low Rayleigh numbers in the range  $1 < R_1 < 50$  and an estimate of  $\bar{c}$  found from the formula

$$\bar{c}_N = \bar{\theta}_N + \bar{x} - R_1 G(z) \quad (2.10.1)$$

where  $\bar{\theta}_N$  is the temperature profile computed numerically at a reasonably large distance from the wall ( $\bar{x} = 4$ ). For small  $R_1$ , this produced the behaviour

$$\bar{c}_N = -1.38 \times 10^{-3} R_1 - 1.88 \times 10^{-5} R_1^2, \quad R_1 \rightarrow 0, \quad (2.10.2)$$

the two coefficients being within 0.4% of the values predicted by the asymptotic analysis of section 2.9. The numerical computations also produced streamlines almost identical to those given in figure 2.15, confirming excellent agreement between the analytical and numerical solutions. It is hoped that further numerical work will give values for the constants  $\bar{c}$  and  $c$  at moderate and at large  $R_1$  and show how the stream function and temperature profiles behave in the end zones as the Rayleigh number increases. Experiments by Simpkins and Chen (1986) suggest that for the rigid-surface case there is an almost stagnant core with jet-like motion near the horizontal boundaries at large Rayleigh number.

It is also possible to consider an asymptotic theory for the flow development as  $R_1 \rightarrow \infty$ . Daniels (1993) argued for the rigid surface case that consideration of the vertical boundary layer and the horizontal heat transfer balance in the end zones leads to a prediction of the leading order behaviour of  $c(R_1, \sigma)$  as  $R_1 \rightarrow \infty$  of the form

$$c(R_1, \sigma) = R_1^{\frac{7}{5}} c_0(\sigma) + \dots, \quad (2.10.3)$$

The same arguments are equally applicable in the free surface case, the only difference being the contribution to  $c_0$  from the horizontal heat flux  $Q$ , so that for both end zones it can be argued that

$$c \sim \bar{c} \sim R_1^{\frac{7}{5}} c_0(\sigma), \quad R_1 \rightarrow \infty, \quad (2.10.4)$$

where

$$c_0 = \left( \frac{3Q}{4\lambda} \right)^{\frac{4}{5}}, \quad (2.10.5)$$

$$\lambda = \frac{3}{4} \sigma^{\frac{1}{4}} \left( 2.436 + 4.884 \sigma^{\frac{1}{2}} + 4.952 \sigma \right)^{-\frac{1}{4}} \quad (2.10.6)$$

and in the free surface case the heat flux is given by

$$Q = \int_0^1 G'^2 dz = 19/1451520 = 4.75Q_{\text{rigid}}. \quad (2.10.7)$$

Finally, an indication of the free-surface end zone flow at moderate Rayleigh numbers was obtained by extending the analysis of section 2.9 in an approximate manner as follows. The low Rayleigh number eigenfunctions were replaced by those obtained numerically in the eigenfunction analysis of section 2.7 and the boundary conditions on the velocity field applied at  $x = 0$  and  $\bar{x} = 0$ . This procedure is not strictly valid because the exponential eigensolutions are not relevant close to the wall at finite non-zero values of  $R_1$ . However, the results probably provide a good indication of how the flow develops as  $R_1$  increases. The results shown in figure 2.17 are for  $R_1 = 3000$  and  $\sigma = \infty$  and indicate a downward shift of the streamlines in the cold end zone and an upward shift in the hot end zone.

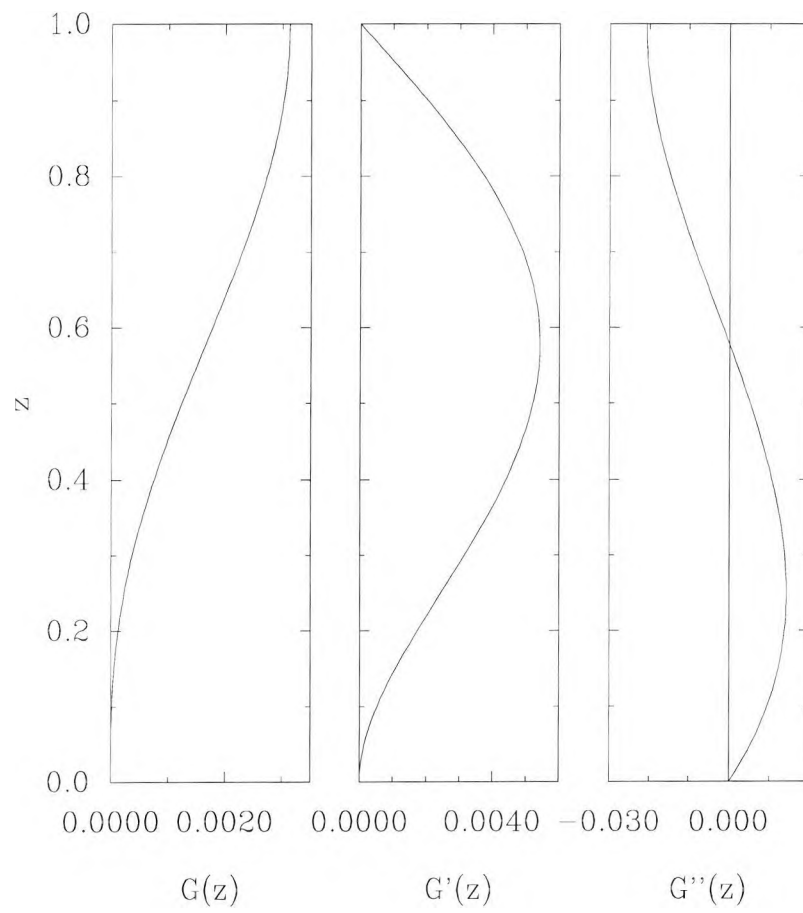


Figure 2.1: Plots between  $z = 0$  and 1 of  $G(z)$  (core temperature profile),  $G'$  (core stream function profile) and  $G''$  (core horizontal velocity profile).

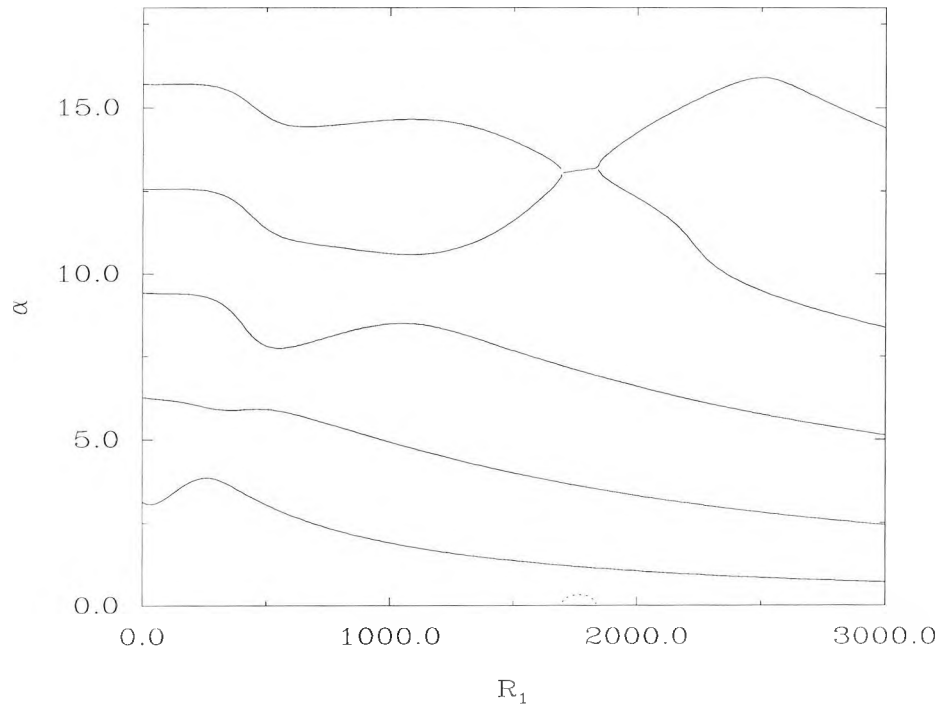


Figure 2.2: Eigenvalues  $\alpha$  of the first five real modes of the hot end as a function of  $R_1$  for  $\sigma = \infty$ . The dotted line is the imaginary part of the fourth/fifth modes.

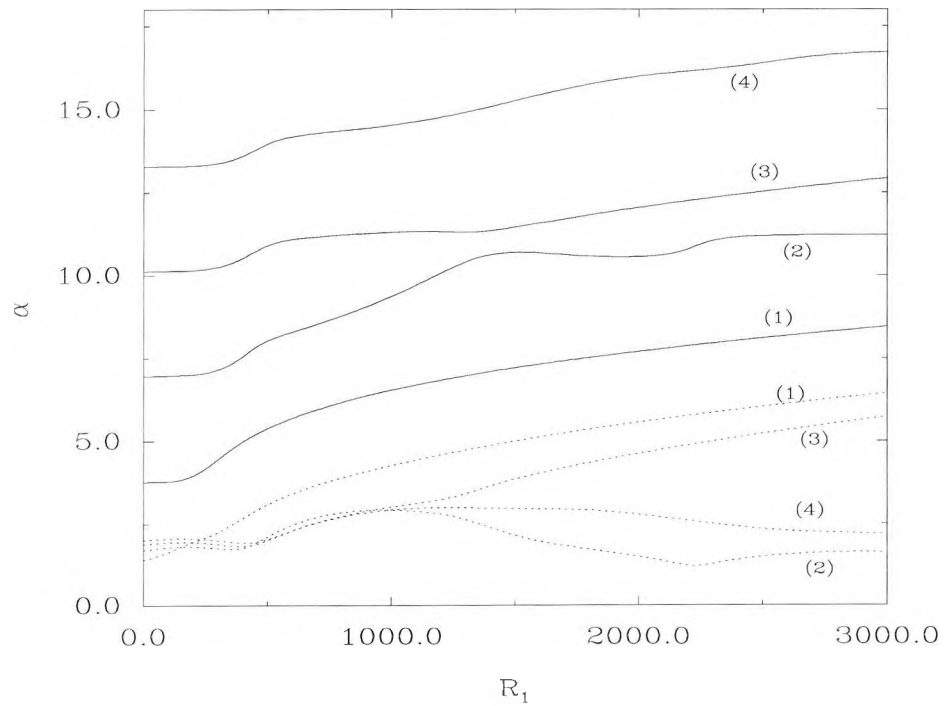


Figure 2.3: Real (solid lines) and imaginary parts of the first four (numbered) complex mode eigenvalues  $\alpha$  of the hot end as a function of  $R_1$  for  $\sigma = \infty$ .

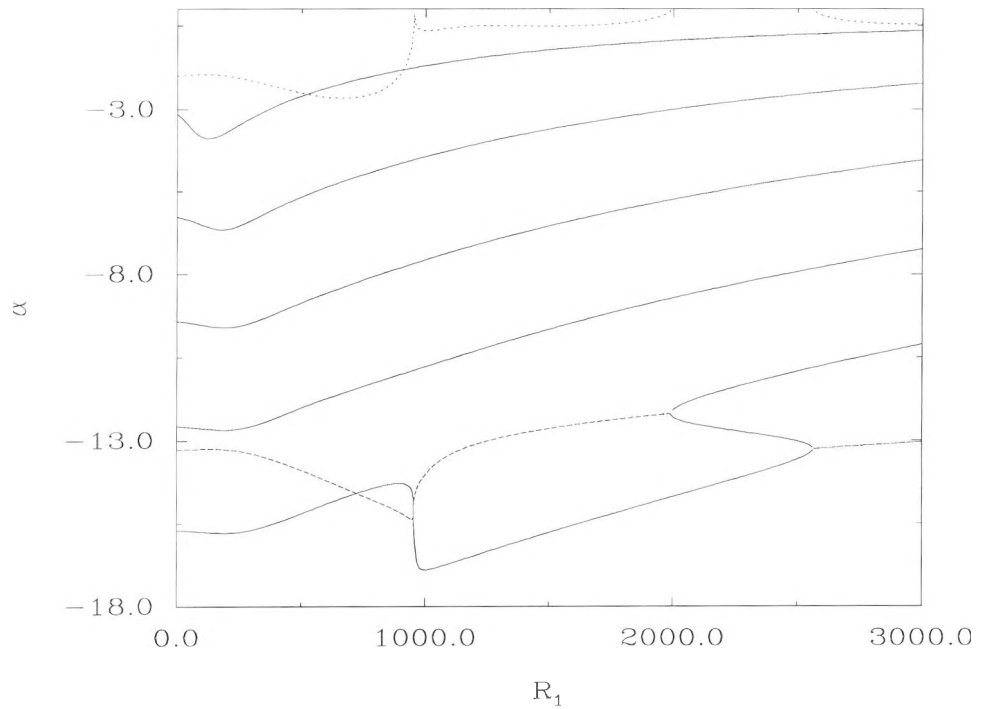


Figure 2.4: Eigenvalues  $\alpha$  of the first five real modes and the fourth complex mode (real part dashed line, imaginary part dotted line) of the cold end as a function of  $R_1$  for  $\sigma = \infty$ .

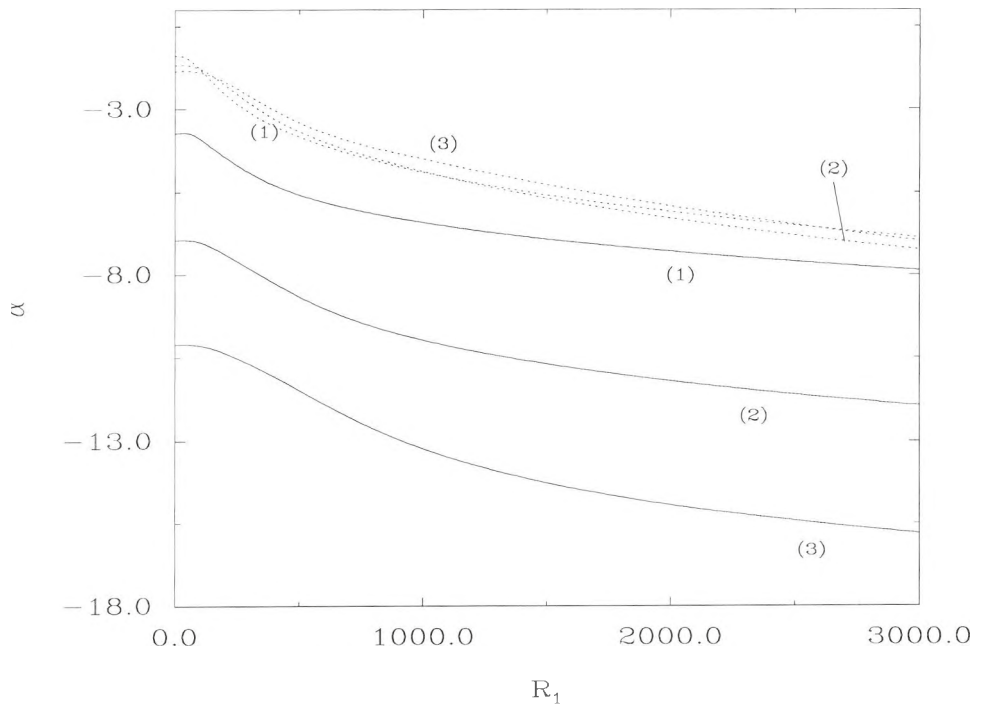


Figure 2.5: Real (solid line) and imaginary parts of the first three (numbered) complex eigenvalues  $\alpha$  of the cold end as a function of  $R_1$  for  $\sigma = \infty$ .

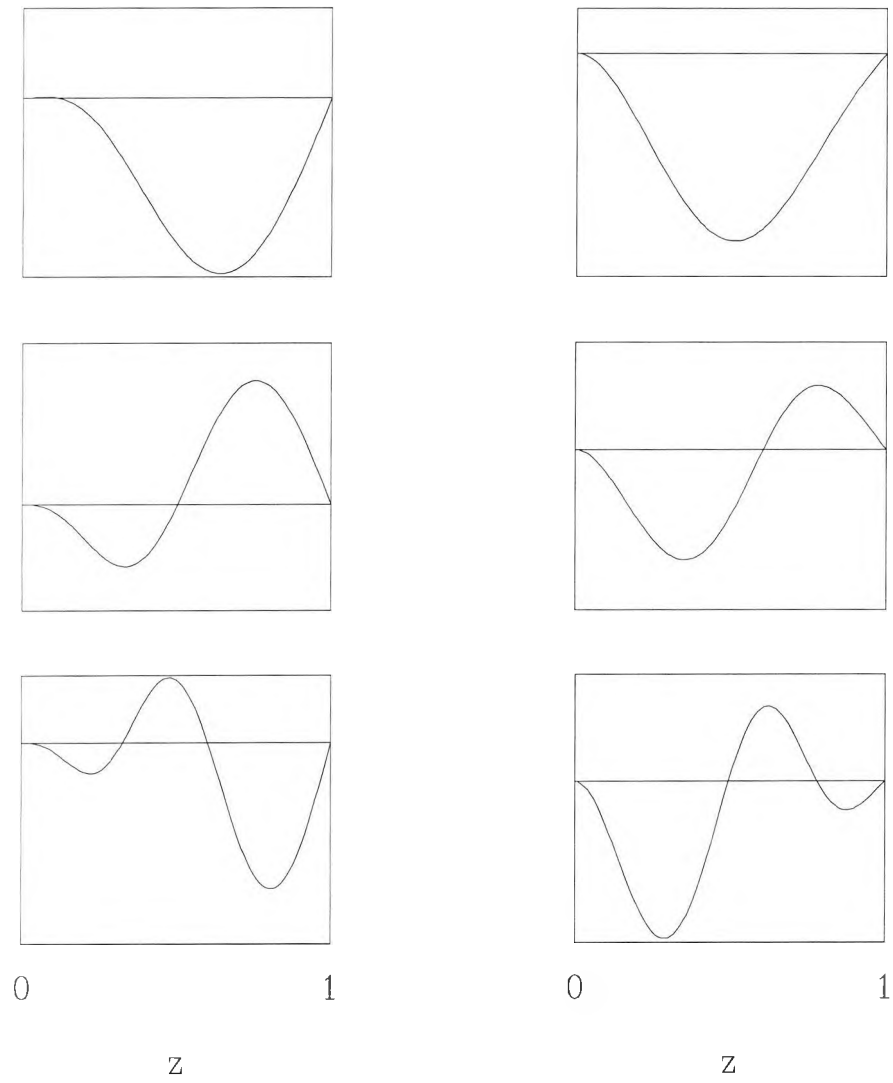


Figure 2.6: First three  $\phi$ -eigenfunctions (from the top down) of the cold (left) and hot (right) end solutions at  $R_1 = 3000$  and  $\sigma = \infty$  as functions of  $z$ .

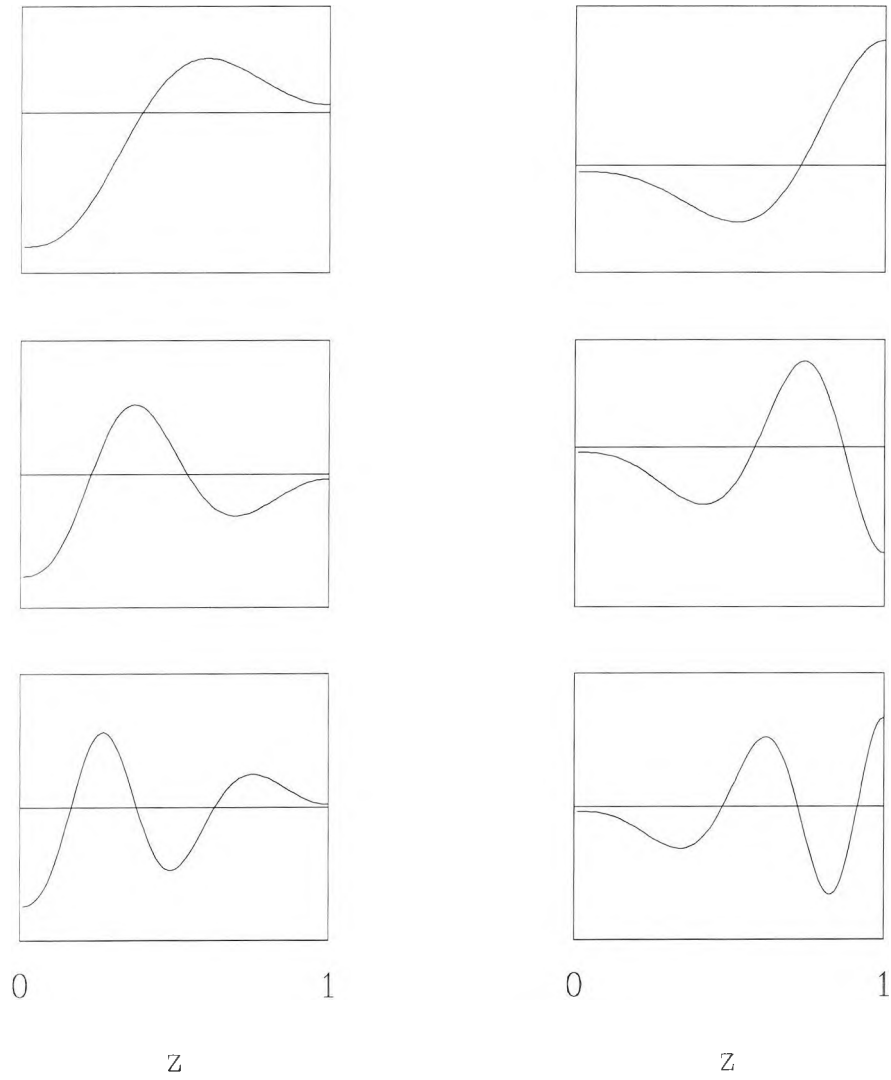


Figure 2.7: First three  $\Theta$ -eigenfunctions (from the top down) of the cold (left) and hot (right) end solutions at  $R_1 = 3000$  and  $\sigma = \infty$  as functions of  $z$ .

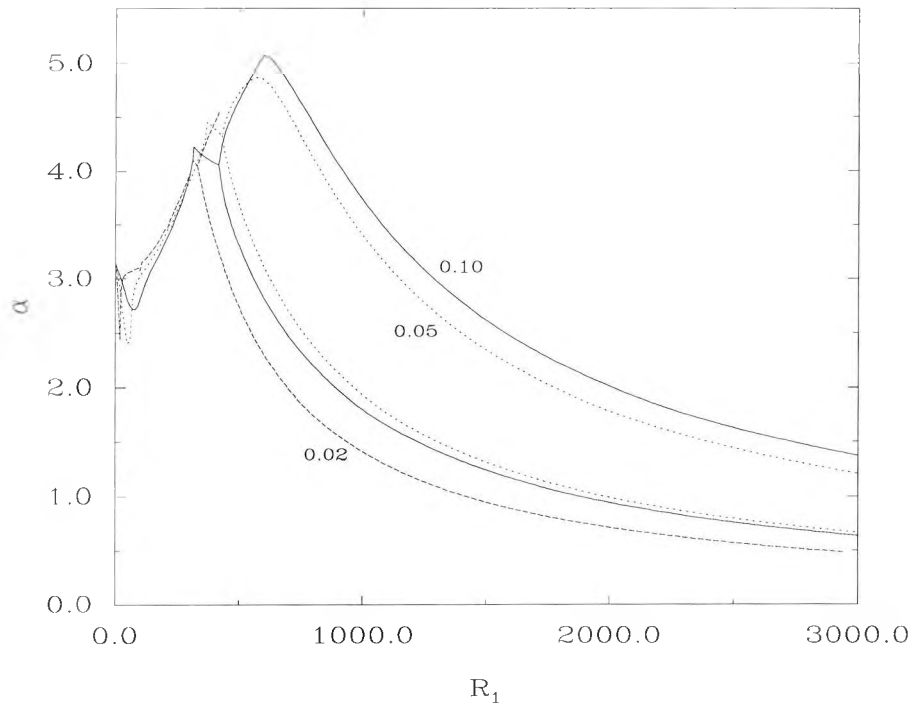


Figure 2.8: First two real mode eigenvalues  $\alpha$  for small Prandtl numbers as a function of  $R_1$  (hot end).

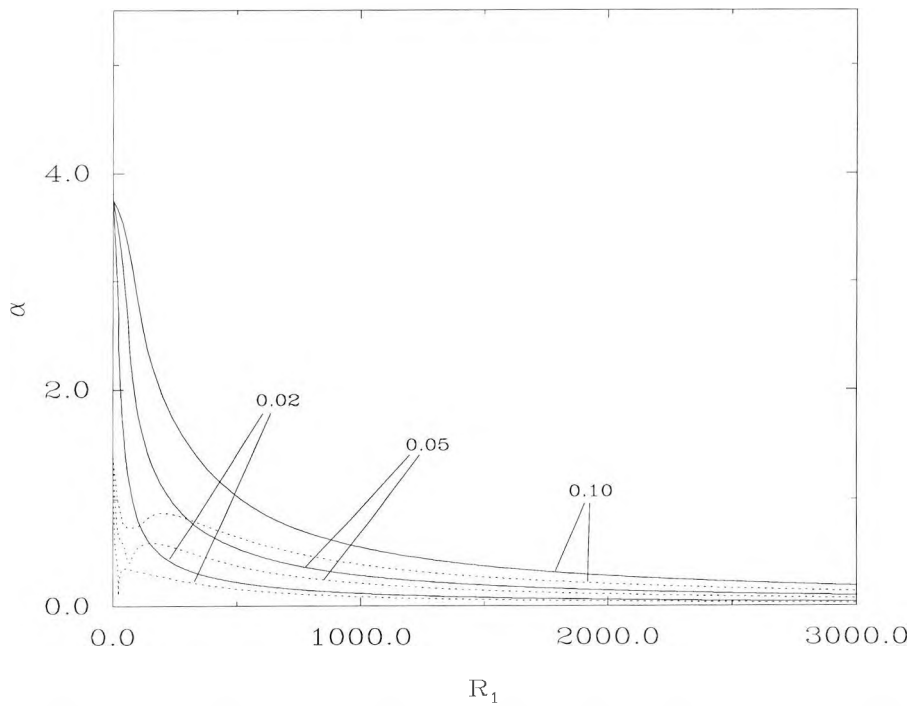


Figure 2.9: Real (solid line) and imaginary parts of the first complex mode eigenvalues  $\alpha$  for small Prandtl numbers as a function of  $R_1$  (hot end).

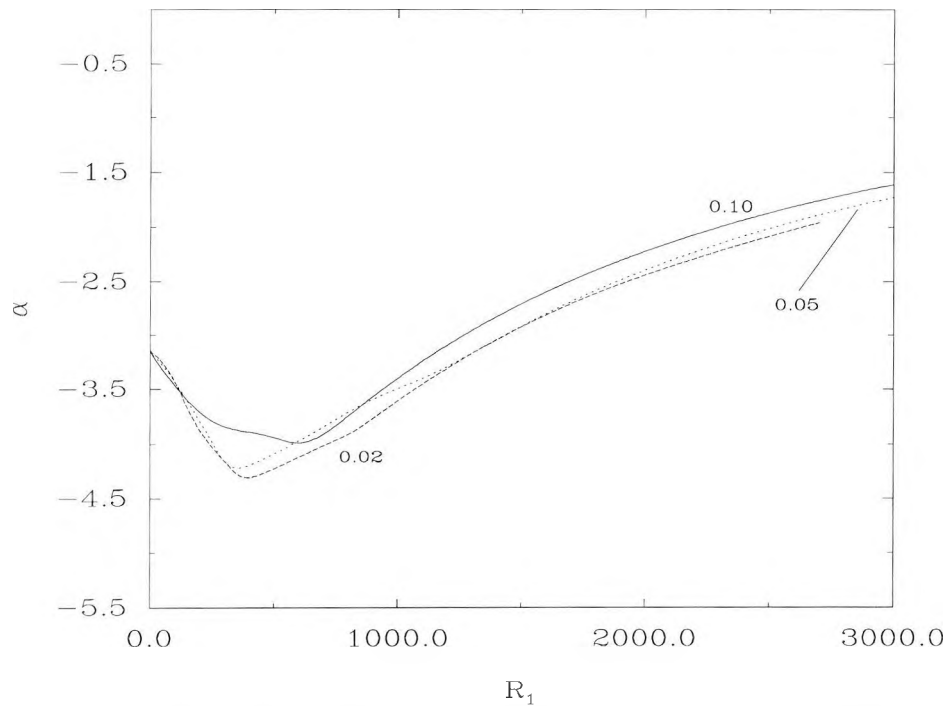


Figure 2.10: First real mode eigenvalues  $\alpha$  for small Prandtl numbers as a function of  $R_1$  (cold end).

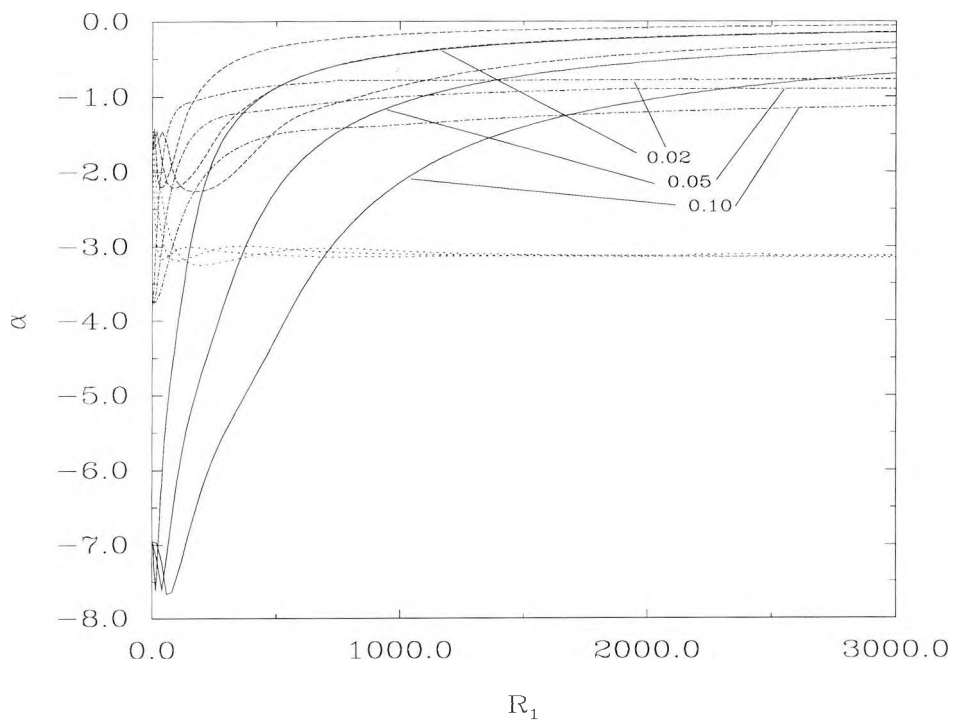


Figure 2.11: Real (dot-dashed line) and imaginary (dotted line) parts of the first, and real (solid) and imaginary (dashed) parts of the second, complex mode eigenvalues  $\alpha$  for small Prandtl numbers as a function of  $R_1$  (cold end).

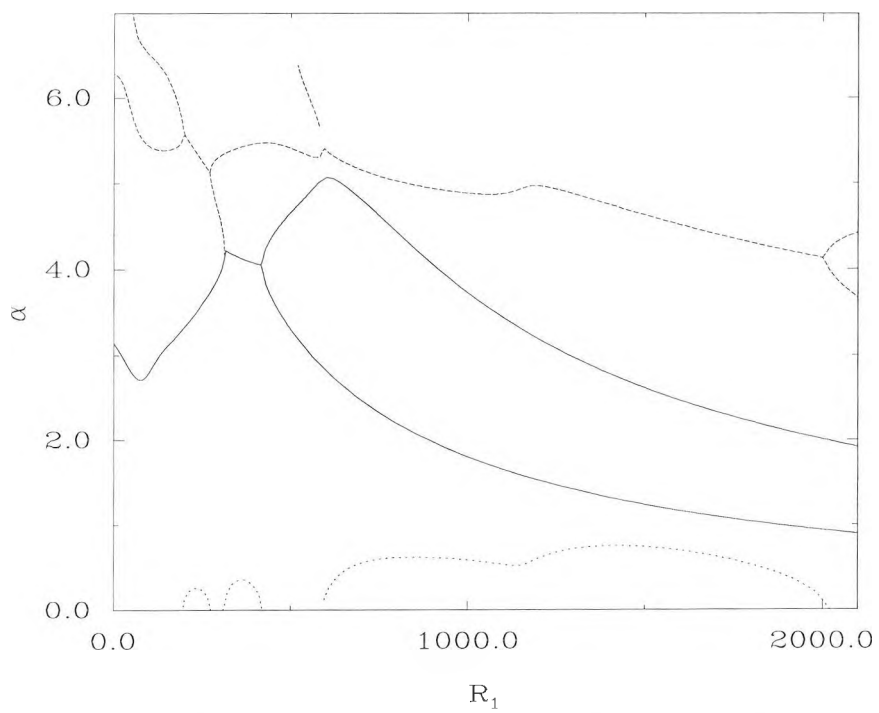


Figure 2.12: Interaction of the first few real mode eigenvalues at Prandtl number  $\sigma = 0.1$ . The first mode is the solid line, other modes are dashed lines; the dotted lines are imaginary parts of the eigenvalues.

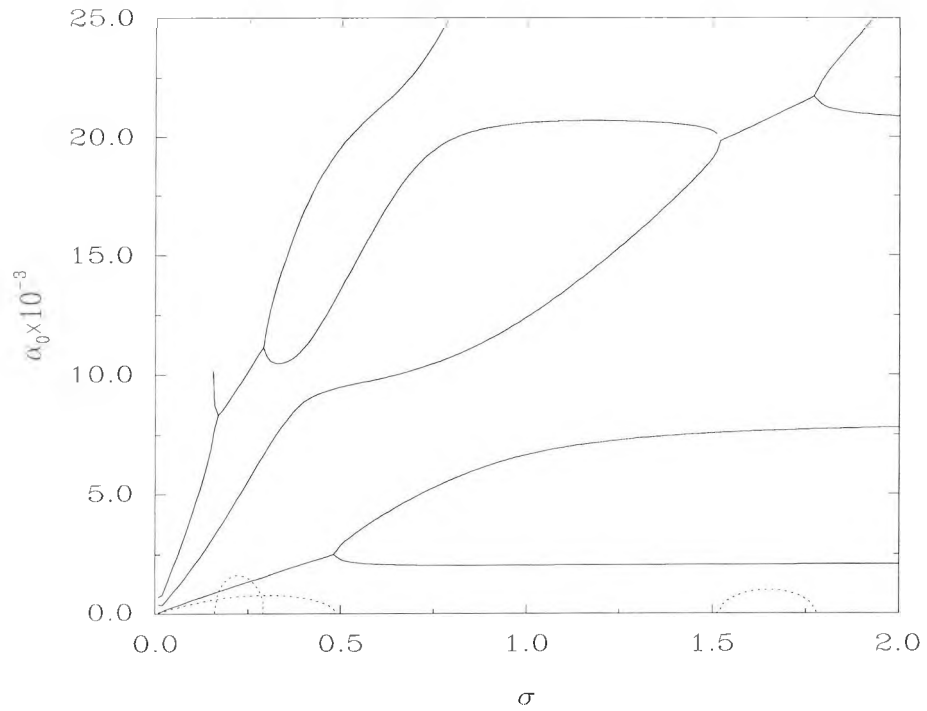


Figure 2.13: Real (solid lines) and imaginary parts of the reduced eigenvalues  $\alpha_0$  as a function of the Prandtl number for the hot end-zone.

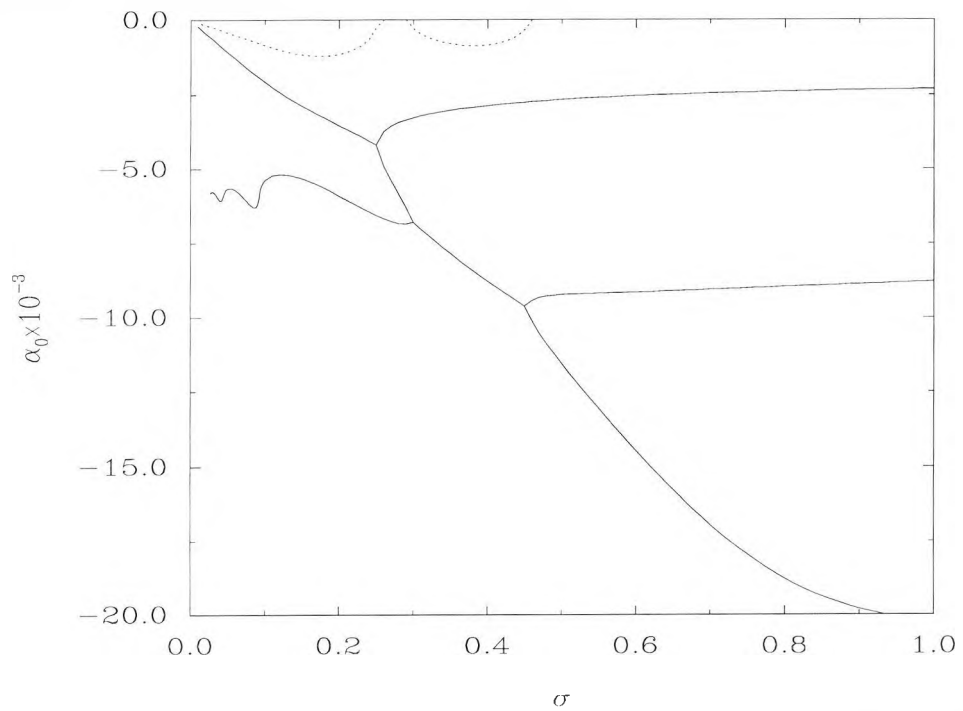


Figure 2.14: Real (solid lines) and imaginary parts of the reduced eigenvalues  $\alpha_0$  as a function of the Prandtl number for the cold end-zone.

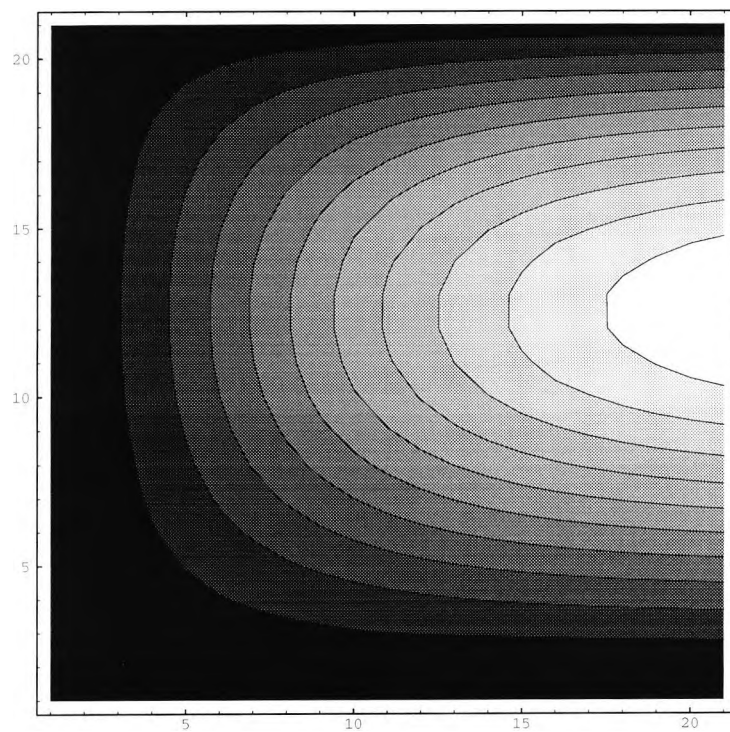


Figure 2.15: Contour plot of the first order stream function  $\psi_1$ .

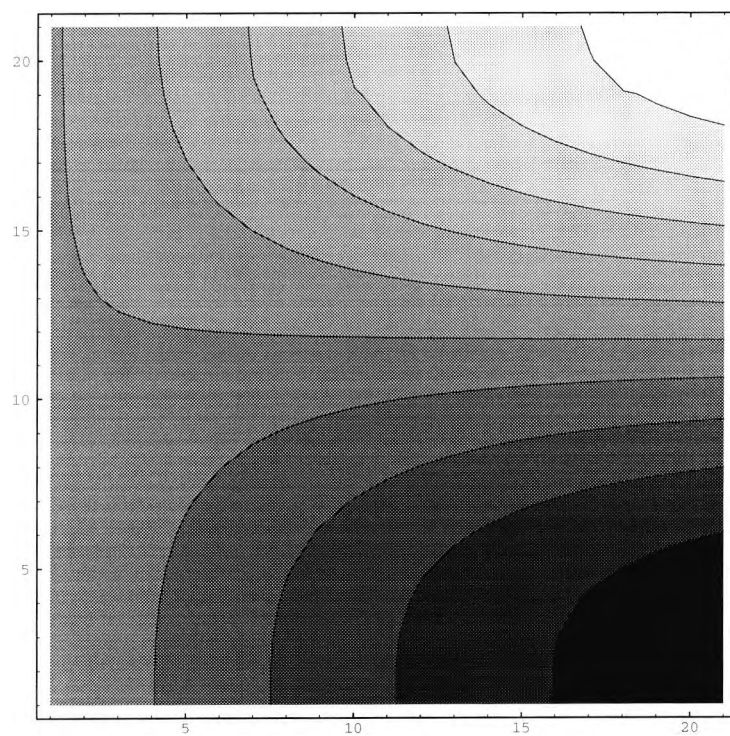


Figure 2.16: Contour plot of the first order temperature function  $\theta_1$ .

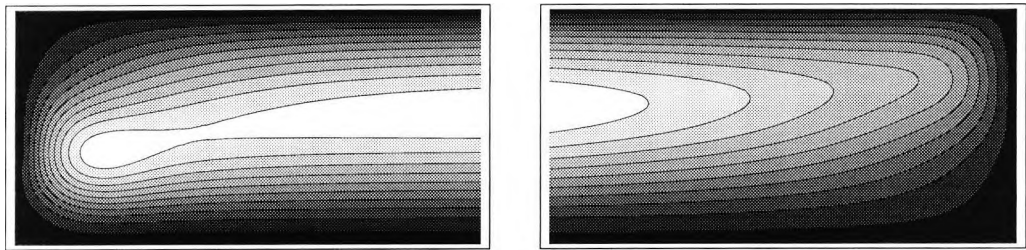


Figure 2.17: Approximate solutions for the streamlines in the two end zones based on the eigensolution of section 2.7 (cold on the left, hot on the right) for  $R_1 = 3000$  and  $\sigma = \infty$ .

## Chapter 3

# Stability of the non-rotating core flow

### 3.1 Introduction

The stability of the system to transverse and longitudinal disturbances is investigated in this chapter, by considering perturbations to the core solution of the full governing equations. Previous work has mostly been concerned with the problem with a rigid upper surface, although the stability of the free upper surface system has been studied before both analytically and experimentally. Hart (1983) discussed the onset of longitudinal instabilities and obtained the critical Grashof number as a function of Prandtl number,  $\sigma$ , as did Laure and Roux (1989) using a variant of the Galerkin method. Gill (1974) did not consider transverse mode instability for the rigid and free upper and lower surface problems because of its non-oscillatory character, but on discussing earlier experimental results concluded “that the side walls of the box stabilized this form of disturbance, or that the measurement techniques were not sensitive to its presence.” The Galerkin-method/QR-algorithm scheme used by Hart(1983) did not converge very well for  $\sigma > 0.1$ , and so “these modes being of less interest” no calculations were made beyond this point.

In this chapter the whole neutral curve is described for both transverse and longitudinal disturbances and a detailed asymptotic analysis is undertaken to describe the limiting structure of the curve for large Rayleigh numbers. Using both asymptotic and numerical techniques, estimates are found for the critical Prandtl

numbers,  $\sigma_c$ , above which the system is stable.

The chapter is split into two main sections: one for the transverse modes of instability, and one for the longitudinal modes. For each problem the linear stability equations are derived assuming that the perturbations are made to a parallel free-surface core flow. The stability equations are solved analytically for perturbations with zero wavenumber  $k$  and general  $R_1$ , and for general wavenumber at  $R_1 = 0$ , where the system is stable. These results then assist in solving the problem for general  $R_1$  and general  $k$  using a Runge–Kutta scheme with Newton iteration.

For both transverse and longitudinal modes, the large  $R_1$  asymptotes are examined in detail. The development of boundary layers for finite wavenumber and large Rayleigh number makes the numerical solution of the full stability problem less accurate in this limit, but leads to an interesting asymptotic theory, the physical interpretation of which is discussed in section 3.5.

## 3.2 The transverse stability equations

The full equations governing two dimensional motion parallel to the cross-sectional plane of the cavity are

$$\nabla^4 \bar{\psi} - R \frac{\partial \bar{\theta}}{\partial x} = \sigma^{-1} \frac{\partial(\nabla^2 \bar{\psi}, \bar{\psi})}{\partial(x, z)} + \sigma^{-1} \frac{\partial \nabla^2 \bar{\psi}}{\partial t}, \quad (3.2.1)$$

$$\nabla^2 \bar{\theta} = \frac{\partial(\bar{\theta}, \bar{\psi})}{\partial(x, z)} + \frac{\partial \bar{\theta}}{\partial t}, \quad (3.2.2)$$

with  $\bar{\psi} = \frac{\partial \bar{\psi}}{\partial z} = \frac{\partial \bar{\theta}}{\partial z} = 0$  on  $z = 0$  and  $\bar{\psi} = \frac{\partial^2 \bar{\psi}}{\partial z^2} = \frac{\partial \bar{\theta}}{\partial z} = 0$  on  $z = 1$ . As shown in the previous chapter, away from the end walls (3.2.1) and (3.2.2) have an exact steady parallel-flow core solution  $\bar{\psi} = \bar{\psi}_s$ ,  $\bar{\theta} = \bar{\theta}_s$ , where to a first approximation

$$\bar{\psi}_s = R_1 G'(z), \quad (3.2.3)$$

$$\frac{\partial \bar{\theta}_s}{\partial x} = 1, \quad \frac{\partial \bar{\theta}_s}{\partial z} = R_1 G'(z), \quad (3.2.4)$$

with  $R_1 = R/L$  and  $G = \frac{1}{120}z^5 - \frac{5}{192}z^4 + \frac{1}{48}z^3$ .

To study the stability of the system to transverse disturbances, the core solution is perturbed by functions  $\hat{\phi}$  and  $\hat{\Theta}$  which are assumed to depend on  $x, z$

and  $t$ , so that

$$\bar{\psi} = \bar{\psi}_s + \epsilon \hat{\phi}(x, z, t), \quad (3.2.5)$$

$$\bar{\theta} = \frac{1}{L}(\bar{\theta}_s + \epsilon \hat{\Theta}(x, z, t)). \quad (3.2.6)$$

The transverse perturbations are assumed to be oscillatory in the  $x$  direction with axes perpendicular to the core flow, and have the form

$$\hat{\phi}, \hat{\Theta} = \{\phi(z), \Theta(z)\} e^{\omega t} e^{ikx}, \quad (3.2.7)$$

where the wavenumber  $k$  is real and  $\omega = \omega_r + i\omega_i$ .

Substituting the perturbed core flow (3.2.5), (3.2.6) into the governing equations (3.2.3), (3.2.4) and linearising in  $\epsilon$  yields the perturbation equation for the transverse modes:

$$\phi^{iv} - 2k^2 \phi'' + k^4 \phi - R_1 ik \Theta = \frac{ikR_1}{\sigma} (G''(\phi'' - k^2 \phi) - \phi G^{iv}) + \frac{\omega}{\sigma} (\phi'' - k^2 \phi), \quad (3.2.8)$$

$$\Theta'' - k^2 \Theta - \phi' = R_1 ik (G'' \Theta - G' \phi) + \omega \Theta, \quad (3.2.9)$$

with  $\phi = \phi' = \Theta' = 0$  on  $z = 0$  and  $\phi = \phi'' = \Theta' = 0$  on  $z = 1$ . These are solved for  $\omega = \omega(R_1, k, \sigma)$ , where it is required physically that  $R_1, \sigma \geq 0$ . If  $\omega(R_1, k, \sigma)$  is the eigenvalue corresponding to the eigenfunctions  $\phi$  and  $\Theta$ , then  $\omega^*(R_1, -k, \sigma)$  is the eigenvalue that corresponds to the eigenfunctions  $\phi^*(R_1, -k, \sigma)$  and  $\Theta^*(R_1, -k, \sigma)$  (where the asterisk denotes the complex conjugate) and thus solutions are only required for  $k \geq 0$ . The system is stable if  $\omega_r < 0$  and unstable if  $\omega_r > 0$ . From the previous chapter it can be noted that there are no solutions for  $\omega = 0$ .

### 3.2.1 Solution of the transverse stability equations

An analytic solution of the stability equations (3.2.8) and (3.2.9) is possible when  $kR_1 = 0$ , that is for general  $R_1$  when  $k = 0$ , and for general  $k$  when  $R_1 = 0$ .

When  $k = 0$  the perturbation equations (3.2.8) and (3.2.9) are independent of  $R_1$  and have the form

$$\phi^{iv} - \frac{\omega}{\sigma} \phi'' = 0, \quad (3.2.10)$$

$$\Theta'' - \phi' = \omega \Theta, \quad (3.2.11)$$

with  $\phi = \phi' = \Theta' = 0$  on  $z = 0$  and  $\phi = \phi'' = \Theta' = 0$  on  $z = 1$ . The 'thermal' eigenvalues

$$\omega = -(n\pi)^2, \quad n = 0, 1, 2, \dots \quad (3.2.12)$$

are defined from the solution of (3.2.11) for the trivial case of (3.2.10) ( $\phi \equiv 0$ ), with eigenfunctions

$$\Theta = \cos n\pi z. \quad (3.2.13)$$

A second set of solutions arises from the non-trivial solutions of (3.2.10) given by

$$\phi = \Gamma(\cos \Gamma z + z - 1) - \sin \Gamma z, \quad (3.2.14)$$

where values of  $\Gamma = \sqrt{-\omega/\sigma}$  are determined as the roots of

$$\tan \Gamma = \Gamma. \quad (3.2.15)$$

This corresponds to a set of real negative values of  $\omega$  given by

$$\omega = -\{20.191, 59.680, 118.900, 197.858, \dots\}\sigma \quad (3.2.16)$$

and which approach the asymptote  $\omega \sim -(2n + 1)^2(\pi/2)^2\sigma$  for large integer values of  $n$ .

When  $R_1 = 0$ , the stability equations (3.2.8) and (3.2.9) simplify to

$$\phi^{iv} - 2k^2\phi'' + k^4\phi = \frac{\omega}{\sigma}(\phi'' - k^2\phi), \quad (3.2.17)$$

$$\Theta'' - k^2\Theta - \phi' = \omega\Theta, \quad (3.2.18)$$

with  $\phi = \phi' = \Theta' = 0$  on  $z = 0$  and  $\phi = \phi'' = \Theta' = 0$  on  $z = 1$ .

For the trivial solution of (3.2.17), (3.2.18) has the solution

$$\Theta = \cos n\pi z \quad (3.2.19)$$

corresponding to the thermal eigenvalues

$$\omega = -(n\pi)^2 - k^2, \quad n = 0, 1, 2, \dots \quad (3.2.20)$$

which reproduce (3.2.12) and (3.2.13) as  $k \rightarrow 0$ . Thus, for  $R_1 = 0$  the thermal eigenvalues are independent of the Prandtl number. Equation (3.2.17) has non-trivial solutions of the form  $\phi = e^{mz}$  where in order that  $\phi$  may satisfy the boundary

conditions, it is necessary for there to be an oscillatory component to the solution. This is the case if  $\omega$  is real and  $-\omega/\sigma - k^2 > 0$  so that

$$m = \pm k, \pm i\Gamma, \quad (3.2.21)$$

where

$$\Gamma = \sqrt{\frac{-\omega}{\sigma} - k^2}. \quad (3.2.22)$$

The required solution of (3.2.17) is

$$\phi = [e^{kz} - e^{k(2-z)} - \frac{(1 - e^{2k})}{(1 - e^{2i\Gamma})}(e^{i\Gamma z} - e^{i\Gamma(2-z)})] \quad (3.2.23)$$

where values of  $\Gamma$  are determined as the roots of

$$\frac{\tanh k}{k} = \frac{\tan \Gamma}{\Gamma}. \quad (3.2.24)$$

Note that as  $k \rightarrow 0$  this reproduces (3.2.15).

Numerical solutions of (3.2.17) and (3.2.18), initiated from the results (3.2.12) and (3.2.16) at  $k = 0$ , are shown in figure 3.1 as plots of  $\omega$  against  $k$  for  $\sigma = 7$ , corresponding to the Prandtl number of water. The shallow curves are the thermal eigenvalues that correspond to the analytic solution (3.2.20), and the steep curves are the stream function eigenvalues corresponding to the solutions of (3.2.24). Since for the latter curves  $\omega$  is directly proportional to the Prandtl number at fixed  $k$ , these curves become less steep as the Prandtl number decreases and then lie above the thermal eigenvalue curves at sufficiently high values of  $k$ . This suggests the possibility that it is these modes that will provide a mechanism for instability at small Prandtl number and non-zero values of  $R_1$ .

The results of this section show, via (3.2.12) and (3.2.15), that the system is always stable for  $k = 0$ , and via (3.2.20),(3.2.24) and figure 3.1 that the system is always stable for  $R_1 = 0$ . These results are used to initiate numerical solutions of the full system (3.2.8), (3.2.9) for non-zero values of  $k$  and  $R_1$ , to be described next.

### 3.2.2 Numerical solution of the transverse stability equations

The full stability equations (3.2.8) and (3.2.9) were solved numerically using a fourth order Runge-Kutta scheme with Newton iteration, similar to that used in the previous chapter. The stability equations were rewritten as twelve simultaneous first

order equations. Then for given  $R_1$ ,  $k$  and  $\sigma$ , and an initial estimate of  $\omega$ , the Runge-Kutta scheme was used usually with 100 steps to integrate the equations from  $z = 0$  (where the boundary conditions are prescribed) to  $z = 1$ ; the full solutions for  $\phi$ ,  $\Theta$  and their derivatives are then constructed from linear combinations of the solutions for the three different initial conditions  $\phi'' = 1$ ,  $\phi''' = 1$  and  $\Theta = 1$  at  $z = 0$ . The three values of  $\phi$ ,  $\phi''$  and  $\Theta'$  at  $z = 1$  then form a matrix, the determinant of which must vanish in order that the boundary conditions at  $z = 1$  are satisfied. The Newton iteration used the values of the determinant at the points  $\omega$ ,  $\omega + \Delta\omega_r$  and  $\omega + \Delta\omega_i$  to refine the estimate of  $\omega$  and bring the determinant close to zero. The iterative scheme was halted when the refinement to  $\omega$  became less than  $\Delta\omega$ . In most cases the value of  $\Delta\omega$  was taken to be  $10^{-4}$ . Computations were usually started from  $k = 0$  where the values of  $\omega$  are known from the results of section 3.2.1. This, together with the results for  $R_1 = 0$  and general  $k$ , also provides an opportunity to check the numerical results against the analytical solutions. Eigenvalue curves were traced out by keeping  $R_1$  and  $\sigma$  constant and incrementing  $k$  (usually by  $\sim 10^{-2}$ ) and using the result at the previous value of  $k$  as an initial estimate of  $\omega$ .

### 3.2.3 Numerical results

As discussed in section 3.2, solutions are only required for positive  $R_1$ ,  $k$  and  $\sigma$ . Work by Hart(1983) on similar problems suggests that the system becomes unstable for small Prandtl numbers, and so attention was focused on values of  $\sigma$  around 0.1 or less. Modes associated with the thermal eigenvalues at  $k = 0$  are referred to as 'thermal modes', and those associated with the stream function eigenvalues at  $k = 0$  are referred to as 'stream function modes'.

The curves of the real and imaginary parts of  $\omega$  as a function of  $k$  at  $R_1 = 4000$  and small  $\sigma$  for the first three thermal modes are given in figures 3.2 and 3.3. It can be observed that (in the calculated range) although the behaviour of the thermal eigenvalues is not simple, these modes are stable. Figure 3.3 suggests that there is a strong linear relationship between  $\omega_i$  and  $k$ .

The modes of greatest interest are the first two modes corresponding to the stream function perturbation. Plots of the real and imaginary parts of  $\omega$  for the first two stream function modes as functions of  $k$  at  $R_1 = 4000$  for small Prandtl number

are shown in figures 3.4 and 3.5 and figures 3.6 and 3.7. These become unstable for certain values of  $\sigma$  and  $k$  and have a certain predictability in that the higher the Prandtl number, the greater the value of  $k$  needed for instability. There also seems to be a link between these two modes: for  $\sigma < 0.065$  the first mode becomes unstable and the second mode remains stable, but for  $\sigma > 0.070$ , the rôles are interchanged. The exact point in  $(\sigma, \omega, k)$  space and method of interchange are difficult to define, but the point is at approximately  $(\sigma_{int}, \omega_{int}, k_{int}) = (0.0668, -2.83 + 4.15i, 0.126)$ . Figures 3.8 and 3.9 show a neighbourhood of  $(\sigma_{int}, \omega_{int}, k_{int})$ . The  $\omega_r$  curves are crossed for  $\sigma < \sigma_{int}$ , and uncrossed for  $\sigma > \sigma_{int}$ ; the  $\omega_i$  curves are crossed for  $\sigma < \sigma_{int}$  and uncrossed for  $\sigma > \sigma_{int}$ . The crossing of these modes does not seem to represent any physical effect on the system: the value of  $k$  for which  $\omega_r = 0$  is 'predictable' as  $\sigma$  moves through  $\sigma_{int}$ , and the eigenfunction  $\phi$  when  $\omega_r = 0$  for mode 1 at  $\sigma = 0.06$  and mode 2 when  $\sigma = 0.07$  are very similar, as shown by the plots of the two complex eigenfunctions against  $z$  in figure 3.10.

Although not shown in the figures, the third stream function eigenvalues were calculated for Prandtl numbers 0.05, 0.10 and 0.15, and were found to be stable. It seems likely that further modes are stable.

### 3.2.4 Neutral Curves

The results described above demonstrate the instability of the system as a function of  $k$  and  $\sigma$  at fixed Rayleigh number. For example in figure 3.6, for  $\sigma = 0.09$  and  $R_1 = 4000$ , the system is unstable for values of  $k$  approximately in the range  $0.8 < k < 1.3$ . As the system is stable at  $R_1 = 0$ , this region of instability must contract and disappear between  $R_1 = 4000$  and  $R_1 = 0$ .

In order to visualise the values of  $R_1$  and  $k$  for which the system is unstable, the neutral curves ( $\omega_r = 0$ ) were calculated and are shown in figure 3.11 for various values of  $\sigma$ . These curves were found using an extended version of the Runge-Kutta-Newton scheme which used an additional Newton iteration to bring  $\omega_r$  to within  $10^{-4}$  of zero. Where the change in  $R_1$  was small compared with the change in  $k$ , the value of  $k$  was fixed and  $R_1$  found by the second Newton iteration considering  $\omega$  as a function of  $R_1$  only; where the change in  $R_1$  was large compared with the change in  $k$ , the value of  $R_1$  was fixed and  $k$  found by treating  $\omega$  as a function of  $k$  only.

Computations of the neutral curves for large values of  $R_1/\sigma$  become less accurate and are not shown.

The regions above the neutral curves in figure 3.11 are where the system is unstable. As  $\sigma$  increases, these regions become more narrow, and are confined to higher values of  $R_1$ . This behaviour can be seen graphically in the logarithmic plot of  $Gr_c = R_{1c}/\sigma$  versus  $\sigma$  (figure 3.12), where  $R_{1c}$  (the critical value of  $R_1$ ) is the minimum point of the neutral curve, that is the smallest value of  $R_1$  for which the system is unstable. The critical Grashof numbers for the longitudinal modes are also shown and will be discussed in section 3.5 below. The results indicate that there is a critical value of the Prandtl number,  $\sigma_c$ , above which the system is stable for all values of  $R_1$ . For the transverse modes, when  $\sigma = 0.11$ ,  $R_{1c} \sim 9 \times 10^4$ ; at such large values of  $R_1$  the accuracy of the results is reduced and it becomes difficult to trace the critical Grashof curve at higher values of  $\sigma$ . However, this corresponds to the results of Hart(1972) and of Daniels *et al.*(1987) for the system with a rigid upper surface which suggest that in that case the system is always stable for  $\sigma > 0.12$ . A better estimate of this critical Prandtl number  $\sigma_c$  for the free-surface case is obtained in section 3.3.3.

The ratio of the wave speed of the neutral disturbances ( $c = \omega_i/k$ ) to the free surface speed  $R_1/48$  is shown in figure 3.13. This indicates the neutral disturbances moving in the same direction as the free surface, but at between one third and one fifth of the speed. As expected, there is a non-zero value for  $\omega_{0i}$  when  $\omega_{0r} = 0$ , and so there are no steady oscillatory solutions similar to those found in the system with a rigid surface where stationary multiple cells extend throughout the cavity. The perturbation fields corresponding to the critical point on the neutral curve for  $\sigma = 0.04$  are shown in figure 3.14; the contours represent the stream function perturbation  $\phi(z)e^{ikx+\omega t}$  and the shading represents the temperature perturbation  $\Theta(z)e^{ikx+\omega t}$  at a fixed time  $t$ . The effect of these perturbations on the core is demonstrated in figure 3.15 which shows the contours of the overall stream function (3.2.5) and the contours of the overall temperature (3.2.6) represented by the shading. For the given instant  $t$  the value of  $\epsilon$  has been chosen so that the overall behaviour is easily discernible.

### 3.3 Asymptotic solution of the transverse stability equations for large $R_1$

Solutions of the stability equations for large Rayleigh number and moderate and large wavenumbers can not easily be found with the numerical method used in the previous section. Most physical applications of the system occur at large Rayleigh number though, and so this is an important region of parameter space to understand. Two asymptotic regimes are considered: where  $k = O(R_1^{-1})$  and  $\omega = O(1)$ , and where  $k = O(1)$  and  $\omega = O(R_1)$ , encompassing the two branches of the neutral stability curve. Reduced forms of the stability equations, derived by substituting these scalings into the full stability equations, are solved numerically with the fourth order Runge-Kutta-Newton iteration scheme, for various Prandtl numbers  $\sigma$ . These results show how  $\omega$  depends on  $k$  and  $\sigma$  for large  $R_1$ , and provide a useful check on the numerical solutions of the full stability equations.

The extremes of both regimes approach a single problem, the solution of which leads to an estimate of the critical Prandtl number,  $\sigma_c$ , above which all solutions are stable.

#### 3.3.1 Asymptotic results for $k = O(R_1^{-1})$ , $\omega = O(1)$ .

The neutral curves in figure 3.11 show the locus of  $\omega_r = 0$  as a function of  $R_1$  and  $k$ . For small  $k$  and large  $R_1$ , the leading behaviours of the left-hand branches of the neutral curves are identified with the scalings

$$k = \frac{k_0}{R_1}, \quad \omega = \omega_0 + \dots, \quad R_1 \rightarrow \infty, \quad (3.3.1)$$

where  $k_0$  and  $\omega_0$  are finite. Substituting this into the stability equations (3.2.8) and (3.2.9), and letting  $R_1 \rightarrow \infty$  yields the simplified problem:

$$\phi^{iv} - ik_0\Theta = \frac{ik_0}{\sigma}(G''\phi'' - \phi G''v) + \frac{\omega_0}{\sigma}\phi'', \quad (3.3.2)$$

$$\Theta'' - \phi' = ik_0(G''\Theta - G'\phi) + \omega_0\Theta, \quad (3.3.3)$$

with  $\phi = \phi' = \Theta' = 0$  on  $z = 0$  and  $\phi = \phi'' = \Theta' = 0$  on  $z = 1$ .

This was solved numerically using the fourth order Runge-Kutta scheme with Newton iteration. Here  $k_0$  was fixed and  $\omega$  found to an accuracy of  $10^{-4}$ , then  $k_0$

was incremented in steps of 10 and the new value of  $\omega$  found using the previous estimate. The curves were traced out in this way starting from  $k_0 = 0$  where (from section 3.2.1) the values of  $\omega$  are known.

For small Prandtl number ( $\sigma < 0.065$ ), the first stream function mode is the only mode to become unstable; the values of  $\omega$  for the first stream function mode are plotted against  $k_0$  in figure 3.16. For large  $k_0$  the system is unstable with the disturbance traveling in the direction of the free surface flow, as seen in the previous section. The critical values of  $k_0 = k_{0c}$  for which instability sets in for different  $\sigma$ , are given in Table 3.1, and it can be seen from figure 3.16 that as  $\sigma$  increases  $k_{0c}$  also increases rapidly. Also, at large  $k_0$ ,  $\omega$  behaves almost as a linear function of  $k_0$ , with its slope becoming more shallow with increasing Prandtl number.

Table 3.1 compares the values at of  $R_1 k$  and  $\omega_i$  at which  $\omega_r = 0$  found from the full stability equations when  $R_1 = 4000$  with  $k_0$  and  $\omega_{0i}$  found asymptotically for small Prandtl number. This confirms the validity of the limiting forms of the left-hand branches of the neutral curves, shown graphically in figure 3.11.

$\sigma$	Full solution		Asymptotic solution	
	$R_1 k(R_1=4000)$	$\omega_i$	$k_0$	$\omega_{0i}$
0.01	82.4	0.553	81.9	0.550
0.02	214	1.49	213	1.48
0.03	460	3.08	458	3.08
0.04	723	4.65	720	4.65

Table 3.1: Comparison of  $R_1 k$  and  $\omega_i$  at  $\omega_r = 0$  and  $R_1 = 4000$  found from the full stability equations with  $k_0$  and  $\omega_{0i}$  found asymptotically for small Prandtl number.

The left hand plot of figure 3.18 shows the ratio of the wave speed  $c = R_1 \omega_{0i} / k_0$  to the free surface speed  $R_1 / 48$ . The scaled growth rate is also shown. This plot shows that the perturbations travel in the direction of the free surface flow but at around 35% of the speed. This is even slower than the maximum speed of the return core flow. On the neutral curve ( $\omega_{0r} = 0$ ) the wave speed is close to a minimum; there is a maximum wave speed for longer waves.

### 3.3.2 Asymptotic results for $k = O(1)$ , $\omega = O(R_1)$

At large  $R_1$  the right-hand branch of the neutral curve is identified with finite values of  $k$  and the scaling

$$\omega = \omega_1 R_1 + \dots, \quad R_1 \rightarrow \infty. \quad (3.3.4)$$

Substitution of (3.3.4) into the stability equations (3.2.8),(3.2.9) gives at leading order the inviscid, convection-dominated system

$$-ik\Theta = \frac{ik}{\sigma}(G'''(\phi'' - k^2\phi) - \phi G''') + \frac{\omega_1}{\sigma}(\phi'' - k^2\phi), \quad (3.3.5)$$

$$0 = ik(G''\Theta - G'\phi) + \omega_1\Theta, \quad (3.3.6)$$

which can be simplified to the single second order equation for  $\phi$ :

$$\Omega^2\phi'' - (k^2\Omega^2 + G''\omega_1 + \sigma k^2 G')\phi = 0, \quad (3.3.7)$$

with  $\phi = 0$  on  $z = 0, 1$ , and where

$$\Omega(z) = \omega_1 + ikG''. \quad (3.3.8)$$

A fourth order Runge-Kutta scheme with Newton iteration is used to solve (3.3.7) for  $\omega_1$  at specified values of  $\sigma$  and  $k$ , but because of the magnitudes of  $\omega_1$  involved,  $\omega_1$  is found to an accuracy of  $10^{-8}$ . In general there are values of  $z$  for which  $\omega_1 + kG''(z) = 0$ . Thus, at a neutral point where  $\omega_{1r} = 0$ ,  $\Omega(z) = 0$  for some  $z$ , causing a singularity in the system. This did not cause a problem as  $k \rightarrow 0$ , but for finite non-zero  $k$  it was necessary to use up to  $10^4$  steps in the Runge-Kutta scheme to achieve an accurate result near the point of neutral stability. Initial estimates for  $\omega_1$  were obtained from the asymptotic solutions of section (3.3.1), where for large  $k_0$ ,  $\omega_0$  behaves like  $ak_0$  where  $a$  is a constant. As  $k_0 \rightarrow R_1$ ,  $k \rightarrow 1$  and  $\omega \sim aR_1$ ; that is the slopes of the eigenvalue curves in figure 3.16 were used as initial estimates of  $\omega_1$  at  $k = 1$ .

On taking the complex conjugate of (3.3.7) it can be seen that if  $\omega_1$  is the eigenvalue corresponding to  $\phi(k; z)$  then  $-\omega_1^*$  is the eigenvalue that corresponds to  $\phi^*(k; z)$ , where the asterisk denotes the complex conjugate. All numerical solutions are therefore for positive  $\omega_{1r}$  – the region of instability of the system.

The numerical solutions of (3.3.7) for small Prandtl numbers are plotted in figure 3.17. As  $k \rightarrow 0$  it can be seen that  $\omega_1 \sim ak$ . The right hand side of figure

3.17 indicates the value of  $k$  for which  $\omega_{1r} = 0$ . These are the values of  $k$  which the  $R_1$ - $k$  neutral curves approach for large  $R_1$ , and are shown in figure 3.11 as dashed lines.

The neutral curves found by the numerical solution of the full stability equations become less and less accurate for large  $R_1$  and moderate  $k$ , until the curves can not be computed any further. This means that a close comparison of the solutions of the full stability equations with the large  $R_1$  asymptotic solutions is not possible. However, it can be seen from Table 3.2 that although there is a large difference in the  $k$  values, the values of  $\omega_i/R_1$  and  $\omega_{1i}$  compare quite well. The plots of the neutral curves and their asymptotes in figure 3.11 help to confirm, if only intuitively, the suitability of the limiting form.

$\sigma$	Full solution		Asymptotic solution	
	$\omega_i/R_1 \times 10^3$	$k$	$\omega_{1i} \times 10^3$	$k$
0.01	9.48	2.23	9.25	2.65
0.02	9.57	2.16	9.61	2.59
0.03	9.64	2.07	9.96	2.52
0.04	9.75	1.98	10.3	2.45

Table 3.2: Comparison of  $\omega_i/R_1$  and  $k$  at  $\omega_r = 0$ ,  $R_1 = 4000$  found from the full stability equations with  $\omega_{1i}$  and  $k$  found asymptotically for small Prandtl number.

The right hand plot of figure 3.18 shows the ratio of the wave speed  $c = R_1\omega_{1i}/k$  to the free surface speed  $R_1/48$  for the region of instability; at the right-hand branch of the neutral curve the wave speed is always less than half the free surface speed. The wave speed decreases with decreasing wavelength but is always non-zero. Both  $\omega_{1i}$  and  $\omega_{1r}$  confirm the behaviour  $\omega_1 \sim ak$  as  $k \rightarrow 0$ .

### 3.3.3 Collapse of the neutral stability curve

In section 3.3.1 the numerical results suggest that

$$\omega_0 \sim ak_0, \quad k_0 \rightarrow \infty, \quad (3.3.9)$$

where  $a$  is a finite constant depending only on the Prandtl number of the fluid. Substituting this into the reduced stability equations (3.3.2) and (3.3.3) yields

$$-i\Theta = \frac{i}{\sigma}(G''\phi'' - \phi G''') + \frac{a}{\sigma}\phi'', \quad (3.3.10)$$

$$0 = i(G''\Theta - G'\phi) + a\Theta, \quad (3.3.11)$$

which simplifies to

$$(a + iG'')^2\phi'' - (iG''(a + iG'') + \sigma G')\phi = 0 \quad (3.3.12)$$

with

$$\phi = 0 \text{ on } z = 0, 1. \quad (3.3.13)$$

Similarly in section 3.3.2 it was noted that  $\omega_1$  is proportional to  $k$  as  $k \rightarrow 0$  and substitution of the form  $\omega_1 = ak$  into the Rayleigh equation (3.3.7) gives the same limiting problem for  $\phi$  and the eigenvalue  $a$ . Thus the real parts of the complex eigenvalues  $a$  given by the solution of (3.3.12) are the slopes of the growth rate curves of figure 3.17 as  $k \rightarrow 0$ . These slopes become shallower with increasing Prandtl number, and the non-zero value of  $k$  for which  $\omega_{1r} = 0$  decreases with increasing Prandtl number until the entire growth rate curve shrinks to a point in the neighbourhood of  $k = 0$ . This occurs when the slope reaches zero at which point there will be no unstable solutions of the system associated with transverse modes. This behaviour can also be seen in figure 3.16 where the slopes of the curves representing the real part of the eigenvalue  $\omega_0$  as  $k_0 \rightarrow \infty$  decrease with increasing Prandtl number.

The Rayleigh problem (3.3.12) was solved for  $a$  as a function of  $\sigma$  using the fourth order Runge-Kutta scheme with the Newton iteration. This allowed the value of  $a$  to be found to within  $10^{-8}$  for general values of  $\sigma$ . An initial estimate of  $a$  was made from the graph of  $\omega_0$  against  $k_0$  (figure 3.16) at  $\sigma = 0.01$ , and  $\sigma$  was then incremented in steps of  $10^{-3}$ . As  $a_r$  approached zero it was necessary to take up to  $10^4$  steps in the Runge-Kutta scheme to counteract the effect of the approaching singularity at the value of  $z$  for which  $a_r = -G''(z)$ . The results are shown as a plot of  $a$  against  $\sigma$  in figure 3.19. For increasing  $\sigma$ , the final result obtained at  $\sigma = 0.161$  is  $a = 2.59 \times 10^{-5} + 9.93 \times 10^{-3}i$ . This produces a very good estimate for the critical Prandtl number ( $\sigma_c$ ) above which all solutions of the system are stable: linear interpolation from the last few points suggests that when  $a_r = 0$ , to three significant figures,  $\sigma = \sigma_c = 0.162$ . This compares with the estimate of  $\sigma_c \approx 0.12$  obtained by Daniels *et al.* (1987) for the rigid surface problem, although it should be noted that their estimate was not based on the use of an accurate asymptotic analysis of the kind used here. It would be of interest to calculate  $\sigma_c$  for the rigid surface problem using the present approach.

### 3.4 Stability of the core flow to longitudinal perturbations

The stability of the core solution to longitudinal perturbations (perturbations oscillatory in the  $y$  direction with axes parallel to the core flow) is investigated in this section. Numerical results are obtained for general values of  $R_1$  and an asymptotic theory is developed for large Rayleigh numbers which indicates qualitative differences from the results obtained for the transverse modes of instability. This theory shows that at finite Prandtl numbers only long wavelength disturbances are unstable although shorter wavelength longitudinal instabilities do exist, in the limit of vanishingly small Prandtl number. The full governing equations for three dimensional flow derived in section 1.3 are

$$\frac{\partial \bar{\mathbf{u}}}{\partial t} + \bar{\mathbf{u}} \cdot \nabla \bar{\mathbf{u}} = -\nabla \bar{p} + \sigma \nabla^2 \bar{\mathbf{u}} + R\bar{\theta} \sigma \mathbf{k}, \quad (3.4.1)$$

$$\frac{\partial \bar{\theta}}{\partial t} + \bar{\mathbf{u}} \cdot \nabla \bar{\theta} = \nabla^2 \bar{\theta}, \quad (3.4.2)$$

$$\nabla \cdot \bar{\mathbf{u}} = 0 \quad (3.4.3)$$

where  $\bar{\mathbf{u}} = (\bar{u}, \bar{v}, \bar{w})$  is the velocity field,  $\bar{p}$  is the pressure and  $\bar{\theta}$  is the temperature. The boundary conditions are

$$\bar{\mathbf{u}} = \mathbf{0} \text{ on } z = 0, \quad \frac{\partial \bar{u}}{\partial z} = \frac{\partial \bar{v}}{\partial z} = \bar{w} = 0 \text{ on } z = 1, \quad (3.4.4)$$

$$\frac{\partial \bar{\theta}}{\partial z} = 0 \text{ on } z = 0, 1. \quad (3.4.5)$$

Away from the end walls the steady parallel-flow core solution is  $\bar{\mathbf{u}} = \bar{\mathbf{u}}_s$ ,  $\bar{p} = \bar{p}_s$ ,  $\bar{\theta} = \bar{\theta}_s$  where to a first approximation

$$\bar{\mathbf{u}}_s = (R_1 G'''(z), 0, 0), \quad (3.4.6)$$

$$\frac{\partial \bar{\theta}_s}{\partial x} = 1, \quad \frac{\partial \bar{\theta}_s}{\partial y} = 0, \quad \frac{\partial \bar{\theta}_s}{\partial z} = R_1 G'(z) \quad (3.4.7)$$

with  $R_1 = R/L$  and  $G(z) = \frac{1}{120}z^5 - \frac{5}{192}z^4 + \frac{1}{48}z^3$ . The explicit form of  $\bar{p}_s$  can also be written down and is independent of  $y$  but it is not needed in order to determine the stability equations.

Longitudinal perturbations are made to the core flow, such that

$$\bar{\mathbf{u}} = \bar{\mathbf{u}}_s + \epsilon (U(z), V(z), W(z)) e^{\omega t + iky}, \quad (3.4.8)$$

$$\bar{p} = \bar{p}_s + \epsilon P(z)e^{\omega t + iky}, \quad (3.4.9)$$

$$\bar{\theta} = \frac{1}{L}(\bar{\theta}_s + \epsilon \Theta(z)e^{\omega t + iky}), \quad (3.4.10)$$

Here it is assumed that the perturbations are independent of  $x$  although it is necessary to incorporate a velocity component in that direction.

Substituting the perturbed solution into the governing equations and linearising in  $\epsilon$  yields the perturbation equations for the longitudinal modes:

$$\omega U + R_1 G''' W = \sigma(U'' - k^2 U), \quad (3.4.11)$$

$$\omega(W'' - k^2 W) = \sigma(W'' - 2k^2 W'' + k^4 W) - k^2 R_1 \sigma \Theta, \quad (3.4.12)$$

$$\omega \Theta + U + R_1 G' W = \Theta'' - k^2 \Theta, \quad (3.4.13)$$

to be solved subject to the boundary conditions,

$$U = W = W' = \Theta' = 0 \text{ on } z = 0, \text{ and } U' = W = W'' = \Theta' = 0 \text{ on } z = 1. \quad (3.4.14)$$

Here  $V$  has been eliminated from the equations and boundary conditions by use of the relation

$$V = \frac{i}{k} W', \quad (3.4.15)$$

obtained from the equation of continuity. The perturbation equations are to be solved, as previously, for  $\omega = \omega(R_1, k, \sigma)$  where it is required physically that  $R_1, \sigma \geq 0$ . The wave number  $k$  appears only in the forms  $k^2$  and  $k^4$  in the perturbation equations and so solutions are found for  $k \geq 0$ , the problem being symmetric about  $k = 0$ .

### 3.4.1 Solution of the perturbation equations

For general  $R_1, \sigma$  and  $k$ , the perturbation equations were solved using a fourth order Runge-Kutta scheme with Newton iteration as discussed in detail in sections 2.6 and 3.2.2. This method traces out values of  $\omega$  using a previously known value as a first estimate. Initial values of  $\omega$  can be calculated analytically when  $R_1 = 0$ , when the perturbation equations (3.4.11)-(3.4.13) simplify to three independent problems.

When  $R_1 = 0$ , (3.4.11) becomes

$$U'' = \left( \frac{\omega}{\sigma} + k^2 \right) U, \quad (3.4.16)$$

with  $U = 0$  on  $z = 0$  and  $U' = 0$  on  $z = 1$ . This has solutions

$$U = \sin(2n + 1)\frac{\pi}{2}z, \quad n = 0, 1, 2, \dots, \quad (3.4.17)$$

where the 'horizontal velocity' eigenvalues are given by

$$\omega = - \left[ (2n + 1)\frac{\pi}{2} \right]^2 \sigma - k^2 \sigma \quad n = 0, 1, 2, \dots \quad (3.4.18)$$

The second perturbation equation, (3.4.12), becomes

$$W^{iv} - \left( 2k^2 + \frac{\omega}{\sigma} \right) W'' + \left( k^4 + \frac{\omega}{\sigma} k^2 \right) W = 0, \quad (3.4.19)$$

with  $W = W' = 0$  on  $z = 0$  and  $W = W'' = 0$  on  $z = 1$ . Solutions of this problem, described in more detail in section 3.2.1, are given by

$$W = \left[ e^{kz} - e^{k(2-z)} - \frac{(1 - e^{2k})}{(1 - e^{2i\Gamma})} (e^{i\Gamma z} - e^{i\Gamma(2-z)}) \right], \quad (3.4.20)$$

where  $\Gamma$  is defined in terms of  $\omega$  by the relation

$$\Gamma = \sqrt{\frac{-\omega}{\sigma} - k^2}. \quad (3.4.21)$$

and is any solution of the equation

$$\frac{\tanh k}{k} = \frac{\tan \Gamma}{\Gamma}. \quad (3.4.22)$$

It was also seen in section 3.2.1 that for  $k = 0$  these eigenvalues reduce to the solutions of

$$\tan \sqrt{\frac{-\omega}{\sigma}} = \sqrt{\frac{-\omega}{\sigma}}. \quad (3.4.23)$$

Finally, the 'thermal' eigenvalues at  $R_1 = 0$  are obtained from the solution of (3.4.13) when  $U = 0$ :

$$\Theta'' = (\omega + k^2)\Theta, \quad (3.4.24)$$

with  $\Theta' = 0$  on  $z = 0, 1$ . This has solutions  $\Theta = \cos n\pi z$  and eigenvalues

$$\omega = -(n\pi)^2 - k^2, \quad n = 0, 1, 2, \dots \quad (3.4.25)$$

It can be observed by inspecting the full perturbation equations (3.4.11)–(3.4.13), that in the limit as  $k \rightarrow 0$  these three sets of eigenvalues also provide the

solutions to the perturbation equations when  $k = 0$  for general  $R_1$ . This is because when  $k = 0$  the ‘horizontal velocity’ and ‘thermal’ eigenvalues each correspond to the trivial solution  $W = 0$  of (3.4.12) even when  $R_1$  is non-zero. Thus for  $k = 0$  and general  $R_1$  leading eigenvalues,  $\omega$ , all of which are real, can be listed as

$$\begin{aligned} \omega = & -\{0, 9.87, 39.5, \dots\}, \\ & -\{2.47, 22.21, 61.7, \dots\}\sigma, \\ & -\{20.19, 59.7, 119, \dots\}\sigma. \end{aligned} \tag{3.4.26}$$

### 3.4.2 Numerical results

The above values of  $\omega$  at  $k = 0$  are used to initiate the fourth order Runge-Kutta scheme with Newton iteration that solves the full perturbation equations (3.4.11)–(3.4.13) for general  $R_1$  and  $k$ . This scheme is similar to the one discussed in detail in chapter 2, except that here there are 16 first order equations and eight boundary conditions requiring that four independent solutions are computed from the four boundary conditions at  $z = 0$  and that a complex determinant is constructed from the  $4 \times 4$  matrix of boundary values at  $z = 1$ . Newton iteration is then used to find the zeros of the determinant.

Figure 3.20 shows the behaviour of the first few eigenvalues  $\omega$  for  $R_1 = 4000$ ,  $\sigma = 0.1$  and non-zero  $k$ . These parameter values were chosen following the results for the transverse problem which show that instabilities occur at large Rayleigh number and small Prandtl number. The eigenvalues ‘pair up’ quite quickly with increasing wavenumber to become one complex eigenvalue instead of two real eigenvalues. Although it is not obvious what happens at large values of the wavenumber, at small values of  $k$  the real part of only the first ‘paired’ eigenvalue becomes positive.

The neutral curves, defining the values of  $R_1$  and  $k$  for which  $\omega_r = 0$ , were calculated as before by using an additional Newton iteration to bring  $\omega_r$  to within  $10^{-4}$  of zero. These are shown in figure 3.21, along with their asymptotic forms which are described later. It becomes difficult to compute the neutral curves for large  $R_1$  and moderately large  $k$ , and the longer curves in this region were computed with less accuracy. However the behaviour of the neutral curves is still discernible. The critical Rayleigh number — the lowest value of  $R_1$  on a given neutral curve — becomes smaller with decreasing Prandtl number. It can be seen in figure 3.12 that

for most values of the Prandtl number, the longitudinal mode becomes unstable at a lower Grashof number than the transverse mode. Although not obvious in figure 3.12, it was shown by Laure and Roux (1987) that for very small Prandtl number the critical Grashof number ( $R_{1c}/\sigma$ ) for the transverse perturbation is lower than that of the longitudinal perturbation and so the transverse mode is the first to become unstable there. This has been observed experimentally for the rigid surface problem by Gill (1966). Laure and Roux (1987) suggested that the increased stabilization when the temperature field tends to be “frozen” indicates that the origin of the oscillations is mainly thermal. Figure 3.20 shows how it is the first thermal eigenvalue (paired with the first horizontal velocity eigenvalue) that becomes unstable. In the transverse case the thermal modes are stable and the stream function modes are unstable (section 3.2.3).

At sufficiently large Prandtl number it can be seen from both the neutral curves (figure 3.21) and the critical Grashof numbers (figure 3.12) that there is a critical Prandtl number above which the system is stable to longitudinal disturbances, and that this is greater than that of the transverse mode case. At large Rayleigh number the left hand branch of the neutral curve seems to have a behaviour in which  $k$  is proportional to  $1/R_1$  as in the transverse case. For the transverse mode the right-hand branch of the neutral curve asymptotes a finite value of  $k$ , but for the longitudinal mode the neutral curve turns back on itself. This is described in greater detail by the asymptotic analysis to be presented in the next section, and it emerges that the right-hand branch also has a behaviour in which  $k$  is proportional to  $1/R_1$  as  $R_1 \rightarrow \infty$ .

As in the transverse case, an instantaneous ‘snapshot’ of the perturbations at a point on the neutral curve is shown in figures 3.22 and 3.23. Figure 3.22 shows the contours of the perturbation  $iW$  as the solid lines and the temperature perturbation as the shading. The contours of the perturbation  $iW$  are equivalent to instantaneous streamlines of the flow perturbation in the  $y, z$  plane. Being at right angles to the core flow means that for the overall flow the instantaneous streamlines spiral in the  $x$  direction, unlike the overall flow for the transverse case shown in figure 3.14. For the longitudinal case there is also a velocity perturbation in the direction of the core flow. This is represented in figure 3.23 by the ‘height’ of the streamline perturbations.

### 3.4.3 Asymptotic solution of the stability equations for large $R_1$

Substituting the assumptions

$$k = \frac{k_0}{R_1}, \quad \omega = \omega_0 + \dots, \quad \bar{W} = \frac{\bar{W}}{R_1}, \quad R_1 \rightarrow \infty, \quad (3.4.27)$$

into (3.4.11)–(3.4.13) yields the reduced problem

$$\omega_0 U + \bar{W} G''' = \sigma U'', \quad (3.4.28)$$

$$\omega_0 \bar{W}'' = \sigma \bar{W}'' - k_0^2 \sigma \Theta, \quad (3.4.29)$$

$$\omega_0 \Theta + U + G' \bar{W} = \Theta'', \quad (3.4.30)$$

with  $U = \bar{W} = \bar{W}' = \Theta' = 0$  on  $z = 0$ , and  $U' = \bar{W} = \bar{W}'' = \Theta' = 0$  on  $z = 1$ .

This was solved numerically by the ubiquitous Runge-Kutta scheme, tracing out values of  $\omega_0$  by incrementing  $k_0$ , starting from the known values of  $\omega_0$  at  $k_0 = 0$ . The results of this are plotted in figure 3.24 which shows the wave speed and growth rate scaled, as before, with the free surface speed. Although the wave motion is perpendicular to the direction of the free surface flow, this plot shows that the waves are travelling at a similar speed to the transverse waves, with a maximum speed for relatively long wavelength perturbations. In contrast to the asymptotic behaviour for the transverse mode perturbations, where  $\omega_0$  behaved like  $ak_0$  as  $k_0 \rightarrow \infty$  with  $a > 0$ , here there are two values of  $k_0$  for which  $\omega_{0r} = 0$ . This suggests that both left and right hand sides of the neutral curve behave like  $R_1^{-1}$  as  $R_1 \rightarrow \infty$  and that the curves turn back on themselves. These asymptotes are plotted with the neutral curves obtained from the full perturbation equations in figure 3.21.

The two values of  $k_0$  for which  $\omega_{0r} = 0$  are best visualised by figure 3.26, the plot of those values against the Prandtl number. The corresponding values of  $\omega_{0i}$  are shown in figure 3.27 as a function of the Prandtl number. It can be seen that for Prandtl numbers greater than approximately 0.415 the system is always stable. The accuracy of this value was checked with the Runge-Kutta scheme running over 200 rather than the usual 100 points. For Prandtl numbers below about 0.08 there is one small value of  $k_0$ , but the ‘large’ value (corresponding to the right hand side of the  $R_1$ - $k$  neutral curve) is difficult to calculate. This behaviour is investigated by performing an asymptotic expansion as  $k_0 \rightarrow \infty$ .

### 3.4.4 Asymptotic analysis of the reduced problem at large $k_0$

The large  $k_0$  problem was first studied for finite  $\sigma$ , expanding  $\omega_0$  in terms of  $k_0^{-1/2}$ :

$$\omega_0 = \hat{\omega}_0 k_0 + \hat{\omega}_1 k_0^{\frac{1}{2}} + \hat{\omega}_2 + \dots \quad k_0 \rightarrow \infty. \quad (3.4.31)$$

At the leading order,  $\hat{\omega}_0$  is imaginary. The second order component  $\hat{\omega}_1$  has a negative real part implying that at finite Prandtl number the system is stable. As  $\sigma \rightarrow 0$ ,  $\hat{\omega}_0$  and  $\hat{\omega}_1$  are of order  $\sigma^{1/2}$  and  $\sigma^{3/4}$  respectively. However,  $\hat{\omega}_2$  is of order unity as  $\sigma \rightarrow 0$ , and thus the expansion (3.4.31) breaks down when  $k_0 = O(\sigma^{-3/2})$ . There is then the possibility of neutral stability because the contribution to the growth rate from  $\hat{\omega}_2$  becomes comparable with that from  $\hat{\omega}_1$ .

With this *a priori* assumption a more detailed theory is now given, where it is assumed that

$$k_0 = \kappa_0 \sigma^{-\frac{3}{2}} + \kappa_1 \sigma^{-\frac{1}{2}} + \dots, \quad \text{as } \sigma \rightarrow 0, \quad (3.4.32)$$

and where  $U$ ,  $\bar{W}$  and  $\Theta$  are expanded for small Prandtl number as

$$\left. \begin{aligned} U &= U_0(z) + \sigma U_1(z) + \dots, \\ \bar{W} &= \sigma^{-1} W_0(z) + W_1(z) + \dots, \\ \Theta &= \Theta_0(z) + \sigma \Theta_1(z) + \dots, \end{aligned} \right\} \quad (3.4.33)$$

with

$$\omega_0 = \sigma^{-1} \tilde{\omega}_0 + \tilde{\omega}_1 + \dots \quad (3.4.34)$$

At leading order the reduced problem (3.4.28)–(3.4.30) becomes

$$\left. \begin{aligned} \tilde{\omega}_0 U_0 + G''' W_0 &= 0, \\ \tilde{\omega}_0 W_0'' &= -\kappa_0^2 \Theta_0, \\ \tilde{\omega}_0 \Theta_0 + G' W_0 &= 0, \end{aligned} \right\} \quad (3.4.35)$$

giving  $U_0 = -G''' \tilde{\omega}_0^{-1} W_0$ , and  $\Theta_0 = -G' \tilde{\omega}_0^{-1} W_0$ . Thus  $W_0$  must be found by solving

$$W_0'' = -\frac{G'}{\Omega_0^2} W_0, \quad (3.4.36)$$

where  $\tilde{\omega}_0 = i\Omega_0 \kappa_0$ , and  $\Omega_0$  is real, subject to the boundary conditions  $W_0 = 0$  on  $z = 0, 1$ . Solutions for  $\Omega_0$  and  $W_0$  were found using the Runge-Kutta scheme and normalised such that  $W_0' = 1$  on  $z = 0$ , and then  $W_0'(1) = a_0$  where  $a_0$  is a constant.

The profile of the leading solution  $W_0$  is shown in figure 3.25. The first few values of  $\Omega_0$  in descending order are

$$\Omega_0 = 0.0211, 0.0093, 0.0060 \dots \quad (3.4.37)$$

Neglect of the highest derivatives in (3.4.36) infers the presence of boundary layers near the upper and lower surfaces where an adjustment to the full boundary conditions is made. These provide conditions which allow the second order core problem to be solved and the point of neutral stability to be determined. There are two boundary layers associated with this problem: a viscous boundary layer where the scaling  $z = \sigma \bar{z}$  ensures that viscous effects come into play, and a thermal boundary layer where the scaling  $z = \sigma^{1/2} \tilde{z}$  allows the inclusion of the highest thermal derivatives.

In the lower thermal boundary layer

$$U = \sigma^{1/2} \tilde{U}_0(\tilde{z}) + \dots, \quad \bar{W} = \sigma^{-1/2} \tilde{W}_0(\tilde{z}) + \dots, \quad \Theta = \sigma^{3/2} \tilde{\Theta}_0(\tilde{z}) + \dots, \quad (3.4.38)$$

where  $\tilde{W}_0 = \tilde{z}$ ,  $\tilde{U}_0 = -\tilde{z}/(8\tilde{\omega}_0)$ , and  $\tilde{\Theta}_0$  satisfies

$$\tilde{\Theta}_0'' - \tilde{\omega}_0 \tilde{\Theta}_0 = -\frac{1}{8\tilde{\omega}_0} \tilde{z} + \frac{1}{16} \tilde{z}^3, \quad (3.4.39)$$

with boundary conditions

$$\tilde{\Theta}_0' = 0 \text{ on } \tilde{z} = 0, \text{ and } \tilde{\Theta}_0 \sim -\tilde{z}^3/(16\tilde{\omega}_0) \text{ as } \tilde{z} \rightarrow \infty, \quad (3.4.40)$$

implied by the wall condition and matching with the core. Thus

$$\tilde{\Theta}_0 = -\left( \frac{1}{4\tilde{\omega}_0^{5/2}} e^{-\sqrt{\tilde{\omega}_0} \tilde{z}} + \frac{1}{16\tilde{\omega}_0} \tilde{z}^3 + \frac{1}{4\tilde{\omega}_0^2} \tilde{z} \right) \quad (3.4.41)$$

at leading order as  $\sigma \rightarrow 0$ . Although this gives a contribution to  $\Theta$  in the viscous boundary layer, it is too small to affect the viscous boundary layer problem at leading order.

The lower viscous boundary layer expansion as  $\sigma \rightarrow 0$  is,

$$U = \sigma \bar{U}_0(\bar{z}) + \dots, \quad \bar{W} = \bar{W}_0(\bar{z}) + \dots, \quad \Theta = \sigma^{3/2} \bar{\Theta}_0(\bar{z}) + \dots \quad (3.4.42)$$

The leading order problem is to solve

$$\bar{W}_0^{iv} = \tilde{\omega}_0 \bar{W}_0'', \quad (3.4.43)$$

subject to the boundary conditions  $\bar{W}_0 = \bar{W}'_0 = 0$  on  $\bar{z} = 0$  and  $\bar{W}'_0 \rightarrow 1$  as  $\bar{z} \rightarrow \infty$ . This has the solution

$$\bar{W}_0 = \tilde{\omega}_0^{-\frac{1}{2}} e^{-\sqrt{\tilde{\omega}_0} \bar{z}} + \bar{z} - \tilde{\omega}_0^{-\frac{1}{2}}. \quad (3.4.44)$$

The corresponding solution for  $\bar{U}_0$  is

$$\bar{U}_0 = \frac{1}{8} \tilde{\omega}_0^{-\frac{3}{2}} \left( 1 - e^{-\tilde{\omega}_0^{1/2} \bar{z}} \right) - \frac{1}{16} \tilde{\omega}_0^{-1} \bar{z} e^{-\tilde{\omega}_0^{1/2} \bar{z}} - \frac{1}{8} \tilde{\omega}_0^{-1} \bar{z}, \quad (3.4.45)$$

and matching with the thermal boundary layer gives  $\bar{\Theta}_0 = -1/(4\tilde{\omega}_0^{5/2})$ .

Similar scalings are used to reveal the behaviour near the upper boundary where  $\bar{W} \sim \sigma^{-1} a_0 (1 - z)$ , but here no exponential components are generated at leading order. In the upper thermal boundary layer,

$$\Theta \sim -\sigma a_0 \left( \frac{1}{48\tilde{\omega}_0} \bar{Z}^2 + \frac{1}{24\tilde{\omega}_0^2} \right) \quad (3.4.46)$$

where  $\bar{Z} = \sigma^{1/2}(1 - z)$ . In the upper viscous layer,

$$U \sim a_0 \sigma^2 \left( \frac{3}{8\tilde{\omega}_0} \bar{Z}^2 + \frac{3}{4\tilde{\omega}_0^2} \right), \quad (3.4.47)$$

where  $\bar{Z} = \sigma(1 - z)$ , showing that the surface temperature and flow speed are given by

$$\Theta \sim -a_0 \sigma \frac{1}{24\tilde{\omega}_0^2}, \quad U \sim a_0 \sigma^2 \frac{3}{4\tilde{\omega}_0^2}, \quad V \sim \frac{a_0 i R_1}{\kappa_0} \sigma^{\frac{3}{2}}. \quad (3.4.48)$$

The second order equations in the core are

$$\left. \begin{aligned} \tilde{\omega}_0 U_1 + \tilde{\omega}_1 U_0 + G''' W_1 &= 0, \\ \tilde{\omega}_0 W_1'' + \tilde{\omega}_1 W_0'' &= -\kappa_0^2 \Theta_1 - 2\kappa_0 \kappa_1 \Theta_0, \\ \tilde{\omega}_0 \Theta_1 + \tilde{\omega}_1 \Theta_0 + U_0 + G' W_1 &= \Theta_0'' \end{aligned} \right\} \quad (3.4.49)$$

and from matching with (3.4.44) across the thermal layer it is found that a solution is required for which

$$W_1 = -\tilde{\omega}_0^{-\frac{1}{2}} \text{ on } z = 0, \quad W_1 = 0 \text{ on } z = 1, \quad (3.4.50)$$

Using (3.4.49) and the first order problem (3.4.35) the second order problem can be written as

$$W_1'' - \frac{\kappa_0^2 G'}{\tilde{\omega}_0^2} W_1 = \frac{\kappa_0^2}{\tilde{\omega}_0^3} \left( 2G'' W_0' - 2\tilde{\omega}_1 G' W_0 + \left( \frac{\kappa_0 G'}{\tilde{\omega}_0} \right)^2 W_0 + \frac{2\kappa_1 \tilde{\omega}_0}{\kappa_0} G' W_0 \right). \quad (3.4.51)$$

A solvability condition can now be found using (3.4.36) and (3.4.51), together with the boundary conditions (3.4.50) to give  $\tilde{\omega}_1$  as

$$\tilde{\omega}_1 = \frac{-\int_0^1 G'''' W_0^2 dz + \frac{\kappa_0^2}{\tilde{\omega}_0^2} \int_0^1 G''^2 W_0^2 dz + \frac{2\kappa_1 \tilde{\omega}_0}{\kappa_0} \int_0^1 G' W_0^2 dz + \frac{\tilde{\omega}_0^{5/2}}{\kappa_0^2}}{2 \int_0^1 G' W_0^2 dz} \quad (3.4.52)$$

Noting that  $\tilde{\omega}_0 = i\Omega_0 \kappa_0$ , along the neutral curve where  $\tilde{\omega}_{0,r} = 0$ , the real part of (3.4.52) vanishes when

$$\kappa_0^{\frac{1}{2}} = -\frac{\sqrt{2}}{\Omega_0^{5/2}} \left( \int_0^1 G'''' W_0^2 dz + \frac{1}{\Omega_0^2} \int_0^1 G''^2 W_0^2 dz \right). \quad (3.4.53)$$

Values of  $\kappa_0$  were computed by Simpson's rule. It can be noted that it is necessary for  $\kappa_0^{1/2}$  to be positive for the exponential decay of the lower boundary layer solution. Only the leading value of  $\Omega_0$  and the corresponding eigenfunction  $W_0$  leads to a solution giving a consistent theory, so that

$$k_0 \sim 12.77\sigma^{-\frac{3}{2}} \text{ as } \sigma \rightarrow 0. \quad (3.4.54)$$

This asymptote is shown with the numerically calculated values of  $k_0$  in figure 3.26. For small Prandtl number the results become inaccurate and are not plotted. The difference between the numerical results and the first order asymptote is because the asymptote comes from the lower boundary layers which have not properly formed for the smallest Prandtl number numerical results. The e-folding decay lengths of the viscous and thermal boundary layers are 0.22 and 0.77 respectively when  $\sigma = 0.08$ . For the lower thermal boundary layer to be of a more reasonable size, less than a quarter of the cavity depth for example, the Prandtl number must be less than 0.008.

### 3.4.5 Asymptotic analysis of the full problem with $k = O(1)$

Having completed the above analysis, the correct scalings for the Rayleigh problem can be introduced, and a simpler and more general solution for large  $R_1$  and finite  $k$  can be found for small Prandtl number. Since  $k = k_0/R_1$  and  $k_0 \sim \sigma^{-3/2}$  as  $\sigma \rightarrow 0$  it follows that neutrally stable solutions should exist for  $k = O(1)$  when  $\sigma = O(R_1^{-2/3})$ . Thus  $\sigma$  is expanded as

$$\sigma = R_1^{-\frac{2}{3}} \sigma_0 + \dots, \quad R_1 \rightarrow \infty, \quad (3.4.55)$$

and substitution into the full perturbation equations (3.4.11)–(3.4.13), gives

$$\omega U + R_1 G''' W = R_1^{-\frac{2}{3}} \sigma_0 (U'' - k^2 U), \quad (3.4.56)$$

$$\omega (W'' - k^2 W) = R_1^{-\frac{2}{3}} \sigma_0 (W'' - 2k^2 W + k^4 W) - k^2 R_1^{\frac{1}{3}} \sigma_0 \Theta, \quad (3.4.57)$$

$$\omega \Theta + U + R_1 G' W = \Theta'' - k^2 \Theta. \quad (3.4.58)$$

Now it is only necessary to go to second order in the expansion of the solution in the core region of the flow. This expansion is given by

$$\left. \begin{aligned} U &= U_0(z) + U_1(z) R_1^{-\frac{2}{3}} + \dots, \\ W &= W_0(z) R_1^{-\frac{1}{3}} + W_1(z) R_1^{-1} + \dots, \\ \Theta &= \Theta_0(z) + \Theta_1(z) R_1^{-\frac{2}{3}} + \dots, \end{aligned} \right\} \quad (3.4.59)$$

with

$$\omega = \hat{\omega}_0 R_1^{\frac{2}{3}} + \hat{\omega}_1 + \dots \quad (3.4.60)$$

The expansion in the lower viscous boundary layer of thickness  $R_1^{-2/3}$ , is given by

$$\left. \begin{aligned} U &= R_1^{-\frac{2}{3}} \bar{U}_0(\bar{z}) + \dots, \\ W &= R_1^{-1} \bar{W}_0(\bar{z}) + \dots, \\ \Theta &= R_1^{-1} \bar{\Theta}_0(\bar{z}) + \dots, \end{aligned} \right\} \quad (3.4.61)$$

where

$$z = \bar{z} R_1^{-\frac{2}{3}}, \quad (3.4.62)$$

and at this order there is effectively no upper boundary layer. The thermal boundary layer does not contribute to the viscous solution at this order and is not discussed here.

The leading order core problem can be written as

$$\hat{\omega}_0 U_0 + G''' W_0 = 0, \quad (3.4.63)$$

$$\hat{\omega}_0 (W_0'' - k^2 W_0) = -k^2 \sigma_0 \Theta_0, \quad (3.4.64)$$

$$\hat{\omega}_0 \Theta_0 + G' W_0 = 0, \quad (3.4.65)$$

and combination of (3.4.64) and (3.4.65) gives

$$W_0'' = \frac{k^2}{\hat{\Omega}^2} (\hat{\Omega}^2 - G') W_0, \quad (3.4.66)$$

where  $\hat{\omega}_0 = i \hat{\Omega} \sigma_0^{1/2}$ , to be solved subject to the boundary conditions  $W_0 = 0$  at  $z = 0, 1$ . The earlier limit is recovered in the limit as  $k \rightarrow 0$  for  $k/\hat{\Omega} = O(1)$ , but

here the behaviour of  $\hat{\Omega}$  for finite  $k$  can be gleaned: for a non-trivial solution of (3.4.66) to exist it is necessary that  $\hat{\Omega}^2 - G' < 0$ . The maximum of  $G'$  is  $5.42 \times 10^{-3}$  and hence

$$\hat{\Omega} < 0.0736. \quad (3.4.67)$$

This limit can be seen for large  $k$  in figure 3.29, the plot of  $\hat{\Omega}$  against  $k$  for the first five leading modes. The largest mode is the leading mode. Equation (3.4.66) was integrated from  $z = 0$  to  $z = 1$  using a fourth order Runge-Kutta scheme and finding  $\hat{\Omega}$  from the requirement that  $W_0(1) = 0$ . Figure 3.30 shows the dependence of  $W_0(1)$  on  $\hat{\Omega}$  for  $k = 3$  and in this case the leading eigenvalue is found to be  $\hat{\Omega} = 0.045$ .

The leading order lower boundary layer problem for  $\bar{W}_0$  is

$$\bar{W}_0^{iv} = \frac{\hat{\omega}_0}{\sigma_0} \bar{W}_0'' \quad (3.4.68)$$

with the conditions  $\bar{W}_0 = \bar{W}_0' = 0$  on  $\bar{z} = 0$  and  $\bar{W}_0' \rightarrow 1$  as  $\bar{z} \rightarrow \infty$ , having assumed a normalisation of the core solution such that  $W_0'(0) = 1$ . This has the solution

$$\bar{W}_0 = \left( \sqrt{\frac{\sigma_0}{\hat{\omega}_0}} e^{-\sqrt{\frac{\hat{\omega}_0}{\sigma_0}} \bar{z}} + \bar{z} - \sqrt{\frac{\sigma_0}{\hat{\omega}_0}} \right) \quad (3.4.69)$$

where  $\sqrt{\hat{\omega}_0/\sigma_0} = (1+i)\hat{\Omega}^{1/2}\sigma_0^{1/4}/\sqrt{2}$ .

The second order core problem is

$$\hat{\omega}_0 U_1 + \hat{\omega}_1 U_0 + G''' W_1 = 0, \quad (3.4.70)$$

$$\hat{\omega}_0 (W_1'' - k^2 W_1) + \hat{\omega}_1 (W_0'' - k^2 W_0) = -k^2 \sigma_0 \Theta_1, \quad (3.4.71)$$

$$\hat{\omega}_0 \Theta_1 + \hat{\omega}_1 \Theta_0 + U_0 + G' W_1 = \Theta_0'' - k^2 \Theta_0. \quad (3.4.72)$$

Using the leading order core equations, (3.4.63)–(3.4.66) to rewrite  $U_0$ ,  $\Theta_0$  and  $W_0''$  in terms of  $W_0$ , substitution of (3.4.72) into (3.4.71) yields

$$\begin{aligned} \hat{\omega}_0 \left( W_1'' - k^2 \left( 1 + \frac{\sigma_0 G'}{\hat{\omega}_0^2} \right) W_1 \right) = \\ \frac{-k^2 \sigma_0}{\hat{\omega}_0^2} \left( 2\hat{\omega}_1 G' W_0 - 2G''' W_0' - \sigma_0 \left( \frac{kG'}{\hat{\omega}_0} \right)^2 W_0 \right), \end{aligned} \quad (3.4.73)$$

with the boundary conditions

$$W_1 = -\sqrt{\frac{\sigma_0}{\hat{\omega}_0}} \text{ on } z = 0, \quad W_1 = 0 \text{ on } z = 1. \quad (3.4.74)$$

Multiplying (3.4.73) by  $W_0$ , subtracting (3.4.66) multiplied by  $W_1$  and integrating from  $z = 0$  to  $z = 1$ , leads to the solvability condition

$$[W_0 W_1']_0^1 - [W_0' W_1]_0^1 = \frac{-k^2 \sigma_0}{\hat{\omega}_0^3} \left( \int_0^1 G'' W_0^2 dz + 2\hat{\omega}_1 \int_0^1 G' W_0^2 dz - \frac{k^2 \sigma_0}{\hat{\omega}_0^2} \int_0^1 G'^2 W_0^2 dz \right), \quad (3.4.75)$$

which with the boundary conditions (3.4.74) can be written as

$$\hat{\omega}_1 = \left( \frac{\hat{\omega}_0^{\frac{5}{2}}}{k^2 \sigma_0^{\frac{1}{2}}} - \int_0^1 G''' W_0^2 dz + \frac{k^2 \sigma_0}{\hat{\omega}_0^2} \int_0^1 G'^2 W_0^2 dz \right) \frac{1}{2 \int_0^1 G' W_0^2 dz} \quad (3.4.76)$$

so that, the real and imaginary parts of  $\hat{\omega}_1$  are given by

$$Re(\hat{\omega}_1) = \frac{-\hat{\Omega}^{\frac{5}{2}} \sigma_0^{\frac{3}{4}}}{\sqrt{2} k^2} - \int_0^1 G''' W_0^2 dz - \frac{k^2}{\hat{\Omega}^2} \int_0^1 G'^2 W_0^2 dz, \quad (3.4.77)$$

$$Im(\hat{\omega}_1) = \frac{-\hat{\Omega}^{\frac{5}{2}} \sigma_0^{\frac{3}{4}}}{2\sqrt{2} k^2 \int_0^1 G' W_0^2 dz}. \quad (3.4.78)$$

The theory has thus been completed to second order. Thus finite wavenumber longitudinal instabilities are possible at large Rayleigh number, but only at vanishingly small Prandtl number.

### 3.5 Discussion

The instability of the parallel-flow core to two dimensional transverse waves and three dimensional longitudinal waves has been studied in this chapter. For  $R_1 k = 0$ , or for large enough Prandtl number, the system is always stable; for the transverse case the Prandtl number must be greater than 0.162 and in the longitudinal case the Prandtl number must be greater than 0.415. These critical Prandtl numbers were found using both analytic and numerical techniques.

For finite Rayleigh and wave numbers, and small Prandtl number, the system may become unstable. Previous work such as that by Hart(1972,1983) has concentrated on the onset of instabilities. Laure and Roux (1989) give plots of the critical Grashof number ( $Gr_c = R_{1c}/\sigma$ ) against Prandtl number for the onset of instabilities

for both transverse and longitudinal modes which show that in general the longitudinal modes become unstable at lower Grashof number than the transverse modes, and are therefore considered more 'dangerous'. They suggested that the 'freezing' of the temperature field causes an increase in the stability of the longitudinal modes as  $\sigma \rightarrow 0$ , so that the transverse modes become more important than the longitudinal modes, and that this was due to the origin of the oscillations being thermal in the latter case. In the course of this work, this has been shown to be so, and that in contrast the origin of the transverse oscillations is associated with the velocity field. The eigenfunctions associated with the perturbations are represented graphically in figures 3.14 and 3.22, the transverse oscillations propagating parallel to the direction of the free surface flow and the longitudinal oscillations propagating perpendicular to the free surface flow, both with wave speeds of about one third of the speed of the free surface.

The asymptotic behaviour for large  $R_1$  has not been studied before. The large Rayleigh number, small Prandtl number regime is of particular interest in the semi-conductor crystal growing application of the system. The large Rayleigh number asymptotic analysis shows that the two modes behave very differently at large Rayleigh number. Both modes support longer wavelength instabilities with increasing Rayleigh number: the left hand branches of the neutral curves correspond to wavelengths of order  $R_1$ . However, only the transverse mode supports finite wavelength instabilities for finite Prandtl number; the right hand branch of the neutral curves for the longitudinal mode corresponds to wavelengths of order  $R_1$ . If the width of the cavity (which has been assumed to be infinite in this theory) was restricted by vertical walls in the  $y$  direction, for example, the long wavelength longitudinal mode instabilities may be damped, suggesting that the transverse mode may become more important at high Rayleigh numbers.

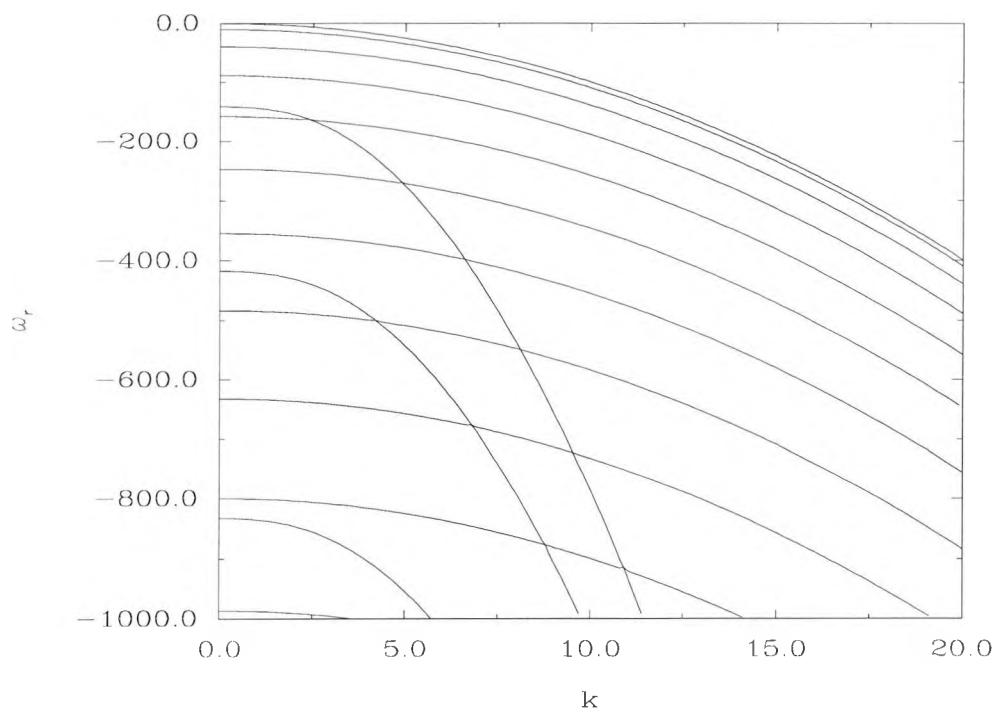


Figure 3.1: Real eigenvalues  $\omega$  of the thermal modes (shallow curves) and the stream function curves at  $R_1 = 0$  for  $\sigma = 7$ .

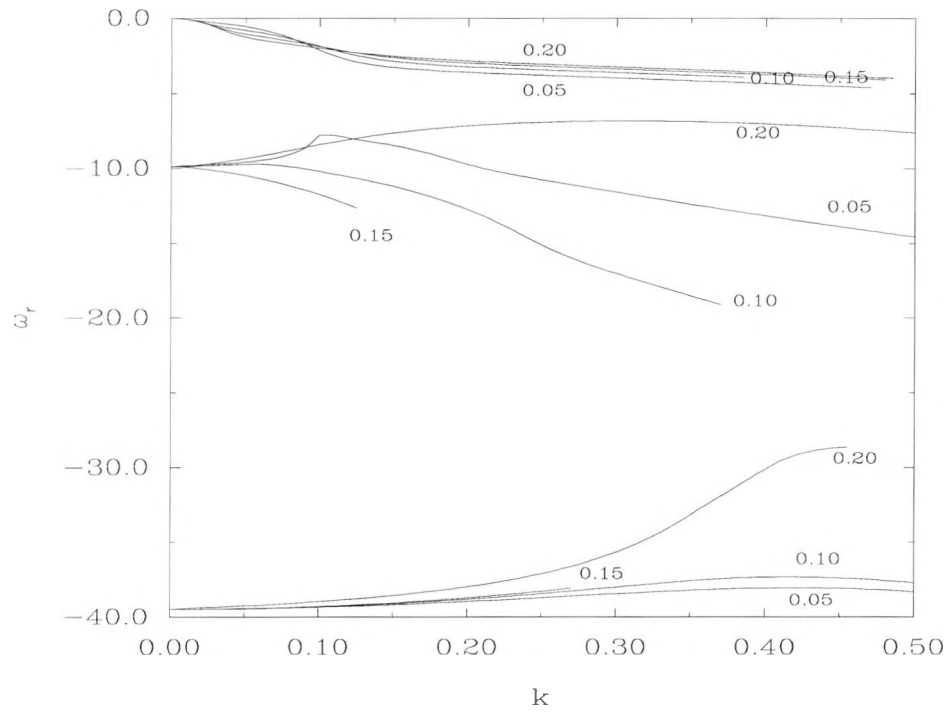


Figure 3.2: Real part of eigenvalues  $\omega$  of the first three  $\Theta$  modes for small Prandtl number (as indicated) when  $R_1 = 4000$ .

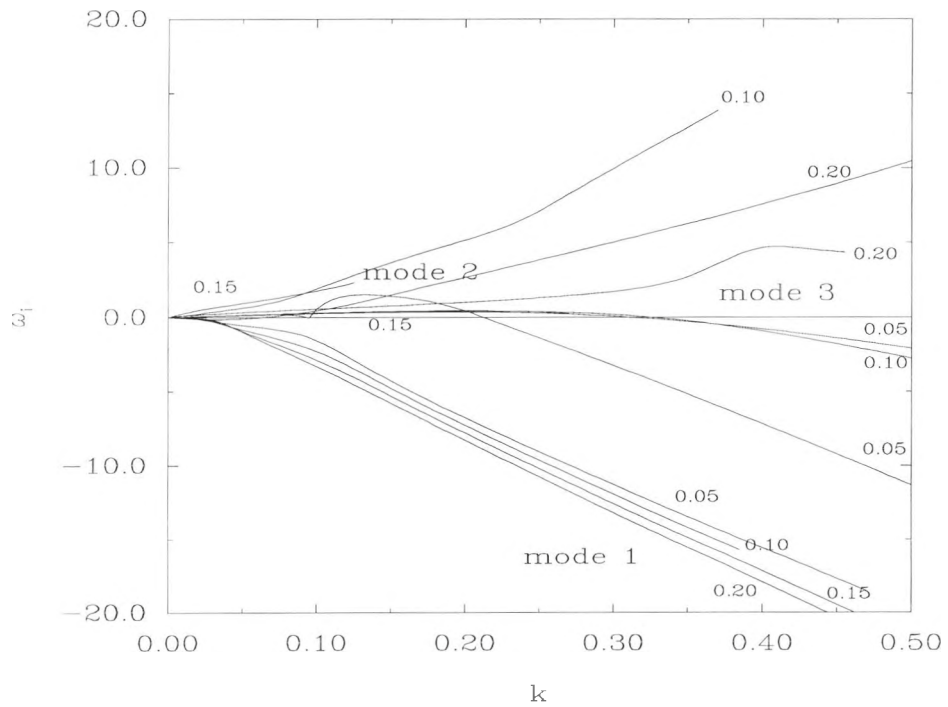


Figure 3.3: Imaginary part of eigenvalues  $\omega$  of the first three  $\Theta$  modes for small Prandtl number when  $R_1 = 4000$ .

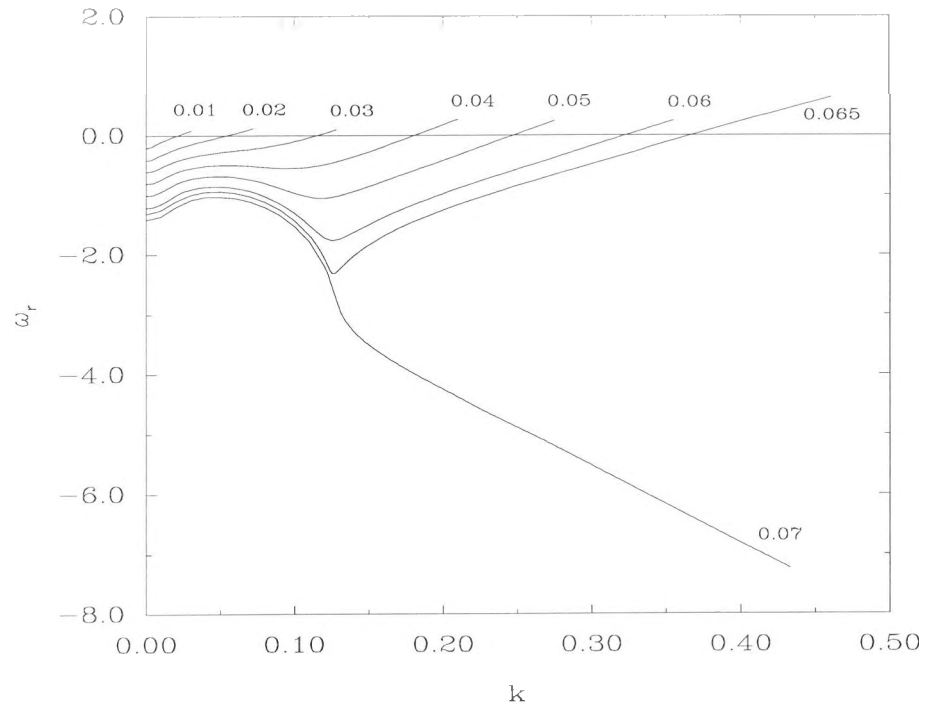


Figure 3.4: Real part of eigenvalues  $\omega$  of the first  $\phi$  mode for small Prandtl numbers when  $R_1 = 4000$ .

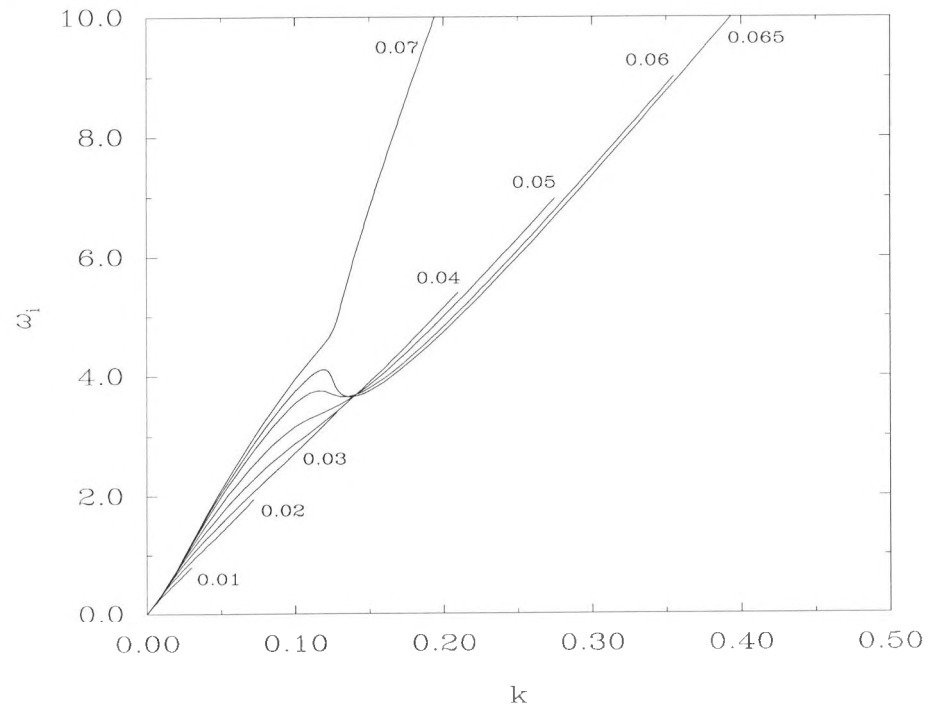


Figure 3.5: Imaginary part of eigenvalues  $\omega$  of the first  $\phi$  mode for small Prandtl numbers when  $R_1 = 4000$ .

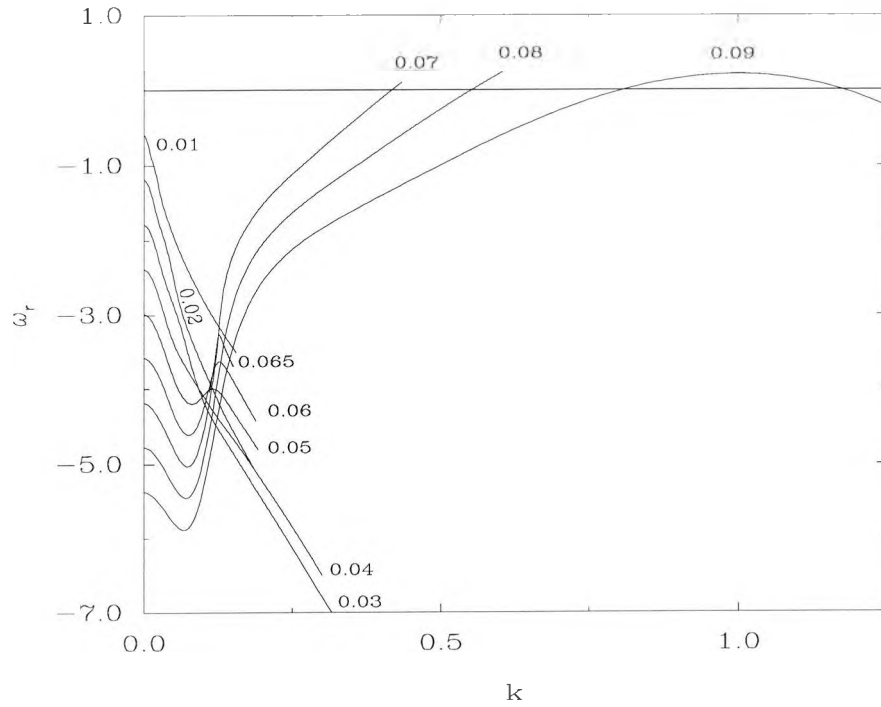


Figure 3.6: Real part of eigenvalues  $\omega$  of the second  $\phi$  mode for small Prandtl numbers when  $R_1 = 4000$ .

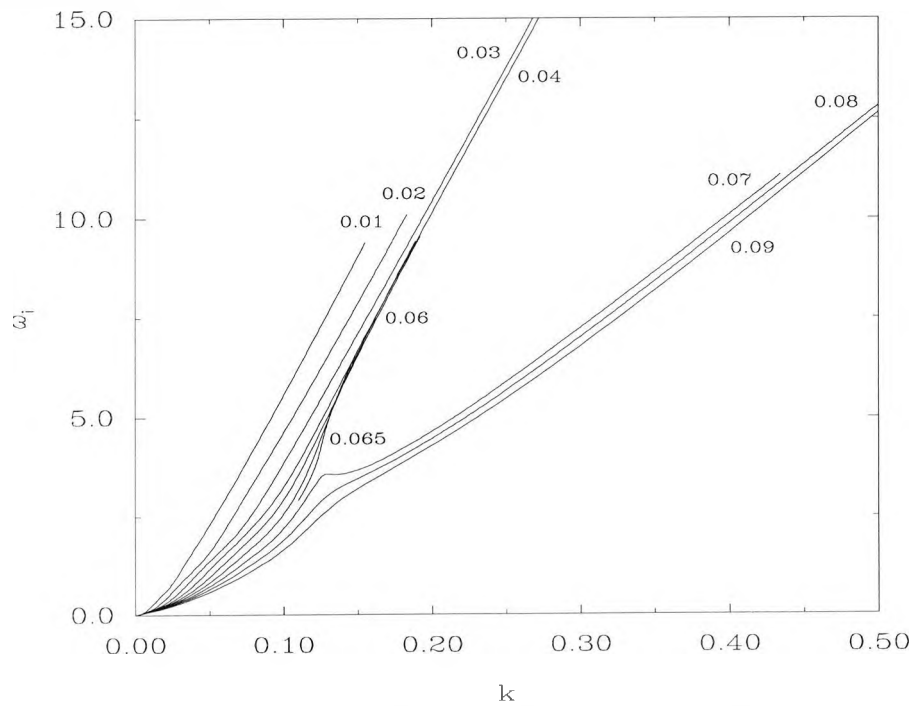


Figure 3.7: Imaginary part of eigenvalues  $\omega$  of the second  $\phi$  mode for small Prandtl numbers when  $R_1 = 4000$ .

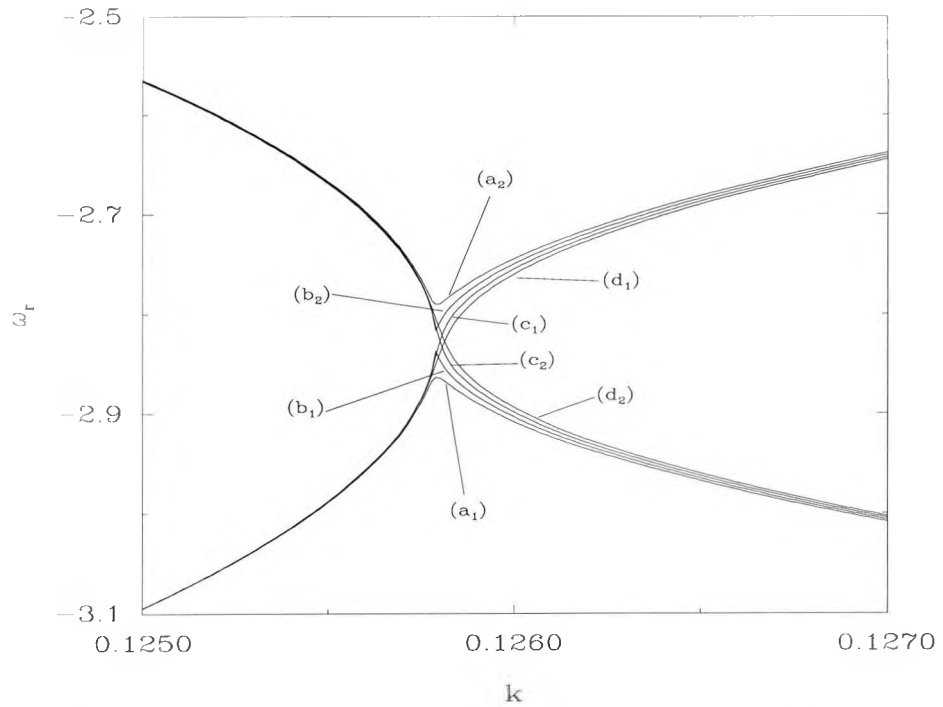


Figure 3.8: Real parts of eigenvalues  $\omega$  of the first (1) and second (2)  $\phi$  modes for Prandtl numbers 0.06681 (a), 0.06682 (b), 0.06683 (c), and 0.06684 (d) when  $R_1 = 4000$ .

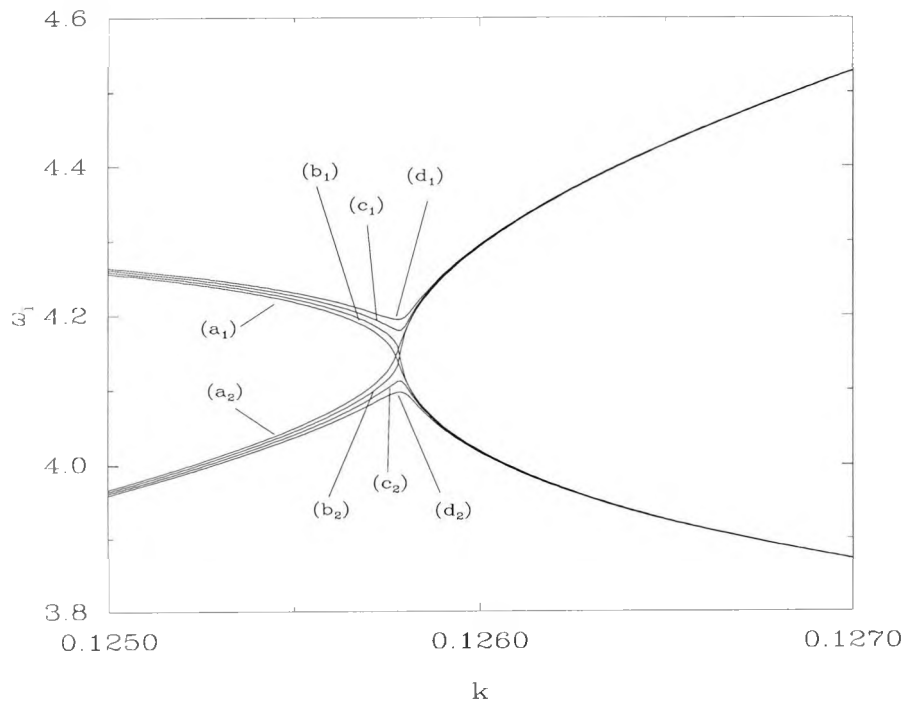


Figure 3.9: Imaginary part of eigenvalues  $\omega$  of the first two  $\phi$  modes for small Prandtl numbers when  $R_1 = 4000$ . Key as above.

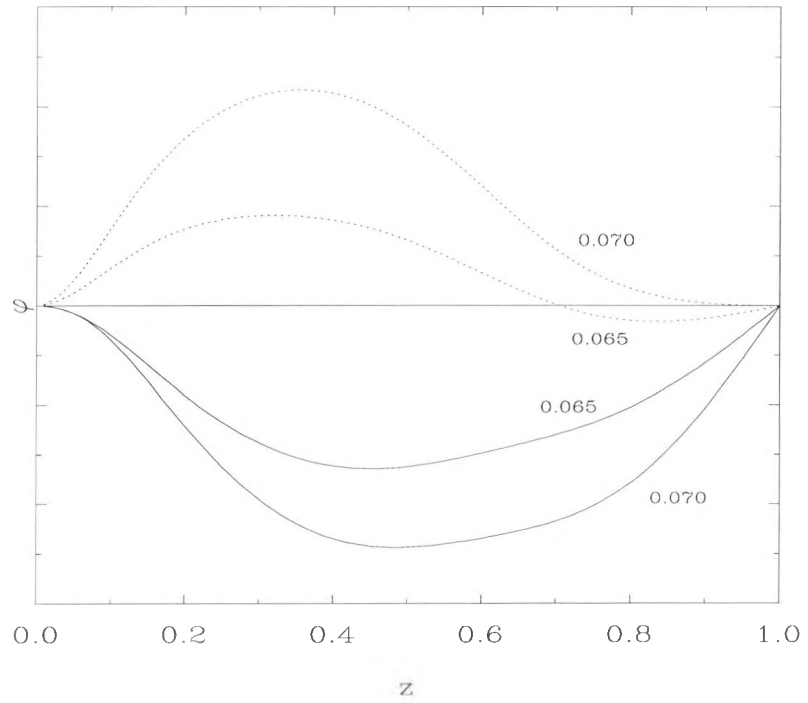


Figure 3.10: Profiles of  $\phi_r$  (solid lines) and  $\phi_i$  for  $\sigma = 0.065, 0.070$  when  $\omega_r = 0$  and  $R_1 = 4000$ .

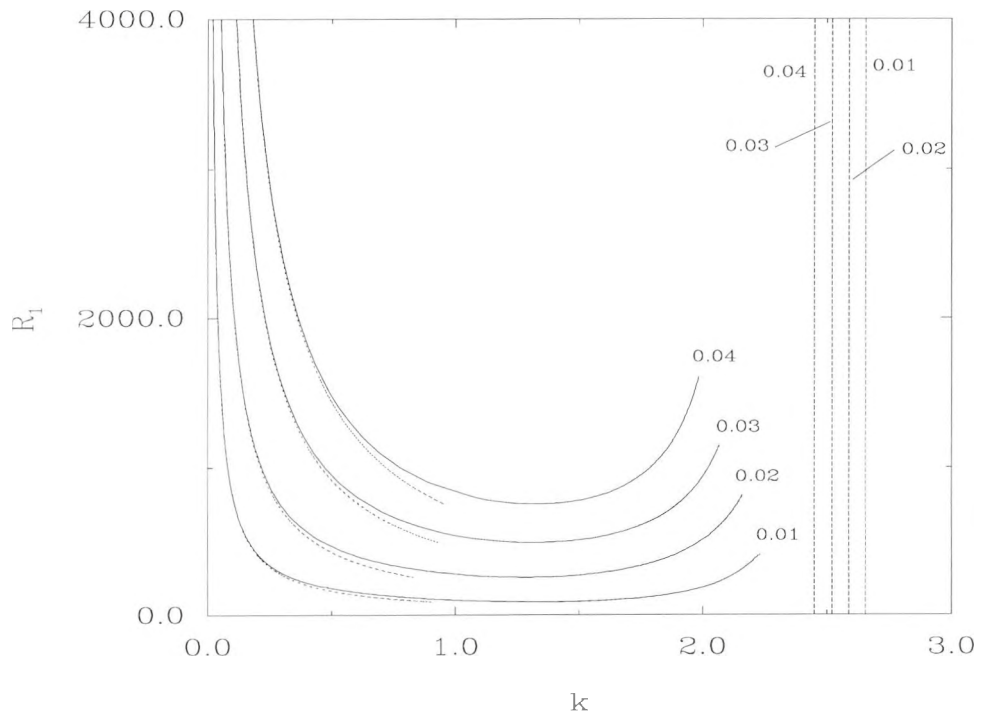


Figure 3.11: Neutral curves (solid lines) for various Prandtl numbers and their asymptotic forms as  $R_1 \rightarrow \infty$ :  $k \sim k_{0c}/R_1$  dotted line;  $k \rightarrow k_c$  dashed line.

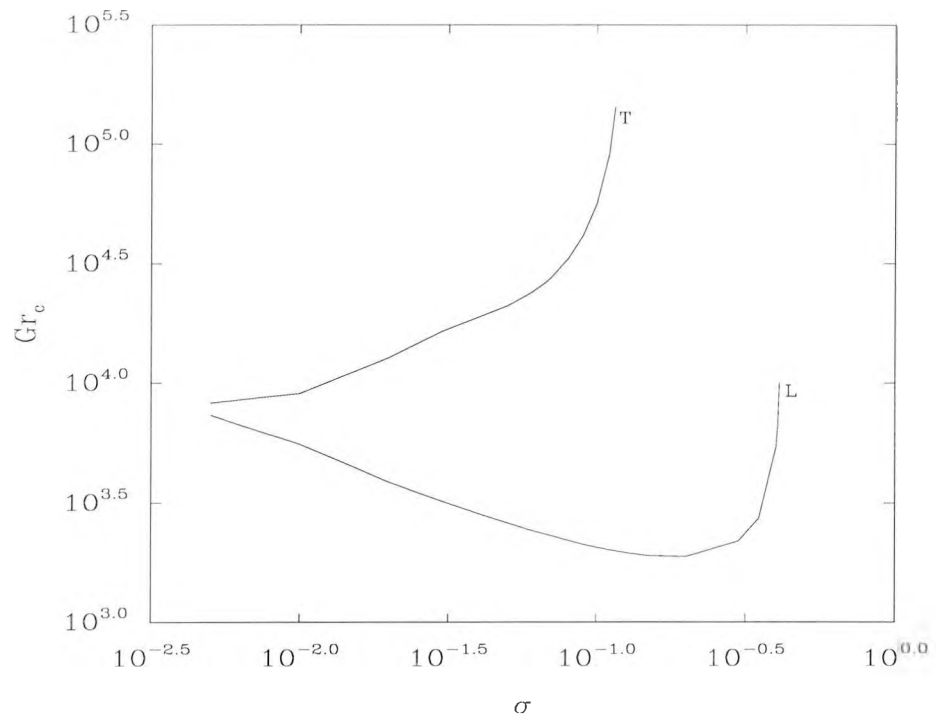


Figure 3.12: Critical Grashof numbers for the onset of instabilities for transverse (T) and longitudinal (L) modes as a function of the Prandtl number.

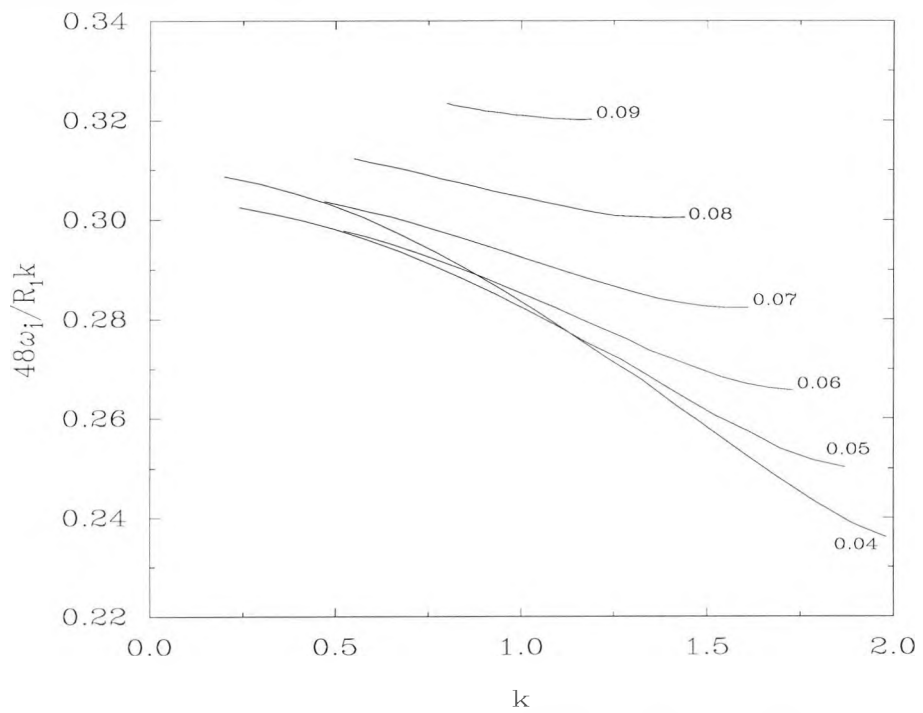


Figure 3.13: Ratio of the wave speed on the neutral curves to the speed of the free surface for various Prandtl numbers.

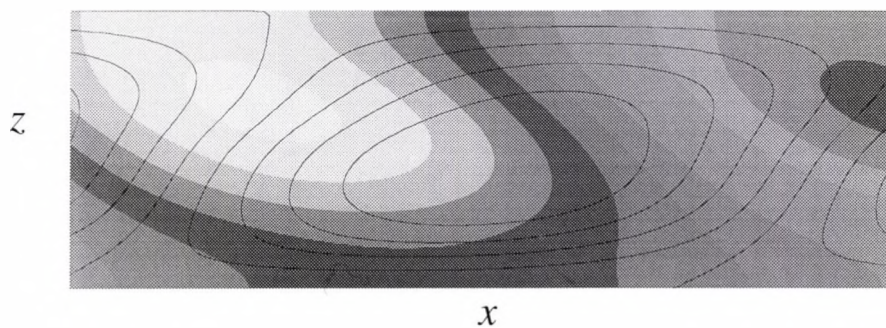


Figure 3.14: The transverse perturbations. The solid line is the instantaneous stream function perturbation  $\hat{\phi}$ , and the shading represents the thermal perturbation  $\hat{\theta}$ . ( $\sigma = 0.04$ ,  $k = 1.36$ ,  $R_1 = 754 \approx R_{1c}$ .)

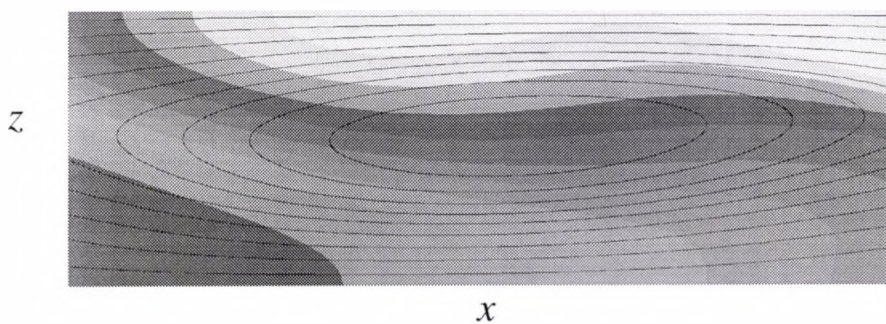


Figure 3.15: Instantaneous stream lines  $\bar{\psi}$  (solid lines) and temperature  $\bar{\theta}$  (shading) of a typical overall flow in the perturbed core. ( $\sigma = 0.04$ ,  $k = 1.36$ ,  $R_1 = 754 \approx R_{1c}$ .)

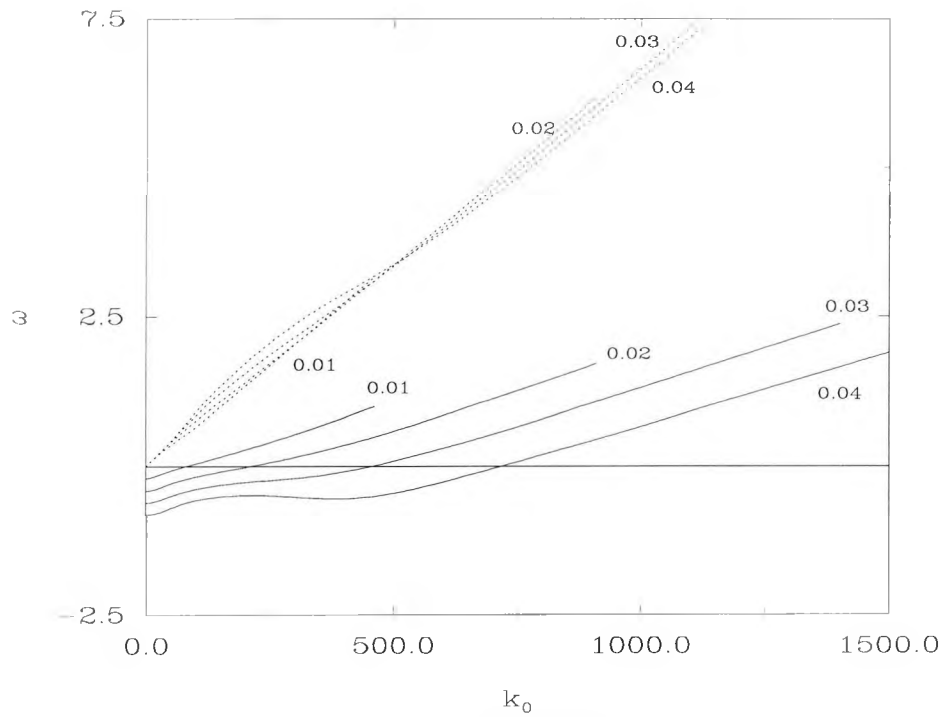


Figure 3.16: Asymptotic solutions of the real (solid line) and the imaginary (dashed line) parts of the eigenvalue  $\omega$  for the first stream function mode for small Prandtl numbers.

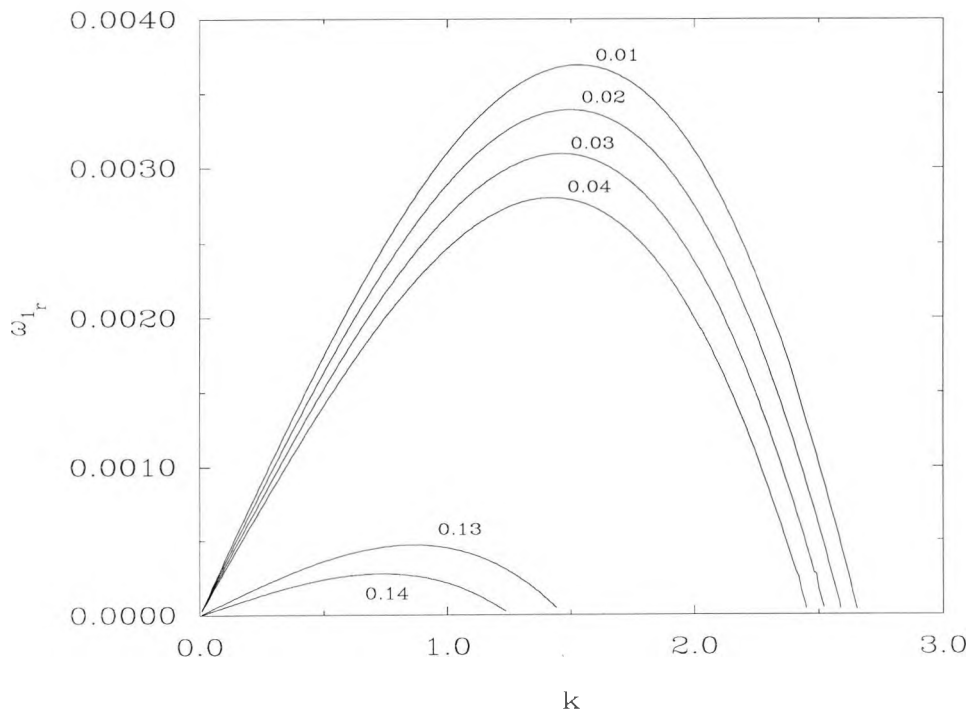


Figure 3.17: Asymptotic solutions of the real part of the eigenvalue  $\omega$  for the first stream function mode for small Prandtl numbers.

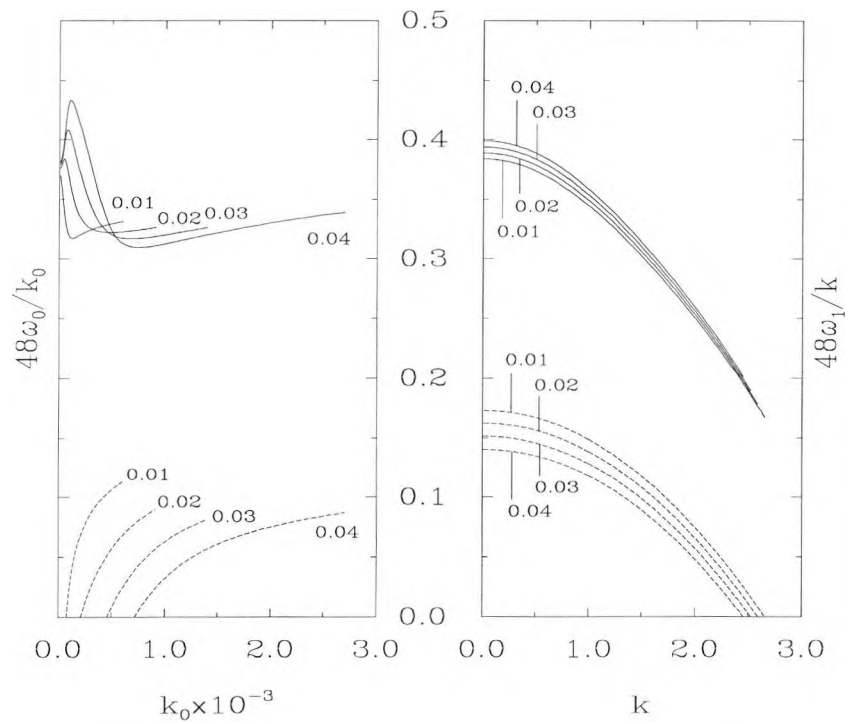


Figure 3.18: Real and imaginary parts of the normalised eigenvalues  $c = 48\omega_0/k_0$  (left), and  $c = 48\omega_1/k$  (right), of the asymptotic solutions as  $R_1 \rightarrow \infty$  for small Prandtl numbers. The wave speed is the solid line, the dashed line is the growth rate.

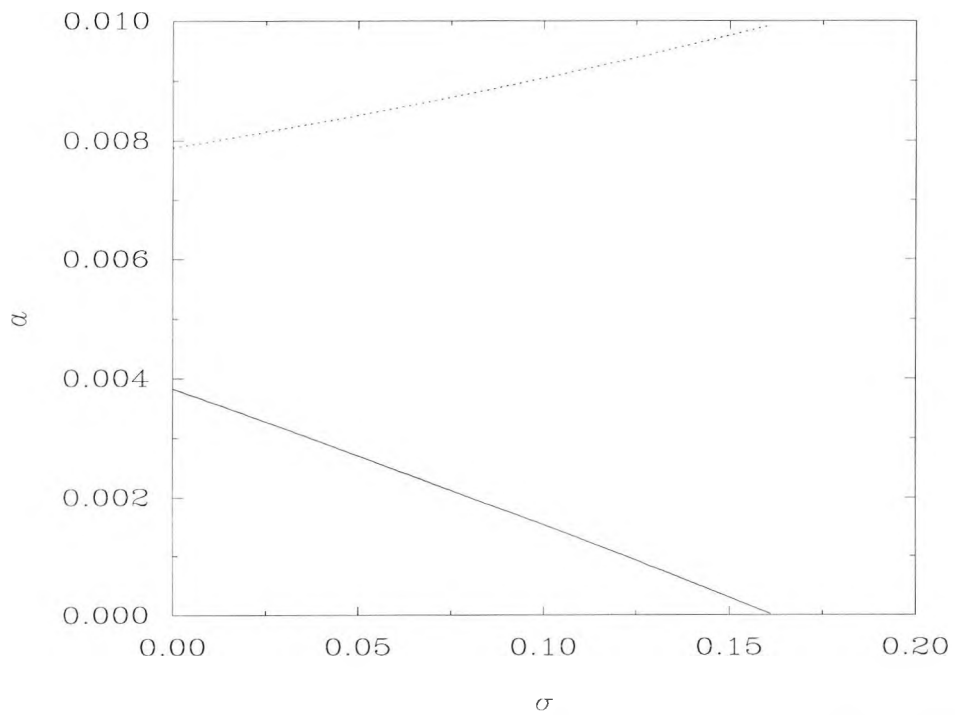


Figure 3.19: Real (solid line) and imaginary (dashed line) parts of the eigenvalue  $a$  as a function of the Prandtl number.

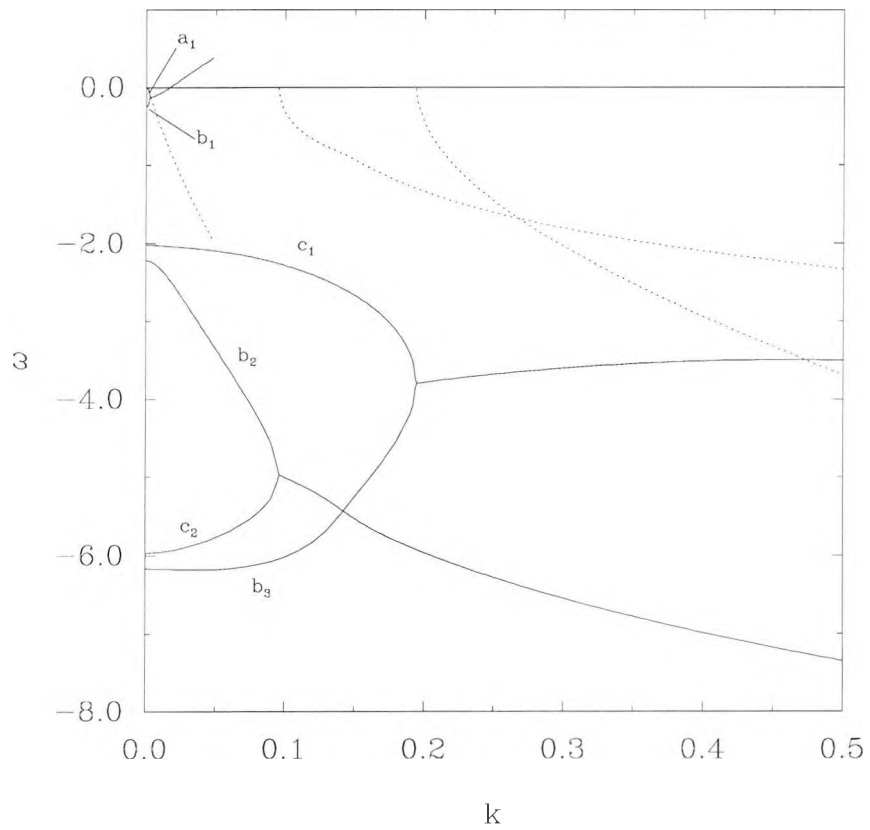


Figure 3.20: Values of the eigenvalue  $\omega$  for small  $k$  when  $R_1 = 4000$  and  $\sigma = 0.10$ , traced out from the known values at  $k = 0$ ; ‘a’ represents the  $-(n\pi)$  ‘thermal’ eigenvalues, ‘b’ represents the ‘horizontal velocity’ eigenvalues and ‘c’ represents the ‘vertical velocity’ eigenvalues.

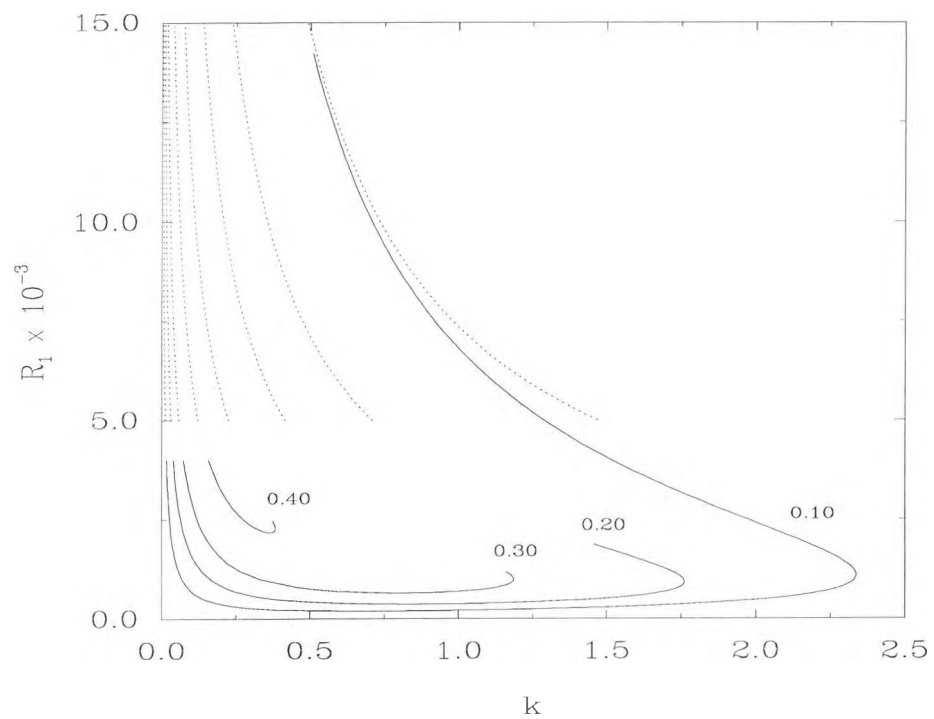


Figure 3.21: Neutral curves for small Prandtl numbers (as indicated) along with their asymptotes for  $R_1 \rightarrow \infty$ .

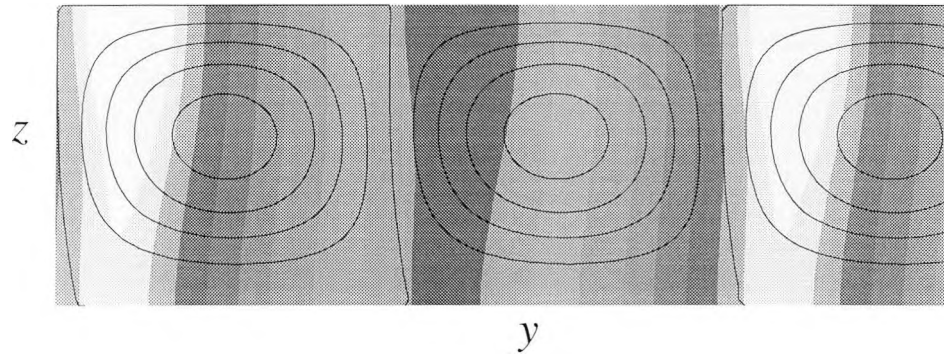


Figure 3.22: The longitudinal perturbations. The solid lines are the contours of the perturbation  $iWe^{iky}$ , and the shading represents the thermal perturbation  $\Theta e^{iky}$ . ( $\sigma = 0.10$ ,  $k = 0.77$ ,  $R_1 = 207 \approx R_{1c}$ .)

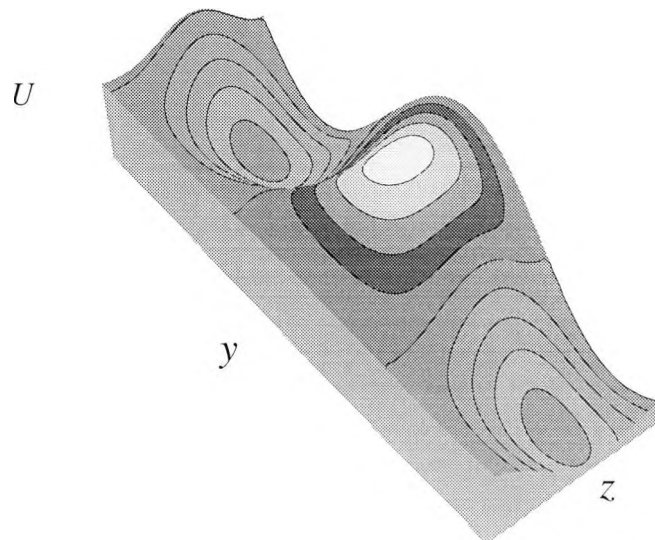


Figure 3.23: The longitudinal perturbations. The contours are the streamlines of the perturbation  $iWe^{iky}$ , and the height represents the horizontal velocity perturbation  $Ue^{iky}$ . ( $\sigma = 0.10$ ,  $k = 0.77$ ,  $R_1 = 207 \approx R_{1c}$ .)

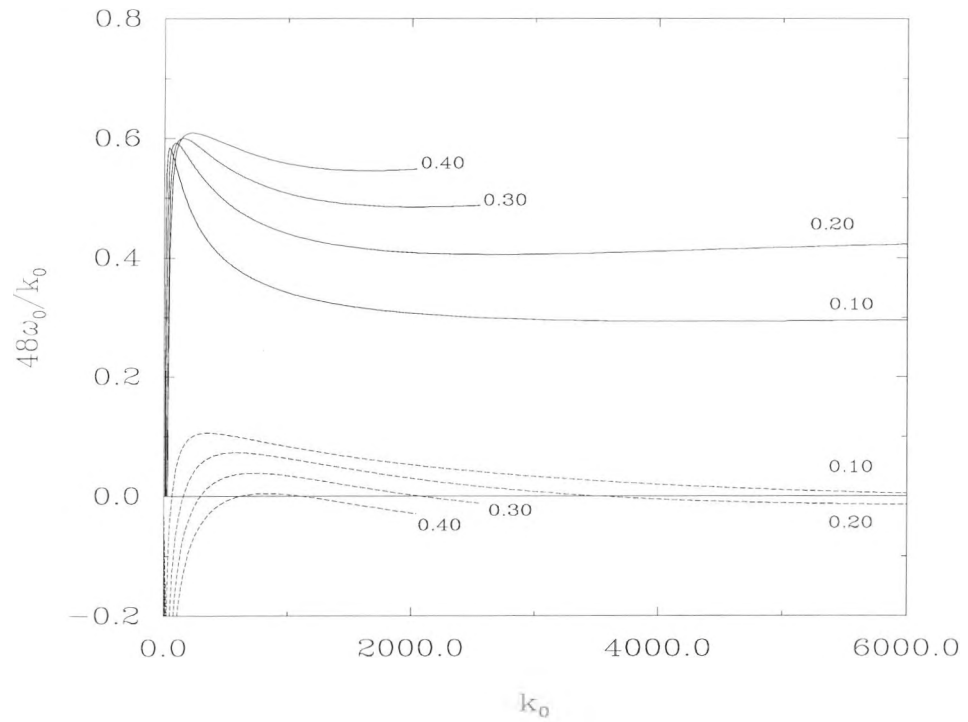


Figure 3.24: Real and imaginary parts of the normalised eigenvalues  $c = 48\omega_0/k_0$  of the asymptotic solutions as  $R_1 \rightarrow \infty$  for small Prandtl numbers. The wave speed is the solid line, the dotted line is the growth rate.

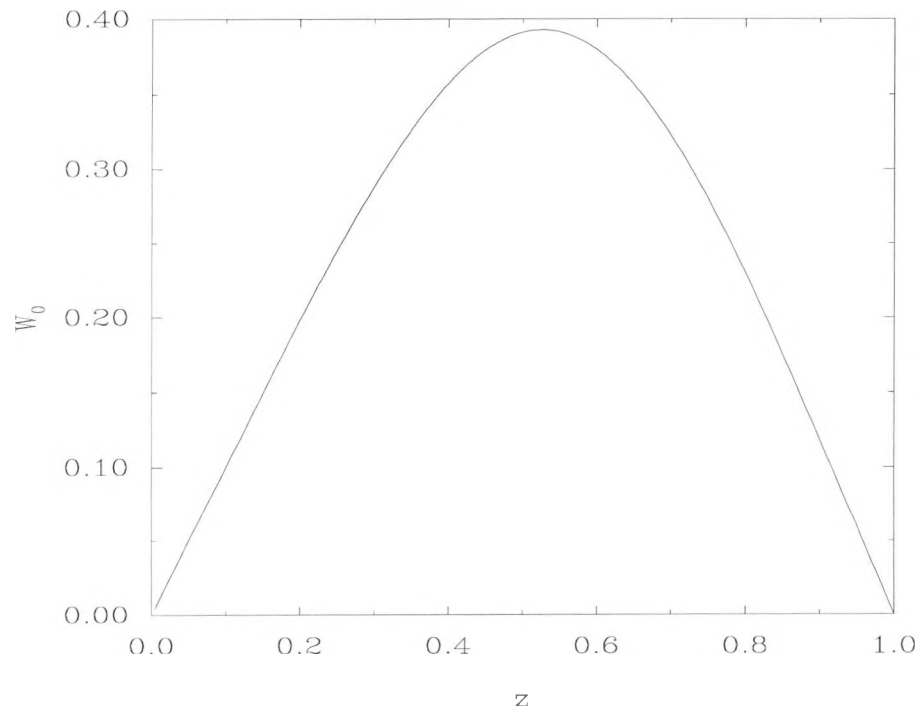


Figure 3.25: The profile of  $W_0$  as a function of  $z$  for  $\Omega = 0.0211$ .

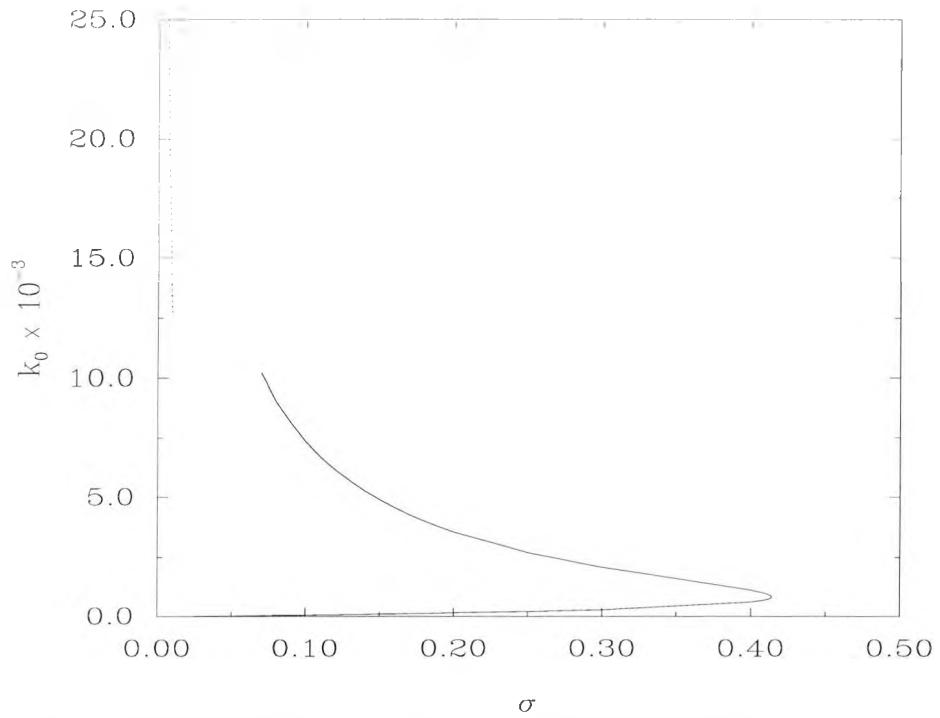


Figure 3.26: Neutral curve for  $k_0$  with the large  $k_0$  asymptote  $k_0 \sim \kappa_0 \sigma^{-3/2}$ ,  $\sigma \rightarrow 0$ .

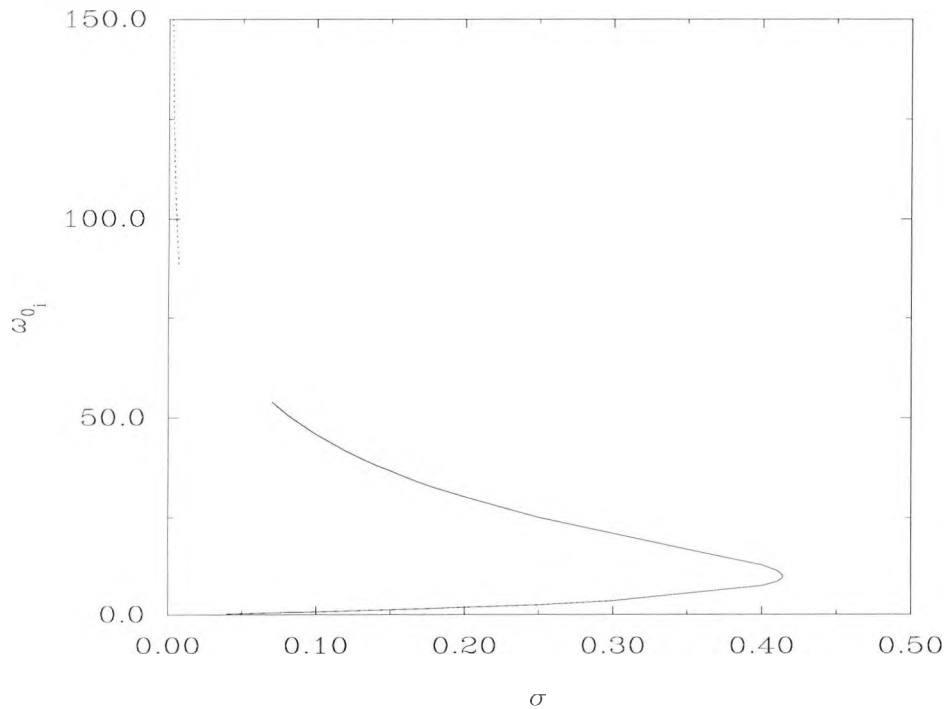


Figure 3.27: Values of  $\omega_{0i}$  along the neutral curve  $\omega_{0r} = 0$  as a function of  $\sigma$  with the asymptote  $\omega_{0i} \sim i\Omega_0 \kappa_0 \sigma^{-1}$ ,  $\sigma \rightarrow 0$ .

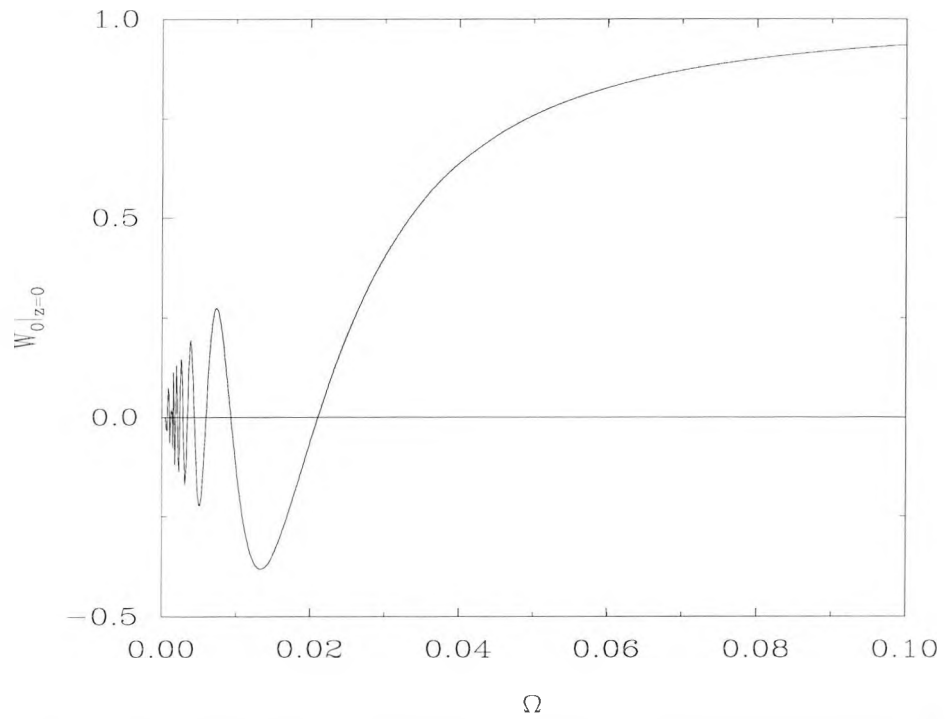


Figure 3.28: Values of  $W_0(0)$  against  $\Omega$ . Relevant values of the eigenvalue  $\Omega$  are those for which  $W_0(0) = 0$ .

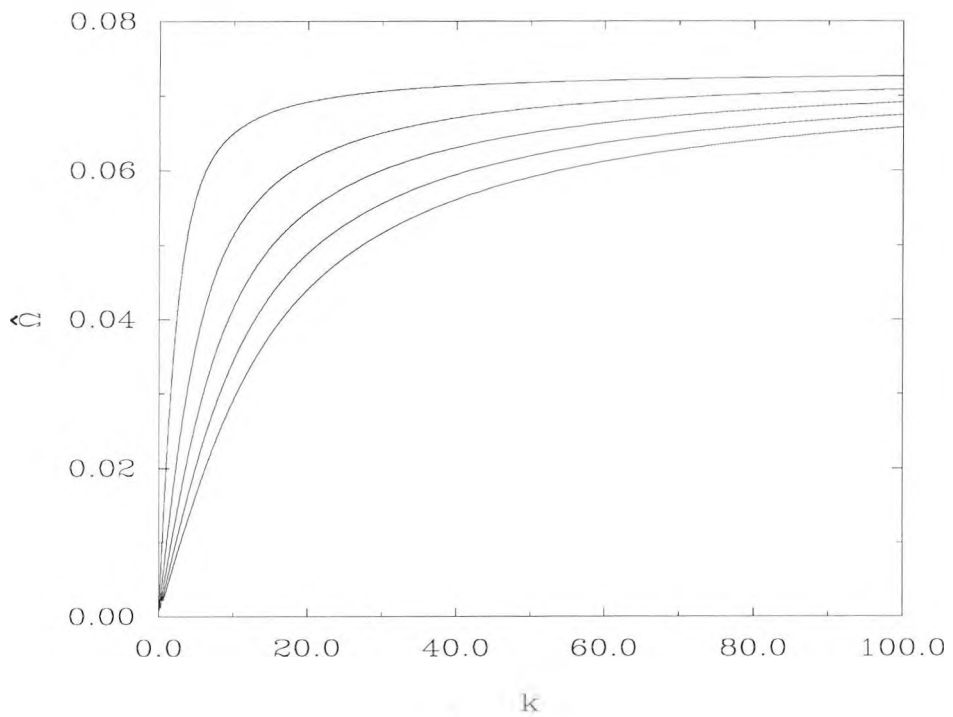


Figure 3.29: The first four eigenvalues  $\hat{\Omega}$  (from the largest down) as a function of  $k$ .

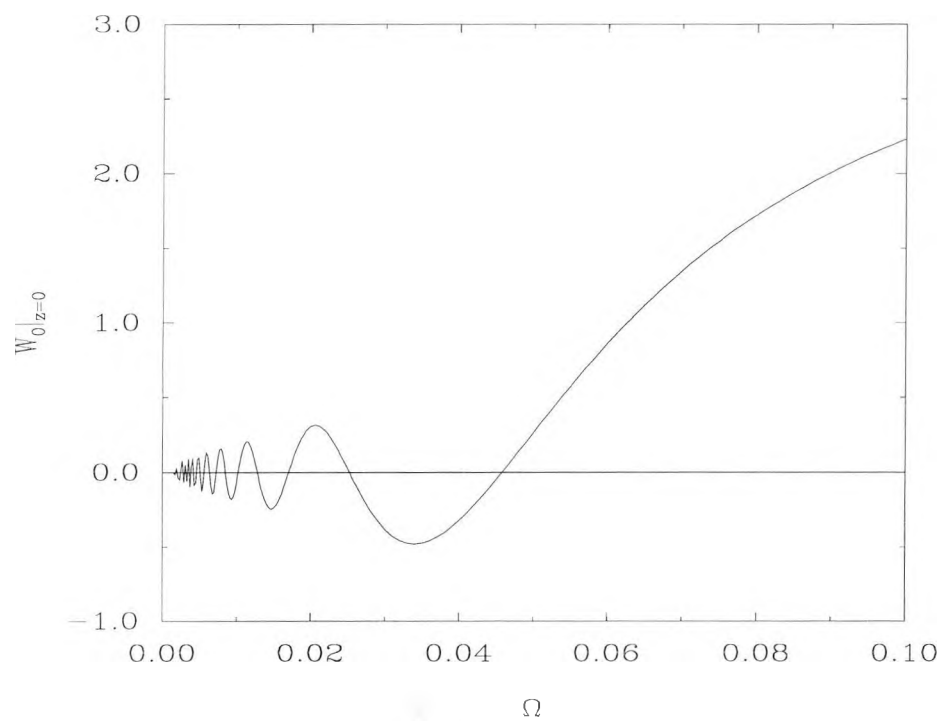


Figure 3.30: Values of  $W_0(0)$  against  $\Omega$  when  $k = 3$ . Relevant values of the eigenvalue  $\hat{\Omega}$  are those for which  $W_0(0) = 0$ .

# Chapter 4

## Steady-state solutions for the rotating cavity

### 4.1 Introduction

The effects of rotation are investigated by regarding the two-dimensional cavity previously looked at as the cross-section of an annulus or rotating channel. The rotation of the annulus or channel about a vertical axis produces an azimuthal velocity perpendicular to the plane of the two-dimensional cavity, and the theory is then more applicable to geophysical phenomena: Stone (1968), for example, describes the application of a rotating annulus with a vertical temperature difference to the atmospheric circulations on Venus and in the tropics of the Earth, and to the oceanic sinking regions. Using an annulus with a horizontal temperature difference, a rigid upper surface and small cross sectional aspect ratio ( $L < 1$ ), Douglas and Mason (1973) describe experiments relating to the temperature structure and to the transition from axisymmetric to non-axisymmetric flow. Hide (1967) gives a range of parameters for axisymmetric flow for a similar geometry but with free or rigid upper surface, and suggests that the azimuthal velocity in the axisymmetric flow “resembles the trade wind circulation occurring in the atmosphere in the tropics”.

The theory for an axisymmetric annulus with a square cross section and rigid upper surface is given by McIntyre (1968), who makes comparisons with the non-rotating rectangular cavity. An assumption that the Prandtl number was large was considered to place “not too serious a restriction on the applicability of the theory”.

Rotating thermal convection has also been discussed by Hignett *et al.* for a cylinder with a radial temperature gradient heated from below, and by Hopfinger and Linden (1990) in the review of the Euromech conference on rotation. The instability of rotating convective flows has been studied in a cylindrical annulus by Busse (1986), Busse and Or (1986) and Or and Busse (1987) and in a channel by Finlay (1990, 1992).

In this chapter, a theory for an infinite rotating channel, or equivalently an axisymmetric flow in a rotating annulus, with rectangular cross section of large aspect ratio ( $L \gg 1$ ) and free upper surface, is described. This is undertaken in a similar manner to the non-rotating theory of the previous chapters, by regarding the cavity as having a parallel flow core away from the vertical walls and two roughly square end zones near the walls where the flow is turned. This geometry is similar to that of Hunter (1967), who considered the case of finite aspect ratio and rapid rotation. Here the theory is developed first for general rotation speeds, measured by the Taylor number

$$T = \frac{4\Omega^2 h^4}{\nu^2} \quad (4.1.1)$$

where  $\Omega$  is the rate of rotation,  $h$  is the height of the cavity and  $\nu$  is the kinematic viscosity of the fluid. Nonlinear effects in the end regions are incorporated by assuming that

$$R_1 = \frac{R}{L} \quad (4.1.2)$$

is of order one. The governing equations are given in section 4.2, and then a parallel flow solution is found for the core of the cavity away from the vertical walls. The equations governing the behaviour in the end regions are given in section 4.4, and the matching of the solution of these with the core flow is discussed. Comparisons with the non-rotating case are made in section 4.5.

In the subsequent chapters results for small and general Taylor number at small and finite Rayleigh number are also presented and a description is given of the behaviour of the end zones at large  $R_1$  and  $T$ .

## 4.2 Governing equations

The non-dimensional governing equations in the rotating case are derived in Chapter 1. In addition to the vorticity and thermal energy equations, for the rotating case there is also an azimuthal momentum equation. Although the azimuthal velocity is in the  $y$  direction, there is no dependence on  $y$  in the governing equations as the cavity is assumed to have infinite length, or equivalently be an axisymmetric annulus in which curvature effects are ignored. A stream function may therefore be used and the governing equations for steady flow relative to the rotating frame of reference may be written in the form

$$\nabla^4 \bar{\psi} - R \frac{\partial \bar{\theta}}{\partial x} + T^{\frac{1}{2}} \frac{\partial \bar{v}}{\partial z} = \sigma^{-1} \frac{\partial(\nabla^2 \bar{\psi}, \bar{\psi})}{\partial(x, z)}, \quad (4.2.1)$$

$$\nabla^2 \bar{v} - T^{\frac{1}{2}} \frac{\partial \bar{\psi}}{\partial z} = \sigma^{-1} \frac{\partial(\bar{v}, \bar{\psi})}{\partial(x, z)}, \quad (4.2.2)$$

$$\nabla^2 \bar{\theta} = \frac{\partial(\bar{\theta}, \bar{\psi})}{\partial(x, z)}, \quad (4.2.3)$$

where  $\bar{\theta}$  is the temperature and the velocity components in the  $x$ ,  $y$  and  $z$  directions are  $\bar{u}$ ,  $\bar{v}$  and  $\bar{w}$  respectively, with

$$\bar{u} = \frac{\partial \bar{\psi}}{\partial z} \text{ and } \bar{w} = -\frac{\partial \bar{\psi}}{\partial x}, \quad (4.2.4)$$

where  $\bar{\psi}$  is the stream function. The Cartesian frame of reference rotates about a vertical axis (in the  $z$  direction) and it is assumed that centrifugal effects may be neglected. The theory also applies to a rotating annulus provided its radius is large enough for curvature effects to be ignored (Hunter 1967). The cavity, whose cross section occupies  $0 \leq x \leq L$ ,  $0 \leq z \leq 1$  is assumed to have thermally insulated upper and lower surfaces and a stress-free upper surface; the motion is driven by a horizontal temperature difference between the ends. Thus the full set of boundary conditions is

$$\bar{\psi} = \frac{\partial \bar{\psi}}{\partial z} = \bar{v} = \frac{\partial \bar{\theta}}{\partial z} = 0 \text{ on } z = 0, \quad (4.2.5)$$

$$\bar{\psi} = \frac{\partial^2 \bar{\psi}}{\partial z^2} = \frac{\partial \bar{v}}{\partial z} = \frac{\partial \bar{\theta}}{\partial z} = 0 \text{ on } z = 1, \quad (4.2.6)$$

with

$$\bar{\psi} = \frac{\partial \bar{\psi}}{\partial x} = \bar{v} = 0 \text{ on } x = 0, L, \quad (4.2.7)$$

$$\bar{\theta} = 0 \text{ on } x = 0 \text{ and } \bar{\theta} = 1 \text{ on } x = L. \quad (4.2.8)$$

As in the non-rotating problem the length of the cavity is assumed to be much greater than its depth so that  $L \gg 1$ . As before, in the regime for which  $R_1 = R/L$  is of order 1, this allows the cavity to be considered as having a parallel-flow core away from the vertical walls and two roughly square end regions where the flow is turned through 180 degrees. These regions are considered next.

### 4.3 Core flow

In the core region away from the end walls, the order one variable  $\xi = x/L$  is used so that  $0 < \xi < 1$ . In this region the flow is assumed to be parallel to the horizontal boundaries and the temperature is assumed to be linearly dependent on  $\xi$ , allowing an exact solution to be found in the form

$$\bar{\psi} = f(z), \quad \bar{v} = s(z), \quad \bar{\theta} = A\xi + g(z), \quad (4.3.1)$$

where  $A$  is a constant. The governing equations then become

$$f^{iv} - R_1 A + T^{\frac{1}{2}} s' = 0, \quad (4.3.2)$$

$$s'' - T^{\frac{1}{2}} f' = 0, \quad (4.3.3)$$

$$g'' - \frac{A}{L} f' = 0, \quad (4.3.4)$$

where  $R_1 = R/L$ , and the boundary conditions become

$$f = f' = s = g' = 0 \text{ on } z = 0, \quad (4.3.5)$$

$$f = f'' = s' = g' = 0 \text{ on } z = 1, \quad (4.3.6)$$

where primes denote the derivatives with respect to  $z$ .

Integrating (4.3.3) and using  $f = s' = 0$  on  $z = 1$  leads to

$$s' = T^{\frac{1}{2}} f, \quad (4.3.7)$$

which can be substituted into (4.3.2) to yield

$$f^{iv} + T f = R_1 A. \quad (4.3.8)$$

It is convenient to set

$$s(z) = R_1 T^{\frac{1}{2}} A G(z; T) \quad (4.3.9)$$

so that

$$f = R_1 A G'(z; T). \quad (4.3.10)$$

The function  $G$  may now be determined by solving (4.3.8) subject to  $G' = G'' = 0$  on  $z = 0$  and  $G' = G''' = 0$  on  $z = 1$ . Since in addition  $G = 0$  on  $z = 0$  it follows that

$$\begin{aligned} G(z; T) = & D_1(\sinh \gamma z \cos \gamma z - \cosh \gamma z \sin \gamma z) \\ & + D_2(1 - e^{-\gamma z} \cos \gamma z - \cosh \gamma z \sin \gamma z) \\ & - \frac{1}{\gamma T} \cosh \gamma z \sin \gamma z + \frac{z}{T}, \end{aligned} \quad (4.3.11)$$

where

$$D_1 = \frac{1}{2\gamma T} \left[ D_2 T \gamma \left( \frac{e^{-\gamma}(\sin \gamma - \cos \gamma)}{\cosh \gamma \cos \gamma} + \tanh \gamma \tan \gamma - 1 \right) + \tanh \gamma \tan \gamma - 1 \right], \quad (4.3.12)$$

$$D_2 = \frac{1}{\gamma T D_3} (1 - \cosh \gamma \cos \gamma - \tanh \gamma \tan \gamma \sinh \gamma \sin \gamma), \quad (4.3.13)$$

and

$$\begin{aligned} D_3 = & e^{-\gamma}(\sin \gamma - \cos \gamma) \tanh \gamma \tan \gamma - e^{-\gamma}(\sin \gamma + \cos \gamma) \\ & + \cosh \gamma \cos \gamma + \tanh \gamma \tan \gamma \sinh \gamma \sin \gamma \end{aligned} \quad (4.3.14)$$

where  $\gamma = T^{1/4}/\sqrt{2}$ . Finally, integration of (4.3.4) twice with use of  $g'(0) = 0$  yields

$$g(z) = R_1 A^2 G(z; T) L^{-1} + B \quad (4.3.15)$$

where  $B$  is a constant, and it is noted that this solution also satisfies  $g'(1) = 0$ . The parallel flow core solution can now be written as

$$\bar{\psi} = R_1 A G', \quad (4.3.16)$$

$$\bar{v} = R_1 T^{1/2} A G, \quad (4.3.17)$$

$$\bar{\theta} = A \xi + B + R_1 A^2 G L^{-1}. \quad (4.3.18)$$

In order that the temperature conditions on  $x = 0$  and  $L$  are satisfied, it is required that

$$A = 1 + A_1 L^{-1} + \dots, \text{ and } B = 0 + B_1 L^{-1} + \dots \quad (4.3.19)$$

in the limit as  $L \rightarrow \infty$ . The order  $L^{-1}$  corrections are generated as in the non-rotating case by the temperature field produced in the end regions of the cavity to be discussed in section 4.4 below.

Plots of  $G(z; T)$  and its first two derivatives are shown in figure 4.1, for  $T = 2000, 5000$  and  $10000$ , where it is seen that the amplitude decreases with increasing  $T$ . As  $T \rightarrow 0$ ,  $G(z; T) = G(z; 0) + O(T)$ , where  $G(z; 0)$  is the non-rotating core function defined in (2.3.7), that is

$$G(z; 0) = \frac{1}{120}z^5 - \frac{5}{192}z^4 + \frac{1}{48}z^3, \quad (4.3.20)$$

and for  $T = 2000$ , the three profiles are seen to be similar to those for  $T = 0$  shown in figure 2.1. From (4.3.11) it can be shown that away from the horizontal boundaries, as  $T \rightarrow \infty$ ,

$$G(z; T) \sim zT^{-1} - \sqrt{2}T^{-\frac{5}{4}}. \quad (4.3.21)$$

This implies that the azimuthal velocity and the convective effect on the temperature are directly proportional to depth, that the stream function,  $G'(z; T)$ , is constant with depth, and that there is effectively no horizontal velocity,  $G''(z; T)$ . It also suggests that convective effects are damped by an increase in rotation rate. This behaviour can be seen in figure 4.1, as can the formation of Ekman layers close to the upper and lower boundaries where  $z$  and  $(1 - z)$  are of order  $T^{-1/4}$ . These are particularly noticeable in the case of  $G'''(z; T)$ , the radial velocity, where the only non-zero values are in the Ekman layers for large Taylor number: in figure 4.2 the radial velocity is plotted for  $T = 10^6$ .

The form of  $G(z; T)$  in the Ekman layers is found by rescaling  $z$ . In the lower Ekman layer,  $z$  is rescaled such that  $z = T^{-1/4}\bar{z}$  with  $\bar{z}$  of order one, and

$$G(z; T) \sim \sqrt{2}T^{-\frac{5}{4}}\left(\frac{\bar{z}}{\sqrt{2}} - 1 + e^{-\frac{\bar{z}}{\sqrt{2}}}\cos\frac{\bar{z}}{\sqrt{2}}\right), \quad T \rightarrow \infty. \quad (4.3.22)$$

In the upper Ekman layer the order one variable  $\tilde{z} = T^{-1/4}(1 - z)$  is used and it is found that as  $T \rightarrow \infty$ ,

$$G(z; T) \sim T^{-1}\left(1 + \sqrt{2}T^{-\frac{1}{4}}\left(\frac{1}{2}e^{-\frac{\tilde{z}}{\sqrt{2}}}\left(\sin\frac{\tilde{z}}{\sqrt{2}} - \cos\frac{\tilde{z}}{\sqrt{2}}\right) - \frac{\tilde{z}}{\sqrt{2}} - 1\right)\right). \quad (4.3.23)$$

These are in agreement with the results of Hunter (1967) for the large Taylor number limit.

Interestingly, the form of  $s$  in (4.3.9) suggests that, while the amplitudes of  $f$  and  $g$  are always decreasing with increasing  $T$ , for small  $T$  the amplitude of  $s$  increases with increasing  $T$ , and there is a maximum azimuthal velocity,  $s$ , at the

free surface for some finite value of the Taylor number. This behaviour is shown in the plot of  $s$  at  $z = 1$  against the Taylor number in figure 4.3. The maximum value of the free surface azimuthal velocity can be seen to be at approximately  $T = 250$ . This can be compared with the value of the radial velocity at the free surface shown in figure 4.4 which decreases with increasing Taylor number from a maximum at  $T = 0$ .

The results (4.3.9), (4.3.10) and (4.3.15) can also be obtained by formally expanding the solution in inverse powers of  $L$  and solving the individual problems which arise at each order of magnitude. In summary, the core solution can be expanded in the form

$$\left. \begin{aligned} \bar{\psi} &= R_1(1 + L^{-1}A_1)G' + O(L^{-2}) \\ \bar{v} &= R_1(1 + L^{-1}A_1)T^{\frac{1}{2}}G + O(L^{-2}) \\ \bar{\theta} &= \xi + L^{-1}(A_1\xi + B_1 + R_1G) + O(L^{-2}) \end{aligned} \right\} (L \rightarrow \infty). \quad (4.3.24)$$

As  $T$  tends to zero, the non-rotating solution is recovered as expected, and for large  $T$  convective effects are damped and concentrated in Ekman layers close to the horizontal boundaries.

## 4.4 End regions

The flow across the cavity is turned in approximately square regions at the end walls. Near the cold wall

$$\left. \begin{aligned} \bar{\psi} &= \psi(x, z) + \dots, \\ \bar{v} &= v(x, z) + \dots, \\ \bar{\theta} &= L^{-1}\theta(x, z) + \dots, \end{aligned} \right\} (L \rightarrow \infty), \quad (4.4.1)$$

and substitution into (4.2.1) – (4.2.3) shows that  $\psi$  and  $\theta$  satisfy the full governing equations with  $R$  replaced by  $R_1$ :

$$\nabla^4\psi - R_1\frac{\partial\theta}{\partial x} + T^{\frac{1}{2}}\frac{\partial v}{\partial z} = \sigma^{-1}\frac{\partial(\nabla^2\psi, \psi)}{\partial(x, z)}, \quad (4.4.2)$$

$$\nabla^2v - T^{\frac{1}{2}}\frac{\partial\psi}{\partial z} = \sigma^{-1}\frac{\partial(v, \psi)}{\partial(x, z)}, \quad (4.4.3)$$

$$\nabla^2\theta = \frac{\partial(\theta, \psi)}{\partial(x, z)}. \quad (4.4.4)$$

The solution must satisfy the wall conditions

$$\psi = \frac{\partial\psi}{\partial x} = v = \theta = 0 \text{ on } x = 0, \quad (4.4.5)$$

$$\psi = \frac{\partial\psi}{\partial z} = v = \frac{\partial\theta}{\partial z} = 0 \text{ on } z = 0, \quad (4.4.6)$$

and the free surface conditions

$$\psi = \frac{\partial^2\psi}{\partial z^2} = \frac{\partial v}{\partial z} = \frac{\partial\theta}{\partial z} = 0 \text{ on } z = 1. \quad (4.4.7)$$

Also, the solution must match with the core solution, requiring that

$$\left. \begin{aligned} \psi &\rightarrow R_1 G' \\ v &\rightarrow R_1 T^{\frac{1}{2}} G \\ \theta &\sim x + c + R_1 G \end{aligned} \right\} (x \rightarrow \infty) \quad (4.4.8)$$

where, from matching with (4.3.24),

$$c = B_1. \quad (4.4.9)$$

Near the hot wall

$$\left. \begin{aligned} \bar{\psi} &= \bar{\psi}(\bar{x}, z) + \dots, \\ \bar{v} &= \bar{v}(\bar{x}, z) + \dots, \\ \bar{\theta} &= 1 + L^{-1}\bar{\theta}(\bar{x}, z) + \dots, \end{aligned} \right\} (L \rightarrow \infty), \quad (4.4.10)$$

where  $\bar{x} = L - x$ . Substitution into (4.2.1) – (4.2.3) yields equations similar to those of the cold end-zone, except that because of the replacement of  $x$  by  $L - x$ , the Jacobian terms and the buoyancy term have opposite sign:

$$\bar{\nabla}^4 \bar{\psi} + R_1 \frac{\partial \bar{\theta}}{\partial \bar{x}} + T^{\frac{1}{2}} \frac{\partial \bar{v}}{\partial z} = -\sigma^{-1} \frac{\partial(\bar{\nabla}^2 \bar{\psi}, \bar{\psi})}{\partial(\bar{x}, z)}, \quad (4.4.11)$$

$$\bar{\nabla}^2 \bar{v} - T^{\frac{1}{2}} \frac{\partial \bar{\psi}}{\partial z} = -\sigma^{-1} \frac{\partial(\bar{v}, \bar{\psi})}{\partial(\bar{x}, z)}, \quad (4.4.12)$$

$$\bar{\nabla}^2 \bar{\theta} = -\frac{\partial(\bar{\theta}, \bar{\psi})}{\partial(\bar{x}, z)}. \quad (4.4.13)$$

The solution must satisfy the wall conditions

$$\bar{\psi} = \frac{\partial \bar{\psi}}{\partial \bar{x}} = \bar{v} = \bar{\theta} = 0 \text{ on } \bar{x} = 0, \quad (4.4.14)$$

$$\bar{\psi} = \frac{\partial \bar{\psi}}{\partial z} = \bar{v} = \frac{\partial \bar{\theta}}{\partial z} = 0 \text{ on } z = 0, \quad (4.4.15)$$

the free surface conditions

$$\bar{\psi} = \frac{\partial^2 \bar{\psi}}{\partial z^2} = \frac{\partial \bar{v}}{\partial z} = \frac{\partial \bar{\theta}}{\partial z} = 0 \text{ on } z = 1, \quad (4.4.16)$$

and must also match with the core solution, requiring that

$$\left. \begin{aligned} \bar{\psi} &\rightarrow R_1 G' \\ \bar{v} &\rightarrow R_1 T^{\frac{1}{2}} G \\ \bar{\theta} &\sim -\bar{x} + \bar{c} + R_1 G \end{aligned} \right\} (\tilde{x} \rightarrow \infty) \quad (4.4.17)$$

where, from (4.3.24),

$$\bar{c} = A_1 + B_1. \quad (4.4.18)$$

The two end region problems must be solved to determine the constant parameters  $c = c(R_1, \sigma, T)$  and  $\bar{c} = \bar{c}(R_1, \sigma, T)$  as functions of  $R_1$ ,  $\sigma$  and  $T$ . The core solution (4.3.24) is then completed to order  $L^{-1}$ , given that

$$A_1 = \bar{c} - c, \quad B_1 = c. \quad (4.4.19)$$

Properties of the end region solutions are considered in Chapters 5 and 6.

## 4.5 Discussion

The work in this chapter extends that of sections 2.2 – 2.4 to incorporate the effect of rotation, the most obvious difference being the inclusion of an azimuthal velocity perpendicular to the plane of the stream function flow. This renders the nonlinear end region flows fully three-dimensional and gives rise to a two-dimensional flow in the core parallel to the plane of rotation. Although the amplitude of the core velocity is still linearly dependent on the Rayleigh number, the velocity profiles themselves are now dependent on the Taylor number as well as being a function of depth. As  $T$  increases, the radial velocity becomes concentrated in thin Ekman layers close to the horizontal boundaries, and its amplitude decreases. The amplitude of the azimuthal velocity initially increases from zero at  $T = 0$  to a maximum at approximately  $T = 250$  before it then also decreases. Thus in general a high rotation rate dampens the effect of convection.

In Chapter 3, the linear stability of the two dimensional, non-rotating core flow was investigated. It seems likely that at small Prandtl numbers the core flow in

the rotating case will also become unstable for sufficiently high Rayleigh numbers, although this is not investigated here. The stability properties of the flow are likely to be quite different at large rotation rates where away from the Ekman layers and the end regions, the only flow is in the azimuthal direction. Chapters 5 and 6 are devoted to a detailed investigation of the properties of the basic steady three-dimensional flow which occurs in the end-regions of the cavity at general rotation rates.

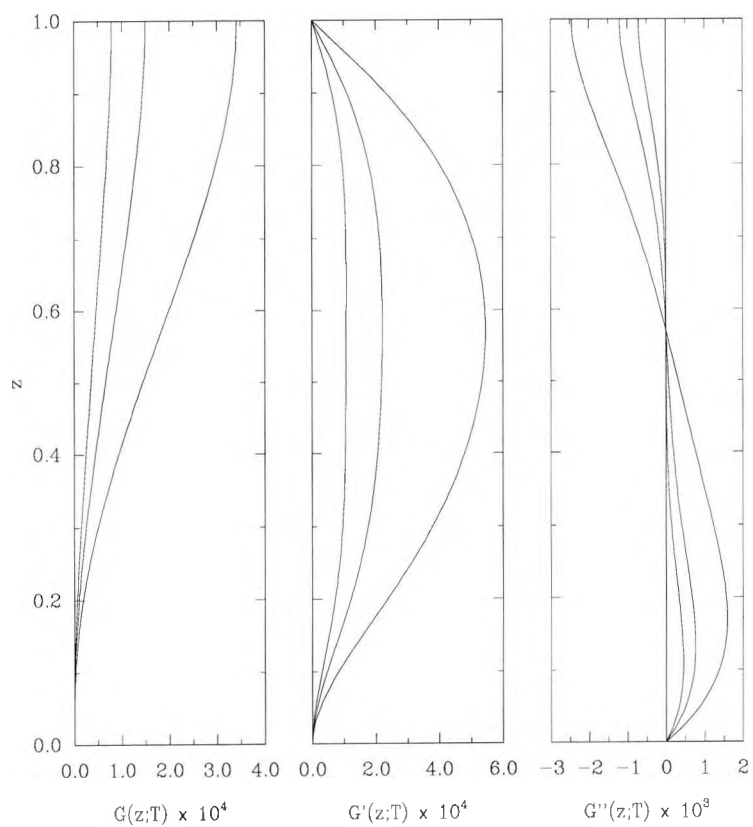


Figure 4.1: Plots of  $G(z;T)$  (core temperature and azimuthal velocity profile),  $G'$  (core stream function profile), and  $G''$  (core radial velocity profile) as functions of  $z$  for  $T=2000,5000,10000$ . In each set of graphs, the amplitude decreases with increasing  $T$ .

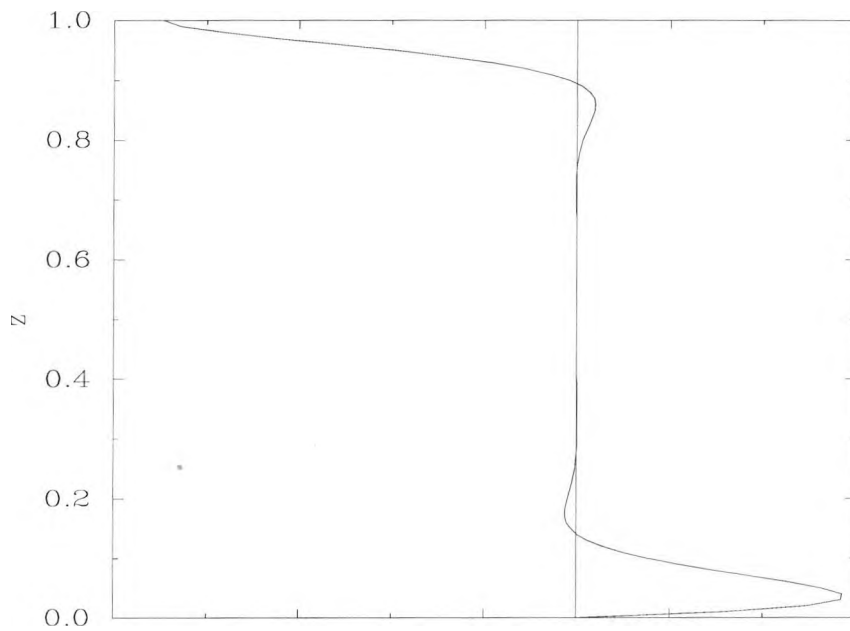


Figure 4.2: Plot of the radial velocity,  $G''(z; T)$ , as a function of  $z$  for  $T = 10^6$ .

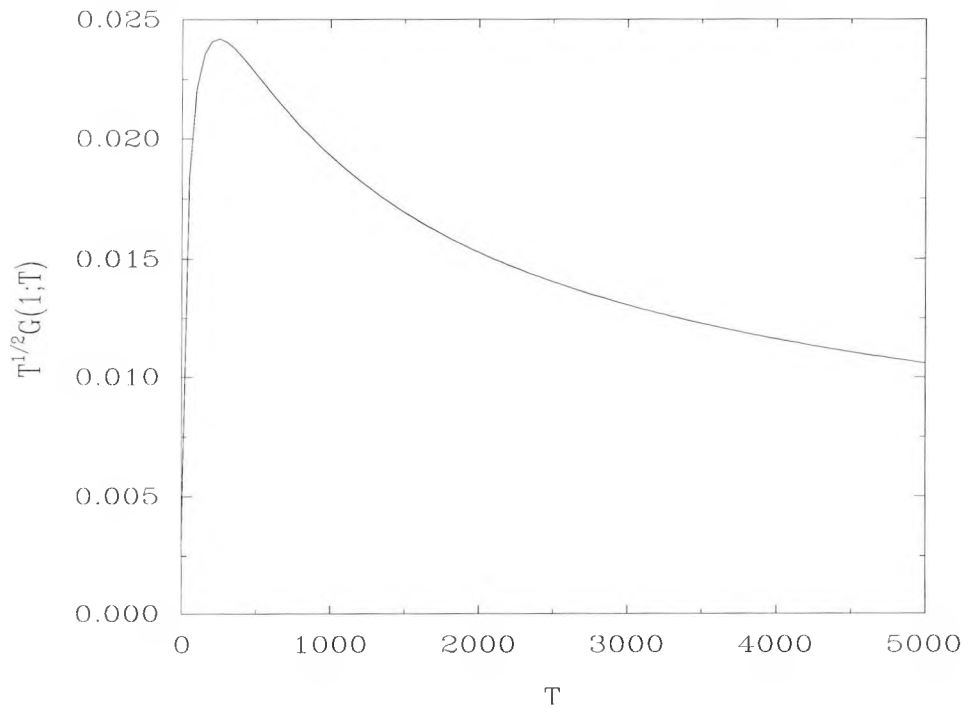


Figure 4.3: The azimuthal velocity  $T^{1/2}G(1; T)$  at the free surface as a function of  $T$ .

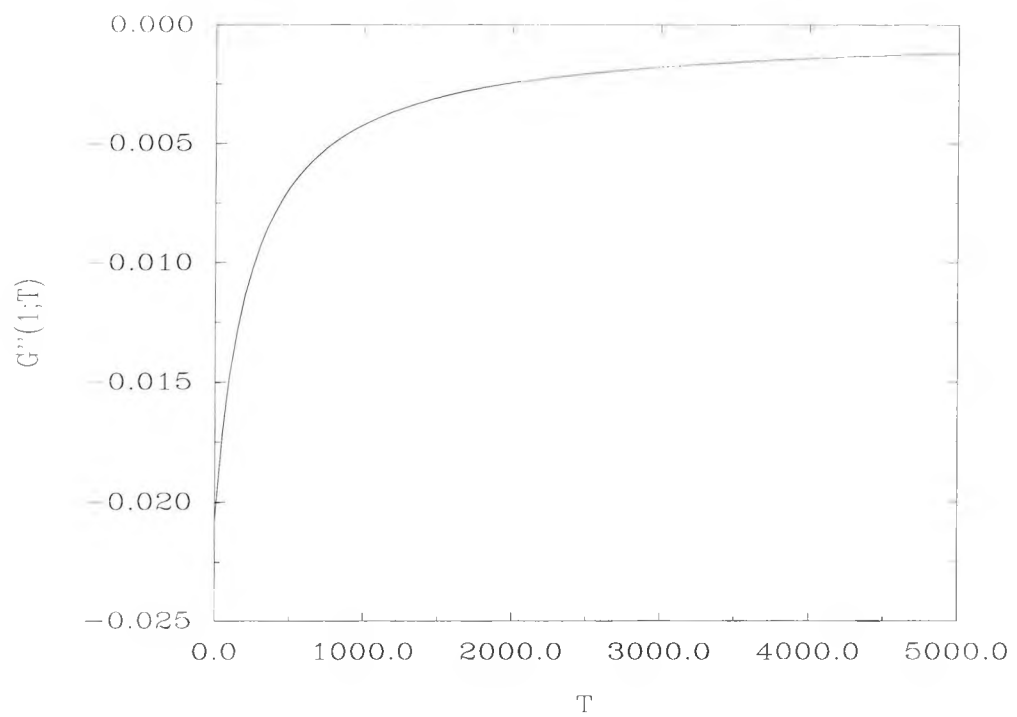


Figure 4.4: The radial velocity  $G''(1;T)$  at the free surface as a function of  $T$ .

## Chapter 5

# Steady-state solution of the rotating end zone eigenvalue problem

### 5.1 Introduction

Solutions in the two end regions of the cavity may be found as an infinite set of eigenfunctions that decay into the parallel-flow core. In this chapter, the eigenvalue problem is derived for general Rayleigh, Taylor and Prandtl numbers. This problem is solved analytically for  $R_1 = T = 0$  and involves the introduction of an ‘azimuthal’ mode in addition to the modes determined previously for the non-rotating problem in chapter 2. The eigenvalues are then ‘traced out’ numerically from these known values to find solutions for general  $R_1$  and  $T$ , allowing the lateral extent of the end regions to be determined. The lack of symmetry between the two ends means that, in general, the hot and cold end regions need to be considered separately.

These results for general  $R_1$  and  $T$  are complemented by asymptotic analyses of the problem for small Rayleigh number and large Taylor number – recovering the double vertical boundary layers, or Stewartson layers, found by Hunter (1967) – and for large  $R_1$  and large  $T$ , where a novel boundary layer structure is identified in Ekman layers along the horizontal boundaries.

## 5.2 Derivation of the eigenvalue problem

Insight into the behaviour of the end region solutions for general  $R_1$ ,  $T$  and  $\sigma$  can be gained by considering the manner in which the core flow is recovered as  $x \rightarrow \infty$  and  $\bar{x} \rightarrow \infty$ . For the cold end-zone it is expected that

$$\psi \sim R_1 G' + \sum_{\alpha} \phi(z; R_1, T, \sigma) e^{\alpha x} \quad (5.2.1)$$

$$v \sim R_1 T^{\frac{1}{2}} G + \sum_{\alpha} V(z; R_1, T, \sigma) e^{\alpha x} \quad (5.2.2)$$

$$\theta \sim x + c + R_1 G + \sum_{\alpha} \Theta(z; R_1, T, \sigma) e^{\alpha x} \quad (5.2.3)$$

for  $Re(\alpha) < 0$ ,  $x \gg 1$ , while for the hot end-zone it is expected that

$$\bar{\psi} \sim R_1 G' + \sum_{\alpha} \phi(z; R_1, T, \sigma) e^{-\alpha \bar{x}} \quad (5.2.4)$$

$$\bar{v} \sim R_1 T^{\frac{1}{2}} G + \sum_{\alpha} V(z; R_1, T, \sigma) e^{-\alpha \bar{x}} \quad (5.2.5)$$

$$\bar{\theta} \sim -\bar{x} + \bar{c} + R_1 G + \sum_{\alpha} \Theta(z; R_1, T, \sigma) e^{-\alpha \bar{x}} \quad (5.2.6)$$

for  $Re(\alpha) > 0$ ,  $\bar{x} \gg 1$ . Substituting (5.2.1)–(5.2.6) into the governing equations (4.4.2) – (4.4.4) and linearising leads to a single eigenvalue problem for both end-zones:

$$\phi^{(3)} + 2\alpha^2 \phi'' + \alpha^4 \phi - \alpha R_1 \Theta + T^{\frac{1}{2}} V' = \frac{\alpha R_1}{\sigma} (G'''(\phi'' + \alpha^2 \phi) - G^{iv} \phi), \quad (5.2.7)$$

$$V'' + \alpha^2 V - T^{\frac{1}{2}} \phi' = \alpha R_1 \sigma^{-1} (G'' V - T^{\frac{1}{2}} G' \phi), \quad (5.2.8)$$

$$\Theta'' + \alpha^2 \Theta - \phi' = \alpha R_1 (G'' \Theta - G' \phi), \quad (5.2.9)$$

with  $\phi = \phi' = V = \Theta' = 0$  on  $z = 0$ , and  $\phi = \phi'' = V' = \Theta' = 0$  on  $z = 1$ . In general the eigenvalue  $\alpha$  is complex, with  $\alpha = \alpha_r + i\alpha_i$ . Solutions where  $\alpha_r > 0$  relate to the hot end-zone; where  $\alpha_r < 0$  the solutions correspond to the cold end-zone. By taking the complex conjugate of (5.2.7) – (5.2.9) it can be seen that if  $\alpha$  is an eigenvalue corresponding to eigenfunctions  $\phi$ ,  $V$  and  $\Theta$  then  $\alpha^*$  is the eigenvalue corresponding to the eigenfunctions  $\phi^*$ ,  $V^*$  and  $\Theta^*$ , where the asterisk denotes the complex conjugate. To avoid confusion, the imaginary part of the eigenvalue,  $\alpha_i$ , is taken to be positive at the hot end and negative at the cold end.

For general  $\sigma$ ,  $R_1$  and  $T$  it is necessary to solve the eigenvalue problem (5.2.7) – (5.2.9) numerically. A fourth order Runge–Kutta scheme was used to compute

solutions from the specified boundary conditions at  $z = 0$  to give accurate results at  $z = 1$ . These results were made consistent with the boundary conditions at  $z = 1$  by combining four independent solutions and using a Newton iteration. This is similar to the scheme discussed in detail in section 2.6.

The eigenvalue problem (5.2.7) – (5.2.9) was first solved numerically for  $R_1 = 0$  and general  $T$ , and then for finite, fixed  $T$  and general  $R_1$ . Results for both the hot and cold ends are given, and each end has both ‘real’ and ‘complex’ eigenvalue branches which stem from the limiting behaviour at  $R_1 = 0$  to be discussed below.

### 5.3 Small Rayleigh numbers, $R_1 \ll 1$

Values of  $\alpha$  were first traced out for  $R_1 = 0$  and general  $T$  by starting from the analytical solution of the eigenvalue problem which is available when  $R_1 = T = 0$ . This analytical solution is described first and then subsequent parts of this section describe solutions obtained for finite and large values of  $T$ , using both numerical and asymptotic methods.

#### 5.3.1 Small $T$

When  $R_1 = T = 0$  the end zone eigenvalue problem simplifies to

$$\phi^{iv} + 2\alpha^2 \phi'' + \alpha^4 \phi = 0, \quad (5.3.1)$$

$$V'' + \alpha^2 V = 0 \quad (5.3.2)$$

$$\Theta'' + \alpha^2 \Theta - \phi' = 0, \quad (5.3.3)$$

with  $\phi = \phi' = V = \Theta' = 0$  on  $z = 0$  and  $\phi = \phi'' = V' = \Theta' = 0$  on  $z = 1$ . For the trivial solutions of (5.3.1) and (5.3.2),  $\phi = V = 0$ , the solution of (5.3.3) yields the real eigenvalues

$$\alpha = \pm n\pi, \quad n = 1, 2, \dots, \quad (5.3.4)$$

with eigenfunctions of the form  $\Theta = \cos n\pi z$ . Alternatively, the relevant non-trivial solution of (5.3.1) is

$$\phi = \sin \alpha z - \alpha z \tan \alpha \sin \alpha z - \alpha z \cos \alpha z, \quad (5.3.5)$$

where  $\alpha$  is a solution of

$$\sin 2\alpha - 2\alpha = 0. \quad (5.3.6)$$

The complex roots of (5.3.6) are tabulated in Hillman and Salzer (1943), giving

$$\alpha = \pm(3.7489 + 1.3844 i), \pm(6.9500 + 1.6761 i), \dots \quad (5.3.7)$$

Unlike the non-rotating case, there is now a third set of eigenvalues that comes from the azimuthal velocity equation; the solution of (5.3.2) yields the eigenvalues

$$\alpha = \pm \frac{(2n+1)\pi}{2}, \quad n = 0, 1, 2, \dots \quad (5.3.8)$$

and the eigenfunctions  $V = \sin(2n+1)\pi z/2$ .

### 5.3.2 General $T$

For zero Rayleigh number and general values of  $T$ , equations (5.2.7)–(5.2.9) reduce to

$$\phi^{iv} + 2\alpha^2 \phi'' + \alpha^4 \phi + T^{\frac{1}{2}} V' = 0, \quad (5.3.9)$$

$$V'' + \alpha^2 V - T^{\frac{1}{2}} \phi' = 0, \quad (5.3.10)$$

$$\Theta'' + \alpha^2 \Theta - \phi' = 0 \quad (5.3.11)$$

with boundary conditions,

$$\phi = \phi' = V = \Theta' = 0 \text{ on } z = 0 \quad \text{and} \quad \phi = \phi'' = V' = \Theta' = 0 \text{ on } z = 1. \quad (5.3.12)$$

It can be seen that, as all the powers of the eigenvalue  $\alpha$  are even, this problem is the same for both hot and cold end regions, with the eigenvalues for the cold end equal and opposite to those for the hot end. Thus only the results for the hot end zone where  $Re(\alpha) > 0$  are given.

The results of solving (5.3.9)–(5.3.12) numerically with the fourth order Runge-Kutta scheme from the known values at  $R_1 = T = 0$  are given in figure 5.1, which shows how the real azimuthal velocity mode and the complex stream function mode depend on the Taylor number for zero Rayleigh number. These modes remain independent of thermal effects. The thermal eigenvalues ( $\alpha = n\pi$ ) determined by (5.3.11) remain unchanged with increasing Taylor number and are not shown; these correspond to the trivial solution  $\phi = V = 0$  of (5.3.9) and (5.3.10).

The complex stream function modes differ from the real azimuthal modes in that initially they decrease with increasing but small Taylor number. The first real mode is always dominant though, and for large  $T$ , all the modes are increasing with increasing  $T$ , so that the end regions contract as the rotation rate increases. Greater insight into the end region structure can be gained by a study of the asymptotic structure for large  $T$ .

### 5.3.3 Large $T$

At general values of  $T$ , the vorticity and momentum equations (5.3.9) and (5.3.10) together with the boundary condition (5.3.12) can be written as the single sixth order problem

$$V^{vi} + 3\alpha^2 V^{iv} + 3\alpha^4 V'' + \alpha^6 V + TV'' = 0, \quad (5.3.13)$$

with boundary conditions

$$V = V'' = V^v + 3\alpha^2 V''' + 2\alpha^4 V' + TV' = 0 \text{ on } z = 0, \quad (5.3.14)$$

and

$$V' = V''' = V^v = 0 \text{ on } z = 1. \quad (5.3.15)$$

As  $T \rightarrow \infty$ , there are two different behaviours of  $\alpha$ . In general,  $\alpha$  is proportional to  $T^{1/6}$ , but for the leading mode, of greatest importance in terms of the decay length of the end regions, the value of  $\alpha$  is proportional to  $T^{1/8}$ . The analysis for each case is given below in terms of asymptotic expansions for  $\alpha$  and  $V$  as  $T \rightarrow \infty$ . The two behaviours correspond to the inner and outer vertical boundary layer scales discussed by Hunter (1967) and originally identified by Stewartson (1957) in his analysis of the flow generated between differentially rotating disks.

A balance between the final two terms on the left-hand side of (5.3.13) suggests that in general the expansion of the eigenvalue  $\alpha$  as  $T \rightarrow \infty$  can be expressed in the form

$$\alpha = T^{\frac{1}{6}} \bar{\alpha}, \quad \bar{\alpha} = \bar{\alpha}_0 + \dots, \quad T \rightarrow \infty. \quad (5.3.16)$$

Neglect of the highest order derivatives then leads to the existence of boundary layer regions near  $z = 0$  and  $z = 1$ . Expansions for the azimuthal velocity  $V$  in the core

and the Ekman layers in the limit as  $T \rightarrow \infty$  are shown below.

$$\begin{array}{c} \hline z = 1 - \bar{z}T^{-\frac{1}{4}} \quad V = \bar{V}_0 + \dots \\ \hline V = V_0 + \dots \\ \hline z = \bar{z}T^{-\frac{1}{4}} \quad V = \bar{V}_0 + \dots \\ \hline \end{array}$$

In order to obtain the correct boundary conditions for the core region it is useful to first consider the problems arising in each Ekman layer. In the lower Ekman layer it is assumed that  $V = \bar{V}(\bar{z})$  in which case it follows from (5.3.13) and (5.3.14) that  $\bar{V}$  satisfies the equation

$$\bar{V}^{iv} + \bar{V}'' + 3T^{-\frac{1}{6}}\bar{\alpha}^2\bar{V}^{iv} + 3T^{-\frac{1}{3}}\bar{\alpha}^4\bar{V}'' + T^{-\frac{1}{2}}\bar{\alpha}^6\bar{V} = 0, \quad (5.3.17)$$

with boundary conditions

$$\bar{V} = \bar{V}'' = \bar{V}^v + \bar{V}' + 3T^{-\frac{1}{6}}\bar{\alpha}^2\bar{V}''' + 2T^{-\frac{1}{3}}\bar{\alpha}^4\bar{V}' = 0 \text{ on } \bar{z} = 0. \quad (5.3.18)$$

Integrating (5.3.17) once yields

$$\bar{V}^v + \bar{V}' + 3T^{-\frac{1}{6}}\bar{\alpha}^2\bar{V}''' + 3T^{-\frac{1}{3}}\bar{\alpha}^4\bar{V}' = O(T^{-\frac{1}{2}}) + d_1, \quad (5.3.19)$$

where  $d_1$  is a constant of integration. However, the third boundary condition at  $\bar{z} = 0$  implies that  $d_1 = O(T^{-1/3})$ , and therefore letting  $\bar{z} \rightarrow \infty$  in (5.3.19) implies that  $\bar{V}'(\infty) = O(T^{-1/3})$ . This implies that the leading order term in the expansion of the core solution must satisfy

$$V_0'(0) = 0. \quad (5.3.20)$$

A similar consideration of the problem in the upper boundary layer, where  $V = \tilde{V}(\tilde{z})$  implies that

$$\tilde{V}^v + \tilde{V}' + 3T^{-\frac{1}{6}}\bar{\alpha}^2\tilde{V}''' + 3T^{-\frac{1}{3}}\bar{\alpha}^4\tilde{V}' = O(T^{-\frac{1}{2}}) + d_2, \quad (5.3.21)$$

where  $d_2$  is a constant of integration and  $\tilde{V}$  satisfies the boundary conditions  $\tilde{V}' = \tilde{V}''' = \tilde{V}^v = 0$  on  $\tilde{z} = 0$ . These conditions imply that  $d_2 = O(T^{-1/2})$ , and thus, letting  $\tilde{z} \rightarrow \infty$  in (5.3.21) implies that,  $\tilde{V}'(\infty) = O(T^{-1/2})$ . This implies that the leading order term in the expansion of the core solution must satisfy

$$V_0'(1) = 0. \quad (5.3.22)$$

The leading order core equation

$$V_0'' = -\bar{\alpha}_0^6 V_0, \quad (5.3.23)$$

can now be solved with the boundary conditions  $V_0' = 0$  on  $z = 0, 1$  to give the eigenfunctions  $V_0 = \cos n\pi z$  and the eigenvalues

$$\bar{\alpha}_0 = (n\pi)^{\frac{1}{3}} \left( 1, \frac{1 \pm i\sqrt{3}}{2} \right), \quad n = 1, 2, \dots \quad (5.3.24)$$

Here only the eigenvalues with positive real part are selected, equivalent to solutions which decay into the core as required — those with negative real part are the eigenvalues for the other (cold) end. In fact it will be shown below that the leading eigenvalue actually corresponds to the solution (5.3.24) with  $n = 0$ . From (5.3.16) this is equivalent to a scaling of  $\alpha$  with  $T^{1/6}$  which is much smaller than  $T^{1/6}$  as  $T \rightarrow \infty$  and so a separate asymptotic analysis is required for this mode.

For the modes with  $n \geq 1$  the leading order solution in the lower Ekman layer can now also be found explicitly by solving

$$\bar{V}_0^{vi} + \bar{V}_0'' = 0, \quad (5.3.25)$$

subject to

$$\bar{V}_0 = \bar{V}_0'' = \bar{V}_0^v + \bar{V}_0' = 0 \text{ on } \bar{z} = 0, \quad (5.3.26)$$

and matching with the core which requires that  $\bar{V}_0 \rightarrow 1$  as  $\bar{z} \rightarrow \infty$ . This gives

$$\bar{V}_0 = \frac{1}{2} (2 - e^{\omega_1 \bar{z}} - e^{\omega_2 \bar{z}}), \quad (5.3.27)$$

where

$$\omega_{1,2} = \frac{-1 \pm i}{\sqrt{2}}. \quad (5.3.28)$$

There are no exponential terms in the leading order upper Ekman layer solution, which is simply  $\bar{V}_0 = (-1)^n$ . Thus there is effectively no upper Ekman layer at this order.

For  $n = 0$  the above theory predicts an eigenvalue  $\bar{\alpha}_0$  associated with a core eigenfunction  $V_0 = 1$  independent of  $z$ . For this special case it emerges that there is a solution for  $\alpha$  with positive real part as  $T \rightarrow \infty$  and that the asymptotic form (5.3.16) must be replaced by

$$\alpha = T^{\frac{1}{6}} \bar{\alpha}, \quad \bar{\alpha} = \bar{\alpha}_0 + \bar{\alpha}_1 T^{-\frac{1}{6}} + \dots, \quad T \rightarrow \infty \quad (5.3.29)$$

and that the azimuthal velocity,  $V$ , must be expanded in powers of  $T^{-1/4}$  in the core and in the two Ekman layers, as shown below.

$$\begin{array}{c} \hline z = 1 - \bar{z}T^{-\frac{1}{4}} \quad V = \bar{V}_0 + \bar{V}_1T^{-\frac{1}{4}} + \bar{V}_2T^{-\frac{1}{2}} + \dots \\ \hline V = V_0 + V_1T^{-\frac{1}{4}} + \dots \\ \hline z = \bar{z}T^{-\frac{1}{4}} \quad V = \bar{V}_0 + \bar{V}_1T^{-\frac{1}{4}} + \bar{V}_2T^{-\frac{1}{2}} + \dots \\ \hline \end{array}$$

It is again helpful to first consider general properties of the Ekman layers in order to identify the correct boundary conditions for the core. In the lower Ekman layer it is again assumed that  $V = \bar{V}(\bar{z})$ , in which case  $\bar{V}$  satisfies

$$\bar{V}^{iv} + \bar{V}'' + 3T^{-\frac{1}{4}}\bar{\alpha}^2\bar{V}^{iv} + 3T^{-\frac{1}{2}}\bar{\alpha}^4\bar{V}'' + T^{-\frac{3}{4}}\bar{\alpha}^6\bar{V} = 0, \quad (5.3.30)$$

with boundary conditions

$$\bar{V} = \bar{V}'' = \bar{V}^v + \bar{V}' + 3T^{-\frac{1}{4}}\bar{\alpha}^2\bar{V}''' + 2T^{-\frac{1}{2}}\bar{\alpha}^4\bar{V}' = 0 \text{ on } \bar{z} = 0. \quad (5.3.31)$$

Integrating (5.3.30) once yields

$$\bar{V}^v + \bar{V}' + 3T^{-\frac{1}{4}}\bar{\alpha}^2\bar{V}''' + 3T^{-\frac{1}{2}}\bar{\alpha}^4\bar{V}' = O(T^{-\frac{3}{4}}) + d_3, \quad (5.3.32)$$

where  $d_3$  is a constant of integration. The third boundary condition at  $\bar{z} = 0$  implies that

$$d_3 = \bar{\alpha}^4T^{-\frac{1}{2}}\bar{V}'(0) + O(T^{-\frac{3}{4}}), \quad (5.3.33)$$

and letting  $\bar{z} \rightarrow \infty$  in (5.3.32) it follows that to a first approximation as  $T \rightarrow \infty$ ,

$$\bar{V}'(\infty) = \bar{\alpha}_0^4T^{-\frac{1}{2}}\bar{V}'(0). \quad (5.3.34)$$

The leading order boundary layer problem for  $\bar{V}_0$  is the same as that for the case when  $n \geq 1$ , so that

$$\bar{V}_0 = \frac{1}{2}(2 - e^{\omega_1\bar{z}} - e^{\omega_2\bar{z}}), \quad \text{where } \omega_{1,2} = \frac{-1 \pm i}{\sqrt{2}}, \quad (5.3.35)$$

and since  $\bar{V}'_0(0) = \frac{1}{\sqrt{2}}$  it follows from (5.3.34) that to a first approximation

$$\bar{V}'(\infty) = \frac{\bar{\alpha}_0^4}{\sqrt{2}}T^{-\frac{1}{2}}. \quad (5.3.36)$$

Matching with the core solution then implies that the core boundary conditions for the first two terms in the core expansion are

$$V'_0(0) = 0 \quad \text{and} \quad V'_1(0) = \frac{\bar{\alpha}_0^4}{\sqrt{2}}, \quad (5.3.37)$$

In the upper Ekman layer where  $V = \tilde{V}(\tilde{z})$ , similar considerations lead to the results that

$$\tilde{V}^v + \tilde{V}' + 3T^{-\frac{1}{4}}\bar{\alpha}^2\tilde{V}''' + 3T^{-\frac{1}{2}}\bar{\alpha}^4\tilde{V}' = O(T^{-\frac{3}{4}}) + d_4, \quad (5.3.38)$$

where  $d_4$  is a constant of integration and  $\tilde{V}$  satisfies the boundary conditions  $\tilde{V}' = \tilde{V}''' = \tilde{V}^v = 0$  on  $\tilde{z} = 0$ . These conditions imply that  $d_4 = O(T^{-3/4})$ , and therefore letting  $\tilde{z} \rightarrow \infty$  in (5.3.38) it follows that  $\tilde{V}'(\infty) = O(T^{-3/4})$ . Thus, matching with the core solution as  $z \rightarrow 1$  implies that the leading two terms must satisfy the boundary conditions

$$V_0'(1) = V_1'(1) = 0. \quad (5.3.39)$$

As in the case where  $n \geq 1$ , there is effectively no upper Ekman layer at this level of approximation.

The leading order core problem is now to solve

$$V_0'' = 0, \quad (5.3.40)$$

with  $V_0' = 0$  on  $z = 0$  and 1. Assuming a suitable normalisation, this has the constant solution  $V_0 = 1$ .

The equation for the first order core function  $V_1$  is

$$V_1'' = -\bar{\alpha}_0^6 V_0, \quad (5.3.41)$$

and since  $V_0 = 1$ , this yields

$$V_1 = -\frac{\bar{\alpha}_0^6}{2}z^2 + d_5z + d_6, \quad (5.3.42)$$

where  $d_5$  and  $d_6$  are constants of integration. The constant  $d_6$  is equivalent to a normalisation of the solution and so can be taken as zero without loss of generality, and using  $V_1'(1) = 0$ , this gives

$$V_1 = \frac{\bar{\alpha}_0^6}{2}(2z - z^2). \quad (5.3.43)$$

Finally, from (5.3.37), it is required that  $V_1'(0) = \bar{\alpha}_0^4/\sqrt{2}$  which implies that non-zero solutions for  $\bar{\alpha}_0$  satisfy  $\bar{\alpha}_0^2 = 2^{-1/2}$ . Thus for the hot end zone the relevant solution is

$$\bar{\alpha}_0 = 2^{-\frac{1}{4}}, \quad (5.3.44)$$

and the negative root provides the corresponding solution for the cold end.

In the lower Ekman layer the first order solution for  $\bar{V}_1$  can now also be found by solving the equation

$$\bar{V}_1^{vi} + 3\bar{\alpha}_0^2 \bar{V}_0^{iv} + \bar{V}_1'' = 0, \quad (5.3.45)$$

subject to the boundary conditions  $\bar{V}_1 = \bar{V}_1'' = 0$  on  $\bar{z} = 0$  and  $\bar{V}_1' \rightarrow 0$  as  $\bar{z} \rightarrow \infty$  to give

$$\bar{V}_1 = -\frac{3\bar{\alpha}_0^2 i}{4} (e^{\omega_1 \bar{z}} - e^{\omega_2 \bar{z}}) + \frac{3}{8} \bar{\alpha}_0^2 \bar{z} \left( \frac{1}{\omega_1} e^{\omega_1 \bar{z}} + \frac{1}{\omega_2} e^{\omega_2 \bar{z}} \right). \quad (5.3.46)$$

The third boundary condition on  $\bar{z} = 0$ ,  $\bar{V}_1^v + 3\bar{\alpha}_0^2 \bar{V}_0''' + \bar{V}_1' = 0$ , is automatically satisfied in line with the general argument leading to (5.3.34).

In the upper Ekman layer the corresponding problem for  $\tilde{V}_1$  simplifies to

$$\tilde{V}_1^{vi} + \tilde{V}_1'' = 0, \quad (5.3.47)$$

which by matching with the core and using  $\tilde{V}_1' = \tilde{V}_1''' = 0$  on  $\tilde{z} = 0$  yields the simple solution  $\tilde{V}_1 = \bar{\alpha}_0^6/2$ , equivalent to the fact that at this level of approximation there is no variation across the upper Ekman layer.

These asymptotes are not shown explicitly with the numerically calculated curves shown in figure 5.1 as the numerical and asymptotic curves are indistinguishable at all but very small Taylor number.

## 5.4 General Rayleigh numbers

The eigenvalues  $\alpha$  are now traced out for fixed Taylor number and general Rayleigh numbers using the Runge-Kutta numerical scheme from the values found for  $R_1 = 0$  in section 5.3.2. In this regime the eigenvalues are dependent on the Prandtl number. However, following the findings of McIntyre (1968) and the results of chapter 2, which suggest that there is little variation with Prandtl number for  $\sigma > 1.5$ , the Prandtl number is taken to be infinite in this section.

Figures 5.2 and 5.3 show results for  $T = 500$  for the ‘real’ and ‘complex’ modes in the hot end region. The eigenvalues are referred to as ‘real’ and ‘complex’ by reference to their form at  $R_1 = 0$ , but as can be seen in figure 5.2, the ‘real’

azimuthal and thermal eigenvalues interact at certain values of  $R_1$  to become a single complex eigenvalue, the real part being given by a solid line and the imaginary part by a dotted line.

Plots of  $\alpha$  against  $R_1$  are given in figures 5.4 and 5.5 for  $T = 5000$ , and similar plots of ‘real’ and ‘complex’ eigenvalues against  $R_1$  for  $T = 500$  and  $T = 5000$  are given in figures 5.6–5.9 for the cold end.

In both hot and cold end zones, the ‘real’ eigenvalues appear to decrease in size with increasing Rayleigh number, but the increase in  $T$  causes this decrease to become less. (These results can be compared with those for  $T = 0$  and infinite Prandtl number in chapter 2.) As in the non-rotating case, the real part of the ‘complex’ modes increases with increasing Rayleigh number. The behaviour of the ‘complex’ modes with  $T$  is not as obvious as with the ‘real’ modes, but it appears that the value of the real part of  $\alpha$  at large  $R_1$  decreases with increasing  $T$ . This value is still a lot larger than the smallest ‘real’ eigenvalue, and it is suspected that the ‘complex’ modes only become dominant for small Prandtl number ( $\sigma < 1$ ), as in the non-rotating case, or possibly for general  $R_1$  and large  $T$ , but this is not investigated here.

The ‘real’ and ‘complex’ eigenvalues behave in a similar manner for both hot and cold end zones, especially the complex modes when  $T = 5000$ . At large  $R_1$ , the leading ‘real’ eigenvalue in the cold end is slightly smaller in size than the leading eigenvalue of the hot end, suggesting that the cold end extends further into the core than the hot end. This is investigated further in the next section.

## 5.5 Large Rayleigh numbers, $R_1 \gg 1$

The similarity in the results for the rotating and non-rotating ‘real’ modes suggests that, as in the non-rotating case, the ‘real’ eigenvalues may depend inversely on the Rayleigh number at large  $R_1$ .

For the rotating case with infinite Prandtl number the reduced problem equivalent to that of section 2.8.1 is obtained by setting  $\alpha = \alpha_0/R_1$  and letting  $R_1 \rightarrow \infty$

to obtain

$$\phi^{iv} + T^{\frac{1}{2}}V' - \alpha_0\Theta = 0, \quad (5.5.1)$$

$$V'' - T^{\frac{1}{2}}\phi' = 0, \quad (5.5.2)$$

$$\Theta'' - \phi' = \alpha_0(G''\Theta - G'\phi). \quad (5.5.3)$$

This system must satisfy the boundary conditions

$$\phi = \phi' = V = \Theta' = 0 \text{ on } z = 0, \quad (5.5.4)$$

$$\phi = \phi'' = V' = \Theta' = 0 \text{ on } z = 1, \quad (5.5.5)$$

and was solved numerically for general Taylor number, starting from the known results at  $T = 0$  found in chapter 2. Positive values of  $\alpha_0$  correspond to the hot end zone and negative values to the cold end zone; results for the two leading modes are given in figure 5.10. Although these curves are similar for the two end zones, the slightly smaller size of the cold end zone eigenvalue curves suggests that the cold end zone is of slightly larger lateral extent than the hot end zone for general  $T$ .

In many applications both the Rayleigh number and the speed of rotation are large and it is therefore of interest to consider the large  $T$  asymptotic behaviour of the solution of (5.5.1)–(5.5.3) as  $T \rightarrow \infty$ . As discussed below, it will be required that the Taylor number, although large, is smaller than the Rayleigh number as  $R_1 \rightarrow \infty$ . It is convenient to set  $G = T^{-1}\hat{G}(z; T)$  so that  $\hat{G}$  is finite as  $T \rightarrow \infty$ . In the core then, away from the horizontal Ekman layers,  $\hat{G}'(z) \sim 1$ . In the lower Ekman layer  $\hat{G}(z) \sim T^{-1/4}\bar{G}(\bar{z})$  with

$$\hat{G}'(z) \sim \bar{G}'(\bar{z}) = 1 - e^{-\frac{1}{\sqrt{2}}\bar{z}} \left( \cos \frac{1}{\sqrt{2}}\bar{z} + \sin \frac{1}{\sqrt{2}}\bar{z} \right), \quad (5.5.6)$$

$$T^{-\frac{1}{4}}\hat{G}''(z) \sim \bar{G}''(\bar{z}) = \sqrt{2}e^{-\frac{1}{\sqrt{2}}\bar{z}} \sin \frac{1}{\sqrt{2}}\bar{z}, \quad (5.5.7)$$

and in the upper Ekman layer,  $\hat{G}(z) \sim 1 - T^{-1/4}\tilde{G}(\tilde{z})$  with

$$\hat{G}'(z) \sim \tilde{G}'(\tilde{z}) = 1 - e^{-\frac{1}{\sqrt{2}}\tilde{z}} \cos \frac{1}{\sqrt{2}}\tilde{z}, \quad (5.5.8)$$

and

$$T^{-\frac{1}{4}}\hat{G}''(z) \sim -\tilde{G}''(\tilde{z}) = -\frac{1}{\sqrt{2}}e^{-\frac{1}{\sqrt{2}}\tilde{z}} \left( \cos \frac{1}{\sqrt{2}}\tilde{z} + \sin \frac{1}{\sqrt{2}}\tilde{z} \right). \quad (5.5.9)$$

Using  $\phi(1) = V'(1) = 0$ , integration of (5.5.2) yields

$$V' = T^{\frac{1}{2}}\phi \quad (5.5.10)$$

and so the reduced system (5.5.1)–(5.5.5) can be simplified to

$$\phi^{iv} + T\phi - \alpha_0\Theta = 0, \quad (5.5.11)$$

$$\Theta'' - \phi' = \alpha_0 T^{-1}(\bar{G}''\Theta - \bar{G}'\phi), \quad (5.5.12)$$

with boundary conditions

$$\phi = \phi' = \Theta' = 0 \text{ on } z = 0, \quad \text{and} \quad \phi = \phi'' = \Theta' = 0 \text{ on } z = 1. \quad (5.5.13)$$

Once  $\Theta$  and  $\phi$  are determined, the remaining boundary condition  $V(0) = 0$  is used when finding  $V$  from integration of (5.5.10).

For large  $T$ , it emerges that  $\alpha_0$  can be written in terms of an expansion in  $T$  as follows:

$$\alpha_0 = \alpha_1 T + \alpha_2 T^{\frac{3}{4}} + \dots, \quad (5.5.14)$$

Note that since the derivation of (5.5.1)–(5.5.3) requires  $\alpha$  to be small, it is necessary here that  $1 \ll T \ll R_1$  and a new behaviour would be expected to develop when  $T \geq R_1$ , consistent with the results for large  $T$  and finite  $R_1$  determined in sections 5.3.2 and 5.4. The eigenfunctions  $\phi$  and  $\theta$  are also expanded in terms of  $T$  in the core and the two Ekman layers as outlined below.

$z = 1 - \bar{z}T^{-\frac{1}{4}}$	$\phi = \bar{\phi}_0 + \bar{\phi}_1 T^{-\frac{1}{4}} + \dots$
	$\Theta = \bar{\Theta}_0 + \bar{\Theta}_1 T^{-\frac{1}{4}} + \dots$
	$\phi = \phi_0 + \phi_1 T^{-\frac{1}{4}} + \dots$
	$\Theta = \Theta_0 + \Theta_1 T^{-\frac{1}{4}} + \dots$
$z = \bar{z}T^{-\frac{1}{4}}$	$\phi = \bar{\phi}_0 + \bar{\phi}_1 T^{-\frac{1}{4}} + \dots$
	$\Theta = \bar{\Theta}_0 + \bar{\Theta}_1 T^{-\frac{1}{4}} + \dots$

These expansions are substituted into the reduced system (5.5.11)–(5.5.13) to yield a series of problems at each order of magnitude in  $T$ . The leading problems in the Ekman layers are solved first to find the correct boundary conditions for the core.

The leading order lower Ekman layer problem is

$$\bar{\Theta}_0'' = 0, \quad (5.5.15)$$

and using  $\bar{\Theta}'_0(0) = 0$ , this implies that  $\bar{\Theta}_0$  is a constant. Matching with the core implies that

$$\bar{\Theta}_0 = \Theta_0(0). \quad (5.5.16)$$

At first order the lower Ekman layer problem is

$$\bar{\Theta}''_1 - \bar{\phi}'_0 = \alpha_1 \bar{G}'' \bar{\Theta}_0, \quad (5.5.17)$$

which can be integrated to give

$$\bar{\Theta}'_1 = \bar{\phi}_0 + \alpha_1 \bar{G}' \bar{\Theta}_0, \quad (5.5.18)$$

where the condition  $\bar{\Theta}'_1(0) = 0$  has been used. As  $\bar{z} \rightarrow \infty$ , to match with the core solution, it is required that  $\bar{\Theta}'_1 \rightarrow \Theta'_0(0)$  and  $\bar{\phi}_0 \rightarrow \phi_0(0)$ , and hence (5.5.18) implies that

$$\Theta'_0(0) = \phi_0(0) + \alpha_1 \Theta_0(0). \quad (5.5.19)$$

A similar argument in the upper Ekman layer leads to the condition on the core solution that

$$\Theta'_0(1) = \phi_0(1) + \alpha_1 \Theta_0(1). \quad (5.5.20)$$

The leading order equations in the core are

$$\phi_0 - \alpha_1 \Theta_0 = 0, \quad (5.5.21)$$

$$\Theta''_0 - \phi'_0 = -\alpha_1 \phi_0. \quad (5.5.22)$$

These can be written as a single second order equation for  $\Theta_0$ ,

$$\Theta''_0 - \alpha_1 \Theta'_0 + \alpha_1^2 \Theta_0 = 0, \quad (5.5.23)$$

and using (5.5.21), the boundary conditions (5.5.19) and (5.5.20) become

$$\Theta'_0 - 2\alpha_1 \Theta_0 = 0 \text{ on } z = 0 \text{ and } z = 1. \quad (5.5.24)$$

The general solution of (5.5.23) is

$$\Theta_0 = e^{\frac{\alpha_1}{2}z} \left( A \sin \frac{\sqrt{3}}{2} \alpha_1 z + B \cos \frac{\sqrt{3}}{2} \alpha_1 z \right). \quad (5.5.25)$$

The condition at  $z = 0$  implies that  $A = \sqrt{3}B$ , and the condition at  $z = 1$  yields

$$\alpha_1 = \frac{2n\pi}{\sqrt{3}}, \quad (n \text{ integer.}) \quad (5.5.26)$$

Negative values of  $n$  correspond to the cold end zone and positive values to the hot end zone. The solution is normalised such that  $\phi_0(0) = 1$ , so that

$$\Theta_0 = \frac{1}{\alpha_1} e^{\frac{\alpha_1}{2} z} (\cos n\pi z + \sqrt{3} \sin n\pi z), \quad (5.5.27)$$

and

$$\phi_0 = e^{\frac{\alpha_1}{2} z} (\cos n\pi z + \sqrt{3} \sin n\pi z). \quad (5.5.28)$$

The leading order eigenfunction for the hot end ( $n = 1$ ) is plotted in figure 5.11. It can be noted then that  $\phi_0(\alpha_1, 1 - z) = e^{\alpha_1/2} (-1)^n \phi(-\alpha_1, z)$ ; ignoring the normalisation, the hot end eigenfunction is the upside-down image of the cold end eigenfunction. This suggests that towards the cold wall the flow at the top of the cavity slows down and the flow at the bottom speeds up. The area of greatest circulation thus appears to have moved down. The opposite is true near the hot wall: the area of greatest circulation appears to have moved up. This behaviour was shown numerically for  $R_1 = 3000$  and  $T = 0$  in figure 2.17 and discussed in section 2.10. The solution is dominated by thermal effects and at this level of approximation the asymmetry of the free surface has no effect on the form of the eigenfunction. Using (5.5.10) and  $V(0) = 0$ , the leading order term in the expansion for  $V$ ,

$$V = V_0 T^{1/2} + V_1 T^{1/4} + \dots, \quad (5.5.29)$$

is

$$V_0 = \frac{1}{\alpha_1} e^{\frac{\alpha_1}{2} z} (\sqrt{3} \sin n\pi z - \cos n\pi z) + \frac{1}{\alpha_1}. \quad (5.5.30)$$

The leading order Ekman layer solutions can now be completed. In the lower layer  $\bar{\Theta}_0 = 1/\alpha_1$  and  $\bar{\phi}_0$  satisfies

$$\bar{\phi}_0^{iv} + \bar{\phi}_0 - 1 = 0, \quad (5.5.31)$$

with  $\bar{\phi}_0 = \bar{\phi}_0' = 0$  on  $\bar{z} = 0$ , giving

$$\bar{\phi}_0 = 1 - e^{-\frac{1}{\sqrt{2}} \bar{z}} \left( \cos \frac{1}{\sqrt{2}} \bar{z} + \sin \frac{1}{\sqrt{2}} \bar{z} \right) = \bar{G}'. \quad (5.5.32)$$

In the upper layer  $\tilde{\Theta}_0 = e^{\alpha_1/2} (-1)^n / \alpha_1$  and  $\tilde{\phi}_0$  satisfies

$$\tilde{\phi}_0^{iv} + \tilde{\phi}_0 - (-1)^n e^{\frac{\alpha_1}{2}} = 0 \quad (5.5.33)$$

with  $\tilde{\phi}_0 = \tilde{\phi}_0'' = 0$  on  $\tilde{z} = 0$ , giving

$$(-1)^n e^{-\frac{\tilde{z}}{2}} \tilde{\phi}_0 = 1 - e^{-\frac{\tilde{z}}{\sqrt{2}}} \cos \frac{\tilde{z}}{\sqrt{2}} = \tilde{G}'. \quad (5.5.34)$$

The theory is now extended to determine the second term in the eigenvalue  $\alpha_0$  as  $T \rightarrow \infty$ . At first order in the lower Ekman layer, (5.5.18) gives

$$\bar{\Theta}'_1 = 2\bar{G}', \quad (5.5.35)$$

and one integration, together with matching to the core solution, implies that

$$\bar{\Theta}_1 = 2(\bar{z} + \sqrt{2}e^{-\frac{1}{\sqrt{2}}\bar{z}} \cos \frac{1}{\sqrt{2}}\bar{z}) + \Theta_1(0). \quad (5.5.36)$$

The first order stream function equation,

$$\bar{\phi}_1^{iv} + \bar{\phi}_1 - \alpha_1 \bar{\Theta}_1 - \alpha_2 \bar{\Theta}_0 = 0, \quad (5.5.37)$$

can then be solved to give

$$\begin{aligned} \bar{\phi}_1 = & e^{-\frac{1}{\sqrt{2}}\bar{z}}(d_1 \cos \frac{1}{\sqrt{2}}\bar{z} + d_2 \sin \frac{1}{\sqrt{2}}\bar{z}) \\ & + \frac{1}{2}\alpha_1 \bar{z} e^{-\frac{1}{\sqrt{2}}\bar{z}}(\cos \frac{1}{\sqrt{2}}\bar{z} + \sin \frac{1}{\sqrt{2}}\bar{z}) + 2\alpha_1 \bar{z} + \alpha_1 \Theta_1(0) + \frac{\alpha_2}{\alpha_1}, \end{aligned} \quad (5.5.38)$$

where the boundary conditions  $\bar{\phi}_1(0) = \bar{\phi}'_1(0) = 0$  imply that

$$d_1 = -\alpha_1 \Theta_1(0) - \frac{\alpha_2}{\alpha_1} \quad \text{and} \quad d_2 = d_1 - \frac{5}{2}\sqrt{2}\alpha_1. \quad (5.5.39)$$

In a similar fashion the first order equations in the upper Ekman layer,

$$\tilde{\Theta}'_1 = -\tilde{\phi}_0 - \alpha_1 \tilde{G}' \tilde{\Theta}_0, \quad (5.5.40)$$

$$\tilde{\phi}_1^{iv} + \tilde{\phi}_1 - \alpha_1 \tilde{\Theta}_1 - \alpha_2 \tilde{\Theta}_0 = 0, \quad (5.5.41)$$

have the solutions

$$\tilde{\Theta}_1 = -2(-1)^n e^{\frac{\alpha_1}{2}}(\tilde{z} + \frac{1}{\sqrt{2}}e^{-\frac{1}{\sqrt{2}}\tilde{z}}(\cos \frac{1}{\sqrt{2}}\tilde{z} - \sin \frac{1}{\sqrt{2}}\tilde{z})) + \Theta_1(1), \quad (5.5.42)$$

$$\begin{aligned} \tilde{\phi}_1 = & e^{-\frac{1}{\sqrt{2}}\tilde{z}}(\tilde{d}_1 \cos \frac{1}{\sqrt{2}}\tilde{z} + \tilde{d}_2 \sin \frac{1}{\sqrt{2}}\tilde{z}) \\ & - 2\alpha_1(-1)^n e^{\frac{\alpha_1}{2}}(\tilde{z} + \frac{1}{4}\tilde{z}e^{-\frac{1}{\sqrt{2}}\tilde{z}} \cos \frac{1}{\sqrt{2}}\tilde{z}) + \alpha_1 \Theta_1(1) + \frac{\alpha_2}{\alpha_1}(-1)^n e^{\frac{\alpha_1}{2}}, \end{aligned} \quad (5.5.43)$$

where the boundary conditions  $\tilde{\phi}(0) = \tilde{\phi}''(0) = 0$  imply that

$$\tilde{d}_1 = -\alpha_1 \Theta_1(1) - \frac{\alpha_2}{\alpha_1}(-1)^n e^{\frac{\alpha_1}{2}} \quad \text{and} \quad \tilde{d}_2 = -\frac{\alpha_1}{2}(-1)^n e^{\frac{\alpha_1}{2}} \quad (5.5.44)$$

At second order in the lower Ekman layer, the equation for  $\bar{\Theta}_2$  is

$$\bar{\Theta}_2'' - \bar{\phi}_1' = \alpha_1 \bar{G}'' \bar{\Theta}_1 + \alpha_2 \bar{G}'' \bar{\Theta}_0 - \alpha_1 \bar{G}' \bar{\phi}_0. \quad (5.5.45)$$

This is integrated with respect to  $\bar{z}$  to yield

$$\bar{\Theta}_2' - \bar{\phi}_1 - \alpha_2 \bar{G}' \bar{\Theta}_0 - \alpha_1 \bar{G}' \bar{\Theta}_1 = -\alpha_1 \int_0^{\bar{z}} \bar{G}' (\bar{\Theta}_1 + \bar{\phi}_0) d\bar{z}, \quad (5.5.46)$$

where the boundary condition  $\bar{\Theta}_2'(0) = 0$  has been applied. Noting that  $\bar{\Theta}_1'/2 = \bar{\phi}_0 = \bar{G}'$ , the integration on the right hand side can be carried out to obtain

$$\begin{aligned} -\alpha_1 \int_0^{\bar{z}} \bar{G}' (\bar{\Theta}_1 + \bar{\phi}_0) d\bar{z} = & \quad (5.5.47) \\ -3\alpha_1 \left( \bar{z} + 2\sqrt{2}e^{-\frac{1}{\sqrt{2}}\bar{z}} \cos \frac{1}{\sqrt{2}}\bar{z} - \frac{1}{2\sqrt{2}}e^{-\sqrt{2}\bar{z}}(2 + \cos \sqrt{2}\bar{z} + \sin \sqrt{2}\bar{z}) \right) + C. \end{aligned}$$

where

$$C = \frac{15\sqrt{2}\alpha_1}{4}. \quad (5.5.48)$$

From matching with the core as  $\bar{z} \rightarrow \infty$ , (5.5.46) gives the core boundary condition

$$\bar{\Theta}_1'(0) - \bar{\phi}_1(0) - \alpha_1 \bar{\Theta}_1(0) - \alpha_2 \bar{\Theta}_0(0) = C. \quad (5.5.49)$$

In the upper Ekman layer, there is a similar second order problem for  $\tilde{\Theta}_2$  that on integration with respect to  $\tilde{z}$  yields

$$\tilde{\Theta}_2' + \tilde{\phi}_1 + \alpha_2 \tilde{G}' \tilde{\phi}_0 + \alpha_1 \tilde{G}' \tilde{\Theta}_1 = \alpha_1 \int_0^{\tilde{z}} \tilde{G}' (\tilde{\Theta}_1' - \tilde{\phi}_0) d\tilde{z}, \quad (5.5.50)$$

where the boundary condition  $\tilde{\Theta}_2'(0) = 0$  has been applied. From the first order solution it can be noted that  $-\tilde{\Theta}_1'/2 = \tilde{\phi}_0 = e^{\alpha_1/2}(-1)^n \tilde{G}'$  and thus the integration on the right hand side can be completed, giving

$$\begin{aligned} \alpha_1 \int_0^{\tilde{z}} \tilde{G}' (\tilde{\Theta}_1' - \tilde{\phi}_0) d\tilde{z} = & \\ -3\alpha_1(-1)^n e^{\frac{\alpha_1}{2}} \left( \tilde{z} + \sqrt{2}e^{-\frac{1}{\sqrt{2}}\tilde{z}} \left( \cos \frac{1}{\sqrt{2}}\tilde{z} - \sin \frac{1}{\sqrt{2}}\tilde{z} \right) \right. & \\ \left. - \frac{\sqrt{2}}{8}e^{-\sqrt{2}\tilde{z}}(2 + \cos \sqrt{2}\tilde{z} - \sin \sqrt{2}\tilde{z}) \right) + \tilde{C}, & \quad (5.5.51) \end{aligned}$$

where

$$\tilde{C} = \frac{15\sqrt{2}\alpha_1}{8}(-1)^n e^{\frac{\alpha_1}{2}} = \frac{1}{2}C(-1)^n e^{\frac{\alpha_1}{2}}. \quad (5.5.52)$$

From matching with the core as  $\bar{z} \rightarrow \infty$ , (5.5.50) now gives the core boundary condition

$$\Theta_1'(1) - \phi_1(1) - \alpha_1\Theta_1(1) - \alpha_2\Theta_0(1) = -\frac{1}{2}C(-1)^n e^{\frac{\alpha_1}{2}}. \quad (5.5.53)$$

The second order core equations are

$$\phi_1 - \alpha_1\Theta_1 - \alpha_2\Theta_0 = 0, \quad (5.5.54)$$

$$\Theta_1'' - \phi_1' = -\alpha_1\phi_1 - \alpha_2\phi_0, \quad (5.5.55)$$

which reduce to a single second order equation for  $\Theta_1$ :

$$\Theta_1'' - \alpha_1\Theta_1' + \alpha_1^2\Theta_1 = \alpha_2\Theta_0' - 2\alpha_1\alpha_2\Theta_0, \quad (5.5.56)$$

to be solved subject to the boundary conditions (5.5.49) and (5.5.53). Equation (5.5.56) has general solution

$$\begin{aligned} \Theta_1 = e^{\frac{\alpha_1}{2}z} & \left( d_3 \cos \frac{\sqrt{3}}{2}\alpha_1 z + d_4 \sin \frac{\sqrt{3}}{2}\alpha_1 z \right) \\ & - \frac{\sqrt{3}\alpha_2}{2\alpha_1} z e^{\frac{\alpha_1}{2}z} \left( \sin \frac{\sqrt{3}}{2}\alpha_1 z - \sqrt{3} \cos \frac{\sqrt{3}}{2}\alpha_1 z \right). \end{aligned} \quad (5.5.57)$$

Substitution of  $\Theta_1$  into the two boundary conditions (5.5.49) and (5.5.53), use of (5.5.54) and subtraction of the two expressions leads to the result

$$\alpha_2 = \frac{1}{2}C = \frac{15\sqrt{2}\alpha_1}{8}. \quad (5.5.58)$$

The theory has now been completed to first order, giving the first two terms in the expansion of  $\alpha_0$  for large Taylor number as

$$\alpha_0 = \frac{2n\pi}{\sqrt{3}}T + \frac{15\sqrt{2}n\pi}{4\sqrt{3}}T^{\frac{3}{4}} + \dots, \quad (T \gg 1). \quad (5.5.59)$$

This result compares well with numerical results for  $\alpha_0$  obtained by solving the reduced problem (5.5.1)–(5.5.3) for large values of  $T$ , as shown by the plot of  $\alpha_0/T$  against  $\log(T)$  in figure 5.12. The difference between the hot and cold end eigenvalues caused by the free surface asymmetry and apparent in the numerical results of figure 5.10 is not evident in the two-term asymptotic expansion (5.5.59). The asymmetry is small and is expected to affect higher order terms in the expansion (5.5.59).

## 5.6 Discussion

In this chapter a combination of asymptotic and numerical methods has been used to investigate the lateral extent of the end zones for a range of Rayleigh numbers and Taylor numbers, with attention focused on the limit of large Prandtl number. At small Rayleigh numbers, the two end zones contain symmetric turning motions which contract towards the walls as the speed of rotation increases. At large  $T$ , the results of section 5.3.3 identify two length scales for the decay of the eigenfunctions into the core,  $x = O(T^{-1/6})$  and  $x = O(T^{-1/8})$ . These correspond to the two Stewartson layers described by Hunter (1967). The flow in these layers is described in more detail in the next chapter. The results show how the size of the end regions decrease with increasing Taylor number, the slowest decay being associated with the outer layer for which, from (5.3.44), the e-folding decay length is

$$x \sim 2^{\frac{1}{4}} T^{-\frac{1}{8}}, \quad T \rightarrow \infty. \quad (5.6.1)$$

The effect of rotation is generally opposite to the effect of increasing the Rayleigh number where the sizes of the end regions increase. In general the end regions are not symmetric, but for small rotation rates the results of chapter 2 indicate that their lateral scales are quite similar, with

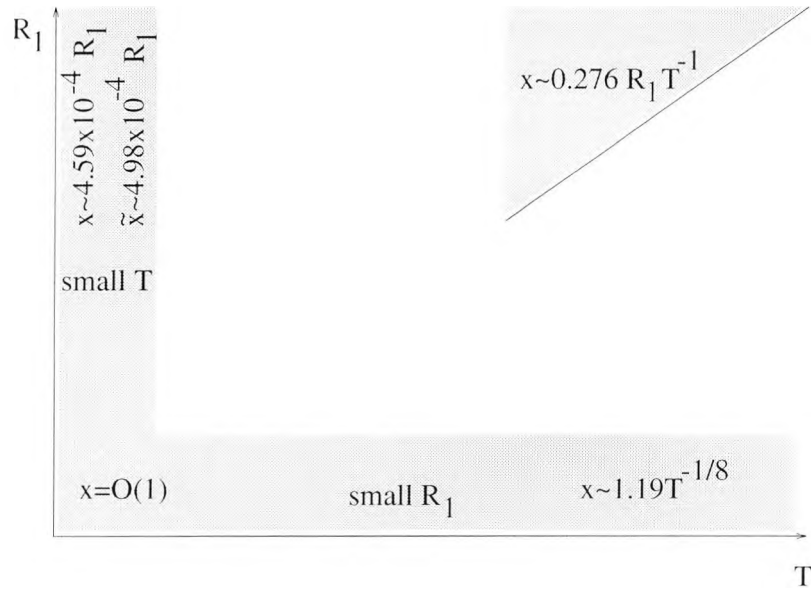
$$x \sim 4.59 \times 10^{-4} R_1 \text{ (cold)}, \quad \bar{x} \sim 4.98 \times 10^{-4} R_1 \text{ (hot)}, \quad R_1 \rightarrow \infty. \quad (5.6.2)$$

The effect on these long, order  $R_1$  scales of increasing the speed of rotation was examined in section 5.5 both numerically for general Taylor numbers and also in the limit as  $T \rightarrow \infty$ . This confirmed that the effect of rotation is to reduce the scale of decay so that for both end zones

$$x \sim \left( \frac{\sqrt{3}}{2\pi} \right) R_1 T^{-1} \quad (5.6.3)$$

when  $1 \ll T \ll R_1$ . For large rotation speeds, the end zone flows are centrosymmetric to a first approximation, except in the Ekman layers adjacent to the horizontal boundaries where the asymmetry caused by the free surface is significant. This means that the lateral scale of decay is the same at both ends to a first approximation as  $T \rightarrow \infty$ . The implication of (5.6.3) is that as  $T$  increases the decay scale is eventually reduced to order one values of  $x$ , possibly when  $T \sim R_1$ , and then to the even shorter scale (5.6.1) when  $T$  is much larger than  $R_1$ . Further study is

needed to fully investigate the transition from (5.6.3) to (5.6.1) at large values of  $T$ . It is believed that the Ekman boundary-layer structure is much more complicated in this case. The e-folding decay lengths of the end regions in the various regions of parameter space are summarised in the diagram below for the case of infinite Prandtl number.



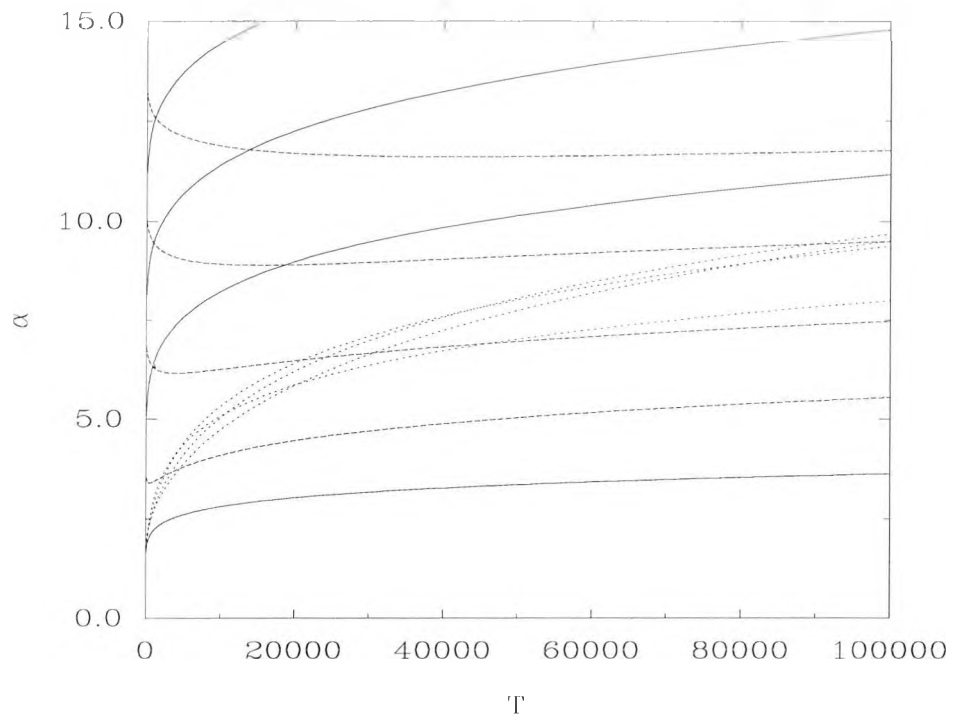


Figure 5.1: The real and complex eigenvalues  $\alpha$  for general  $T$  when  $R_1 = 0$ . The solid lines are the real modes; the dashed and dotted lines are the real and imaginary parts of the complex modes.

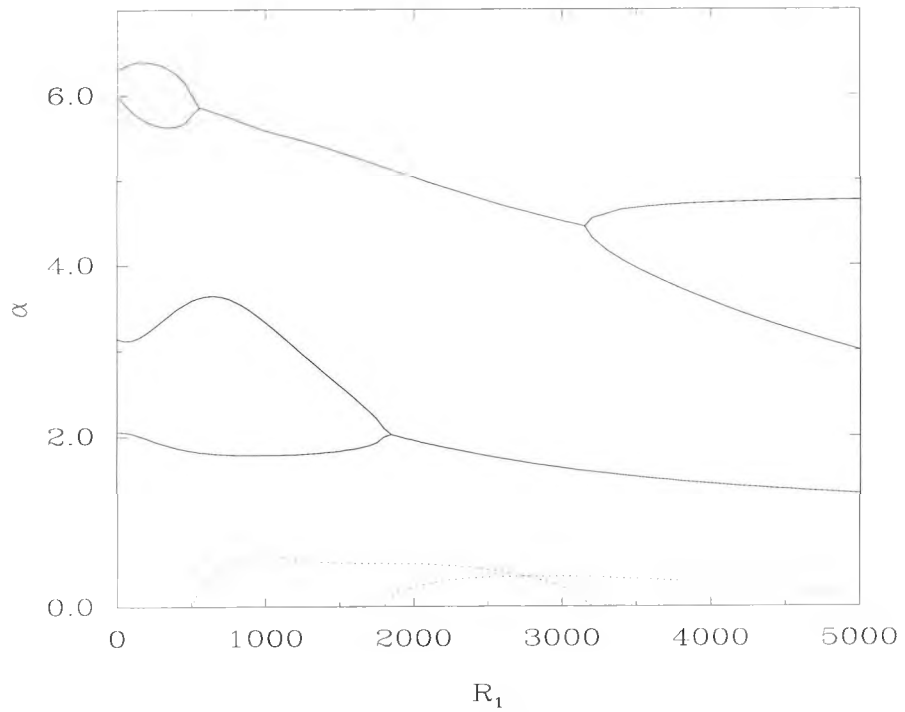


Figure 5.2: The ‘real’ eigenvalues  $\alpha$  for finite  $R_1$  when  $T = 500$  in the hot end zone. The solid lines are the real parts and the dotted lines are the imaginary parts.

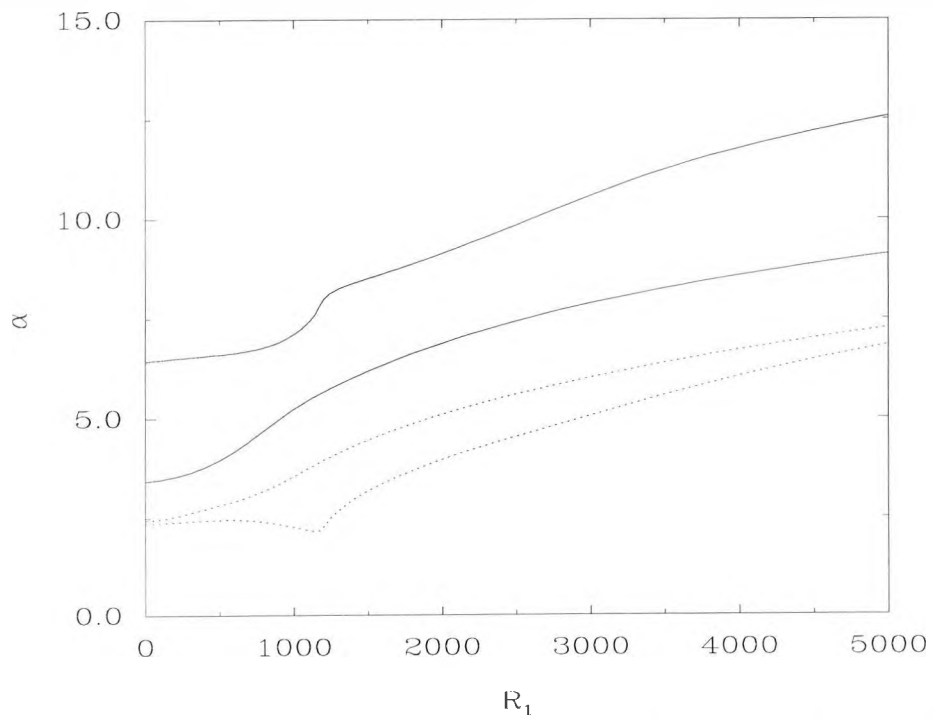


Figure 5.3: The ‘complex’ eigenvalues  $\alpha$  for finite  $R_1$  when  $T = 500$  in the hot end zone. The solid lines are the real parts and the dotted lines are the imaginary parts.

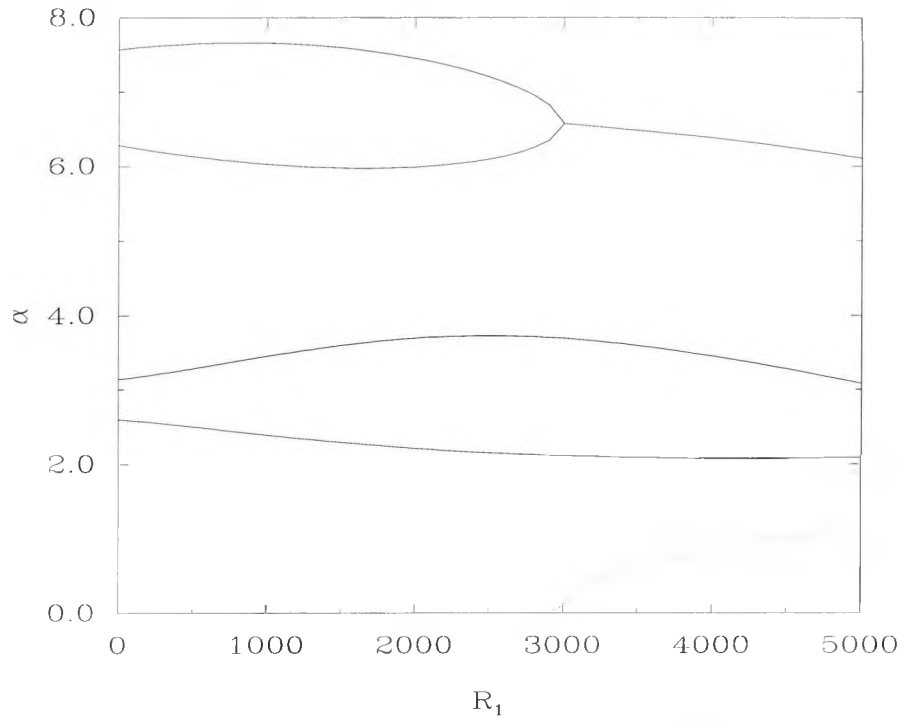


Figure 5.4: The ‘real’ eigenvalues  $\alpha$  for finite  $R_1$  when  $T = 5000$  in the hot end zone. The solid lines are the real parts and the dotted lines are the imaginary parts.

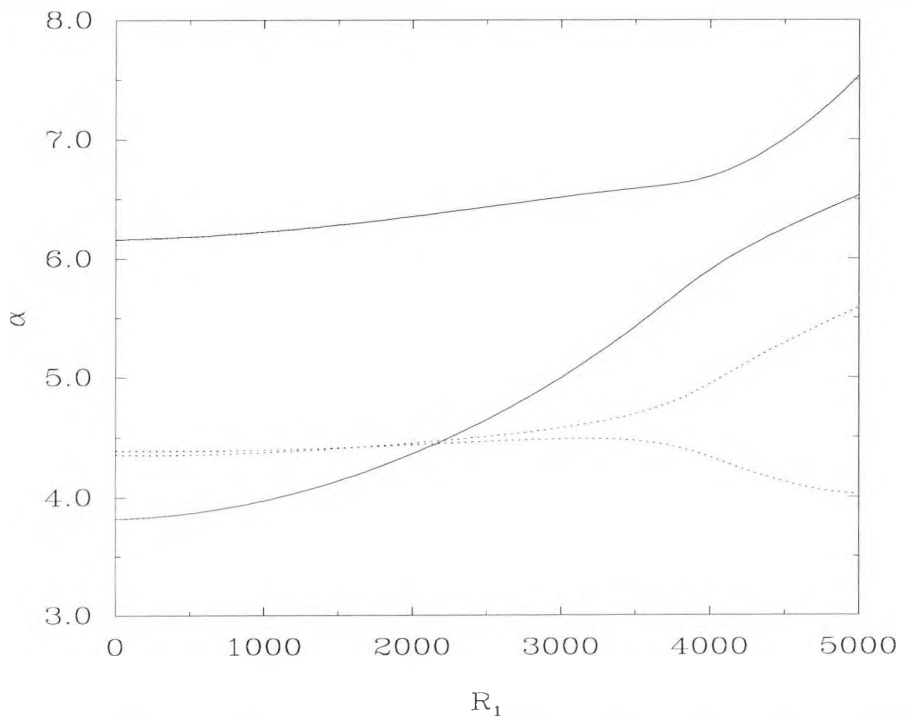


Figure 5.5: The ‘complex’ eigenvalues  $\alpha$  for finite  $R_1$  when  $T = 5000$  in the hot end zone. The solid lines are the real parts and the dotted lines are the imaginary parts.

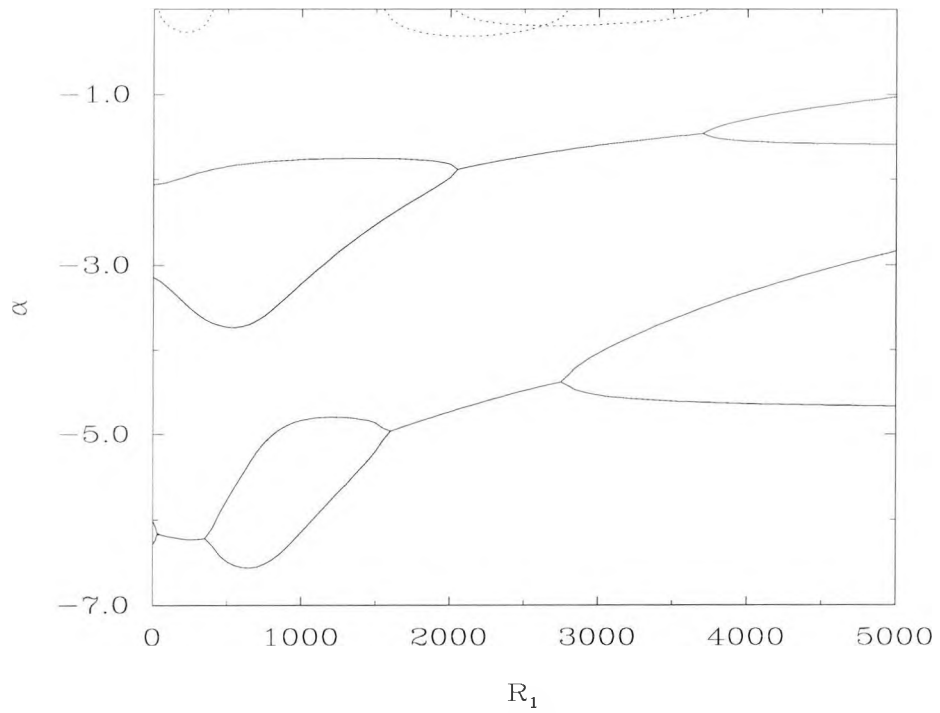


Figure 5.6: The ‘real’ eigenvalues  $\alpha$  for finite  $R_1$  when  $T = 500$  in the cold end zone. The solid lines are the real parts and the dotted lines are the imaginary parts.

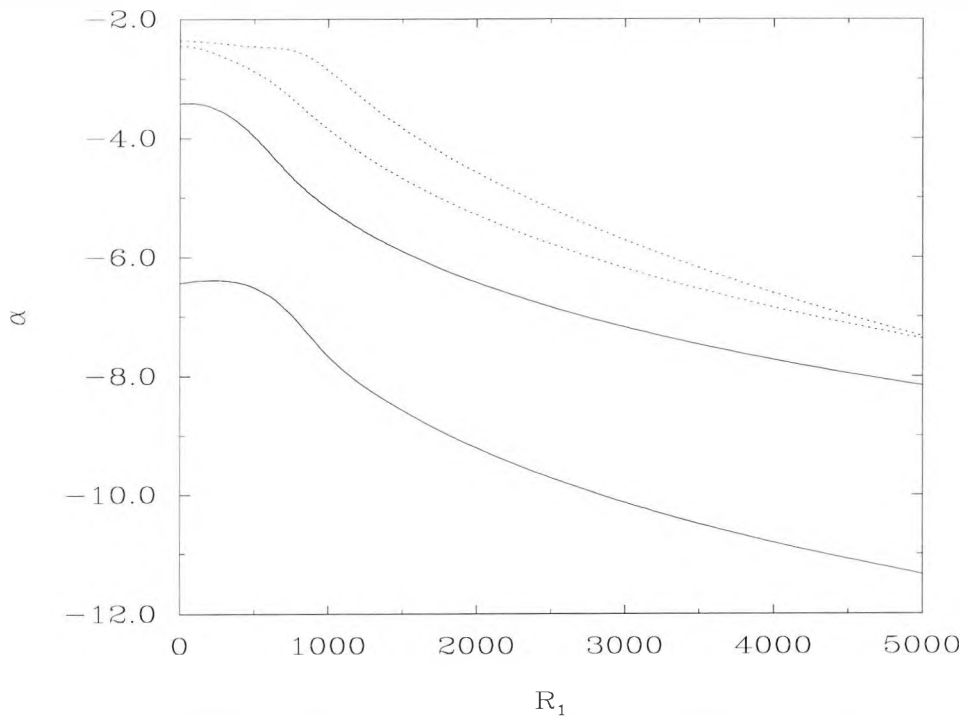


Figure 5.7: The ‘complex’ eigenvalues  $\alpha$  for finite  $R_1$  when  $T = 500$  in the cold end zone. The solid lines are the real parts and the dotted lines are the imaginary parts.

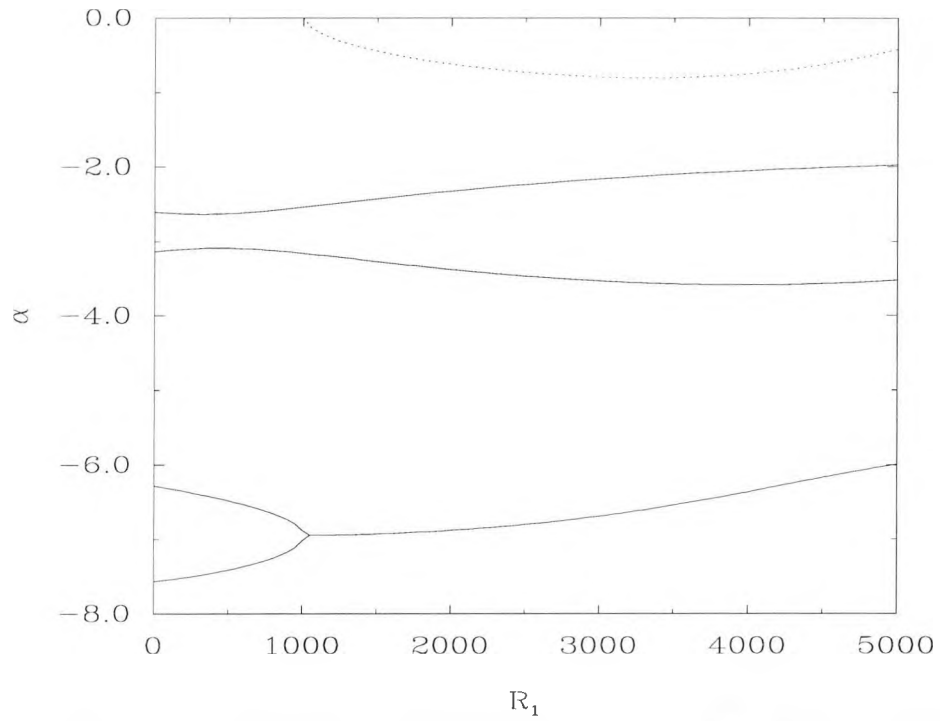


Figure 5.8: The ‘real’ eigenvalues  $\alpha$  for finite  $R_1$  when  $T = 5000$  in the cold end zone. The solid lines are the real parts and the dotted lines are the imaginary parts.

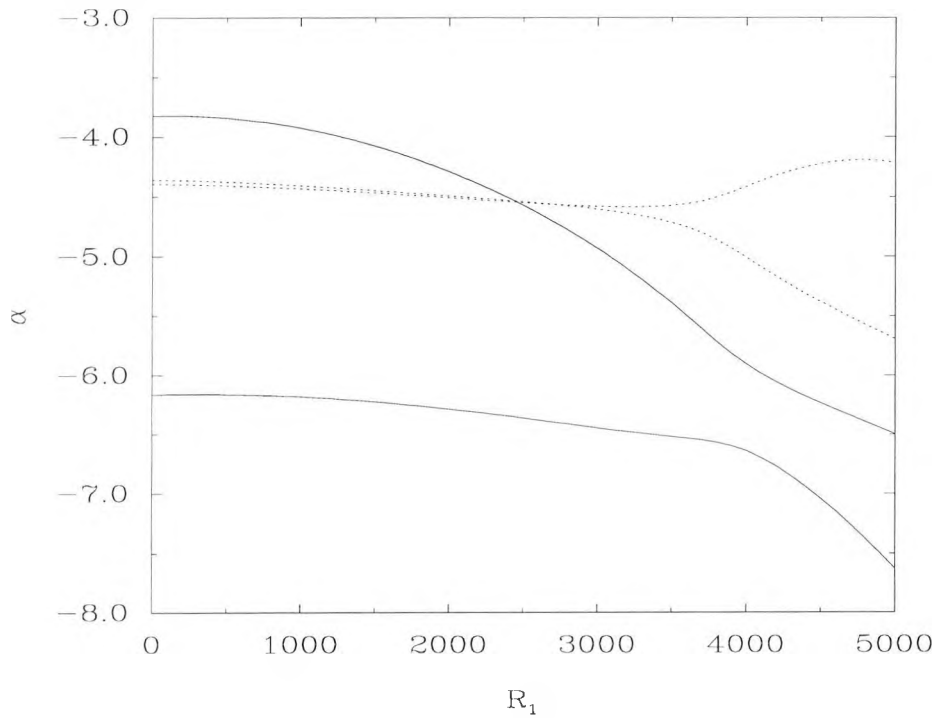


Figure 5.9: The ‘complex’ eigenvalues  $\alpha$  for finite  $R_1$  when  $T = 5000$  in the cold end zone. The solid lines are the real parts and the dotted lines are the imaginary parts.

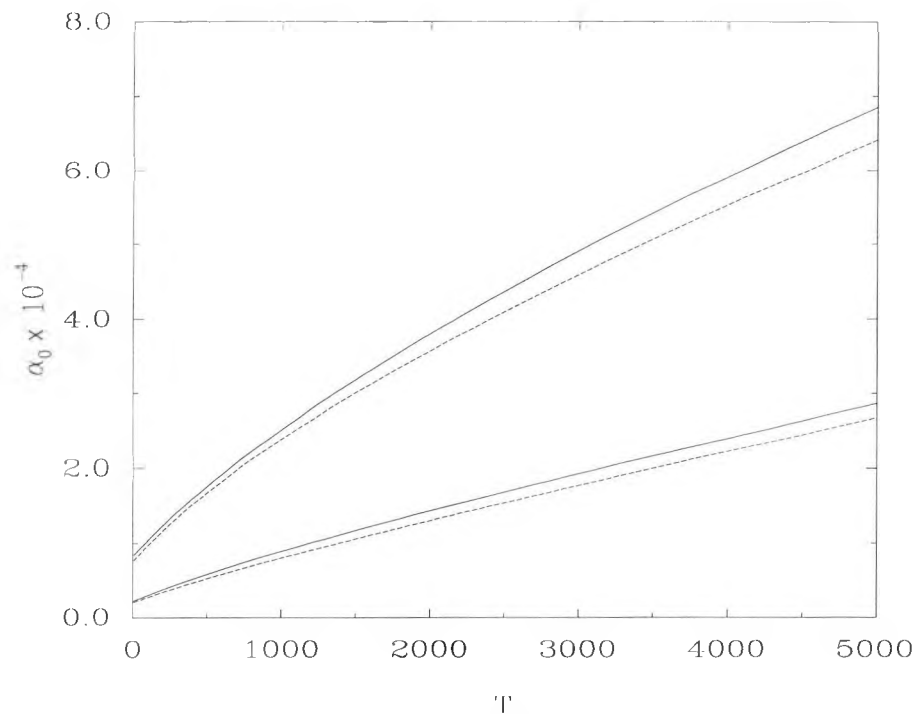


Figure 5.10: The leading real eigenvalue  $\alpha_0$  for general  $T$ . The solid line is the hot end zone eigenvalue and the dashed line is the (negative) cold end zone eigenvalue.

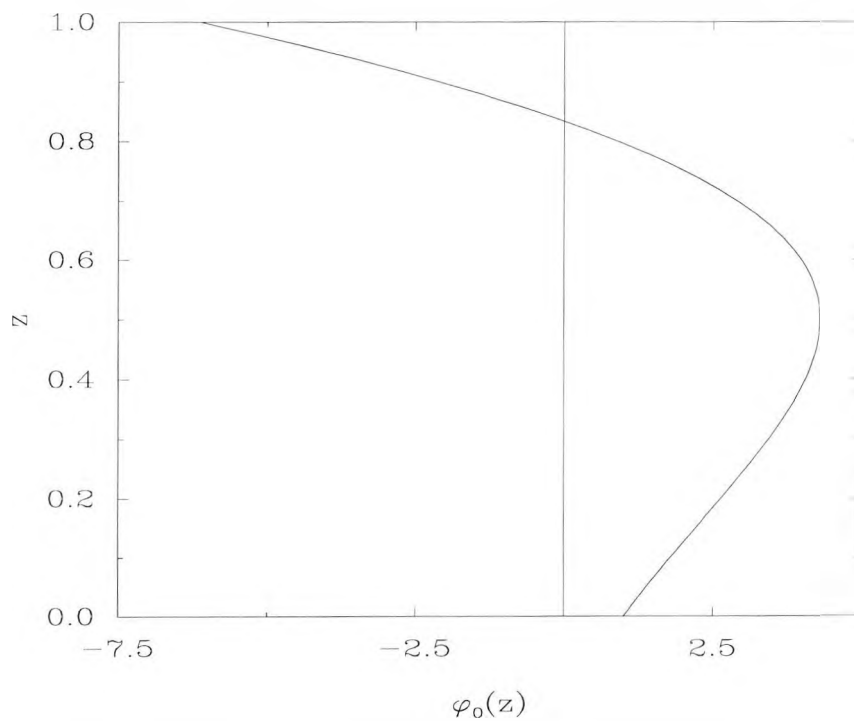


Figure 5.11: The leading order eigenfunction  $\phi_0$ , in the hot end. The cold end eigenfunction is the other way up.

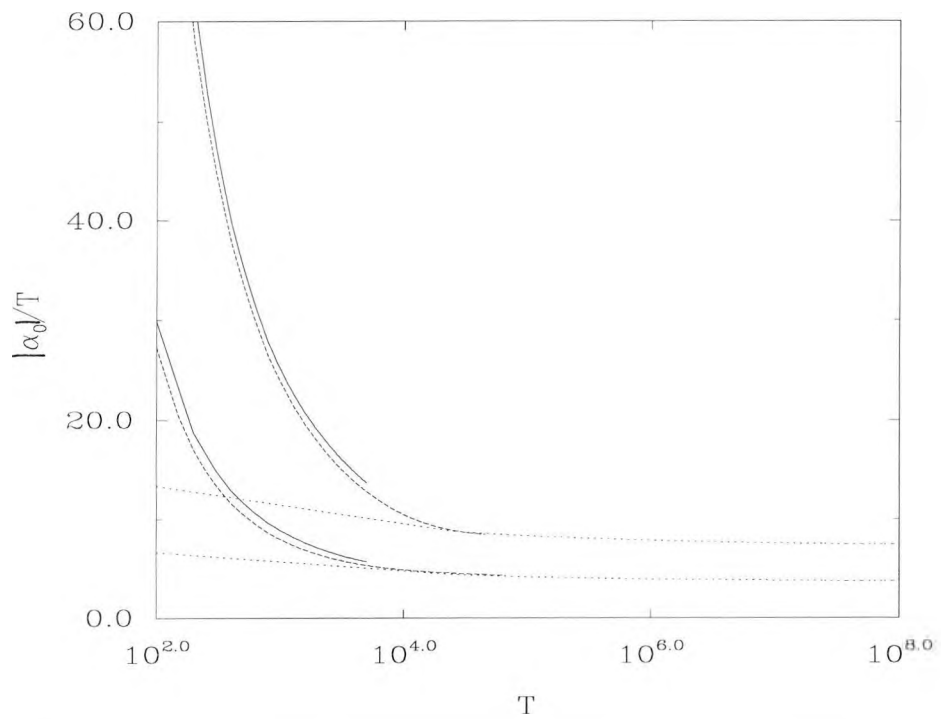


Figure 5.12: Values of  $|\alpha_0|/T$  for general  $T$ . The solid line is the hot end zone eigenvalue and the dashed line is the (negative) cold end zone eigenvalue. The dotted line is the large  $T$  asymptote.

# Chapter 6

## Solutions for the rotating end zones at low Rayleigh numbers

### 6.1 Introduction

The basic steady-state flow in the end regions at small Rayleigh numbers and general Taylor numbers is discussed in this chapter. A combined analytical and numerical method of solution based on the results of the Runge-Kutta scheme already obtained in chapter 5 and a numerical Fourier series routine, is presented in sections 6.2 and 6.3. This is used to determine the flow in the end regions of the cavity for finite Taylor numbers. The main results are presented graphically in section 6.4. The solution of the end region equations, both analytical and numerical, yield the constants  $c$  and  $\bar{c}$  which are needed to match with the core solution for a complete description of the flow in the cavity at leading order as  $R_1 \rightarrow 0$ .

Previous work, such as that by Hunter (1967), has described the large Taylor number structure of the flow in the cavity, consisting of horizontal Ekman layers and vertical Stewartson layers near the boundaries and free surface, already referred to in chapter 5. In section 6.6 it is shown that this large Taylor number structure emerges from the numerical solution of the problem presented in section 6.3 as  $T \rightarrow \infty$ . Likewise, in section 6.5, an analytical solution for small Taylor number is found which is consistent with the small Rayleigh number solution of chapter 2 for the non-rotating case.

The numerical and analytical results together provide a complete description of the transition from small to large Taylor number flow.

## 6.2 End region solution for small $R_1$ and general $T$

With the Taylor number of order one, the stream function, azimuthal velocity and temperature in the cold end are written as asymptotic expansions for small Rayleigh number as follows:

$$\psi = R_1\psi_0 + R_1^2\psi_1 + \dots, \quad (6.2.1)$$

$$v = R_1v_0 + R_1^2v_1 + \dots, \quad (6.2.2)$$

$$\theta = x + R_1\theta_1 + R_1^2\theta_2 + \dots \quad (6.2.3)$$

The leading term in the temperature field follows from the same argument as that used in the non-rotating case (section 2.9). These expansions are substituted into the governing equations (4.4.2)-(4.4.7) to yield a set of problems at each order of magnitude. Recalling that  $\theta \sim x + R_1G(z; T) + c$  as  $x \rightarrow \infty$ , the constant  $c$  is also expanded in terms of  $R_1$ , such that

$$c = R_1c_1 + R_1^2c_2 + \dots \quad (6.2.4)$$

At order  $R_1$ ,

$$\nabla^4\psi_0 = 1 - T^{\frac{1}{2}}v_{0z}, \quad (6.2.5)$$

$$\nabla^2v_0 = T^{\frac{1}{2}}\psi_{0z}, \quad (6.2.6)$$

$$\nabla^2\theta_1 = \psi_{0z}, \quad (6.2.7)$$

with boundary conditions,

$$\psi_0 = \psi_{0z} = v_0 = \theta_{1z} = 0 \text{ on } z = 0, \quad (6.2.8)$$

$$\psi_0 = \psi_{0zz} = v_{0z} = \theta_{1z} = 0 \text{ on } z = 1, \quad (6.2.9)$$

$$\psi_0 = \psi_{0x} = v_0 = \theta_1 = 0 \text{ on } x = 0, \quad (6.2.10)$$

and

$$\psi_0 \rightarrow G'(z; T), \quad v_0 \rightarrow G(z; T), \quad \theta_1 \rightarrow G(z; T) + c_1 \text{ as } x \rightarrow \infty. \quad (6.2.11)$$

The solution is clearly independent of the Prandtl number and is considered in detail in section 6.3. Although the problem is not completely solvable analytically, unlike the order  $R_1$  problem when  $T = 0$ , a hot-end/cold-end symmetry exists as in the  $T = 0$  case so that it is unnecessary to solve a separate problem at the hot end of the cavity where  $\tilde{\psi}$ ,  $\tilde{v}$  and  $\tilde{\theta}$  are expanded in the form

$$\tilde{\psi} = R_1 \tilde{\psi}_0 + R_1^2 \tilde{\psi}_1 + \dots, \quad (6.2.12)$$

$$\tilde{v} = R_1 \tilde{v}_0 + R_1^2 \tilde{v}_1 + \dots, \quad (6.2.13)$$

$$\tilde{\theta} = -\tilde{x} + R_1 \tilde{\theta}_1 + R_1^2 \tilde{\theta}_2 + \dots, \quad (6.2.14)$$

with

$$\tilde{c} = R_1 \tilde{c}_1 + R_1^2 \tilde{c}_2 + \dots. \quad (6.2.15)$$

Thus the solution for the hot end is

$$\tilde{\psi}_0(\tilde{x}, z) = \psi_0(\tilde{x}, z), \quad (6.2.16)$$

$$\tilde{v}_0(\tilde{x}, z) = v_0(\tilde{x}, z), \quad (6.2.17)$$

$$\tilde{\theta}_1(\tilde{x}, z) = \theta_1(\tilde{x}, z). \quad (6.2.18)$$

and

$$\tilde{c}_1 = c_1 \quad (6.2.19)$$

where  $\tilde{x} = L - x$ .

The constant  $c_1$  can be found as follows. Integration of (6.2.7) with respect to  $z$  yields

$$\int_0^1 \frac{\partial^2 \theta_1}{\partial x^2} dz + \left[ \frac{\partial \theta_1}{\partial z} \right]_0^1 = [\psi_0]_0^1, \quad (6.2.20)$$

which with the boundary conditions (6.2.8) and (6.2.9) becomes

$$\int_0^1 \frac{\partial^2 \theta_1}{\partial x^2} dz = 0. \quad (6.2.21)$$

This can be integrated twice with respect to  $x$ , using the conditions on  $\theta_1$  given in (6.2.10) and (6.2.11) to yield

$$c_1 = - \int_0^1 G(z; T) dz. \quad (6.2.22)$$

The core function  $G(z; T)$  is given analytically by (4.3.11) and it can be shown that

$$c_1 = \frac{1}{2\gamma^2 T} \tanh \gamma \tan \gamma - \frac{1}{2T} - \frac{D_2}{2\gamma} \left( 2\gamma - 1 - \tanh \gamma \tan \gamma - \frac{e^{-\gamma}(\sin \gamma - \cos \gamma)}{\cosh \gamma \cos \gamma} \right), \quad (6.2.23)$$

where  $D_2$  is as defined in (4.3.13). The solution for  $c_1$  is shown in figure 6.1. As described in chapter 4,  $G(z; T) = G(z; 0) + O(T)$  as  $T \rightarrow 0$  where  $G(z; 0)$  is the non-rotating core solution, the integral of which is known to be  $1/720$ . The order  $T$  term can also be determined so that as  $T \rightarrow 0$ ,

$$c_1 \sim -\frac{1}{720} + \frac{1}{22800}T + \dots \quad (6.2.24)$$

Also, it is known that as  $T \rightarrow \infty$ ,  $G(z, T) \sim zT^{-1}$ , and thus

$$c_1 \sim -\frac{1}{2}T^{-1} \text{ as } T \rightarrow \infty. \quad (6.2.25)$$

These asymptotic values of  $c_1$  are included in figure 6.1.

As shown earlier, the hot-end/cold-end symmetry means that  $\tilde{c}_1 = c_1$ , and so from (4.4.19),

$$A_1 = O(R_1^2) \quad \text{and} \quad B_1 = c_1 R_1 + O(R_1^2), \quad R_1 \rightarrow 0. \quad (6.2.26)$$

The constant  $B_1$  in (4.3.24) represents a correction to the core temperature field arising from convective effects and the presence of the end walls. The rapid increase in  $c_1$  with  $T$  shown in figure 6.1 implies that these effects are damped by rotation.

At order  $R_1^2$  the cold end problem for  $\psi_1$ ,  $v_1$  and  $\theta_2$  is to solve the equations

$$\nabla^4 \psi_1 - \frac{\partial \theta_1}{\partial x} + T^{\frac{1}{2}} \frac{\partial v_1}{\partial z} = \sigma^{-1} \frac{\partial(\nabla^2 \psi_0, \psi_0)}{\partial(x, z)}, \quad (6.2.27)$$

$$\nabla^2 v_1 - T^{\frac{1}{2}} \frac{\partial \psi_1}{\partial z} = \sigma^{-1} \frac{\partial(v_0, \psi_0)}{\partial(x, z)}, \quad (6.2.28)$$

$$\nabla^2 \theta_2 = \frac{\partial(\theta_1, \psi_0)}{\partial(x, z)} + \frac{\partial \psi_1}{\partial z}, \quad (6.2.29)$$

with boundary conditions

$$\psi_1 = \psi_{1z} = v_1 = \theta_{2z} = 0 \text{ on } z = 0, \quad (6.2.30)$$

$$\psi_1 = \psi_{1zz} = v_{1z} = \theta_{2z} = 0 \text{ on } z = 1, \quad (6.2.31)$$

$$\psi_1 = \psi_{1x} = v_1 = \theta_2 = 0 \text{ on } x = 0, \quad (6.2.32)$$

and

$$\psi_1 \rightarrow 0, \quad v_1 \rightarrow 0, \quad \theta_2 \rightarrow c_2 \text{ as } x \rightarrow \infty. \quad (6.2.33)$$

The velocity field can in principle be found first and then the temperature field is generated by convective effects in equation (6.2.29). The hot end solution then follows by antisymmetry, as in the equivalent non-rotating problem considered in section 2.9, so that here

$$\tilde{\psi}_1(\tilde{x}, z) = -\psi_1(\tilde{x}, z), \quad (6.2.34)$$

$$\tilde{v}_1(\tilde{x}, z) = -v_1(\tilde{x}, z), \quad (6.2.35)$$

$$\tilde{\theta}_2(\tilde{x}, z) = -\theta_2(\tilde{x}, z) \quad (6.2.36)$$

and

$$\tilde{c}_2 = -c_2. \quad (6.2.37)$$

Integration of (6.2.29) with respect to  $z$  yields

$$\int_0^1 \frac{\partial^2 \theta_2}{\partial x^2} dz + \left[ \frac{\partial \theta_2}{\partial z} \right]_0^1 = \int_0^1 \frac{\partial(\theta_1, \psi_0)}{\partial(x, z)} dz + [\psi_1]_0^1. \quad (6.2.38)$$

This can be simplified with the use of  $\psi_1 = \theta_{2z} = 0$  on  $z = 0$  and  $1$ , and integrated twice with respect to  $x$ , using (6.2.32) and (6.2.33) to give

$$c_2 = - \int_{x=0}^{\infty} \int_{x'=x}^{\infty} \int_{z=0}^1 \frac{\partial(\theta_1, \psi_0)}{\partial(x', z)} dz dx' dx. \quad (6.2.39)$$

Since  $\theta_1$  and  $\psi_0$  are independent of the Prandtl number, it follows that  $c_2$  is a function of  $T$  only and can be determined once the leading order end-zone solution is known. This solution is discussed in the next section.

### 6.3 Leading order end-zone solution for general $T$

The stream function, azimuthal velocity and temperature in the end region are written in terms of infinite sets of eigenfunctions that decay exponentially into the core. These are the eigenfunctions determined for small values of  $R_1$  and large values of  $x$  in section 5.3.2, but here, interpreted as solutions of the linear system (6.2.5)–(6.2.11), they are valid for general values of  $x$ . Thus the general solution in

the cold end zone can be written as

$$\psi_0 = G' + Re \left\{ \sum_{k=1}^{\infty} \mu_k \phi_k(z) e^{\alpha_k x} \right\} + \sum_{k=1}^{\infty} \bar{\mu}_k \bar{\phi}_k(z) e^{\bar{\alpha}_k x}, \quad (6.3.1)$$

$$v_0 = T^{\frac{1}{2}} G + Re \left\{ \sum_{k=1}^{\infty} \mu_k V_k(z) e^{\alpha_k x} \right\} + \sum_{k=1}^{\infty} \bar{\mu}_k \bar{V}_k(z) e^{\bar{\alpha}_k x}, \quad (6.3.2)$$

$$\theta_1 = G + Re \left\{ \sum_{k=1}^{\infty} \mu_k \Theta_k(z) e^{\alpha_k x} \right\} + \sum_{k=1}^{\infty} \bar{\mu}_k \bar{\Theta}_k(z) e^{\bar{\alpha}_k x} + \sum_{n=0}^{\infty} \eta_n \cos n\pi z e^{-n\pi x}, \quad (6.3.3)$$

where  $\mu_k$  ( $k = 1, 2, \dots$ ) are complex constants to be determined and  $\bar{\mu}_k$  and  $\eta_n$  are real constants to be determined. The complex 'stream function' modes are represented by the unbarred variables and from (6.2.5)–(6.2.7) are solutions of

$$\phi_k^{iv} + 2\alpha^2 \phi_k'' + \alpha^4 \phi_k + T^{\frac{1}{2}} V_k' = 0, \quad (6.3.4)$$

$$V_k'' + \alpha^2 V_k - T^{\frac{1}{2}} \phi_k' = 0, \quad (6.3.5)$$

$$\Theta_k'' + \alpha^2 \Theta_k - \phi_k' = 0, \quad (6.3.6)$$

with the usual boundary conditions at  $z = 0$  and  $z = 1$ . The real 'azimuthal velocity' modes are represented by the barred variables and are the real solutions of the same coupled system. It is evident that the stream function and azimuthal velocity are independent of the temperature, and that the complementary solution of (6.2.7) yields the thermal modes associated with  $\eta_n$ .

The eigenvalues and corresponding eigenfunctions are produced by the Runge-Kutta scheme in the manner already described in section 5.3.2. The eigenfunctions are normalised such that  $\phi_k'(1)$  has the same value (for all rotation speeds) as in the non-rotating case discussed in chapter 2. This allows the results obtained numerically at small  $T$  in this chapter to be compared with the results of chapter 2. The real variables are normalised such that  $\bar{\Theta}_k(1) = (-1)^{k-1}$  for all rotation speeds.

The constants  $\mu_k$ ,  $\bar{\mu}_k$  and  $\eta_n$ , are now found by considering the boundary conditions at  $x = 0$ . Since the velocity field is independent of the thermal field it is found first and then the thermal field is determined. The conditions  $v_0 = \psi_0 = \psi_{0,x} = 0$  on  $x = 0$  become

$$Re \left\{ \sum_{k=1}^{\infty} \mu_k V_k \right\} + \sum_{k=1}^{\infty} \bar{\mu}_k \bar{V}_k = -T^{\frac{1}{2}} G, \quad (6.3.7)$$

$$Re \left\{ \sum_{k=1}^{\infty} \mu_k \phi_k \right\} + \sum_{k=1}^{\infty} \bar{\mu}_k \bar{\phi}_k = -G', \quad (6.3.8)$$

$$Re \left\{ \sum_{k=1}^{\infty} \alpha_k \mu_k \phi_k \right\} + \sum_{k=1}^{\infty} \bar{\alpha}_k \bar{\mu}_k \bar{\phi}_k = 0. \quad (6.3.9)$$

These three conditions determine the constants  $\mu_k$  and  $\bar{\mu}_k$ . The functions  $V_k$ ,  $\bar{V}_k$ ,  $\phi_k$ ,  $\bar{\phi}_k$ ,  $G$  and  $G'$  are written as Fourier sine series

$$V_k = \sum_{n=1}^{\infty} d_{n,k} \sin \beta_n z, \quad \bar{V}_k = \sum_{n=1}^{\infty} \bar{d}_{n,k} \sin \beta_n z, \quad (6.3.10)$$

$$\phi_k = \sum_{n=1}^{\infty} f_{n,k} \sin n\pi z, \quad \bar{\phi}_k = \sum_{n=1}^{\infty} \bar{f}_{n,k} \sin n\pi z, \quad (6.3.11)$$

$$G = \sum_{n=1}^{\infty} e_n \sin \beta_n z \quad \text{and} \quad G' = \sum_{n=1}^{\infty} g_n \sin n\pi z, \quad (6.3.12)$$

where  $\beta_n = (2n-1)\pi/2$ . These representations are chosen taking into account as far as possible the behaviour of the azimuthal velocity and stream function near  $z = 0$  and  $z = 1$ . The Fourier coefficients are given by

$$d_{n,k} = 2 \int_0^1 V_k \sin \beta_n z \, dz, \quad \bar{d}_{n,k} = 2 \int_0^1 \bar{V}_k \sin \beta_n z \, dz, \quad (6.3.13)$$

$$f_{n,k} = 2 \int_0^1 \phi_k \sin n\pi z \, dz, \quad \bar{f}_{n,k} = 2 \int_0^1 \bar{\phi}_k \sin n\pi z \, dz, \quad (6.3.14)$$

$$e_n = \int_0^1 G \sin \beta_n z \, dz = \frac{1}{\beta_n^4 + T} \left( TD_2 + \frac{(-1)^n}{\beta_n^2} \right), \quad (6.3.15)$$

$$g_n = \int_0^1 G' \sin n\pi z \, dz = \frac{-2(n\pi)T}{(n\pi)^4 + T} \left( G'''(0; T) - \frac{1 - (-1)^n}{(n\pi)^2} \right). \quad (6.3.16)$$

Equations (6.3.7)–(6.3.9) now become

$$Re \left\{ \sum_{k=1}^{\infty} \mu_k \sum_{n=1}^{\infty} d_{n,k} \sin \beta_n z \right\} + \sum_{k=1}^{\infty} \bar{\mu}_k \sum_{n=1}^{\infty} \bar{d}_{n,k} \sin \beta_n z = -T^{\frac{1}{2}} \sum_{n=1}^{\infty} e_n \sin \beta_n z, \quad (6.3.17)$$

$$Re \left\{ \sum_{k=1}^{\infty} \mu_k \sum_{n=1}^{\infty} f_{n,k} \sin n\pi z \right\} + \sum_{k=1}^{\infty} \bar{\mu}_k \sum_{n=1}^{\infty} \bar{f}_{n,k} \sin n\pi z = -\sum_{n=1}^{\infty} g_n \sin n\pi z, \quad (6.3.18)$$

$$Re \left\{ \sum_{k=1}^{\infty} \alpha_k \mu_k \sum_{n=1}^{\infty} f_{n,k} \sin n\pi z \right\} + \sum_{k=1}^{\infty} \bar{\alpha}_k \bar{\mu}_k \sum_{n=1}^{\infty} \bar{f}_{n,k} \sin n\pi z = 0, \quad (6.3.19)$$

and comparing coefficients of  $\sin \beta_n z$  in (6.3.17) and  $\sin n\pi z$  in (6.3.18) and (6.3.19) leads to the triply infinite linear system

$$Re \left\{ \sum_{k=1}^{\infty} \mu_k d_{n,k} \right\} + \sum_{k=1}^{\infty} \bar{\mu}_k \bar{d}_{n,k} = -T^{\frac{1}{2}} e_n, \quad (6.3.20)$$

$$Re \left\{ \sum_{k=1}^{\infty} \mu_k f_{n,k} \right\} + \sum_{k=1}^{\infty} \bar{\mu}_k \bar{f}_{n,k} = -g_n, \quad (6.3.21)$$

$$Re \left\{ \sum_{k=1}^{\infty} \alpha_k \mu_k f_{n,k} \right\} + \sum_{k=1}^{\infty} \bar{\alpha}_k \bar{\mu}_k \bar{f}_{n,k} = 0, \quad (6.3.22)$$

for the unknowns  $\mu_{k_r}$ ,  $\mu_{k_i}$  and  $\bar{\mu}_k$  ( $k = 1, 2, \dots$ ) where  $\mu_k = \mu_{k_r} + i\mu_{k_i}$ . This can be written in matrix form as

$$\begin{pmatrix} d_{1,1_r} & -d_{1,1_i} & \bar{d}_{1,1} & d_{1,2_r} & \dots \\ f_{1,1_r} & -f_{1,1_i} & \bar{f}_{1,1} & f_{1,2_r} & \dots \\ (\alpha_{1_r} f_{1,1_r} - \alpha_{1_i} f_{1,1_i}) & -(\alpha_{1_r} f_{1,1_i} + \alpha_{1_i} f_{1,1_r}) & \bar{\alpha}_{1_r} \bar{f}_{1,1} & (\alpha_{2_r} f_{1,2_r} - \alpha_{2_i} f_{1,2_i}) & \dots \\ d_{2,1_r} & -d_{2,1_i} & \bar{d}_{2,1} & d_{2,2_r} & \dots \\ f_{2,1_r} & -f_{2,1_i} & \bar{f}_{2,1} & f_{2,2_r} & \dots \\ (\alpha_{1_r} f_{2,1_r} - \alpha_{1_i} f_{2,1_i}) & -(\alpha_{1_r} f_{2,1_i} + \alpha_{1_i} f_{2,1_r}) & \bar{\alpha}_{1_r} \bar{f}_{2,1} & (\alpha_{2_r} f_{2,2_r} - \alpha_{2_i} f_{2,2_i}) & \dots \\ \vdots & & & & \end{pmatrix} \begin{pmatrix} \mu_{1_r} \\ \mu_{1_i} \\ \bar{\mu}_1 \\ \mu_{2_r} \\ \mu_{2_i} \\ \bar{\mu}_2 \\ \vdots \end{pmatrix} = \begin{pmatrix} -T^{\frac{1}{2}} e_1 \\ -g_1 \\ 0 \\ -T^{\frac{1}{2}} e_2 \\ -g_2 \\ 0 \\ \vdots \end{pmatrix}$$

This was solved to find the constants  $\mu_k$  and  $\bar{\mu}_k$  using Gaussian elimination with partial pivoting, truncating the infinite series at  $k = 4, 6$  and  $8$ . Results for  $k = 4$  were found to give the first two modes accurately to three significant figures and the next two modes accurate to two significant figures by comparing with the results for  $k = 6$  and  $k = 8$ .

The remaining constants  $\eta_n$  can now be determined as follows. The functions  $G$ ,  $\Theta$  and  $\bar{\Theta}$  are expressed as Fourier cosine series

$$G = \sum_{n=0}^{\infty} a_n \cos n\pi z, \quad (6.3.23)$$

$$\bar{\Theta}_k = \sum_{n=0}^{\infty} \bar{b}_{n,k} \cos n\pi z, \quad \text{and} \quad \Theta_k = \sum_{n=0}^{\infty} b_{n,k} \cos n\pi z. \quad (6.3.24)$$

Both  $b_{0,k}$  and  $\bar{b}_{0,k}$  can be shown to be zero by integrating the leading order eigenvalue problem (6.3.5) to give

$$[\Theta'_k]_0^1 + \alpha^2 \int_0^1 \Theta_k dz = [\phi_k]_0^1, \quad (6.3.25)$$

which, using  $\phi_k = \Theta'_k = 0$  on  $z = 0$  and  $1$ , yields

$$\int_0^1 \Theta_k dz = 0. \quad (6.3.26)$$

The constant terms in (6.3.3) thus give

$$a_0 + \eta_0 = 0 \quad (6.3.27)$$

where  $a_0 = \int_0^1 G dz$ , and therefore  $\eta_0$  is equivalent to  $c_1$ , as may be expected by comparing (6.3.3) and the core solution.

Substituting (6.3.23) and (6.3.24) into (6.3.3) and comparing coefficients of  $\cos n\pi z$  yields

$$\eta_n = -a_n - \operatorname{Re} \left\{ \sum_{k=1}^{\infty} \mu_k b_{n,k} \right\} - \sum_{k=1}^{\infty} \bar{\mu}_k \bar{b}_{n,k}, \quad n > 1 \quad (6.3.28)$$

where from (6.3.24),

$$\bar{b}_{n,k} = 2 \int_0^1 \bar{\Theta}_k \cos n\pi z \, dz \quad \text{and} \quad b_{n,k} = 2 \int_0^1 \Theta_k \cos n\pi z \, dz, \quad (6.3.29)$$

and from (6.3.23),

$$a_n = \int_0^1 G \cos n\pi z \, dz = \frac{2}{(n\pi)^2 + T} \left( G'''(0; T) - \frac{1 - (-1)^n}{(n\pi)^2} \right). \quad (6.3.30)$$

Thus formula (6.3.28) enables the coefficients  $\eta_n$  to be determined.

## 6.4 Numerical results

In order to check that the numerical scheme was working properly, the values of the constants  $\mu_k$  and  $\bar{\mu}_k$  were found for  $T = 1$ . These values agreed well with the results at  $T = 0$  of section 2.9 and the small  $T$  results of section 6.5 given below. As would be expected from the non-rotating work of chapter 2 where there is no azimuthal velocity, for small  $T$  the stream function modes  $\phi_k$  and the azimuthal velocity modes  $V_k$  become small compared to  $\psi_k$  and  $\bar{V}_k$  respectively.

Computations were carried out for values of  $T$  up to 5000 and results for  $T = 100, 2000,$  and  $5000$  are shown in figures 6.2–6.7. Streamlines for  $T = 100$  are shown in figure 6.2, and the corresponding lines of constant azimuthal velocity are given in figure 6.3. The streamline pattern is similar to that obtained for small Rayleigh number and  $T = 0$  in chapter 2 (figure 2.15), except for a small region of recirculation just above the mid-height of the cavity. The azimuthal velocity is unidirectional, with  $v_0 > 0$  so that the flow is in the direction of rotation.

For  $T = 2000$ , the recirculation is more obvious, as can be seen in figure 6.4, and is centred at a point closer to the vertical wall. The azimuthal velocity contours shown in figure 6.5 now indicate an area of reverse azimuthal flow near the bottom of the cavity.

In the results shown in figures 6.6 and 6.7 for  $T = 5000$  the region of recirculation has now moved even closer to the vertical wall, and there is evidence of the formation of the Ekman layers near the horizontal boundaries. The greatest changes in the azimuthal velocity are now close to the vertical wall, and the reverse flow at the bottom of the cavity is clear, although its precise form is subject to the limitations of the Fourier series representation which become more severe as the Taylor number increases and the Ekman layers develop.

The solutions for  $\psi_0$  and  $\theta_0$  allow the integration (6.2.39) to be completed numerically to find the values of the constant  $c_2$  for fixed values of  $T$ . The result for  $T = 0$  in section 2.9 acts as a way of checking the integration routine, which was based on Simpson's rule with intervals of  $10^{-2}$  in  $x$  and  $z$ . The results of this integration for finite values of  $T$  are plotted in figure 6.8. The overall trend is for  $c_2$  to decrease with increasing rotation although the curve is not monotonic. Some of the points approaching the small maximum value of  $c_2$  could not be obtained accurately and are not shown, although it is not understood why the scheme did not converge well in this region. The minimum at slightly smaller Taylor number is at a similar value of  $T$  to the maximum of the azimuthal free surface velocity shown in figure 4.3. Comparing the two figures (4.3 and 6.8) suggests that for  $T < 1000$  the behaviour of  $c_2$  may be related to this behaviour of  $v$ , although a physical interpretation of why this may be is not obvious.

The hot-end/cold-end antisymmetry described in section 6.2 above means that in the hot end  $\bar{c}_2 = -c_2$  and thus from (4.4.19),

$$A_1 = -2c_2R_1^2 + \dots \quad \text{and} \quad B_1 = c_1R_1 + c_2R_1^2 + \dots \quad (6.4.1)$$

The constant  $A_1$  determines the first order correction as  $L \rightarrow \infty$  to the horizontal and azimuthal velocity components and the horizontal thermal gradient in the core due to the presence of the end walls (see equation 4.3.24). Thus it appears that the importance of this correction term, which as  $c_2$  is negative represents a reduction in these quantities, diminishes with increasing rotation rate.

## 6.5 Leading order end zone solution for small T

For small Taylor numbers  $G(z; T) \rightarrow G(z; 0)$  and the eigenvalue appearing in (6.3.1)–(6.3.3) have the limiting forms

$$\alpha_k \rightarrow \alpha_{k0}, \quad \bar{\alpha}_k \rightarrow \bar{\alpha}_{k0}, \quad T \rightarrow 0 \quad (6.5.1)$$

where  $\alpha_{k0}$  are the complex roots of  $\sin 2\alpha_{k0} = 2\alpha_{k0}$ . The corresponding eigenfunctions have the limiting forms

$$\left. \begin{aligned} \phi_k &\rightarrow \phi_{k0}, & \bar{\phi}_k &\rightarrow 0, \\ V_k &\sim T^{\frac{1}{2}} V_{k0}, & \bar{V}_k &\sim T^{\frac{1}{2}} \bar{V}_{k0}, \\ \Theta_k &\rightarrow \Theta_{k0}, & \bar{\Theta}_k &\rightarrow 0, \end{aligned} \right\} T \rightarrow 0 \quad (6.5.2)$$

where

$$\phi_{k0} = \sin \alpha_{k0} z - \alpha_{k0} z \cos \alpha_{k0} z - \alpha_{k0} z \tan \alpha_{k0} \sin \alpha_{k0} z, \quad (6.5.3)$$

$$\begin{aligned} \Theta_{k0} &= \frac{-1}{4\alpha_{k0}} \tan \alpha_{k0} \sin \alpha_{k0} z - \frac{\tan \alpha_{k0}}{2} \cos \alpha_{k0} z + \frac{1}{4} z \sin \alpha_{k0} z \\ &+ \frac{1}{4} z \tan \alpha_{k0} \cos \alpha_{k0} z - \frac{\alpha_{k0} \tan \alpha_{k0}}{4} z^2 \sin \alpha_{k0} z - \frac{\alpha_{k0}}{4} z^2 \cos \alpha_{k0} z \end{aligned} \quad (6.5.4)$$

are the non-rotating forms determined in section 2.9; the streamlines and isotherms associated with the limiting forms of  $\psi_0$  and  $\Theta_0$  as  $T \rightarrow 0$  are the ones displayed in figures 2.15 and 2.16. The corresponding azimuthal velocity functions  $V_{k0}$  and  $\bar{V}_{k0}$  are the solutions of the appropriate limiting forms of (4.4.3), namely

$$V_{k0}'' + \alpha_{k0}^2 V_{k0} = \phi_{k0}', \quad (6.5.5)$$

$$\bar{V}_{k0} + \bar{\alpha}_{k0}^2 \bar{V}_{k0} = 0, \quad (6.5.6)$$

which satisfy the boundary conditions  $V_{k0} = \bar{V}_{k0} = 0$  at  $z = 0$  and  $V_{k0}' = \bar{V}_{k0}' = 0$  at  $z = 1$ . Thus

$$\begin{aligned} V_{k0} &= \frac{1}{4} (\tan^2 \alpha_{k0} - 1) + \frac{1}{4} z \sin \alpha_{k0} z \\ &+ \frac{1}{4} z \tan \alpha_{k0} \cos \alpha_{k0} z - \frac{\alpha_{k0}}{4} z^2 \tan \alpha_{k0} \sin \alpha_{k0} z - \frac{\alpha_{k0}}{4} z^2 \cos \alpha_{k0} z. \end{aligned} \quad (6.5.7)$$

and

$$\bar{V}_{k0} = \sin \left( \frac{2k-1}{2} \right) \pi z \quad (6.5.8)$$

with

$$\bar{\alpha}_{k0} = \left( \frac{2k-1}{2} \right) \pi, \quad k = 1, 2, \dots \quad (6.5.9)$$

The overall azimuthal velocity as  $T \rightarrow 0$  is given from (4.4.3) by

$$v_0 \sim T^{\frac{1}{2}} \left\{ G(z; 0) + Re \sum_{k=1}^{\infty} \mu_{k0} V_{k0} e^{\alpha_{k0} x} + \sum_{k=1}^{\infty} \bar{\mu}_{k0} \bar{V}_{k0} e^{\bar{\alpha}_{k0} x} \right\}. \quad (6.5.10)$$

The limiting forms  $\mu_{k0}$  of the coefficients  $\mu_k$  as  $T \rightarrow 0$  are the values determined in the non-rotating case (section 2.9) and the corresponding limiting forms  $\bar{\mu}_{k0}$  of the coefficients  $\bar{\mu}_k$  follow from the boundary condition (6.3.7) which, in the limit as  $T \rightarrow 0$ , gives

$$Re \left\{ \sum_{k=1}^{\infty} \mu_{k0} V_{k0} \right\} + \sum_{k=1}^{\infty} \bar{\mu}_{k0} \bar{V}_{k0} = -G(z; 0) \quad (6.5.11)$$

The functions  $V_{k0}$  and  $G$  may be written as Fourier sine series

$$V_{k0} = \sum_{n=1}^{\infty} a_{n,k} \sin \beta_n z \quad \text{and} \quad G = \sum_{n=1}^{\infty} b_n \sin \beta_n z, \quad (6.5.12)$$

where  $\beta_n = (2n - 1)\pi/2$  and

$$a_{n,k} = \frac{-4\alpha_{k0}^3 \beta_n}{(\alpha_{k0}^2 - \beta_n^2)^3}, \quad b_n = \frac{8(-1)^n - 5\beta_n}{4\beta_n^6}. \quad (6.5.13)$$

Then a Fourier sine series in  $\sin \beta_n z$  of the boundary condition (6.3.7) gives

$$\sum_{n=1}^{\infty} b_n \sin \beta_n z + Re \left\{ \sum_{k=1}^{\infty} \mu_{k0} \sum_{n=1}^{\infty} a_{n,k} \sin \beta_n z \right\} + \sum_{n=1}^{\infty} \bar{\mu}_{n0} \sin \beta_n z = 0, \quad (6.5.14)$$

and equating coefficients of  $\sin \beta_n z$  yields

$$\bar{\mu}_{n0} = -b_n - Re \left\{ \sum_{k=1}^{\infty} \mu_{k0} a_{n,k} \right\}. \quad (6.5.15)$$

The first eight values of  $\mu_{k0}$  found earlier were used in (6.5.15) to give the first four values of  $\bar{\mu}_{k0}$  given in Table 6.1. These were checked using a collocation method where eight values of  $z$  are substituted into (6.3.7) and the resulting matrix problem for the constants  $\bar{\mu}_{k0}$  was solved using Gaussian elimination with partial pivoting.

$\bar{\mu}_{10}$	$= -3.555 \times 10^{-3}$
$\bar{\mu}_{20}$	$= 2.562 \times 10^{-3}$
$\bar{\mu}_{30}$	$= -1.419 \times 10^{-4}$
$\bar{\mu}_{40}$	$= 2.921 \times 10^{-5}$

(6.5.16)

Table 6.1: Estimates of the first four values of  $\bar{\mu}_{k0}$ .

The leading order azimuthal velocity at small Rayleigh numbers and Taylor numbers has thus been found analytically; contours of this function are given in figure 6.9. This shows all the azimuthal flow to be in one direction, so that at small Taylor number there is no return flow.

## 6.6 Leading order end zone solution for large $T$

The form of the eigenvalues for small  $R_1$  and large  $T$  was discussed in chapter 5. For the cold end zone there is a single mode for which

$$\bar{\alpha}_0 \sim -2^{-1/4} T^{1/8} \quad (T \rightarrow \infty), \quad (6.6.1)$$

and a triply infinite set of modes for which

$$\alpha_k \sim -\frac{1}{2}(k\pi)^{1/3}(1+i\sqrt{3})T^{1/6} \text{ and } \bar{\alpha}_k \sim -(k\pi)^{1/3}T^{1/6} \quad (T \rightarrow \infty). \quad (6.6.2)$$

Excluding the Ekman layer regions near  $z = 0$  and  $z = 1$ ,  $G(z; T) \sim zT^{-1}$  as  $T \rightarrow \infty$  so from (6.3.2),  $v_0$  can be written in the form

$$v_0 = T^{-\frac{1}{2}} \left\{ z + \bar{v}_0 V_0 e^{-2^{-\frac{1}{4}} T^{\frac{1}{8}} x} + \sum_{k=1}^{\infty} \left( \text{Re} \{ \nu_k e^{-\frac{1}{2}(k\pi)^{1/3}(1+i\sqrt{3})T^{\frac{1}{6}} x} + \bar{\nu}_k e^{-(k\pi)^{1/3}T^{\frac{1}{6}} x} \} V_k \right) \right\}, \quad (6.6.3)$$

where the coefficients  $\mu_k$  and  $\bar{\mu}_k$  are assumed to have the limiting forms

$$\mu_k \sim T^{-\frac{1}{2}} \nu_k \text{ and } \bar{\mu}_k \sim T^{-\frac{1}{2}} \bar{\nu}_k \text{ as } T \rightarrow \infty. \quad (6.6.4)$$

From the asymptotic analyses of section 5.3.3, away from the Ekman layers,  $V_0 = 1$  and  $V_k = \cos k\pi z$ . Also from (6.2.6) the corresponding leading order stream function in the inner Stewartson layer can be shown to be

$$\psi_0 = T^{-\frac{2}{3}} \sum_{k=1}^{\infty} (k\pi)^{-\frac{1}{3}} \left( \bar{\nu}_k e^{-(k\pi)^{1/3}T^{\frac{1}{6}} x} - \text{Re} \left\{ \frac{1}{2} (1 - i\sqrt{3}) \nu_k e^{-\frac{1}{2}(k\pi)^{1/3}(1+i\sqrt{3})T^{\frac{1}{6}} x} \right\} \right) \sin k\pi z, \quad T \rightarrow \infty. \quad (6.6.5)$$

For the azimuthal velocity to vanish on the vertical wall at  $x = 0$ , it is necessary that

$$\bar{v}_0 + \sum_{k=1}^{\infty} (\text{Re} \{ \nu_k \} + \bar{\nu}_k) \cos k\pi z = -z. \quad (6.6.6)$$

It is also necessary for the stream function and its first derivative with respect to  $x$  to vanish there, so that from (6.6.5) the other two vertical wall conditions at leading order are

$$\sum_{k=1}^{\infty} \left( \operatorname{Re}\left\{-\frac{1}{2}(1-i\sqrt{3})\nu_k\right\} + \bar{\nu}_k \right) = 0, \quad (6.6.7)$$

and

$$\sum_{k=1}^{\infty} (\operatorname{Re}\{\nu_k\} - \bar{\nu}_k) = 0. \quad (6.6.8)$$

By writing  $z$  as a Fourier cosine series and comparing coefficients of  $\cos k\pi z$ , (6.6.6) yields

$$\bar{\nu}_0 = -\frac{1}{2}, \quad (6.6.9)$$

and

$$\operatorname{Re}\{\nu_k\} + \bar{\nu}_k = \frac{2(1-(-1)^k)}{(k\pi)^2}, \quad k \geq 1. \quad (6.6.10)$$

It then follows that

$$\bar{\nu}_k = \frac{(1-(-1)^k)}{(k\pi)^2}, \quad k \geq 1 \quad (6.6.11)$$

and

$$\nu_k = \frac{(1-(-1)^k)(3+i\sqrt{3})}{(k\pi)^2} \frac{1}{6}, \quad k \geq 1. \quad (6.6.12)$$

Thus the azimuthal velocity for small Rayleigh number and large Taylor number has been found at leading order to be

$$\begin{aligned} v_0 \sim T^{-\frac{1}{2}} \left[ z - \frac{1}{2} e^{-2^{-\frac{1}{4}} T^{\frac{1}{8}} x} + \sum_{n=1}^{\infty} \frac{(1-(-1)^n)}{(n\pi)^2} \cos n\pi z \left( e^{-(n\pi)^{\frac{1}{3}} T^{\frac{1}{6}} x} \right. \right. \\ \left. \left. + \frac{(3+i\sqrt{3})}{6} e^{-\frac{1}{2}(n\pi)^{\frac{1}{3}}(1+i\sqrt{3})T^{\frac{1}{6}} x} + \frac{(3-i\sqrt{3})}{6} e^{-\frac{1}{2}(n\pi)^{\frac{1}{3}}(1-i\sqrt{3})T^{\frac{1}{6}} x} \right) \right] \quad (6.6.13) \end{aligned}$$

in the core region excluding the Ekman layers. The corresponding leading order stream function is

$$\begin{aligned} \psi_0 \sim T^{-\frac{2}{3}} \sum_{n=1}^{\infty} \frac{((-1)^n - 1)}{(n\pi)^{7/3}} \sin n\pi z \left( e^{-(n\pi)^{\frac{1}{3}} T^{\frac{1}{6}} x} \right. \\ \left. + (3-i\sqrt{3}) e^{-\frac{1}{2}(n\pi)^{\frac{1}{3}}(1+i\sqrt{3})T^{\frac{1}{6}} x} + (3+i\sqrt{3}) e^{-\frac{1}{2}(n\pi)^{\frac{1}{3}}(1-i\sqrt{3})T^{\frac{1}{6}} x} \right). \quad (6.6.14) \end{aligned}$$

Contours of this stream function and azimuthal velocity are plotted for  $T = 5000$  in figures 6.10 and 6.11, and for  $T = 10^8$  in figures 6.12 and 6.13. The small error on the wall  $x = 0$  in the azimuthal velocity plots is due to taking a finite number of modes, typically eight. The shaded bands in the stream function plot are of circulations with opposing directions of rotation decaying exponentially into the core.

In the inner Stewartson layer, the conditions on  $\theta_1$  at  $x = 0$  and as  $x \rightarrow \infty$  are the same as for  $v_0$ . Consideration of (6.2.7) thus implies that to a first approximation as  $T \rightarrow \infty$ ,  $\theta_1 = T^{1/2}v_0$ . It then follows from (6.2.39), that for large  $T$ , where  $\theta_1 = O(T^{-1})$  and  $\psi_0 = O(T^{-2/3})$  in the inner Stewartson layer,  $c_2 = O(T^{-11/6})$  as  $T \rightarrow \infty$ . This agrees with the numerical results given in figure 6.8 which show  $c_2$  decaying with increasing  $T$ .

The most obvious difference between the small and large Taylor number azimuthal velocity contours is the 'return' flow in the bottom left of the cavity at large Taylor numbers. This is the effect of the  $T^{1/8}$  mode in (6.6.13): in the outer Stewartson layer the integral of  $v$  with respect to  $z$  is reduced to zero at the outer edge of the inner layer. The complex modes then ensure that within the inner Stewartson layer the boundary conditions at  $x = 0$  are met. For the stream function, however, the physical importance of the layers is reversed: in the outer Stewartson layer there is a relatively minor adjustment of the stream function whereas in the inner layer there is a large closed circulation associated with the complex modes in (6.6.14). The difference in the length scales of the return flow in the azimuthal velocity and the circulation in the stream function is most evident in the  $T = 10^8$  plot. Although the Ekman layers are not properly formed at  $T = 5000$ , comparison of the analytical results of figures 6.10 and 6.11 with the numerical results of figure 6.6 and 6.7, suggests that these two results are in good agreement.

## 6.7 Discussion

In this chapter, the nature of the transition from small to large Taylor number flow in the end-regions has been determined by means of numerical results for finite  $T$  linking the analytical solutions for small and large Taylor number. The results are restricted to small Rayleigh numbers.

For small  $T$ , the stream function is the same as in the non-rotating case, and the azimuthal velocity is unidirectional in the direction of the rotation. As  $T$  increases, a region of recirculation, initially centred around the height at which the horizontal core flow vanishes, moves down slightly and towards the cold wall. Away from the cold wall, along the bottom of the cavity, there is a return of the azimuthal flow. As  $T$  becomes larger the region of recirculation moves closer to the vertical

wall to eventually reside within the inner Stewartson layer of thickness  $x \sim T^{-1/6}$  with the centre of circulation at mid-cavity height. At large Taylor number, the core flow away from the inner Stewartson layer and the horizontal Ekman layers is dominated by the azimuthal flow. The return flow of the large Taylor number azimuthal flow is confined to a jet in the lower half of the outer Stewartson layer and there is a further adjustment of the azimuthal flow in the inner Stewartson layer. Outside the outer Stewartson layer and the Ekman layers, the azimuthal velocity is directly proportional to the cavity depth. The radial flow across the cavity is confined to the Ekman layers, which transport fluid from the hot end to the cold end near the free surface and in the opposite direction near the base. This flow becomes slower as the Taylor number increases.

The small Rayleigh number theory for the non-rotating case developed in chapter 2, has been extended in this chapter to give a leading order solution throughout the cavity for general Taylor numbers. Values of the constants  $A_1$  and  $B_1$  which determine the first order correction to the core solution arising from convective effects and the presence of the end walls have been found as a function of the Taylor number. At leading order,  $B_1$  increases to zero with increasing  $T$  indicating that these effects are diminished by rotation and the core temperature becomes conduction dominated. The value of  $A_1$  decreases with increasing  $T$  indicating that the reduction in the stream function, azimuthal velocity and horizontal thermal gradient in the core is also diminished with increasing rotation.

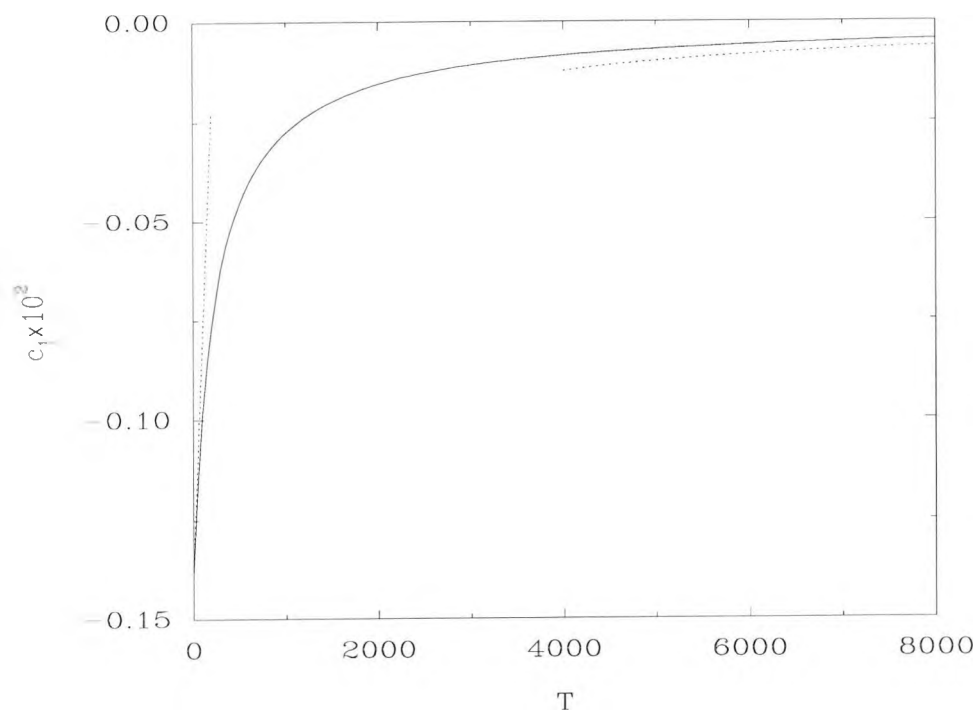


Figure 6.1: Values of  $c_1$  as a function of  $T$ . The dotted lines are the asymptotic solutions.

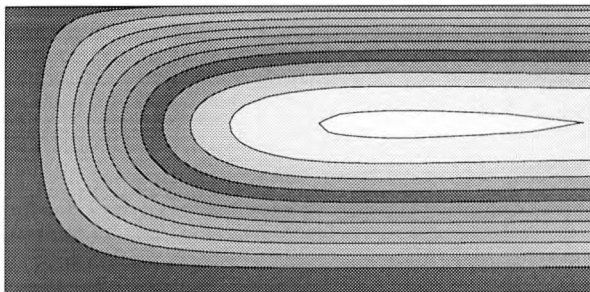


Figure 6.2: Numerical results: streamlines  $\psi_0 = \text{constant}$  for  $T = 100$ .

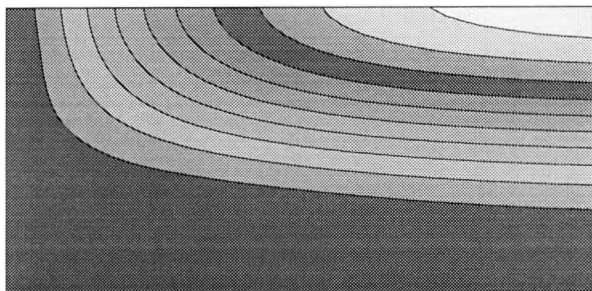


Figure 6.3: Numerical results: contours of constant azimuthal velocity  $v_0$  for  $T = 100$ .

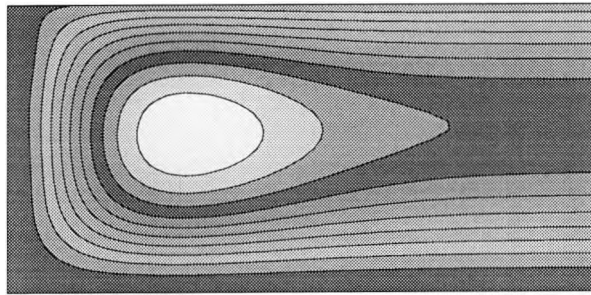


Figure 6.4: Numerical results: streamlines  $\psi_0 = \text{constant}$  for  $T = 2000$ .

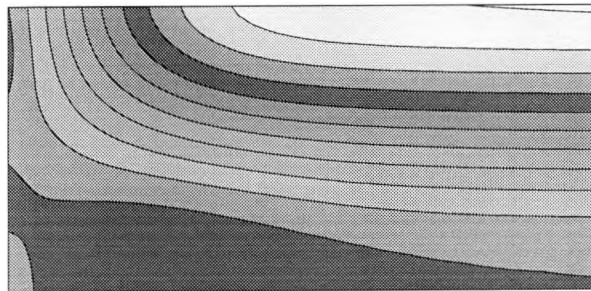


Figure 6.5: Numerical results: contours of constant azimuthal velocity  $v_0$  for  $T = 2000$ .

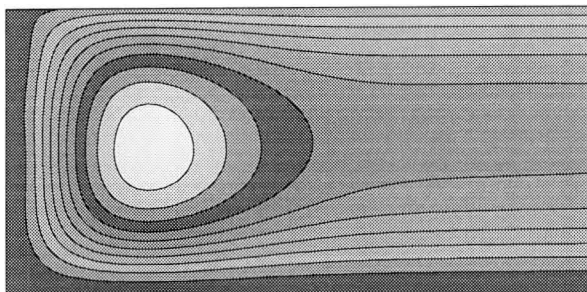


Figure 6.6: Numerical results: Streamlines  $\psi_0 = \text{constant}$  for  $T = 5000$ .

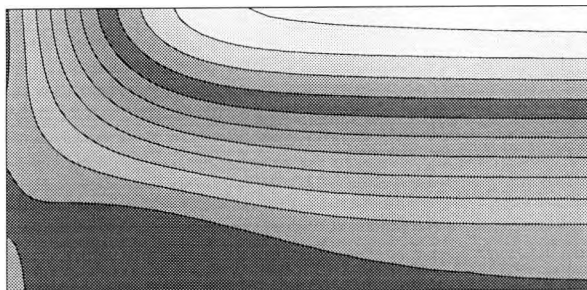


Figure 6.7: Numerical results: contours of constant azimuthal velocity  $v_0$  for  $T = 5000$ .

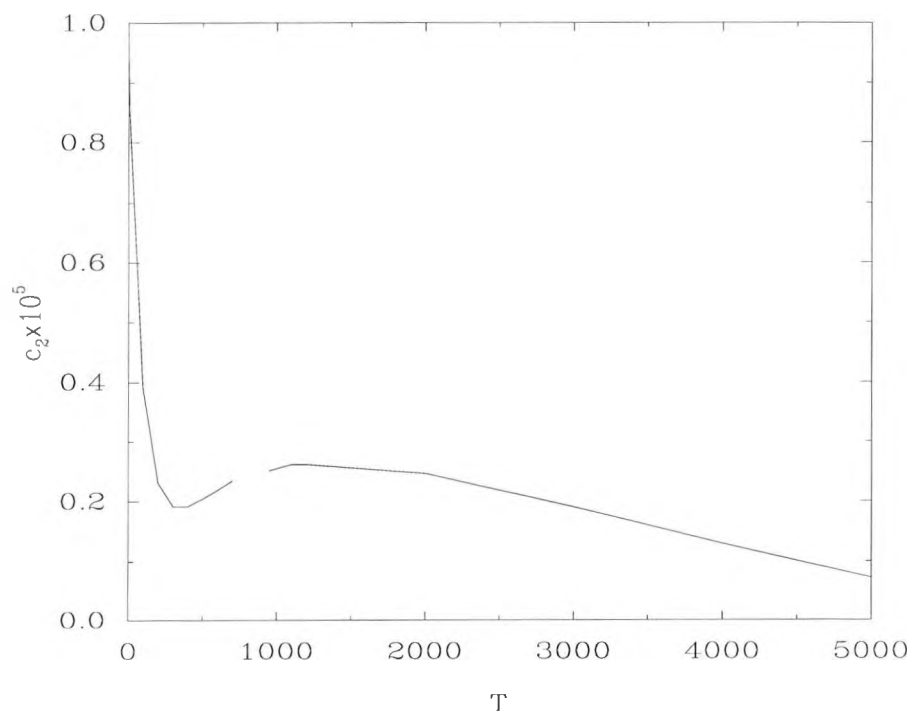


Figure 6.8: Values of  $c_2$  as a function of  $T$ .

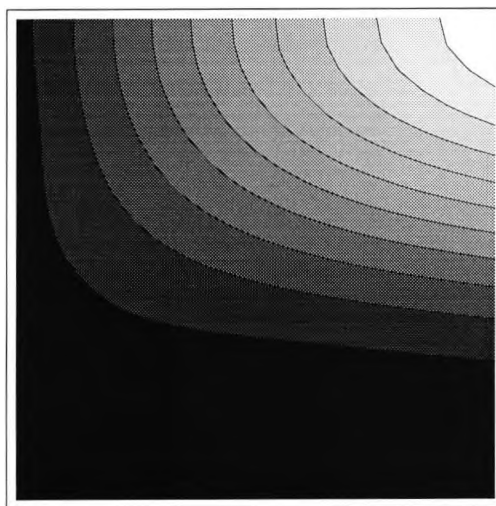


Figure 6.9: Contours of the leading order azimuthal velocity  $v_0$  as  $T \rightarrow 0$ .

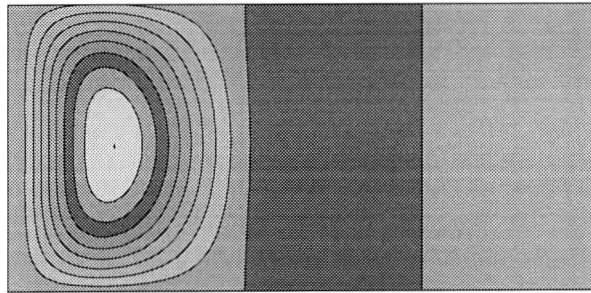


Figure 6.10: Analytical results based on the asymptotic theory: streamlines  $\psi_0 = \text{constant}$  for  $T = 5000$ , excluding the Ekman layers.

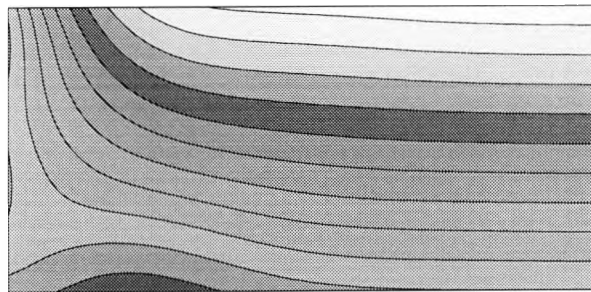


Figure 6.11: Analytical results based on the asymptotic theory: contours of constant azimuthal velocity  $v_0$  for  $T = 5000$ , excluding the Ekman layers.

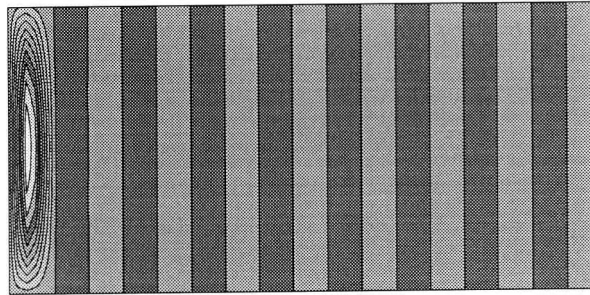


Figure 6.12: Analytical results based on the asymptotic theory: streamlines  $\psi_0 = \text{constant}$  for  $T = 10^8$ , excluding the Ekman layers.

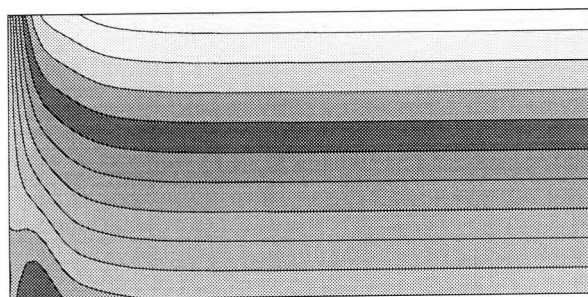


Figure 6.13: Analytical results based on the asymptotic theory: contours of constant azimuthal velocity  $v_0$  for  $T = 10^8$ , excluding the Ekman layers.

# Chapter 7

## Conclusion

### 7.1 Summary

This thesis has been concerned with the flow in a shallow laterally heated cavity with a stress free upper surface, and has considered the two dimensional flow in the non-rotating case and its stability to oscillatory perturbations and the three dimensional flow in the case of a rotating cavity, the latter being analogous to the axisymmetric flow in a rotating annulus with differentially heated vertical walls.

The Hadley cell, formed when the fluid near the hot wall rises and the fluid near the cold wall sinks, consists of a parallel-flow core region and two end regions where the fluid is turned. Unlike in the rigid surface case, the lack of symmetry meant that the end regions had to be considered individually. Also it was seen that, unlike the rigid surface case, there are no steady non-decaying oscillations propagating from the end-regions into the core to formally invalidate the assumption of a parallel flow core. However, like the rigid surface case, the non-rotating flow is unstable at low Prandtl numbers and sufficiently high Rayleigh numbers and then in practice the parallel flow core will be replaced by a travelling wave structure.

In the non-rotating case, approximately the top 40% of the flow in the core is moving from the hot end to the cold end with a maximum speed at the free surface, and the bottom 60% is moving more slowly from the cold end to the hot end. This causes the temperature field to change from one of pure conduction, that is dependent only on the distance from the vertical (differentially heated) walls, to

a depth dependent one – the top of the cavity being hotter than the bottom. The magnitude of the flow speed and vertical temperature difference is directly dependent on the Rayleigh number based on the temperature difference between the two end walls:  $R_1 = \beta g(\Theta_h^* - \Theta_c^*)h^3/\nu\kappa L$ .

The effect of rotation on this core flow is to gradually confine the radial flow to thin Ekman layers close to the horizontal boundaries and to slow the speed of this flow. Outside the Ekman layers, with no radial flow between the two vertical walls, the temperature field becomes conduction dominated. The Ekman layers are of thickness  $T^{-1/4}$  where  $T$  is the Taylor number based on the rate of rotation:  $T = 4\Omega^2 h^4/\nu$ . For non-zero rotation rates, there is an azimuthal velocity in the direction of rotation the magnitude of which grows as  $T^{1/2}$  as  $T$  increases from zero, reaching a maximum at  $T \approx 250$ , before it too is damped by large rotation rates. Outside the Ekman layers, the azimuthal core velocity is directly proportional to depth.

Solutions for the end regions were obtained in the form of an infinite sum of eigenfunctions decaying into the core, the eigenvalues defining the rate of decay and hence the size of the end-regions. The leading order solution for the eigenfunctions was found analytically in the limit of small Rayleigh and Taylor numbers. For small Rayleigh number and general Taylor numbers, the two end regions are symmetric at leading order; the flow is simply turned and the depth dependence on temperature gradually disappears as  $x$  tends to zero, as does the azimuthal velocity. The leading order solution is also independent of the Prandtl number,  $\sigma = \nu/\kappa$ . A numerical scheme based on a Fourier series representation was used to find the relative sizes of the eigenfunctions such that the vertical wall conditions were satisfied, and thus match the end regions to the core to complete a leading order solution for the entire cavity at small Rayleigh numbers and general Taylor numbers. The results of this show the damping effect of rapid rotation on the temperature and velocities.

Solutions of the eigenvalue problems in the end regions were found numerically for general values of the Rayleigh number and Taylor number using a fourth order Runge-Kutta scheme. Results were given for general  $R_1$  and  $T = 0, 500$  and  $5000$ , and for  $R_1 = 0$  and general  $T$ . These numerical results complemented asymptotic theories developed for large  $R_1$  and for large  $T$ . For large  $R_1$  and no rotation ( $T = 0$ ), asymptotic theory showed that the size of the end regions is directly pro-

portional to the Rayleigh number, that the cold end zone is slightly larger than the hot end zone, but that both ends were roughly twice the size of the end regions in the rigid surface case. For small Prandtl number, the end regions are dominated by decaying oscillatory modes, and for infinite Prandtl number they are dominated by decaying non-oscillatory modes. In practice however, it was seen that for  $\sigma > 2$ , the solution behaved as though the Prandtl number was infinite and in the asymptotic theory for large  $T$  and small  $R_1$ , only the case of infinite Prandtl number was investigated. In this case the leading eigenvalue was seen to behave as  $T^{1/8}$  and the subsequent eigenvalues were seen to behave as  $T^{1/6}$ . This corresponds to two vertical boundary layers, or Stewartson layers, of thickness  $T^{-1/8}$  and  $T^{-1/6}$  close to the vertical walls. The outer layer contains an azimuthal jet which flows in the opposite sense to the direction of rotation and the rest of the azimuthal flow. The inner layer contains an intense recirculation flow which lies inside the large-scale Hadley circulation which is completed by the radial flow in the Ekman layers. By use of the Fourier series representation of the eigenfunctions and application of the vertical wall conditions, results for general  $T$  were presented which demonstrated the development of the inner recirculation, the azimuthal jet and the Stewartson layers.

In general terms, the eigenvalue analysis has shown that the lateral extent of the end zones increases with increasing large Rayleigh number and decreases with increasing Taylor number. For finite Taylor numbers, the leading eigenvalues behave as the inverse of the Rayleigh number as  $R_1 \rightarrow \infty$  indicating that the end zones then have a large lateral scale of order  $R_1$ . This scale diminishes with increasing Taylor number and when  $1 \ll T \ll R_1$  the lateral scale is proportional to  $R_1/T$ . An asymptotic solution for this regime led to the identification of a novel structure in which the thermal properties of the Ekman layers are shown to play an important rôle in the determination of the lateral scale.

The stability of the non-rotating parallel-flow core to both transverse and longitudinal perturbations has been investigated in detail in this thesis: numerically for general wave numbers and Rayleigh numbers and asymptotically for large Rayleigh number. Instabilities only occur for small Prandtl numbers: using both numerical and asymptotic techniques it was shown that the core flow is always stable to transverse mode oscillations for Prandtl numbers greater than 0.162, and stable to longitudinal oscillations for Prandtl numbers greater than 0.415.

Neutral curves produced numerically for general Rayleigh numbers and wavenumbers indicate that except at extremely small Prandtl numbers, the longitudinal instabilities are more important than the transverse instabilities in that they occur at smaller values of the Rayleigh number. Numerical solutions were used to show the effect of the neutral perturbations on the core flow and their speed of propagation: approximately one third of the free surface speed. An asymptotic analysis shows that along the left hand branch of both the longitudinal and transverse neutral curves the wavenumber behaves as the inverse of the Rayleigh number as  $R_1 \rightarrow \infty$ , so that the higher the Rayleigh number the larger the wavelength of neutrally stable oscillations. In the case of the transverse oscillations, the right hand branch of the neutral curve was shown to approach a finite wavenumber for large Rayleigh numbers, but for longitudinal mode the wavenumber of the right-hand branch behaves as the inverse of the Rayleigh number. Thus, while finite wavelength transverse instabilities are supported at large  $R_1$  and finite  $\sigma$ , only large wavelength longitudinal instabilities persist. An asymptotic theory showed that finite wavelength longitudinal instabilities can be supported at large Rayleigh number, but only for vanishingly small Prandtl number.

## 7.2 Future work

The work presented in this thesis suggests a number of avenues for further research, both on the stability of the free surface flow and its basic steady-state structure. In connection with the stability of the flow, the asymptotic theory developed in chapter 3 suggests that, in a three dimensional box, if the long wavelength longitudinal modes are excluded by vertical side walls parallel to the  $x, z$  plane, the finite wavelength transverse modes may then be more 'dangerous' at large Rayleigh number. The influence of such side walls is not investigated at all in this thesis, but would be of interest in relating the theory to applications in crystal growth and other areas. In this case the basic core flow and temperature fields will depend on both  $z$  and  $y$  and the end-region flows will become fully three dimensional even in the non-rotating case.

For the two-dimensional cavity, the stability of the rotating core flow has not been addressed here, nor has the stability of the core to three dimensional pertur-

bations that oscillate in both  $x$  and  $y$ . Another much more difficult undertaking would be to study the stability of the flow in the end regions.

The steady state flow has been investigated in depth in this thesis with both numerical and asymptotic results being presented and in particular asymptotic results for both large and small values of the Rayleigh and Taylor numbers. A numerical multigrid scheme was used to check the analytical results in the steady, non-rotating, small  $R_1$  case, but a much more comprehensive numerical study is needed to examine the non-linear flows for finite and large  $R_1$  both for the non-rotating and rotating cases, enabling the constants  $c$  and  $\bar{c}$  to be determined over a much wider region of the three dimensional parameter space  $(R_1, \sigma, T)$ . A numerical study of this kind would complement the asymptotic results obtained here. On the theoretical side, it is envisaged that further analysis could be undertaken to investigate the effect of the Prandtl number in the rotating case; the difficulty of actually viewing the flow in low Prandtl number fluids gives added incentive to theoretical and numerical investigations of this regime. Another area of theoretical interest is the limiting case where both  $R_1$  and  $T$  are large; the asymptotic analysis of chapter 5 for  $1 \ll T \ll R_1$  suggests an interesting boundary layer structure arises in this limit and it may be possible to extend this analysis to investigate the flow structure throughout the end regions and to consider the case where  $R_1$  and  $T$  are of comparable magnitude.

Finally, it would be of interest to carry out a numerical investigation of the full cavity flow for various values of  $R_1$ ,  $\sigma$ ,  $T$  and for moderate to large values of  $L$ . There are few numerical studies for the shallow cavity with a free upper surface, and even fewer for the rotating free surface cavity.

The projects outlined above arise from the studies in this thesis. There are many other interesting problems associated with free surface flow in a shallow laterally heated cavity, such as the inclusion of thermocapillary forces or the consideration of a difference in the depth of fluid in the cold and hot end regions, but it is hoped that this thesis serves as a good basis for study in these areas.

## References and Bibliography

- Batchelor, G.K. 1954 Heat transfer by free convection across a closed cavity between vertical boundaries at different temperatures. *Q. J. Appl. Math.* **12**, 209 - 233.
- Batchelor, G.K. 1967 *An Introduction to Fluid Dynamics*. Cambridge University Press.
- Bejan, A., Al-Houmoud, A.A. and Imberger 1981 Experimental study of high Rayleigh number convection in a horizontal cavity with different end temperatures. *J. Fluid Mech.* **109**, 283 - 299.
- Bejan, A. and Rossie A.N. 1981 Natural-convection in horizontal duct connecting two fluid reservoirs. *J. Heat Trans* **103**, 180 - 113.
- Bell, P.I. and Soward, A.M. 1996 The influence of surface topography in rotating convection. *J. Fluid Mech.* **313**, 147 - 180.
- Ben Hadid, H. and Roux, R. 1992 Buoyancy- and thermocapillary-driven flows in differentially heated cavities for low-Prandtl-number fluids. *J. Fluid Mech.* **235**, 1 - 36.
- Boyack, B.E. and Kearney, D.W. 1972 Heat transfer by laminar natural convection in low aspect ratio cavities. ASME Paper, 72-HT-2.
- Busse, F.H. 1986 Convection in a rotating, cylindrical annulus. *J. Fluid Mech.* **173**, 545 - 556.
- Busse, F.H. and Or, A.C. 1986 Convection in a rotating cylindrical annulus: thermal Rossby waves. *J. Fluid Mech.* **166**, 173 - 187.
- Chandrasekhar, S. 1968 *Hydrodynamic and Hydromagnetic Stability*. Oxford University Press.
- Cormack, D.E., Leal, L.G. and Imberger, J. 1974 Natural convection in a shallow cavity with differentially heated end walls. Part 1. Asymptotic theory. *J. Fluid Mech.* **65**, 209 - 229.
- Cormack, D.E., Leal, L.G. and Seinfeld, J.H. 1974 Natural convection in a shallow cavity with differentially heated end walls. Part 2. Numerical solutions. *J. Fluid Mech.* **65**, 231 - 246.
- Cormack, D.E., Stone, G.P. and Leal, L.G. 1975 The effect of upper surface conditions on convection in a shallow cavity with differentially heated end-walls. *Int. J. Heat Mass Transfer* **18**, 635 - 648.
- Daniels, P.G. 1976 Thermal convection in a differentially heated rotating fluid annulus. *Geophysical Fluid Dynamics* **7**, 297 - 330.
- Daniels, P.G. 1993 High Rayleigh number thermal convection in a shallow laterally heated cavity. *Proc. R. Soc. Lond.* **440**, 273 - 289.
- Daniels, P.G., Blythe, P.A. and Simpkins, P.G. 1987 Onset of multicellular convec-

- tion in a shallow laterally heated cavity. *Proc. R. Soc. Lond.* **411** 327 - 350.
- Daniels, P.G. and Stewartson, K. 1977 On the spatial oscillations of a horizontally heated rotating fluid. *Math. Proc. Camb. Phil. Soc* **81**, 325 - 349.
- Daniels, P.G. and Stewartson, K. 1977 On the spatial oscillations of a horizontally heated rotating fluid II. *Q. J. Mech. Appl. Math.* **31**, 113 - 135.
- Daniels, P.G. and Stewartson, K. 1978 Overstable convection in a horizontally heated rotating fluid. *Math. Proc. Camb. Phil. Soc* **83**, 329 - 345.
- Daniels, P.G. and Wang, P. 1994 On the evolution of thermally driven shallow cavity flows. *J. Fluid Mech.* **259**, 107 - 124.
- Defant, A. 1961 *Physical oceanography*, vol. 1. New York: Pergamon Press.
- Dijkstra, D. and van Heijst, G.J.F. 1983 The flow between two finite rotating disks enclosed by a cylinder. *J. Fluid Mech.* **128**, 123 - 154.
- Douglas, H.A. and Mason, P.J. 1973 Thermal convection in a large rotating fluid annulus: some effects of varying the aspect ratio. *J. Atmos. Sci.* **30**, 1124 - 1134.
- Duncan, I.B. 1966 Axi-symmetric convection between two rotating disks. *J. Fluid Mech.* **24**, 417 - 449.
- Farrow, D.E. and Patterson, J.C. 1993 On the response of a reservoir sidearm to diurnal heating and cooling. *J. Fluid Mech.* **246**, 143 - 161.
- Finlay, W.H. 1990 Transition to oscillatory motions in rotating channel flow. *J. Fluid Mech.* **215**, 209 - 227.
- Finlay, W.H. 1992 Transition to turbulence in a rotating channel. *J. Fluid Mech.* **237**, 73 - 100.
- Fowles, W.W. and Hide, R. 1965 Thermal convection in a rotating annulus of liquid: effect of viscosity on the transition between axisymmetric and non-axisymmetric flow regimes. *J. Atmos. Sci.* **22**, 541 - 558.
- Gill, A.E. 1966 The boundary-layer regime for convection in a rectangular cavity. *J. Fluid Mech.* **26**, 515 - 536.
- Gill, A.E. 1974 A theory of thermal oscillations in liquid metals. *J. Fluid Mech.* **64**, 557 - 588.
- Greenspan, H.P. 1968 *The Theory of Rotating Fluids*. Cambridge University Press.
- Hadley, G.S. 1735 Concerning the cause of the general trade winds. *Phil. Trans.* **29**, 58 - 62.
- Hart, J.E. 1972 Stability of thin non-rotating Hadley circulations. *J. Atmos. Sci.* **29**, 687 - 697.
- Hart, J.E. 1983a Low Prandtl number convection between differentially heated end

- walls. *Int. J. Heat Mass Transfer* **26**, 1069 - 1074.
- Hart, J.E. 1983b A note on the stability of low-Prandtl-number Hadley circulations. *J. Fluid Mech.* **132**, 271 - 281.
- van Heijst, G.J.F., Maas, L.R.M. and Williams, C.W.M. 1994 The spin up of fluid in a rectangular container with a sloping bottom. *J. Fluid Mech.* **265**, 125 - 160.
- Hide, R. 1967 Theory of axisymmetric thermal convection in a rotating fluid annulus. *Phys. Fluids* **10**, 56 - 68.
- Hignett et al. 1981 On rotating thermal convection driven by non-uniform heating from below. *J. Fluid Mech.* **109**, 161 - 187.
- Hillman, A.P. and Salzer, M.E. 1943 Roots of  $\sin z = z$ . *Phil. Mag.* **34**, 575.
- Hopfinger, E.J. and Linden, P.F. 1990 The effect of background rotation on fluid motions: a report on Euromech 245. *J. Fluid Mech.* **211**, 417 - 435.
- Hurle, D.T., Jakeman, E. and Johnson, C.P. 1974 Convective temperature oscillations in molten gallium. *J. Fluid Mech.* **64**, 565 - 576.
- Hunter, C. 1967 The axisymmetric flow in a rotating annulus due to a horizontally applied temperature gradient. *J. Fluid Mech.* **27**, 753 - 778.
- Hurle, D.T. 1966 Temperature oscillations in molten metals and their relationship to the growth state in melt grown crystals. *Phil. Mag.* **13**, 305 - 310.
- Hurle, D.T., Jakeman, E. and Johnson, C.P. 1974 Convective temperature oscillations in molten gallium. *J. Fluid Mech.* **64**, 565
- Imberger, J. 1974 Natural convection in a shallow cavity with differentially heated end walls. Part 3. Experimental results. *J. Fluid Mech.* **65**, 247 - 260.
- Jain, S.C. 1982 Buoyancy-driven circulation in free-surface channels. *J. Fluid Mech.* **122**, 1 - 12.
- Jeffreys, H. 1925 On fluid motions produced by differences of temperature and humidity. *Quart. J. Roy. Met. Soc.* **51**, 347.
- Kristoffersen, R. and Andersson, H.I. 1993 Direct simulations of low-Reynolds-number turbulent flow in a rotating channel. *J. Fluid Mech.* **256**, 163 - 197.
- Kuo, H.P. and Korpela, S.A. Stability and finite amplitude natural convection in a shallow cavity with insulated top and bottom and heated from a side. *Phys. Fluids* **31**, 33 - 42.
- Laure, P. and Roux, B. 1989 Linear and non-linear analysis of the Hadley circulation. *J. Crystal Growth* **97**, 226 - 234.
- Lingwood, R.J. 1995 Absolute instabilities of the boundary layer on a rotating disk. *J. Fluid Mech.* **299**, 17 - 33.

- Lingwood, R.J. 1996 An experimental study of absolute instability of the rotating-disk boundary layer flow. *J. Fluid Mech.* **314**, 373 - 405.
- McIntyre, M.E. 1968 The axisymmetric convective regime for a rigidly bounded rotating annulus. *J. Fluid Mech.* **32**, 625 - 655.
- Miller, T.L. and Reynolds, N.D. 1991 A study of baroclinic instability in a cylindrical annulus with the temperature gradient imposed on the lower surface. *J. Fluid Mech.* **233**, 495 - 518.
- O'Donnell, and Linden 1991 Free-surface effects on the spin up of a fluid in a rotating cylinder. *J. Fluid Mech.* **232**, 439 - 453.
- Or, A.C. and Busse, F.H. 1987 Convection in a rotating, cylindrical annulus. Part 2: Transitions to asymmetric and vacillating flow. *J. Fluid Mech.* **174**, 313 - 326.
- Quon, C. 1972 High Rayleigh number convection in an enclosure - a numerical study. *Physics Fluids* **15**, 12
- Robinson, A.R. 1959 The symmetric state of a rotating fluid differentially heated in the horizontal. *J. Fluid Mech.* **6**, 599 - 620.
- Rosby, H.T. 1965 On thermal convection driven by non-uniform heating from below: An experimental study. *Deep Sea Res.* **12**, 9 - 16.
- Shiralkar, G.S. and Tien, C.L. 1981 A numerical study of laminar natural-convection in shallow cavities. *J. Heat Trans.* **103**, 226 - 231.
- Simpkins, P.G. and Chen, K.S. 1986 Convection in horizontal cavities. *J. Fluid Mech.* **166**, 21 - 39.
- Simpkins, P.G. and Dudderar, T.D. 1981 Convection in rectangular cavities with differentially heated end walls. *J. Fluid Mech.* **110**, 433 - 456 Smith, M.K. and Davis, S.H. 1983 Instabilities of dynamic thermocapillary liquid layers. Part2. Surface-wave instabilities. *J. Fluid Mech.* **132**, 145 - 162.
- Stern, M. 1975 *Ocean Circulation Physics*, Academic Press.
- Stewartson, K. 1957 On almost rigid rotations. *J. Fluid Mech.* **3**, 17-26.
- Stone, P.H. 1968 Some properties of Hadley regimes on rotating and non-rotating planets. *J. Atmos. Sci.* **25**, 644 - 657.
- Stern, M. 1975 *Ocean circulation physics*. New York: Academic Press.
- Sturm, T.W. 1981 Laminar gravitational convection of heat in dead-end channels. *J. Fluid Mech.* **110**, 97 - 114.
- Wang, P. and Daniels, P.G. 1994a Numerical solutions for the flow near the end of a shallow laterally heated cavity. *J. Eng. Math.* **28**, 211 - 226.
- Wang, P. and Daniels, P.G. 1994b Numerical study of thermal convection in shallow cavities with conducting boundaries. *Int. J. Heat Mass Transfer* **37**, 387 - 399.

Wempner, G. 1981 *Mechanics of solids with applications to thin bodies*. Sijthoff and Noordhoff.

Williams, W.J. and Maxworthy, T. 1994 Experiments on spin-up and spin-down on a  $\beta$  plane. *J. Fluid Mech.* **271**, 153 - 172.

Wright, N.G., Gaskell, P.H., and Sleigh, P.A., 1995 Natural convection in a shallow laterally heated air-filled cavity. *Num. Methods Eng.* **11**, 937-950.